Manoeuvring in Shallow Water – A Comprehensive and Detailed Analysis of Shallow-Water Effects on the Manoeuvring Behaviour of Modern Seagoing Vessels

Vom Promotionsausschuss der
Technischen Universität Hamburg

zur Erlangung des akademischen Grades

Doktor-Ingenieur (Dr.-Ing.)

genehmigte Dissertation (Monografie)

von
Marcus Döscher

aus
Hamburg

2026

Vorsitzender des Prüfungsausschusses
Prof. Dr.-Ing. Friedrich Wirz

Gutachter
1. Gutachter: Prof. Dr.-Ing. Moustafa Abdel-Maksoud
2. Gutachter: Prof. Dr.-Ing. Stefan Krüger
3. Gutachter: Dr.-Ing. Carl-Uwe Böttner

Tag der mündlichen Prüfung
12. Oktober 2026

Copyright © Marcus Döscher, 2026
ORCID iD: 0009-0005-3711-919X
Digital Object Identifier (DOI): 10.15480/882.19292

Creative Commons Lizenzvertrag
Der Text steht, soweit nicht anders gekennzeichnet, unter der Creative-Commons-Lizenz Namensnennung 4.0 (CC BY 4.0). Das bedeutet, dass er vervielfältigt, verbreitet und öffentlich zugänglich gemacht werden darf, auch kommerziell, sofern dabei stets der Urheber, die Quelle des Textes und o. g. Lizenz genannt werden.
Die genaue Formulierung der Lizenz kann unter
https://creativecommons.org/licenses/by/4.0/legalcode.de
aufgerufen werden.

Summary

This thesis investigates the altered manoeuvring behaviour of ships in shallow-water conditions using a combined model test–CFD approach. Comprehensive free-running model tests were conducted with two different ship types, a container ship and a bulk carrier, at a scale of 1:60. The experiments covered five different under-keel clearances, up to five advance speeds, and various draught and trim conditions. Ship motions were recorded using a laser tracking system and a fibre-optic gyro compass. In addition, the forces acting on the rudder and propeller were measured separately, enabling a detailed analysis of shallow-water effects as a function of keel clearance, speed, and floating condition.

The experimental findings served as the basis for further investigation using CFD simulations. Direct manoeuvring simulations were performed to analyse the hydrodynamic mechanisms responsible for the observed behaviour. The numerical setup was first verified by grid-convergence studies for resistance simulations and one complete manoeuvring simulation in shallow water for each ship. Subsequently, the simulations were validated against the executed model-test manoeuvres. The validation demonstrated a high level of agreement between numerical and experimental results, confirming the suitability of the simulations for detailed hydrodynamic analysis. By analysing pressure distributions and force contributions along the hull, the CFD simulations provided deeper insight into the flow mechanisms governing manoeuvring behaviour in shallow water.

The results reveal that the manoeuvring characteristics of ships respond differently to decreasing water depth and cannot be described by a single monotonic shallow-water trend. While turning ability generally deteriorates with decreasing under-keel clearance, the present study shows that this decline becomes significantly stronger in extreme shallow water and is accompanied by pronounced speed dependence. At the same time, course-keeping and yaw-checking performance do not continue to improve with decreasing water depth. Instead, stagnation and even deterioration of yaw-checking behaviour occur in extreme shallow water. Furthermore, pronounced directional asymmetries were identified in the course-changing ability of the investigated ships. With decreasing water depth, the asymmetry between port and starboard manoeuvres increases, culminating in a directional trend reversal for the bulk carrier in extreme shallow water. A similar trend reversal is observed for the container ship in its steady turning behaviour. The hydrodynamic analysis of the numerical results shows that shallow-water effects are governed not simply by an increase in global damping but by a depth-dependent redistribution of local hydrodynamic loads along the hull. In particular, a progressive shift of forces from the aft towards the fore ship with decreasing water depth was identified. The resulting balance between fore- and aft-ship forces plays a decisive role in determining the yaw moment and, consequently, the manoeuvring behaviour. The results further indicate that the extreme shallow-water condition corresponding to an under-keel clearance of 10 % of the ship's draught represents a distinct hydrodynamic regime. In this regime, several manoeuvring parameters exhibit trend reversals and increased sensitivity to speed. These findings highlight the importance of explicitly considering extreme shallow-water conditions and depth-Froude-number effects in manoeuvring prediction and the operational assessment of ships navigating in confined waterways.

Acknowledgements

I would like to express my sincere gratitude to Prof. Dr.-Ing. Moustafa Abdel-Maksoud for supervising this thesis and for his valuable professional insights and suggestions throughout my research. I am also grateful to Prof. Dr.-Ing. Stefan Krüger, my second supervisor, for reviewing this thesis and for the inspiring discussion during the defense. I would also like to thank Prof. Dr.-Ing. Friedrich Wirz for chairing the examination committee and for creating a pleasant and positive atmosphere during the defense.

I would like to express my heartfelt thanks to Uwe for his supervision and for his scientific and organizational support on behalf of the BAW. Without your active support, your ideas, and your talent for transforming a vision into concrete projects, this thesis would never have come to fruition. I am also especially grateful to Ingrid for her consistent support and encouragement throughout this research project.

Special thanks go to the technical team – Jonathan, Dirk, and Lars – whose tireless efforts during the extensive measurement campaigns and expertise in equipping the model ships made this thesis possible. In this context, I would like to thank Hanne, whose support and expertise in setting up the measurement equipment contributed significantly to the high-quality measurement data.

I am deeply thankful to my parents, who have invested so much in me, always encouraged me, and made my education and this degree possible in the first place. I am also very grateful to my entire family and my friends for the encouragement they have consistently given me.

To my two wonderful and beautiful daughters: thank you for always bringing a smile back to my face after difficult days and for reminding me of what matters most in life.

My deepest gratitude goes to my beautiful, wonderful, and intelligent wife. You have always believed in me, encouraged me, supported me fully, and had my back. Without you, I would never have been able to complete this work.

Contents

List of Figures III

List of Tables IX

Nomenclature XI

1. Introduction 1
- 1.1. Motivation . . . 1
- 1.2. Brief Literature Review . . . 1
- 1.3. Problem Definition . . . 3
- 1.4. Objectives of the Work . . . 4
- 1.5. Solution Approach . . . 4
- 1.6. Structure of the Doctoral Thesis . . . 4
- 1.7. Achievements Compared to the State of the Art . . . 5

2. State of the Art 7
- 2.1. Foundations of Manoeuvring Research . . . 7
- 2.2. Development of Free-Running Manoeuvring Tests . . . 8
- 2.3. Free-Running Manoeuvring in Shallow Water . . . 9
- 2.4. Captive Manoeuvring Tests in Shallow Water . . . 10
- 2.5. Development of RANS-Based Manoeuvring Simulations . . . 12
- 2.6. Ongoing Role of Experimental Methods in Manoeuvring Research . . . 14
- 2.7. RANS Applications to Shallow Water Manoeuvring . . . 15

3. Fundamentals of Numerical Method 17
- 3.1. Governing Equations . . . 17
- 3.2. Reynolds-Averaged Navier-Stokes Equations . . . 18
- 3.3. Numerical Method . . . 21
- 3.4. Interpolation and Discretisation Methods . . . 22
- 3.5. Solution Approaches . . . 23

4. Manoeuvring 25
- 4.1. Definitions . . . 25
- 4.2. Nomoto Equation . . . 26
- 4.3. Manoeuvring Tests . . . 28
  - 4.3.1. Free-running Tests . . . 28
  - 4.3.2. Captive Model Tests . . . 31
- 4.4. Influence of Shallow Water on Manoeuvrability . . . 31

5. Experimental Investigations **35**
5.1. Model Ships 35
5.2. Experimental Setup 39

6. Numerical Investigations **41**
6.1. Computational Domain 41
6.2. Uncertainty Analysis 44
6.2.1. Verification 44
6.2.2. Validation 47

7. Results and Discussion **59**
7.1. Influence of Depth Froude Number and h/T Ratio on Manoeuvring Behaviour at Design Condition 59
7.1.1. Turning Circle Manoeuvres 60
7.1.2. Zig-Zag Manoeuvres 77
7.2. Influence of Floating Condition on Manoeuvring Behaviour in Shallow Water 100
7.2.1. Turning Circle Manoeuvres 100
7.2.2. Zig-Zag manoeuvres 105

8. Summary, Conclusion and Outlook **111**
8.1. Summary 111
8.2. Conclusion 114
8.3. Outlook 115

Literature **117**

Appendices **129**

A. Turning Circle Parameters as a Function of the h/T Ratio **131**

B. Zig-Zag Parameters as a Function of the h/T Ratio **135**

List of Figures

4.1. Coordinate system 25
4.2. Zig-Zag manoeuvre according to ITTC (Source: ITTC, 2002) 29
4.3. Turning circle manoeuvre according to ITTC (Source: ITTC, 2002) 30
4.4. Sketched principle of manoeuvring ship hull as hydrofoil for stbd turning . . 32

5.1. Perspective view of the DTC aft ship with twisted rudder and propeller . . 35
5.2. Perspective views from the front, rear and side of the DTC (top) and JBC (bottom) 36
5.3. The DTC model ship during a manoeuvre in the BAW shallow-water basin 37
5.4. Fully equipped model ship with measurement applications 39
5.5. Total station measurement during a deep-water manoeuvre outdoors 40
5.6. Central data acquisition diagram 40

6.1. Principle boundary conditions used for the numerical simulations 41
6.2. Different perspectives of the computational mesh for the DTC 43
6.3. Different perspectives of the computational mesh for the JBC 44
6.4. Comparison of EFD and CFD trajectories for the 35° turning circle manoeuvre with an initial speed of 9 kn for the DTC 48
6.5. Validation plots for turning parameters related to 90° heading change with an initial speed of 9 kn for the DTC 49
6.6. Validation plots for steady-state turning parameters with an initial speed of 9 kn for the DTC 51
6.7. Validation plots for the Zig-Zag 35-20 stbd manoeuvre with an initial speed of 9 kn for the DTC 53
6.8. Comparison of EFD and CFD trajectories for the 35° turning circle manoeuvre with an initial speed of 9 kn for the JBC 54
6.9. Validation plots for stbd turning parameters related to 90° heading change with an initial speed of 9 kn for the JBC 55
6.10. Validation plots for steady-state stbd turning parameters with an initial speed of 9 kn for the JBC 56
6.11. Validation plots for the Zig-Zag 35-20 stbd manoeuvre with an initial speed of 9 kn for the JBC 58

7.1. Trajectories of the 35° turning circle manoeuvre for the DTC 60
7.2. Trajectories of the 35° turning circle manoeuvre for the JBC 61
7.3. Tactical diameter and TCR of the 35° turning circle manoeuvre 62
7.4. Advance and transfer of the 35° turning circle manoeuvre 62
7.5. Steady drift angle and surge velocity of the 35° turning circle manoeuvre . . 63

7.6. Steady rudder transverse and longitudinal force of the 35° turning circle manoeuvre 64
7.7. Steady yaw rate and propeller thrust of the 35° turning circle manoeuvre . 65
7.8. Maxiumum yaw rate at the 35° turning circle manoeuvre 66
7.9. Tactical diameter and turning circle radius of the 45° turning circle manoeuvre 67
7.10. Force components acting on the DTC during a 35° stbd turning circle manoeuvre with an initial speed of 9 kn at design condition, nondimensionalised according to Equation 4.4 68
7.11. Force components acting on the JBC during a 35° stbd turning circle manoeuvre with an initial speed of 9 kn at design condition, nondimensionalised according to Equation 4.4 69
7.12. Turning circle parameters and steady-turning values of drift angle β, speed loss u/U_0, and non-dimensional rudder transverse (C_{Y_R}) and longitudinal (C_{X_R}) force coefficients at 90° heading change, and the time history of the non-dimensional yaw rate r' with an initial speed of 19 kn for the 35° turning circle manoeuvre in deep and shallow water. For comparison, the values for port manoeuvres of β, r' and C_{Y_R} are multiplied by -1. 72
7.13. Calculated hydrodynamic yaw moment as a function of heading angle for different ship sections of the DTC for a 35° stbd turning circle manoeuvre with an initial speed of 9 kn, nondimensionalised according to Equation 4.4 73
7.14. Hydrodynamic lateral forces for a 35° stbd turning circle manoeuvre with an initial speed of 9 kn at 15° heading change, nondimensionalised according to Equation 4.4 74
7.15. Hydrodynamic yaw moment for a 35° stbd turning circle manoeuvre with an initial speed of 9 kn at 15° heading change, nondimensionalised according to Equation 4.4 74
7.16. Pressure distribution at 5.5 m below waterline (full scale) for the bow area (left) and the entire hull (right), shown in terms of the pressure coefficient C_P with the initial straight-ahead speed (9 kn) as reference speed, for a 15° heading angle at 35° stbd turning circle manoeuvre for the DTC 76
7.17. Trajectories of the Z 35-20 manoeuvre for different initial speeds at design condition 77
7.18. First (positive) and second (negative) overshoot angles of the Z 35-20 manoeuvre at design condition 78
7.19. Yaw-checking times for the 35-20 Zig-Zag manoeuvre at design condition . . 78
7.20. Initial turning time for the 35-20 Zig-Zag manoeuvre at design condition . . 79
7.21. Yaw rate and drift angle of the 35-20 Zig-Zag manoeuvre with an initial speed of 9 kn at design condition. For comparison, the values for manoeuvres with an initial port rudder are multiplied by -1. 79
7.22. Rudder transverse force for the 35-20 Zig-Zag manoeuvre with an initial speed of 9 kn at design condition. For comparison, the values for manoeuvres with an initial port rudder are multiplied by -1. 82
7.23. Nomoto coefficients K'_N and T'_N for the 35-20 Zig-Zag manoeuvre at design condition 83

7.24. Trajectories of the Z 20-10 manoeuvre for different initial speeds at design conditions 84
7.25. Yaw rate and drift angle of the 20-10 Zig-Zag manoeuvre with an initial speed of 9 kn at design condition. For comparison, the values for manoeuvres with an initial port rudder are multiplied by −1. 84
7.26. First (positive) and second (negative) overshoot angles of the Z 20-10 manoeuvre at design condition 85
7.27. Initial turning time for the 20-10 Zig-Zag manoeuvre at design condition . . 86
7.28. Yaw-checking times for the 20-10 Zig-Zag manoeuvre at design condition . . 87
7.29. Rudder transverse force for the 20-10 Zig-Zag manoeuvre with an initial speed of 9 kn at design condition. For comparison, the values for manoeuvres with an initial port rudder are multiplied by −1. 88
7.30. Heading and rudder angle for the 20-20 Zig-Zag manoeuvre with an initial speed of 6 kn in deep and moderate shallow water for the DTC at design condition 88
7.31. Force components acting on the DTC during a 35-20 Zig-Zag manoeuvre with an initial speed of 9 kn at design condition, nondimensionalised according to Equation 4.4 89
7.32. Summed hydrodynamic forces and moments on the fore ship, aft ship, and entire hull of the DTC for the Z 35-20 manoeuvre with an initial speed of 9 kn 91
7.33. Hydrodynamic forces and moments acting on the DTC as a function of ship's frames for the Z 35-20 manoeuvre with an initial speed of 9 kn 92
7.34. Top view of hydrodynamic pressure distribution at 2.5 m below water line (full scale), shown in terms of the pressure coefficient C_P with the initial straight-ahead speed (9 kn) as reference speed, for deep water (left), $h/T = 1.50$ (mid) and $h/T = 1.10$ (right) for the positions of first counter rudder, mid of first yaw-checking phase, first overshoot and maximum yaw rate to the opposite direction (from top to bottom) for the DTC 94
7.35. Summed hydrodynamic forces and moments on the fore ship, aft ship, and entire hull of the JBC for the Z 35-20 manoeuvre with an initial speed of 9 kn 96
7.36. Hydrodynamic forces and moments acting on the JBC as a function of ship's frames for the Z 35-20 manoeuvre with an initial speed of 9 kn 97
7.37. Top view of hydrodynamic pressure distribution at 6.0 m below water line (full scale), shown in terms of the pressure coefficient C_P with the initial straight-ahead speed (9 kn) as reference speed, for $h/T = 2.00$ (left), $h/T = 1.20$ (mid) and $h/T = 1.10$ (right) for the positions of first counter rudder, mid of first yaw-checking phase, first overshoot and maximum yaw rate to the opposite direction (from top to bottom) for the JBC 99
7.38. Trajectories of the 45° turning circle manoeuvre with an initial speed of 9 kn for different floating conditions 100
7.39. Advance, transfer, tactical diameter and TCR of the 45° turning circle manoeuvre with an initial speed of 9 kn for different floating conditions 101
7.40. Yaw rate and drift angle of the 45° turning circle manoeuvre with an initial speed of 9 kn for different floating conditions 102

7.41. Trajectories of the 35° turning circle manoeuvre for different floating conditions . . . 103
7.42. Advance, transfer, tactical diameter and TCR of the 35° turning circle manoeuvre with an initial speed of 9 kn for different floating conditions 104
7.43. Yaw Rate and drift angle curve progression of the 35° turning circle manoeuvre with an initial speed of 9 kn for different floating conditions 104
7.44. First (pos.) and second (neg.) overshoot angles of the Z 35-20 (left) and 20-10 (right) manoeuvre with an initial speed of 9 kn for different floating conditions . . . 106
7.45. First (top) and second (bottom) yaw-checking time of the Z 35-20 (left) and 20-10 (right) manoeuvre with an initial speed of 9 kn for different floating conditions . . . 106
7.46. First initial turning time of the Z 35-20 (top) and 20-10 (bottom) manoeuvre with an initial speed of 9 kn for different floating conditions . . . 107
7.47. Yaw rate of the Z 20-10 manoeuvre with an initial speed of 9 kn for different floating conditions for the DTC . . . 108
7.48. Nomoto coefficients K'_N and T'_N for the Z 35-20 (top) and 20-10 (bottom) manoeuvre with an initial speed of 9 kn for different floating conditions . . . 108
7.49. Norrbin Parameter P for the Z 35-20 (top) and 20-10 (bottom) manoeuvre with an initial speed of 9 kn for different floating conditions . . . 109
7.50. Trajectories of the Z 35-20 (top) and 20-10 (bottom) manoeuvre with an initial speed of 9 kn for different floating conditions . . . 109

A.1. Tactical diameter and TCR of the 35° turning circle manoeuvre at design condition . . . 131
A.2. Advance and transfer of the 35° turning circle manoeuvre at design condition 131
A.3. Steady drift angle and surge velocity of the 35° turning circle manoeuvre at design condition . . . 132
A.4. Steady rudder transverse and longitudinal force of the 35° turning circle manoeuvre at design condition . . . 132
A.5. Steady yaw rate and propeller thrust of the 35° turning circle manoeuvre at design condition . . . 132
A.6. Maxiumum yaw rate for the 35° turning circle manoeuvre at design condition 133
A.7. Tactical diameter and turning circle radius of the 45° turning circle manoeuvre at design condition . . . 133

B.1. First (positive) and second (negative) overshoot angles of the Z 35-20 manoeuvre at design condition . . . 135
B.2. First (top) and second (bottom) yaw-checking time for the 35-20 Zig-Zag manoeuvre at design condition . . . 135
B.3. Initial turning time for the 35-20 Zig-Zag manoeuvre at design condition . . . 136
B.4. Nomoto coefficients K'_N and T'_N for the 35-20 Zig-Zag manoeuvre at design condition . . . 136
B.5. Initial turning time for the 20-10 Zig-Zag manoeuvre at design condition . . . 136

B.6. First (positive) and second (negative) overshoot angles of the Z 20-10 manoeuvre at design condition 137
B.7. First (top) and second (bottom) yaw-checking time for the 20-10 Zig-Zag manoeuvre at design condition 137

List of Tables

5.1. Main dimensions of the model ships . . . 35
5.2. Main dimensions of the DTC at the investigated floating conditions (full scale) . . . 36
5.3. Main dimensions of the JBC at the investigated floating conditions (full scale) 37
5.4. Manoeuvre matrix for the DTC at design conditions . . . 37
5.5. Manoeuvre matrix for the DTC at partial draught . . . 38
5.6. Manoeuvre matrix for the JBC at design conditions . . . 38
5.7. Manoeuvre matrix for the JBC at partial draught . . . 39

6.1. Boundary conditions . . . 42
6.2. Grid sizes . . . 43
6.3. Grids used for the convergence study . . . 44
6.4. Grid convergence study for the DTC based on resistance tests . . . 46
6.5. Grid convergence study for the JBC based on resistance tests . . . 46
6.6. Grid convergence study for the DTC based on a 35° turning circle manoeuvre at $h/T = 1.50$ . . . 46
6.7. Grid convergence study for the JBC based on a 35° turning circle manoeuvre at $h/T = 1.50$ . . . 47
6.8. Results of the DTC resistance and propulsion tests for EFD and CFD . . . 48
6.9. Results of the JBC straight-ahead tests for EFD and CFD . . . 48
6.10. Differences between CFD and EFD results of the 35° turning circle manoeuvre in % for the DTC . . . 50
6.11. Differences between CFD and EFD results of the Zig-Zag 35-20 manoeuvre in % for the DTC . . . 52
6.12. Differences between CFD and EFD results of the 35° turning circle manoeuvre in % for the JBC . . . 55
6.13. Differences between CFD and EFD results of the Zig-Zag 35-20 Manoeuvre in % for the JBC . . . 57

Nomenclature

Abbreviations

CFD	Computational Fluid Dynamics
CPMC	Computerized Planar Motion Carriage
DoF	Degrees of Freedom
DTC	Duisburg Test Case
EFD	Experimental Fluid Dynamics
EMSA	European Maritime Safety Agency
HSVA	Hamburgische Schiffbau-Versuchsanstalt
IMO	International Maritime Organization
ITTC	International Towing Tank Conference
JBC	Japan Bulk Carrier
MMG	Maneuvering Modeling Group
PMM	Planar Motion Mechanism
RANS	Reynolds-Averaged Navier-Stokes
SST	Shear Stress Transport
stbd	starboard
TC	Turning Circle
URANS	Unsteady Reynolds-Averaged Navier-Stokes
WL	Waterline
Z	Zig-Zag

Symbols

α	Overshoot angle	[°]
β	Drift angle	[°]
δ	Rudder angle	[°]
Ma	Mach number, ratio of flow speed to speed of sound	[-]
Ψ	Heading angle	[°]
ρ	Water density	[kg/m^3]
φ	Heeling angle	[°]
ϑ	Trimm angle	[°]
A_R	Rudder area	[m^2]
B_{wl}	Breadth at waterline	[m]
c_B	Block coefficient	[-]
C_{X_R}	Longitudinal rudder force coefficient, non-dimensionalised with $0.5U_0^2\rho A_R$	[-]
C_{Y_R}	Transverse rudder force coefficient, non-dimensionalised with $0.5U_0^2\rho A_R$	[-]
D_P	Propeller diameter	[m]
Fr_h	Depth Froude number	[-]
GM	Metacentric height	[m]

h	Water depth	[m]
I_{zz}	Moment of inertia relative to the z-axis	[m]
J	Propeller advance coefficient	[-]
K'_N	First order Nomoto coefficient, non-dimensionalised with U_0/L_{PP}	[-]
K_N	First order Nomoto coefficient	[1/s]
k_Q	Propeller torque coefficient	[-]
k_T	Propeller thrust coefficient	[-]
K_{xx}	Radius of gyration relative to the x-axis	[m]
K_{yy}	Radius of gyration relative to the y-axis	[m]
K_{zz}	Radius of gyration relative to the z-axis	[m]
L_{PP}	Length between perpendicular	[m]
N	Hydrodynamic yaw moment	[N]
n	Propeller rotation rate	[1/s]
N'	Hydrodynamic yaw moment, non-dimensionalised with $0.5U_0^2\rho L_{PP}^2 T$	[-]
N_β	Hydrodynamic derivative of yaw moment with respect to drift angle	[Nm/rad]
N_δ	Hydrodynamic derivative of yaw moment with respect to rudder angle	[Nm/rad]
$N_{\dot{r}}$	Hydrodynamic moment of inertia relative to the z-axis	[N · s^2/m]
N_r	Hydrodynamic derivative of yaw moment with respect to yaw rate	[Nms/rad]
N_v	Hydrodynamic derivative of yaw moment with respect to sway velocity	[Ns]
r	Yaw rate	[1/s]
r'	Yaw rate, non-dimensionalised with U_0/L_{PP}	[-]
Re	Reynolds number	[-]
S_w	Wetted hull surface	[m^2]
T	Mean draught	[m]
t	Time	[s]
t'	Time, non-dimensionalised with L_{PP}/U_0	[-]
T'_N	First order Nomoto coefficient, non-dimensionalised with L_{PP}/U_0	[-]
t_a	Initial turning time, non-dimensionalised with L_{PP}/U_0	[-]
T_M	Draught at midship	[m]
T_N	First order Nomoto coefficient	[s]
T_P	Propeller thrust	[N]
t_s	Yaw checking time, non-dimensionalised with L_{PP}/U_0	[-]
T_{APP}	Draught at aft perpendicular	[m]
T_{FPP}	Draught at forward perpendicular	[m]
TCR	Turning circle radius	[L_{PP}]
TD	Tactical diameter	[L_{PP}]
u	Surge velocity	[m/s]
U_0	Steady surge velocity at manoeuvre start	[m/s]
UKC	Under keel clearance	[m]
V	Displacement volume	[m^3]
v	Sway velocity	[m/s]
X	Hydrodynamic longitudinal force	[N]
$X_{\dot{u}}$	Hydrodynamic mass for longitudinal direction	[N · s^2/m]
x_{cg}	Longitudinal centre of gravity	[m]
X_R	Longitudinal rudder force	[N]

Y	Hydrodynamic transversal force	[N]
Y'	Hydrodynamic transversal force, non-dimensionalised with $0.5U_0^2\rho L_{PP}T$	[-]
Y_β	Hydrodynamic derivative of lateral force with respect to drift angle	[N/rad]
Y_δ	Hydrodynamic derivative of lateral force with respect to rudder angle	[N/rad]
$Y_{\dot{v}}$	Hydrodynamic mass for transversal direction	[$\mathrm{N \cdot s^2/m}$]
Y_R	Transverse rudder force	[N]
Y_r	Hydrodynamic derivative of lateral force with respect to yaw rate	[Ns/rad]
Y_v	Hydrodynamic derivative of lateral force with respect to sway velocity	[Ns/m]

1. Introduction

1.1. Motivation

The influence of shallow-water conditions on a vessel's manoeuvring characteristics is significant. According to current IMO regulations, the manoeuvrability of new ships is evaluated during sea trials conducted exclusively in deep water, although some proposals have been made to introduce standardized shallow-water and low-speed manoeuvring tests (e.g. Dand, 2003; Quadvlieg and van Coevorden, 2003; Li et al., 2006). While deep-water transit indeed accounts for the largest portion of a typical voyage, the operational demands on manoeuvring performance in such conditions are relatively low. In contrast, the navigation of harbour approaches generally occurs in restricted, shallow-water environments, where the manoeuvring behaviour of ships is subject to the highest demands and plays a critical role in the design and dimensioning of waterways.

Over recent decades, the size of seagoing vessels has continued to increase in line with the growing volume of goods transported by sea. This trend has significant implications for navigation in sea lanes and approach channels, which cannot always be expanded to accommodate rising demand. As a result, manoeuvring in extreme shallow water occurs more commonly. To ensure that navigation in such areas is not compromised, it is necessary to study the changes in ship manoeuvring behaviour in shallow and laterally restricted waters. In fact most marine disasters takes place close to harbour or coastal areas (Li et al., 2006). According to EMSA (2022) approximately 95 % of their registered navigation accidents occurred in inland waters, port areas, territorial sea and internal waters (like rivers or channels), where shallow-water conditions are usually present. Most of these accidents occurred while manoeuvring/turning (approximately 28 %) and in passage (approximately 27 %). Improving the safety of navigation in confined waters requires a deeper understanding of the dynamics of ships in shallow-water conditions.

1.2. Brief Literature Review

Consequently, numerous studies have already been conducted in this area, employing a variety of focuses and methodologies, particularly in recent years (Maljković et al., 2024). Considering the history of research on shallow-water manoeuvring, knowledge in the field has advanced significantly over the past decades, especially since the 11th International Towing Tank Conference (ITTC) 1966 onwards, when the Manoeuvring Committee firstly made the recommendation to consider the research of manoeuvring behaviour in confined water as duty for the ITTC (ITTC, 1966). Up to that time, there has been a few full-scale trials at shallow water (e.g. Baker, 1924; de Verdieére and Audren, 1951; Motora and Couch, 1961). Among these, the most notable was the subsequent full-scale trial of the Esso Osaka (Crane, 1979), which was later used extensively to investigate scaling effects

(e.g. Bogdanov et al., 1987b) and to validate model tests (e.g. Hirano et al., 1985; Yasukawa and Kobayashi, 1995) and CFD set-up (e.g. Ohmori, 1998; Simonsen and Stern, 2005; Wang et al., 2023). The Esso Osaka exhibited markedly deteriorated turning ability in shallow water (h/T of 1.20), with an increase in advance of over 40 % and an approximately doubled tactical diameter compared with deep-water conditions. In contrast, under moderate shallow water (h/T of 1.50), the tanker initially displayed enhanced turning behaviour. This phenomenon was already observed by Fujino (1968), who performed captive model tests in both deep and shallow water (h/T of 2.50–1.21). The investigated oil tanker (Tokyo Maru) exhibited yaw instability for h/T ratios between approximately 2.5 and 1.5. Furthermore, the model tests revealed a significant increase in added mass and in the linear derivatives of the hydrodynamic coefficients Y_β, N_β, Y_r and N_r. This significant increase in hydrodynamic damping in shallow water was confirmed by many authors subsequently (e.g. Hirano et al., 1985; Yoshimura, 1986, 1988). In general, reduced water depth alters the hydrodynamic forces on the hull, resulting in different manoeuvring characteristics:

- The turning ability decreases (e.g. Schmidt-Stiebitz, 1958b; Milanov and Chotukova, 2009; Kim et al., 2022),
- the course stability increases (e.g. Motora and Couch, 1961; Milanov and Chotukova, 2009; Yeo et al., 2016; Lee and Hong, 2017),
- the yaw-checking ability increases (e.g. Motora and Couch, 1961; Yun et al., 2015; Yeo et al., 2016),
- the initial turning/course-changing ability varies negligibly (e.g. Yun et al., 2015; Yeo et al., 2016),
- the maximum yaw rate decreases (e.g. Bogdanov et al., 1987b; Lu et al., 1987; Milanov and Chotukova, 2009; Yun et al., 2015; Yeo et al., 2016),
- the speed loss at turning decreases (e.g. Bogdanov et al., 1987b; Lu et al., 1987; Kim et al., 2022) and
- the drift angle decreases (e.g. Schmidt-Stiebitz, 1958b; Kim and Lim, 2022).

As performance of model tests is time-consuming and requires extensive testing facilities and highly qualified technical personnel, considerable effort has been invested in developing formulas based on empirical approaches (e.g. Hirano et al., 1985; Ishiguro et al., 1996; Gronarz, 1999; Kijima, 2005) or simplified methods such as slender body theory (e.g. Nakao et al., 1995; Yasukawa, 1997; Kaneko and Kijima, 2001) to determine hydrodynamic derivatives in shallow water, with varying degrees of success. Some of these methods are still employed today to approximate shallow-water manoeuvring behaviour, but additional tools are required to further improve the results (e.g. Eloot et al., 2015; He et al., 2016).

Towards the turn of millennium, research focus shifted strongly towards the performance of RANS-based CFD simulations, initially for resistance and propulsion and later also for manoeuvring issues. With respect to shallow-water conditions, the primary focus of CFD studies was on captive model tests and stationary manoeuvring conditions, investigating qualitative changes in the flow field and hydrodynamic coefficients depending on drift

angle or yaw rate applied (e.g. Toxopeus, 2013; He et al., 2016; Liu et al., 2016; Lee and Hong, 2017; RoyChoudhury et al., 2017; Liu et al., 2019; Wang et al., 2023; Ohmori, 2024; van Hoydonck et al., 2024). Comparisons with model test results, such as hydrodynamic derivatives from PMM tests, generally confirmed the applicability of RANS-based CFD methods in shallow water (e.g. Liu et al., 2016, 2019; Ohmori, 2024) and provided valuable insights into the altered flow conditions, for example the development of vortices under pure drift conditions (e.g. Lee and Hong, 2017; RoyChoudhury et al., 2017).

Despite substantial improvements in numerical methods and computing power, physical model tests remain the state of the art for manoeuvring investigations (Milanov and Chotukova, 2009; Eloot et al., 2015; Yun et al., 2015; Eloot et al., 2016; Yeo et al., 2016; Hinostroza et al., 2019; Mehr and Javanmardi, 2023) and are essential for validating CFD simulations.

1.3. Problem Definition

The numerical investigations outlined above primarily focused on capturing qualitative variations of hydrodynamic coefficients and global flow features in shallow water. Many of these studies concentrated on relatively high drift angles, which rarely occur during practical shallow-water manoeuvres due to increased hydrodynamic damping. Depth-dependent changes in hydrodynamic coefficients have been investigated experimentally (e.g. Fujino, 1968; Bogdanov et al., 1987b) and reproduced in CFD simulations (e.g. Liu et al., 2019; Ohmori, 2024). However, the underlying mechanisms – particularly the redistribution of hydrodynamic forces along the hull with decreasing water depth – have not been systematically analysed. Moreover, a detailed decomposition of the individual force components and their variation with water depth is largely absent in the literature.

Captive manoeuvres inherently rely on modelling assumptions, including dependencies on the chosen mathematical manoeuvring model and potential extrapolation uncertainties. For this reason, the ITTC considers free-running model tests to represent the most realistic experimental approach (ITTC, 2008). For shallow-water conditions, however, CFD simulations of self-propelled free-running manoeuvres are limited (Carrica et al., 2016; Kim et al., 2022). Existing studies have primarily addressed validation of numerical setups and global manoeuvring characteristics, typically focusing on conditions down to $h/T = 1.20$. Likewise, available free-running model experiments have generally been restricted to moderate shallow- and shallow-water conditions, providing limited insight into extreme shallow-water regimes. Consequently, the behaviour of ships in extreme shallow water remains largely unexplored, even as such conditions are becoming increasingly relevant from operational and safety perspectives due to larger ship dimensions and reduced under-keel clearances.

A key governing parameter in shallow-water hydrodynamics is the depth Froude number, which directly links ship speed and water depth. However, its influence on manoeuvring behaviour has often been neglected, as most previous investigations were conducted at a single speed, limiting the ability to evaluate the speed dependency of shallow-water effects. Moreover, earlier studies were frequently restricted to a single draught, trim condition, and turning direction. Consequently, a systematic assessment of the influence of speed – and thus of the depth Froude number – together with trim, draught variation, and directional

dependency as a function of water depth is still lacking.

1.4. Objectives of the Work

The main objective of this study is to investigate ship manoeuvres over a broad range of shallow-water conditions, with particular emphasis on the largely neglected extreme shallow water regime. Ship speed is varied extensively, enabling a systematic and comprehensive assessment of depth-Froude-number effects on manoeuvring behaviour beyond the single-speed conditions typical of earlier studies. The influences of draught, trim, and turning direction are additionally examined to identify parameter dependencies that have not been resolved in earlier shallow-water studies. Finally, the study aims not only to describe global manoeuvring behaviour, but also to connect local hydrodynamic phenomena to observed manoeuvring performance, bridging the gap between qualitative observations and the underlying physical mechanisms.

In this manner, the investigation integrates global manoeuvring performance with local flow phenomena, systematically explores the role of depth-Froude-number effects and extreme shallow-water conditions, and seeks to extend current knowledge beyond previous experimental and numerical studies.

1.5. Solution Approach

The research employs a combined model test–CFD approach to investigate the manoeuvring behaviour of two types of modern seagoing vessels – a container ship (DTC) and a bulk carrier (JBC) – under shallow-water conditions at model scale. The study covers six water depths, extending into the extreme shallow-water regime ($h/T = 1.15$ and 1.10), and systematically varies up to five ship speeds, providing a broad and detailed dataset.

The model tests, conducted with sophisticated instrumentation capturing trajectory, ship motions, rudder forces, moments, and propeller thrust, provide a comprehensive reference for global manoeuvring behaviour and reveal the influence of shallow-water confinement on overall performance. CFD simulations are then used to resolve local hydrodynamic effects along the hull, including the distribution of pressures and forces as a function of water depth. This combination enables a detailed mechanistic understanding of how shallow-water flow confinement redistributes loads and governs the observed manoeuvring response.

1.6. Structure of the Doctoral Thesis

This work is structured as follows. First, an extensive literature review is provided to summarise the current state of research on shallow-water manoeuvring and its development over the past century. The subsequent two chapters briefly introduce the fundamentals of RANS-based CFD simulations and ship manoeuvring, offering a concise overview of the relevant theoretical background. The methods applied in this study are described in detail in chapter 5 and chapter 6. These chapters include a description of the measurement equipment, the execution of the model tests, and the test matrix, as well as the CFD setup

together with its verification and validation. In chapter 7, the results of the model tests and CFD simulations are presented and discussed along thematic lines. This aspect-oriented structure facilitates a clear presentation of the key findings regarding shallow-water effects on manoeuvring performance. The final chapter summarises the work and highlights the main findings of this study, followed by an outline of remaining research gaps and recommendations for future work.

1.7. Achievements Compared to the State of the Art

This study advances the state of the art in shallow-water manoeuvring research by addressing previously unresolved aspects. Extending the investigation into the extreme shallow-water regime revealed manoeuvring responses that are not evident at higher h/T ratios. The manoeuvring behaviour of two modern vessel types – a container ship and a bulk carrier – has been systematically evaluated across multiple ship speeds, enabling quantification of depth-Froude-number effects. The influence of draught, trim, and turning direction has been additionally assessed, uncovering parameter dependencies largely absent from earlier studies. Beyond global manoeuvring characteristics, the study resolves local hydrodynamic pressures and force distributions along the hull, connecting these local effects to observed manoeuvring performance. In doing so, it provides further insight into the governing mechanisms of shallow-water effects, closes key gaps in the literature, and establishes a comprehensive reference dataset for validation, benchmarking, and further methodological developments.

2. State of the Art

The effects of shallow water on ship manoeuvring behaviour have been investigated and discussed in the literature for many decades. However, as in many research fields, progress was limited, and this topic has increasingly become the subject of scientific research, particularly in recent times (Maljković et al., 2024). A major driving factor is the continuous growth in ship size, which compels vessels to operate in progressively shallower conditions at harbour approaches and in constrained waterways that cannot be changed to the same extent. Nevertheless, the difference between manoeuvring behaviour in deep and shallow water has long been recognised as a critical issue for both scientists and engineers.

2.1. Foundations of Manoeuvring Research

Back in the 18th century and earlier, during the era of sailing ships, according to Saunders (1965), attention to manoeuvring was largely confined to rules regarding the rudder and its shape. It was only with the advent of steam-powered vessels that the need for a more detailed investigation of manoeuvrability gradually arose. Until the mid-19th century, efforts to enhance manoeuvring performance were limited to empirical observations and logical reasoning applied to the design of the hull and rudder. (Saunders, 1965)

Early research on the 'steering of ships' focused primarily on the rudder, including its type, size, shape (Barnaby, 1863), and use of twin rudders at the stern and bow (Leigh, 1871). From the mid-19th century onward, ship manoeuvrability began to be investigated through model tests, with a strong emphasis on turning circles, which essentially offered empirical solutions to a complex problem (Saunders, 1965).

At this time, Kempf developed a new type of manoeuvre (Kempf, 1944), which was initially referred to as the 'standard manoeuvre test' or 'serpentine test' (originally in German: 'Schlängelfahrt'). This new manoeuvre was later designated the Z or Zig-Zag manoeuvre. In contrast to turning circle manoeuvres, the benefit of this specific manoeuvre was the possible investigation of smaller rudder and heading angles, and the ease of realisation in towing tanks, which were long but relatively narrow. Concerning ships sailing in shallow water, most of the literature up to the 1960s refers to the increase of resistance in confined water. Particular reference should be made to the well-known publication by Schlichting (1934), who provided a method to estimate the shallow-water resistance curve from the deep-water curve. However, already in the early 20th century Sadler (1911) investigated the altered resistance of a series of merchant ships using a false bottom at a fixed depth. Prior to this, mainly non-public tests for naval vessel were investigated in similar manner. Sadler already used the depth to draught ratio h/T and discovered that resistance humps occurred at the same speeds for all models, indicating that they are a function of water depth rather than ship size. Taylor (1913) conducted similar experiments incorporating a false bottom to generate a range of shallow-water conditions from

approximately $h/T = 1.53$ to 1.33. In shallow water the models were only investigated up to 3 knots, as results above this speed were not consistent due to large unstable eddies that caused a drastic variation in resistance. Sturtzel and Schmidt-Stiebitz (1957) conducted resistance measurements with plates and ship model in shallow water, observing a diffuser effect with corresponding detachments between keel and bottom with forward trim and at the aft of the ship.

2.2. Development of Free-Running Manoeuvring Tests

After the foundation of the Manoeuvring Technical Committee within the 9th ITTC 1960, standard manoeuvres and corresponding parameters were first defined (like turning circle, Zig-Zag or spiral manoeuvre). In addition, it was recognised that manoeuvring tests needed to be carried out in a wide variety of facilities to determine the effect of the different techniques used on the results. The main focus remained on free-manoeuvring models, with only suggestions made for captive tests. The Mariner Class Ship was investigated, with full-scale trial results provided by the David Taylor Model Basin (DTMB) to examine the effects of scaling. The need to obtain data on slow-speed manoeuvres was recognised but postponed for the time being. (ITTC, 1960)

In the 1950s and 1960s, much research was conducted in the field of free-running model tests to obtain simplified manoeuvring indicators (Nomoto and Taguchi, 1957), study scaling effects (e.g. Shiba, 1960; Nomoto, 1966), and to investigate the impact of different settings of manoeuvring devices and hull forms, including the influence of a skeg and variation of block coefficient, beam, and draft on the manoeuvring characteristics (e.g. Bindel, 1960; Yamanouchi, 1966). Nomoto and Taguchi (1957) adopted a simplified mathematical approach based on the Nomoto coefficients K_N and T_N to estimate the manoeuvring motion, especially to assess the turning and steering behaviour of a new vessel in design stage more easily, see also section 4.2. Additionally, Motora derived the relationship between K_N and T_N based on model test results and theoretical considerations. Involving the ratio of the rudder area to the projected area of the ship, which predominantly affects the turning ability, the relation of both indices are almost linear. Hence, it was concluded that the relation K_N/T_N is approximately constant for the same rudder area ratio (Motora, 1960).

In 1966 Nomoto dealt with scaling effects of the free-running Mariner type model ship in regard of these first order Nomoto indices K_N and T_N (Nomoto, 1966). For the investigated ship, the scaling effects on K_N were low for different model sizes and the full scale. Scaling effects were only considered critical for very small models. In general, as the rudder angle increases and the model size decreases, K_N and T_N decrease. For rudder angles over 15°, the scaling effect on K_N was negligible for models over 5 metres in length. However, the scaling effect on T_N was not negligible for slight manoeuvres, like course-keeping, since smaller models were quicker to response (smaller T_N values) than larger models or the full-scale ship. The decrease in the K_N and T_N indices with increasing rudder angle, was assumed to be mainly due to the simultaneous increase in non-linear yaw damping per unit yaw rate.

Shiba (1960) conducted a comprehensive study on free-running turning circle manoeuvres, incorporating different models with varying block coefficients, rudders and propeller

pitch ratios. Rudder area ratio affected tactical diameter differently than advance and transfer. While an optimum ratio minimized the tactical diameter, further increases offered no reduction and could slightly increase it, whereas advance and transfer continued to decrease with larger rudders. In this context, the author explained why the 45° turning circle performed significantly better than the 35° manoeuvre. He attributed this to a stronger propeller flow onto the rudder, due to a higher wake fraction, which reduced stall occurrence, and to the reduced effective rudder inflow angle caused by drift and turning motion. Hull form also strongly affected turning behaviour: the ship with $c_B = 0.6$ had a turning circle radius twice that of the $c_B = 0.8$ model, explained by different yaw moments and higher rudder inflow from increased propeller loading. Trim had a significant effect, whereas the influence of velocity, displacement, and propeller pitch were negligible. Comparison of 6 m and 2.5 m models demonstrated strong correlation with full-scale trials, indicating minimal scaling effects in free-running turning circle tests. This result was explained by two opposing effects of the overestimated model friction: lower rudder inflow outside the propeller stream due to stronger wake, and higher inflow inside the stream as a result of increased propeller loading due to the wake.

2.3. Free-Running Manoeuvring in Shallow Water

At the 11th ITTC 1966, the Manoeuvring Committee first recommended the investigation of manoeuvring behaviour in confined water as a task for the ITTC (ITTC, 1966). Up to this point, there have been only a limited number of full-scale measurements in the Suez Canal (Baker, 1924; de Verdieére and Audren, 1951) and the Great Lakes (Motora and Couch, 1961) as well as some model tests involving free-running and oblique towing in shallow water (e.g. Bindel, 1960; Schmidt-Stiebitz, 1958a,b, 1959; Koseki et al., 1965). Baker (1924) was among the first to investigate the altered steering behaviour of ships in shallow water, conducting full-scale tests in the Suez Canal and self-propelled model tests. He noted the transition from three-dimensional to quasi-two-dimensional flow around the hull with decreasing water depth, particularly affecting pressure and velocity distribution at the aft body. Consequently, the stern streamlines became more horizontal and curved, experiencing greater pressure variations than in deep water. This, the author argued, caused increased eddy formation at the aft in shallow water. The effect on manoeuvrability was a reduced yaw rate at a given rudder angle and a longer path and time to reach a specified small angle.

Motora and Couch (1961) performed full-scale execution tests on the Great Lakes in deep and shallow water with a bulk carrier (SS. Benjamin Fairless), followed by model tests. Spiral tests and Z manoeuvres were carried out in deep water (h/T of approximately 3.0), moderate shallow water (h/T of approximately 1.5 to 2.0) and shallow water (h/T of approximately 1.25). The analysed ship was yaw unstable, which decreased slightly in shallower water, i.e. became slightly more stable. In shallower water, the overshoot angles decreased in the Zig-Zag trial. Furthermore, a decline was observed in the Nomoto coefficients K_N and T_N. The model tests were carried out with a model of the same bulk carrier at a scale of 1/64 for deep and shallow water at an h/T ratio of 1.36. Oblique towing tests and forced yawing technique was used to obtain the hydrodynamic derivatives. Like the full-scale ship, the model exhibited yaw instability in deep water, and, to a lesser

extent, in shallow water. Model tests agreed well with full-scale data for small deviations from a straight course. For higher rudder angles, the model consistently showed higher yaw rates than the full-scale ship. However, the ratio of yaw rate in deep and shallow water of model tests agreed well with full-scale data and the authors concluded that model tests could be used reasonably to obtain the effects of shallow water on manoeuvring behaviour.

Schmidt-Stiebitz (1958b) analysed systematically different aft ship shapes at different draughts and water depths (h/T from approximately 8.4 to 1.86), performing free-running model tests. It was found that a large drift angle strongly correlates with a small turning circle radius and vice versa, and that the turning circle radius increases with decreasing water depths. Koseki et al. (1965) carried out free-running turning and spiral tests with a tanker (c_B of 0.81) and a cargo (c_B of 0.70) model ship for various water depths (h/T ratios of 6.00–1.25). For the cargo ship, shallow-water effects became noticeable only below $h/T \approx 3.50$ and increased markedly for $h/T < 2.50$, with the yaw rate of the 35° turning circle at $h/T = 1.25$ roughly half of the deep-water value. For the tanker, effects appeared from $h/T \approx 6.00$ and intensified below $h/T = 2.30$. The trend of yaw rate in steady turning for all investigated ships was consistent with the findings of Schmidt-Stiebitz (1958a), despite differences in ship type and dimensions.

A particularly comprehensive and influential full-scale study was conducted by Crane (1979) on the oil tanker Esso Osaka, providing data in both deep and shallow water. These results have been widely used for validation and subsequent research, such as Martinussen and Linnerud (1987), who employed free-running model tests of the Esso Osaka to study scale effects on manoeuvring in deep water. The 35° turning circle showed close agreement in steady yaw rate, slightly higher for the model, but with opposing directional asymmetry: the model turned better to port, while the full-scale ship achieved a higher yaw rate to starboard (stbd). In the 10-10 and 20-20 zig-zag manoeuvres, the model exhibited slightly higher course stability and longer initial turning times. Overall, all parameters – including overshoot angles, yaw-checking times, and initial turning times – agreed well with full-scale data, with maximum deviations of about 16 %.

2.4. Captive Manoeuvring Tests in Shallow Water

Concurrently with the implementation of the first PMM systems in the 1950s and 1960s (Grim et al., 1976), there was an increasing adoption of mathematical approaches to the manoeuvring behaviour of ships. One of the first mathematical manoeuvring model was proposed by Abkowitz (1964). A Taylor expansion was employed to discretise the hydrodynamic derivatives of the hull, assuming the ship to be in a straight-ahead motion prior to the initiation of the manoeuvre. He already pointed out that the altered flow in shallow water caused by the flow restriction below the vessel, can affect the hydrodynamic coefficients, and that the proper determination of the derivatives in these conditions requires additional model tests in shallow water. The model of Abkowitz, however, included some shortcomings, particularly due to its global approach, which makes it impossible to assign the individual physical causes to the corresponding coefficients. Hence, in the following decades there has been further mathematical manoeuvring models developed, most importantly tabular models (e.g. Eloot and Vantorre, 2003) and modular models like the MMG standard model (Yasukawa and Yoshimura, 2015) or the HSVA 4-quadrant model

(Oltmann and Sharma, 1984). Most of the captive model tests conducted in this time were performed in deep water only.

Fujino (1968) was among the first, who performed these kind of model tests in shallow water using forced yawing technique and considered the influence of shallow water and restricted width independently. The manoeuvring behaviour of the Mariner ship and oil tanker Toky Maru were analysed at 2 speeds and various water depths (h/T of approximately 1.2, 1.5, 1.9, 2.5 and deep-water condition). Three different measurement methods were used: forced yawing test (PMM), rudder force measurement and oblique towing test. Comparison of PMM and oblique towing showed larger Y_β in the oblique test, with differences increasing as h/T decreases, reflecting non-linearity even at a drift angle of 5°. The author described the influence of shallow water on individual parameters as follows: Shallow-water effects were stronger at higher speeds, except for N_r which showed smaller variation. The influence on the added mass was significantly stronger than that on the added mass moment of inertia. In comparing the two ships, the influence of shallow water on the added mass moment of inertia was found to be considerably greater for the full ship than for the slender ship, whilst the difference in the added mass was negligible. The shallow-water effect on Y_δ and N_δ was minimal, and Y_r exhibited a greater sensitivity to water depth than N_r. In moderate shallow water N_β initially increased more rapidly than Y_β, whereby the point of attack of hydrodynamic transverse force due to drift motion initially moved further forward. In shallower water, with an h/T ratio of 1.50 or less, the point of attack began to move aft towards the centre of gravity again. For the full ship this resulted in an area of yaw instability for an h/T ratio of approximately 2.5 to 1.5, where the point of attack of the hydrodynamic transverse force due to drift motion was ahead the point of attack of the hydrodynamic transverse force due to yaw motion. With further decreasing water depth, an enhancement in yaw stability was observed in both vessels, but simultaneously, there was a deterioration in their turning behaviour.

In the following decades further model tests were performed in shallow water, with a different emphasis of investigation. Bogdanov et al. (1987b) investigated scale effects using PMM model tests with the Esso Osaka at a 1/40 scale in deep and shallow water (h/T ratios of 2.00, 1.50 and 1.20). The advance speed corresponded to an average full-scale speed of 7.2 knots. Forces and moments increased considerably in shallow water, particularly at h/T=1.20, with the added mass increase exceeding that of the mass moment of inertia, consistent with Fujino (1968). Simulations of turning circle, Zig-Zag, and spiral manoeuvres based on the obtained coefficients agreed well with full-scale tests. Deviations were minimal, and while deep-water simulations indicated slight yaw instability, full-scale spiral tests showed only minor instability.

Yoshimura and Sakurai (1989) and Yasukawa and Kobayashi (1995) demonstrated different shallow-water effects on the turning behaviour of wide twin screw ships. Yoshimura and Sakurai (1989) investigated shallow-water effects on the turning behaviour of twin-screw ships through captive model tests and simulations based on predicted manoeuvring coefficients. Two ships were studied: a conventional twin-propeller ship and a wide-beam twin ship. While the conventional ship exhibited the expected deterioration of turning ability in shallow water, the wide-beam ship showed improved turning as water depth decreased. This was attributed to a relatively stronger increase in rudder forces compared

to hull forces for the wide-beam ship, reversing the typical trend. These results were confirmed by free-running model tests by Yasukawa and Kobayashi (1995) in deep and shallow water (h/T ratio of 1.50–1.20). The advance and turning circle radius decreased notably at reduced water depths for the twin-screw ship, already evident at $h/T = 1.50$, with only slight further reduction at $h/T = 1.20$. The effect was explained by a pronounced increase in rudder normal forces due to the distinct resistance characteristics of the wide-beam ship.

In the 1990s, research into ship dynamics focused strongly on prediction and mathematical modelling. Kijima et al. (1997), for instance, performed a sensitivity study of the GM and roll angle utilising a mathematical coefficient-based model. Generally, the findings suggested a smaller advance and tactical diameter, and higher overshoot angles for a smaller GM. However, this relation was most evident for the smallest GM of 0.5 metres, and only at high velocities, while greater GM values and low velocities showed almost no effect. The lowest investigated velocity was still 16 knots and the highest 24 knots.

Vantorre and Eloot (1996) performed captive model tests with a 1/64 Panamax container ship in extreme shallow water (h/T of 1.10), focusing on drift-induced forces at slow-speed. Conventional mathematical drift-force models proved inadequate over all four drift quadrants, indicating the need for higher-order formulations.

Ishiguro et al. (1996) analysed the sensitivity of Kijima's empirical prediction method for hydrodynamic coefficients and found poor performance for unstable ships. Manoeuvring behaviour was most sensitive to Y_r, N_r, Y_β, N_β, the flow straightening factor γ and the wake ratio factor of rudder and propeller inflow ϵ. Turning ability (advance, tactical diameter) was dominated by N_β, N_r, γ and ϵ, whereas Zig-Zag response was about twice as sensitive to Y_β and N_β as to Y_r and N_r.

2.5. Development of RANS-Based Manoeuvring Simulations

Towards the turn of the millennium, RANS-based simulations were first applied to ship manoeuvring in both deep- (e.g. Cura, 1999; Sato et al., 1999) and shallow-water conditions (e.g. Ohmori, 1998; Chen et al., 2001). Cura (1999) simulated turbulent flow around a ship in steady turning without free surface effects. Predicted forces agreed well with model tests and showed the correct trends. Reynolds-stress and k–ω models produced similar forces, but the k–ω model captured the flow field more accurately, including complex three-dimensional separation.

Sato et al. (1999) conducted unsteady RANS simulations for direct manoeuvring using a simplified hybrid approach: hull forces were computed by CFD, while propeller and rudder forces were represented by mathematical models, with propeller thrust assumed equal to ship resistance. A 3-DoF model without free surface was applied. Two geometrically similar ships differing only in aft-body shape (V- and U-type) were examined. Besides drift-force calculations, a 10-10 Zig-Zag manoeuvre was simulated. For the V-type hull, overshoot angles and timing agreed within 10 % of experiments, whereas the U-type showed larger deviations. Drift angles were overpredicted for both ships.

The first applications of RANS-based manoeuvring simulations to shallow-water conditions were not as successful as those to deep-water conditions. Ohmori (1998) simulated steady drift and turning motions in deep and shallow water (h/T ratios of 2.00 and 1.50)

with the Esso Osaka model at a scale of 1/130, neglecting the free surface. In deep water, drift forces and moments agreed well with experiments, while yaw forces deviated significantly. In shallow water, marked differences occurred for both yaw and drift components, especially at $h/T = 1.50$. Considering the flow field, however, one major shallow-water effect of restricted vertical flow below the ship and with this, a rather two dimensional flow, was captured. Chen et al. (2001) applied RANS-based CFD simulations to analyse inland vessels in shallow water (h/T ratios of 3.00–1.20). The study proceeded without the consideration of propeller or rudder effects, focusing exclusively on the velocity field at various cross-sections and the hull pressure distribution. The comparison of CFD and model test results for hull pressure distributions were unsatisfactory for both models and all h/T ratios. The velocity field showed better agreement for some of the selected cross sections, while others showed high deviations from model test results.

In the 2000s, there was a marked increase in the popularity of RANS-based calculations. This can be attributed to the continuous and rapid improvement of hardware, resulting in increased computing capacities, and the development of enhanced CFD codes. Nevertheless, the primary objectives were resistance and propulsion calculations (e.g. Farmer et al., 1995; Xu and Wang, 2001; Azcueta, 2005; Zwart et al., 2008), given that these represent relatively stationary conditions. The implementation of RANS techniques to model the propeller effect and movement of the rudder within the grid proved to be the most challenging aspect of conducting CFD manoeuvring simulations (ITTC, 2005). Consequently, the primary focus of the RANS simulations was on static manoeuvres, particularly in deep-water conditions, like Tahara et al. (2002).

With the further development of CFD codes, propeller modelling and dynamic grid techniques, the application of unsteady RANS-based simulations was adopted. In manoeuvring context, unsteady CFD simulations were applied to either captive model tests to determine the hydrodynamic coefficients (Cura, 2006), or to direct manoeuvring simulations involving appendages such as rudders and propellers, or propeller models (Carrica et al., 2013), but firstly only at deep-water conditions. Virtual PMM tests with a twin-screw, twin-rudder ferry model were conducted by Cura (2006), neglecting the free surface and related movements, sinkage, trim and heeling. A k-ω turbulence model was used and the propeller was modelled using a 3D body-force model. The hydrodynamic coefficients derived from virtual PMM tests showed strong correlation with model test data. The used body force propeller method demonstrated a high degree of agreement, however it appeared to underestimate the propeller thrust in oblique flow conditions.

Carrica et al. (2013) performed URANS simulations of Z 20-20 and 35° turning-circle manoeuvres for a surface combatant at model and full scale using dynamic overset grids. CFD predictions agreed well with model tests (deviations $< 10\,\%$). Only minor scale effects were observed, with slightly improved rudder effectiveness at full scale due to the thinner boundary layer. Remaining discrepancies between CFD and model test results were attributed mainly to the simplified propeller model, which neglected local inflow variations.

2.6. Ongoing Role of Experimental Methods in Manoeuvring Research

Despite the continuing immense development of RANS codes and computing power, model tests are still essential for investigating manoeuvring hydrodynamics. This is either to validate mathematical models and PMM (Eloot et al., 2015; Yeo et al., 2016; Eloot et al., 2016), or to directly analyse changed manoeuvring behaviour (Yun et al., 2015; Milanov and Chotukova, 2009; Mehr and Javanmardi, 2023; Hinostroza et al., 2019). Eloot et al. (2016) carried out pure yaw and pure sway model tests for the DTC at an h/T ratio of 1.20 at two speeds corresponding to 11 and 16 knots at full scale, for benchmarking purposes. These tests included the measured forces and moments, as well as dynamic sinkage and trim.

Milanov and Chotukova (2009) conducted free-running 10-10 Zig-Zag, spiral, and 35° turning circle manoeuvres with the KCS (KRISO Container Ship) model at h/T ratios of 2.50, 2.00, and 1.50. With decreasing water depth, the tactical diameter increased noticeably, while advance changed little, showing a slight dip at $h/T = 2.50$ and recovering at $h/T = 2.00$. The first overshoot angle decreased sharply – already at $h/T = 2.00$, it was only a third of the deep-water value – whereas the second overshoot decreased moderately (3.5–34 % for $h/T = 2.00$–1.50). Shallow water had only a slight effect on the distance travelled until the second rudder was applied, but spiral tests revealed reduced yaw rates and increased course stability. Nomoto indices indicated a decrease in K_N and a substantial increase in T_N with decreasing h/T.

Yun et al. (2015) and Yeo et al. (2016) investigated shallow-water manoeuvring of the KVLCC2 (KRISO Very Large Crude Carrier 2) at a scale of 1/83.7 using free-running and PMM tests, respectively, at h/T ratios of 2.00, 1.50, and 1.20, achieved with a false bottom. Zig-Zag 20-5/20-10 and 35° turning circle manoeuvres were performed at low speeds, with turning circles limited to 40° heading changes. Both studies observed reduced overshoot angles and yaw rates with decreasing h/T, while free-running tests exhibited distinct port-stbd asymmetry, which was only partially captured by PMM-based simulations.

Even if the use of false bottoms seems like a reasonable method for obtaining shallow-water conditions, this technique has some drawbacks, as investigated by Hachiya et al. (2022) and Sakamoto et al. (2023). Hachiya et al. (2022) compared false- and true-bottom configurations in oblique towing tests with the KCS ($h/T = 1.50$, 1.30, 1.20) and found consistently lower sway forces and yaw moments for the false bottom, with deviations increasing as depth decreased. At $h/T = 1.20$, the lateral force and yaw moment were 47 % and 42 % smaller, respectively, than for the true-bottom case.

In connection with the SIMMAN workshop 2014 (Quadvlieg et al., 2014), an extensive set of new benchmark data for the KCS and KVLCC2 in both deep and shallow water (h/T of 1.20 and 1.50 for KVLCC2 and additionally 1.80 for KCS) for both captive and free-running manoeuvres was published. The results of the submissions revealed that URANS-based direct manoeuvring simulations were capable of predicting the free-running model tests quite well, whereas simulations based on mathematical models demonstrated higher deviations as physical details get lost with this schematic approach of the real physics (ITTC, 2017).

2.7. RANS Applications to Shallow Water Manoeuvring

Despite the limitations of mathematical models using coefficients from empirical approaches or PMM tests in shallow water, recent CFD studies have largely concentrated on captive model tests and steady manoeuvring conditions, analysing the hydrodynamic forces and flow field of the manoeuvring ship in shallow water (e.g. Toxopeus, 2013; Liu et al., 2016; He et al., 2016; Lee and Hong, 2017; RoyChoudhury et al., 2017; Liu et al., 2019; Wang et al., 2023; Ohmori, 2024; van Hoydonck et al., 2024).

A detailed numerical investigation of the flow field of the KVLCC2 in deep and shallow water was performed by Toxopeus (2013) and RoyChoudhury et al. (2017), who conducted pure drift and pure yaw tests. Toxopeus (2013) used the MARIN (Maritime Research Institute Netherlands) URANS code ReFRESCO with the k-ω SST turbulence model, investigating deep-water conditions and h/T ratios of 3.00, 1.50, and 1.20. Trim, sinkage, and free-surface effects were neglected due to the low velocities considered. CFD results showed good qualitative agreement with experiments, though quantitative deviations occurred, particularly for longitudinal forces, and flow predictions were accurate only in the most upstream aft sections. Shallow-water influence was noticeable already at $h/T = 3.00$, especially at higher drift angles. For non-dimensional yaw rates below 0.4, the yaw moment was little affected by water depth, but increased significantly at higher yaw rates; overall, drift had a stronger impact on hydrodynamic forces than yaw motion.

RoyChoudhury et al. (2017) extended these analyses to deep water and $h/T = 1.50$, using an Explicit Algebraic Stress Model (EASM) for turbulence closure under the same low-speed assumption. Drift angles of 0°, 6°, and 10° and dimensionless yaw rates of 0.2 and 0.4 were considered. Sway and yaw forces were generally well predicted, although turbulent kinetic energy was underpredicted. Compared to deep water, the shallow-water flow at $h/T = 1.50$ showed increased axial velocity outside the boundary layer, stronger turbulence, enlarged bilge vortices, and a wake field growing by 30–40 % in pure drift and 100–120 % in combined drift and yaw tests. In pure yaw, vortex formation was smaller, and flow separation at the propeller plane in straight-ahead shallow-water conditions disappeared at higher drift angles (6°).

Subsequent studies applied similar captive RANS methods to other ships and manoeuvre types. Liu et al. (2016) performed pure sway and static drift simulations of the DTC at $h/T = 1.20$, reporting good agreement with model tests, but slight underprediction of lateral force and overprediction of yaw moment. He et al. (2016) combined CFD with empirical methods to derive hydrodynamic coefficients for the KVLCC2, showing that substituting CFD-derived coefficients improved Zig-Zag manoeuvre predictions in shallow water.

Lee and Hong (2017) performed full-scale RANS simulations of pure drift and pure yaw for the DTC and KVLCC2 in deep and shallow water ($h/T = 2.00$, 1.50, 1.20) using the realizable k-ε model with wall functions. The analysis focused on course stability via the relative lever arms of lateral forces from sway and yaw. In deep water and at $h/T = 2.00$, both ships were yaw-unstable due to higher sway-force levers. With decreasing depth, KVLCC2 exhibited increasing yaw-damping leverage, becoming slightly yaw-stable at $h/T = 1.50$ and strongly stable at $h/T = 1.20$. In contrast, DTC showed increasing instability down to $h/T = 1.50$, followed by only slight stabilisation at $h/T = 1.20$. Shallow

water also intensified the forebody side vortex and aft bilge vortex in drift motion.

Further RANS-based pure sway and yaw simulations were conducted for various model ships, considering water depths down to $h/T = 1.20$. Both Liu et al. (2019) and Ohmori (2024) reported generally good agreement with experimental data, with Liu et al. (2019) noting that shallow-water hydrodynamic derivatives were sensitive to squat effects only at higher velocities (16 kn full scale). Wang et al. (2023) investigated three different speeds for the Esso Osaka model and observed only minor variations (within 10 %) in drag, lateral, and yaw moment coefficients for pure yaw tests.

According to ITTC (2008), free-running model tests are generally regarded as providing the most realistic representation of manoeuvring behaviour among model test approaches, as they involve fewer modelling assumptions, apart from possible scale effects due to the lower Reynolds number. However, only few CFD applications of free-running manoeuvres in shallow water have been conducted in recent years (e.g. Carrica et al., 2016; Kim et al., 2022), probably due to the high computational costs associated with this kind of manoeuvring simulation. Carrica et al. (2016) conducted 6-DoF URANS free-running simulations of the KCS in a Zig-Zag 20-5 manoeuvre at $h/T = 1.20$ and one speed, with fully discretised propeller and rudder using the k-ω SST model. Grid-convergence studies were applied not only to self-propulsion but, for the first time, to a complete manoeuvre: while self-propulsion showed good convergence, the manoeuvre simulation exhibited oscillatory and partly divergent behaviour. Propulsion predictions agreed well with experiments, whereas yaw and yaw rate were underestimated by about 15–20 %, attributed to rudder-force or hull yaw-moment discrepancies due to inaccurate prediction of separation.

Kim et al. (2022) extended URANS free-running simulations of the KCS to multiple depths (deep water to $h/T = 1.20$) and manoeuvres. Shallow water had little influence on course-keeping without external loads, but at $h/T = 1.20$ the transfer and tactical diameter more than doubled and the advance increased by about 42 % compared to deep water. Flow analysis highlighted strong interactions among hull wake, vortices, seabed, and propeller.

3. Fundamentals of Numerical Method

This chapter provides a brief description of the theory behind the numerical method used to solve the Reynolds-Averaged Navier-Stokes equations. This includes the governing equations, turbulence models, the interpolation method, and the solution approaches.

3.1. Governing Equations

The flow of Newtonian fluids can be described by two conservation equations for mass (continuity equation) and momentum, which are together the so-called 'Navier-Stokes equations'. For speeds far lower than supersonic speed (Ma < 0.3), fluids can be assumed to be incompressible. For incompressible fluid, using the Einstein summation notation, the Navier-Stokes equations in differential form are:

$$\rho \frac{\partial u_i}{\partial x_i} = 0\,, \tag{3.1}$$

$$\frac{\partial u_i}{\partial t} + \frac{\partial u_i u_j}{\partial x_j} = -\frac{1}{\rho}\frac{\partial p}{\partial x_i} + \nu \frac{\partial^2 u_i}{\partial x_j \partial x_j} - f_i\,. \tag{3.2}$$

Here, u represents the velocity of a particle in the flow, ρ is the fluid density, p is the pressure, ν the kinematic viscosity and f a volume force density, such as the gravity. Except for certain highly simplified cases, no general analytical solution to the Navier–Stokes equations exists. Consequently, the resolution of this problem necessitates numerical discretisation. The direct solution of this equation via numerical discretisation is referred to as direct numerical simulation (DNS). Assuming the correct numerical discretisation, with this method all fluctuating conservation variables of the flow can be resolved. However, most applications to engineering problems show high Reynolds numbers, which has a cubic proportionality to the effort of a DNS simulation (Ferziger et al., 2020). Hence, most cases cannot be calculated in reasonable time using DNS due to the very fine grid discretisation, which is necessary to resolve even the smallest eddies in space and time. Another method is the large-eddy simulation (LES), which only considers the large eddies, as they generally possess more energy than the small-scale eddies. Despite the disregarding of the smaller eddies, the computational effort is still high and scales as $Re^{2.7}$ for a wall resolving LES close to the wall and $Re^{0.53}$ for the outer flow (Fröhlich, 2006). Both calculation methods are very complex and resolve many details of a flow that, from an engineer's perspective, are less relevant in many cases. A reasonable approach is to consider the conservation variables in terms of time averaging, as explained in the next section.

3.2. Reynolds-Averaged Navier-Stokes Equations

The Reynolds-Averaged Navier-Stokes (RANS) equations describe the flow behaviour of turbulent viscous flows. Turbulent flows are three-dimensional, highly transient and show strongly increased diffusion. This diffusion results from a cross flow, superimposed on the main direction of motion. For high Reynolds numbers, energy of the main flow is converted into large eddies, i.e. turbulent kinetic energy, while the dissipation of this kinetic energy mainly emerges in the area of boundary layer close to the wall, in the smaller eddies (Schlichting and Gersten, 2006). In mathematical terms, this flow behaviour is described by the Navier-Stokes equations for incompressible fluids, see Equation 3.1 and Equation 3.2. The most important information can be derived by the time averages of the conservation variables. For this purpose, any variable ϕ of a statistical stationary flow can be described by a sum of time mean value and turbulent fluctuation of this mean value:

$$\phi(x_i, t) = \bar{\phi}(x_i) + \phi'(x_i, t)\,, \tag{3.3}$$

with

$$\bar{\phi}(x_i) = \lim_{0 \to T} \frac{1}{T} \int_0^T \phi(x_i, t)\mathrm{d}t\,. \tag{3.4}$$

Here, T is the averaging interval, and t the time. Bringing each variable of the Navier-Stokes equations into a form according to Equation 3.3 and carrying out a time average of this equation, one obtains the Reynolds-averaged Navier-Stokes equations:

$$\rho \overline{\frac{\partial u_i + \partial u_i'}{\partial x_i}} = 0\,, \tag{3.5}$$

$$\overline{\frac{\partial(\bar{u_i} + u_i')}{\partial t}} + \overline{\frac{\partial(\bar{u_i} + u_i')(\bar{u_j} + u_j')}{\partial x_j}} = -\frac{1}{\rho}\overline{\frac{\partial(\bar{p} + p')}{\partial x_i}} + \nu \overline{\frac{\partial^2(\bar{u_i} + u_i')}{\partial x_j \partial x_j}} - f_i\,. \tag{3.6}$$

For $\bar{\phi'} = 0$ follows:

$$\rho \frac{\partial \bar{u_i}}{\partial x_i} = 0\,, \tag{3.7}$$

$$\frac{\partial \bar{u_i}}{\partial t} + \frac{\partial \bar{u_i}\bar{u_j}}{\partial x_j} = -\frac{1}{\rho}\frac{\partial \bar{p}}{\partial x_i} + \frac{\partial}{\partial x_j}(\nu \frac{\partial \bar{u_i}}{\partial x_j} - \overline{u_j' u_i'}) - f_i\,. \tag{3.8}$$

As conservation equations on the right side of Equation 3.8 still includes fluctuations, or to be more precise the correlations of fluctuations, which can not be analytically represented by mean values of the flow, these equations are referred to as not closed. This means there are fewer equations than contained variables, which in the literature is often referred to as the closure problem (Ferziger and Perić, 2008). Multiplying the fluctuations in parentheses on the right side of Equation 3.8 with the density, the so called Reynolds stresses are obtained:

$$\tau_{ij} = -\rho\overline{u_j' u_i'} = -\rho \begin{pmatrix} \overline{u_x' u_x'} & \overline{u_x' u_y'} & \overline{u_x' u_z'} \\ \overline{u_y' u_x'} & \overline{u_y' u_y'} & \overline{u_y' u_z'} \\ \overline{u_z' u_x'} & \overline{u_z' u_y'} & \overline{u_z' u_z'} \end{pmatrix}. \tag{3.9}$$

Hence, the Reynolds stresses introduce six additional unknown terms. Due to these Reynolds stresses, the RANS equation can not be closed by exact equations. Thus, approximations are necessary in order to solve the equation, which are generally referred to as turbulence models. It can be distinguished between such turbulence models which discretise the Reynolds stress tensor directly, like the Reynolds-Stress model (RSM), and such that are based on the Boussinesq assumption (Fröhlich, 2006). The latter, fundamental approach for such approximations, brings the Reynolds stresses into a form that does not contain any fluctuations. The turbulent stress tensor is simplified to the mean strain rate $\overline{S_{ij}} = \frac{1}{2}\left(\frac{\partial u_i}{\partial x_j} + \frac{\partial u_j}{\partial x_i}\right)$. Hence, it is considered that the turbulence can be treated like an increased isotropic viscosity, which is assumed to be equally strong in all directions and it follows for the Reynolds stresses (Ferziger and Perić, 2008):

$$\tau_{ij} = -\rho\overline{u_j' u_i'} = 2\mu_t\overline{S_{ij}} - \frac{2}{3}k\rho\delta_{ij} = \mu_t\left(\frac{\partial \bar{u}_i}{\partial x_j} + \frac{\partial \bar{u}_j}{\partial x_i}\right) - \frac{2}{3}k\rho\delta_{ij}\,, \tag{3.10}$$

with $k = \frac{1}{2}\overline{u_i' u_i'}$ for the turbulent kinetic energy. The factor ν_t or μ_t with $\mu_t = \nu_t/\rho$ is called turbulent viscosity. One model for determination of the dynamic turbulent viscosity μ_t or kinematic turbulent viscosity ν_t is the k-ε model (Jones and Launder, 1972). Here, two additional transport equations are solved for the turbulent kinetic energy k and its dissipation rate ε.

$$\underbrace{\frac{\partial k}{\partial t}}_{\text{Temporal}} + \underbrace{\bar{u}_j\frac{\partial k}{\partial x_j}}_{\text{Convection}} = \underbrace{\frac{\partial}{\partial x_j}\left((\nu + \frac{\nu_t}{\sigma_k})\frac{\partial k}{\partial x_j}\right)}_{\text{Diffusion}} + \underbrace{\nu_t\frac{\partial \bar{u}_i}{\partial x_j}\left(\frac{\partial \bar{u}_i}{\partial x_j} + \frac{\partial \bar{u}_j}{\partial x_i}\right)}_{\text{Production}} - \underbrace{\varepsilon}_{\text{Dissipation}}\,, \tag{3.11}$$

$$\underbrace{\frac{\partial \varepsilon}{\partial t}}_{\text{Temporal}} + \underbrace{\bar{u}_j\frac{\partial \varepsilon}{\partial x_j}}_{\text{Convection}} = \underbrace{\frac{\partial}{\partial x_j}\left((\nu + \frac{\nu_t}{\sigma_\varepsilon})\frac{\partial \varepsilon}{\partial x_j}\right)}_{\text{Diffusion}} + \underbrace{\frac{\varepsilon}{k}C_{1\varepsilon}\nu_t\frac{\partial \bar{u}_i}{\partial x_j}\left(\frac{\partial \bar{u}_i}{\partial x_j} + \frac{\partial \bar{u}_j}{\partial x_i}\right)}_{\text{Production}} - \underbrace{\frac{\varepsilon}{k}C_{2\varepsilon}\varepsilon}_{\text{Dissipation}}\,. \tag{3.12}$$

The turbulent viscosity than results in

$$\nu_t = C_\mu\frac{k^2}{\varepsilon}\,. \tag{3.13}$$

The factors $C_{1\varepsilon}$, $C_{2\varepsilon}$, σ_k, σ_ε and C_μ represents empirical constants and are defined as follows (Launder and Sharma, 1974):

$$C_{1\varepsilon} = 1.44,\, C_{2\varepsilon} = 1.92,\, \sigma_k = 1.0, \sigma_\varepsilon = 1.3,\, C_\mu = 0.09 \tag{3.14}$$

The standard k-ε model is optimised for high Reynolds number flows and requires wall functions for boundary layer treatment. Consequently, there were different approaches to modify this model to account for viscous flow near the wall. One approach is the 'Standard k-ε low-Re model' according to Lien et al. (1996), where additional damping functions are applied to the constants C_μ, $C_{1\varepsilon}$ and $C_{2\varepsilon}$ in Equation 3.11 and Equation 3.12,

incorporating the wall-normal distance in order to resolve the viscous flow regime near the wall, while using the identical coefficients as the standard k-ε model. Equation 3.13 (and therefore also implicitly Equation 3.11) and Equation 3.12 changes to:

$$\nu_t = C_\mu \frac{k^2}{\varepsilon} \cdot f_\mu \,, \tag{3.15}$$

$$\frac{\partial \varepsilon}{\partial t} + u_j \frac{\partial \varepsilon}{\partial x_j} = \frac{\partial}{\partial x_j}\left(\frac{\nu_t}{\sigma_\varepsilon}\frac{\partial \varepsilon}{\partial x_j}\right) + \frac{\varepsilon}{k}\left(C_{1\varepsilon}\nu_t \frac{\partial \bar{u}_i}{\partial x_j}\left(\frac{\partial \bar{u}_i}{\partial x_j} + \frac{\partial \bar{u}_j}{\partial x_i}\right) - C_{2\varepsilon}\varepsilon \cdot f_2\right). \tag{3.16}$$

The damping functions f_2 and f_μ are defined as follows:

$$f_2 = 1 - 0.3e^{-Re_t^2} \tag{3.17}$$

$$f_\mu = 1 - e^{-\left(C_{d0}Re_d + C_{d1}Re_d + C_{d2}Re_d^2\right)} \tag{3.18}$$

where $Re_t = \frac{k^2}{\nu\varepsilon}$ is the turbulent Reynolds number and $Re_d = \frac{\sqrt{k}d}{\nu}$ is the wall-distance Reynolds number, with d as the distance to the wall. C_{d0}, C_{d1} and C_{d2} in Equation 3.18 are empirical coefficients:

$$C_{d0} = 0.091,\ C_{d1} = 0.0042,\ C_{d2} = 0.00011 \tag{3.19}$$

An alternative two-equation approach to the k-ε model is the k-ω model according to Wilcox (1988, 2006), which solves for the specific dissipation rate ω instead of the dissipation ε. This turbulent frequency ω is the dissipation rate ε per unit turbulent kinetic energy k. The Wilcox k-ω model generally achieved better results when describing the mean turbulence of the flow field close to the wall, but had some drawbacks in the free-stream modelling compared to k-ε model (Schwarze, 2012). Therefore, based on the Wilcox k-ω turbulence model, Menter (1994) developed the shear stress transport (SST) k-ω model, which combines the advantages of the k-ω and standard k-ε model. With the help of a blending function, the k-ω model is used in the sub-layer close to the wall, and the standard k-ε model is used for the free stream. With $\nu_t = \frac{k}{\omega}$, the resulting k-ω SST model equation systems are:

$$\frac{\partial k}{\partial t} + \bar{u}_j \frac{\partial k}{\partial x_j} = \frac{\partial}{\partial x_j}\left(\nu + \nu_t \sigma_k \frac{\partial k}{\partial x_j}\right) + \nu_t \frac{\partial \bar{u}_i}{\partial x_j}\left(\frac{\partial \bar{u}_i}{\partial x_j} + \frac{\partial \bar{u}_j}{\partial x_i}\right) - \beta^* k\omega \,, \tag{3.20}$$

$$\begin{aligned}\frac{\partial \omega}{\partial t} + \bar{u}_j \frac{\partial \omega}{\partial x_j} = \frac{\partial}{\partial x_j}\left(\nu + \nu_t \sigma_\omega \frac{\partial \omega}{\partial x_j}\right) + \nu_t \frac{\partial \bar{u}_i}{\partial x_j}\left(\frac{\partial \bar{u}_i}{\partial x_j} + \frac{\partial \bar{u}_j}{\partial x_i}\right)\frac{\gamma}{\nu_t} \\ - \beta\omega^2 + 2(1 - F_1)\sigma_\omega \frac{1}{\omega}\frac{\partial k}{\partial x_j}\frac{\partial \omega}{\partial x_j}\,.\end{aligned} \tag{3.21}$$

The blending function F_1, which takes the value one inside the boundary layer and zero in the free stream, is defined by Menter et al. (2003). The coefficients of the SST model are

$$\beta_1 = 0.075,\ \sigma_{k1} = 0.85,\ \sigma_{\omega 1} = 0.5,\ \gamma_1 = \frac{\beta_1}{\beta^*} - \frac{\sigma_{\omega 1}\kappa^2}{\sqrt{\beta^*}},\ \beta^* = 0.09$$

$$\beta_2 = 0.0828,\ \sigma_{k2} = 1.0,\ \sigma_{\omega 2} = 0.856,\ \gamma_2 = \frac{\beta_2}{\beta^*} - \frac{\sigma_{\omega 2}\kappa^2}{\sqrt{\beta^*}},\ \kappa = 0.41\,.$$

3.3. Numerical Method

For the solution of the conservation equations from section 3.2, it is necessary to convert the partial differential equations into finite difference equations. There are three different approaches of such discretisations: finite difference (FD), finite element (FE) and finite volume method (FV) (Ferziger et al., 2020). The finite volume discretisation is the most commonly used solution method (Schwarze, 2012) and also used by the commercial software package Star-CCM+. The FV method uses the integral form of the equations from section 3.2. One of the main advantages of this integral form, compared to FD method, is the integrated, conservative discretisation of all conservation variables as the conservation equations are applied to each CV and summed up to the whole domain (Schwarze, 2012). A grid is used to discretise the computational domain into small non-overlapping control volumes (CV), defining the CV boundaries (Ferziger et al., 2020). Each CV boundary is an area shared by two neighbouring cells. Similar to Equation 3.2 for the velocity u, the conservation equation for an arbitrary scalar quantity ϕ can be expressed in vector notation for incompressible fluids (compare also Schwarze, 2012):

$$\rho\left(\frac{\partial \phi}{\partial t} + \mathbf{u}\cdot\nabla\phi\right) = \nabla\cdot(\Gamma\nabla\phi) + q_\phi\,, \tag{3.22}$$

with the diffusion coefficient Γ and source term q_ϕ. The FV method evaluates the conservation equations locally by integrating over the volume V_C of each CV:

$$\rho\int_{V_C}\frac{\partial\phi}{\partial t}dV + \rho\int_{V_C}\phi\mathbf{u}\cdot dV = \int_{V_C}\Gamma\nabla\phi\cdot dV + \int_{V_C} q_\phi dV \tag{3.23}$$

Applying the Gauss's theorem, the volume integral of the convection and diffusion terms can be transformed into surface integrals over the boundary surface S_C:

$$\rho\int_{V_C}\frac{\partial\phi}{\partial t}dV + \rho\int_{S_C}\phi\mathbf{u}\cdot d\mathbf{S} = \int_{S_C}\Gamma\nabla\phi\cdot d\mathbf{S} + \int_{V_C} q_\phi dV \tag{3.24}$$

The terms with volume integrations from Equation 3.24 are approximated in second order by midpoint rule, where the integral is transformed into the product of the CV volume and the mean value of the integrand, which in turn is approximated by the value of the CV centre. The surface integrals of the convection and diffusion term can be discretised by the sum of integrals over their cell faces f, which in turn can be approximated by the midpoint rule (Ferziger and Perić, 2008):

$$\rho\int_{S_C}\phi\mathbf{u}\cdot d\mathbf{S} = \rho\sum_f\int_f\phi\mathbf{u}\cdot d\mathbf{S} \approx \rho\sum_f\phi_f(\mathbf{u}\cdot\mathbf{n})_f S_f\,. \tag{3.25}$$

$$\int_{S_C}\Gamma\nabla\phi\cdot d\mathbf{S} = \sum_f\int_f\Gamma\nabla\phi\cdot d\mathbf{S} \approx \sum_f\Gamma_f\nabla\phi_f\cdot\mathbf{n}_f S_f\,. \tag{3.26}$$

These equations are evaluated at the centre of each cell face and need interpolation from the respective neighbouring cells, which stores their values in the centre of the CV.

3.4. Interpolation and Discretisation Methods

The simplest approach of interpolation method is the first order upwind differencing scheme (UDS), which equates the value at the respective cell face ϕ_f to the value in the upwind CV centre ϕ_U (or downwind ϕ_D for negative flux):

$$\phi_f^{UDS} = \phi_U \,. \tag{3.27}$$

The main advantage of this simple approach is the non-oscillating solutions obtained by this approximation (Ferziger et al., 2020). However, the associated error term of this approach is diffusive and leads to numerical diffusion. The central differencing interpolation scheme (CDS) can be obtained by Taylor series expansion, considering also the second term (Schwarze, 2012).

$$\phi_f^{CDS} = \frac{1}{2}(\phi_U + \phi_D) \,. \tag{3.28}$$

The CDS shows higher accuracy than the UDS and lower numerical diffusion. However, the method does not take into account the direction of flow and hence, shows no convection characteristics (Schwarze, 2012). This can lead to numerical instability and oscillating results. However, this is not the case for the diffusive term of the conservation equation. As this term is of elliptic character and independent of flow direction, it can be interpolated by the CDS method. For the convective term (Equation 3.25), the second order upwind differencing scheme (SOU) is often used. It considers also the second term of the Taylor series expansion, but explicitly takes into account the flow direction. Compared to UDS it improves the numerical stability and accuracy of the interpolation. Here, x_U and x_f denote the positions of the upstream cell center and the face, respectively, yielding (Schwarze, 2012):

$$\phi_f^{SOU} = \phi_U + (x_f - x_U) \cdot \nabla\phi_U \,. \tag{3.29}$$

For transient calculations, the first term of Equation 3.24 needs to be discretised by numerical integration as well. The simplest approach is the explicit or forward Euler method (Ferziger and Perić, 2008):

$$\phi^{n+1} = \phi^n + \Delta t \cdot f(t_n, \phi^n) \,. \tag{3.30}$$

This method evaluates the differential equation for the actual time step n and needs no iteration, but causes instabilities when the time step size Δt is too high. The implicit or backward Euler method shows improved stability but requires additional equation systems to be solved iteratively as the differential equation is evaluated for the next time step $n+1$:

$$\phi^{n+1} = \phi^n + \Delta t \cdot f(t_{n+1}, \phi^{n+1}) \,. \tag{3.31}$$

Both methods are first order methods. A common implicit Euler method of second order

is the backward differentiation formula (BDF2), which uses the actual time step n and the previous step $n-1$ (Schwarze, 2012):

$$\phi^{n+1} = \frac{4}{3}\phi^{n} - \frac{1}{3}\phi^{n-1} + \frac{2}{3}\Delta t \cdot f(t_{n+1}, \phi^{n+1})\,. \tag{3.32}$$

3.5. Solution Approaches

These temporal and spatial discretisation and interpolation methods given above are used to solve the discrete form of Equation 3.24 for each cell of the numerical domain. This leads to a linear equation system (Schwarze, 2012):

$$a_P \phi_P + \sum_{NB} a_{NB}\phi_{NB} = b\,. \tag{3.33}$$

The coefficients a originate from the spatial and temporal discretisation of the conservation equations. The linear equation is iteratively solved for the scalars in the centre of the CV ϕ_P and for the adjacent cells ϕ_{NB}. The conservation equations for mass and momentum can be solved in this manner, by using a coupled or segregated method. In the coupled approach, the Navier-Stokes equations are calculated simultaneously. This approach is usually applied for compressible flows as the conservation equations show a strong coupling (Schwarze, 2012). The method more commonly used for incompressible flows, is the segregated approach, which solves for mass and momentum separately. Iterative solution is required due to the coupling between pressure and velocity. One of these predictor-corrector approaches is the common Semi Implicit Method for Pressure Linked Equations (SIMPLE). Here, the linear equation system for momentum conservation is firstly solved with a predicted pressure p^* to obtain the predicted velocity $\mathbf{u}^*$. The pressure correction p' is then determined such that the continuity equation is satisfied. With this corrected pressure the corrected velocity u' can be calculated. The velocity and pressure for the next time steps are then obtained by considering the correction terms and under-relaxation factors α_p and α_u to ensure for convergence (Schwarze, 2012):

$$p^{n+1} = p^{n} + \alpha_p p' \tag{3.34}$$

$$\mathbf{u}^{n+1} = \alpha_u(\mathbf{u}^* + \mathbf{u}') + (1-\alpha_u)\mathbf{u}^{n} \tag{3.35}$$

This iterative procedure is repeated until the residuals are dropped below a specified value.

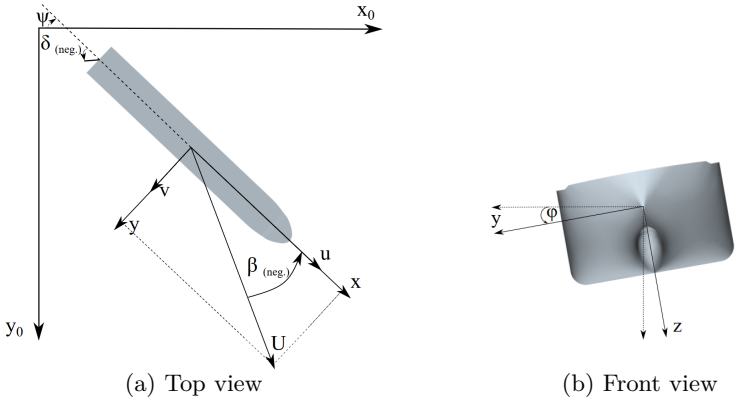
4. Manoeuvring

The principles of manoeuvring of ships in calm water are presented in the following chapter. The mathematical description of the manoeuvring behaviour is introduced and some experimental methods for determining the manoeuvring characteristics are described. Additionally, the fundamental effects of shallow water on ship manoeuvring behaviour are briefly outlined.

4.1. Definitions

The earth-fixed coordinate system x_0, y_0 is oriented to point in the same direction as the ship-fixed coordinate system at the beginning of the manoeuvre. The ship-fixed coordinate system is placed in the centre of gravity, with the longitudinal axis x pointing forward, the transverse axis y pointing to stbd and the vertical axis z pointing downwards. While the trajectory of the ship is described in the earth-fixed coordinate system, all other parameters like forces and velocities are written in ship-fixed coordinate system. The rudder angle δ is positive for port deflection, the yaw angle of the ship is positive for stbd turning. The coordinate system in top and front view of the free-running model is shown in Figure 4.1.

Usually, the manoeuvring of ships in calm water is described in 3 (horizontal movements surge, sway and yaw only) or 4 degrees of freedom (including the heeling). The heeling of the ship is only important for high velocities and small GM values of the ship, resulting in significant heeling angles (e.g. Kijima et al., 1997; ITTC, 2014). This study investigates the manoeuvring motion of ships in calm water with sufficient GM values, focusing primarily on slow velocities. Consequently, only the ship's horizontal movements are considered in the following.



(a) Top view (b) Front view

Figure 4.1.: Coordinate system

The ship-fixed coordinates are functions of time and hence, the velocities obtained by the time derivatives of the spatial variables x, y and ψ. However, the velocities are indeed relative to the earth-fixed system, but described in the ship-fixed system, which is an accelerated and rotating reference frame and hence, no inertial system. For this reason, the time derivative of the positional vector components includes the time derivative of unity vectors, which is the cross product of rotational vector and unity vector. From this derivation and applying Newton's second law, the longitudinal force X, transverse force Y, and yaw moment N are obtained (see Abdel-Maksoud):

$$X = m(\dot{u} - vr - x_G r^2)\,, \tag{4.1}$$

$$Y = m(\dot{v} + ur + x_G \dot{r})\,, \tag{4.2}$$

$$N = I_{zz}\dot{r} + m x_G(\dot{v} + ur)\,, \tag{4.3}$$

where x_G is the distance from the coordinate system and the centre of gravity and I_{zz} is the moment of inertia around the vertical axis. Since the coordinate system here, is placed in the centre of gravity, x_G is zero and the last term in Equation 4.1 to Equation 4.3 can be omitted. The term $-mvr$ of Equation 4.1 and mur of Equation 4.2 are the longitudinal and respectively transverse components of the centrifugal force, which only appears in rotating reference systems. The external forces X and Y and the moment N are hydrodynamic forces and moment acting on hull, rudder and propeller of the ship.

Usually, the forces, velocities and accelerations are considered in non-dimensional form, dividing by dynamic pressure $0.5\rho U_0^2$, ship length L_{PP}, ship draught T, ship velocity at the start of the manoeuvre U_0, or time L_{PP}/U_0:

$$X' = \frac{X}{0.5\rho U_0^2 L_{PP} T}\,, \qquad Y' = \frac{Y}{0.5\rho U_0^2 L_{PP} T}\,, \qquad N' = \frac{N}{0.5\rho U_0^2 L_{PP}^2 T}\,. \tag{4.4}$$

The non-dimensional form of velocities and accelerations are obtained by

$$u' = \frac{u}{U_0}\,, \qquad v' = \frac{v}{U_0}\,, \qquad r' = \frac{r L_{PP}}{U_0}\,, \tag{4.5}$$

$$\dot{u'} = \frac{\dot{u} L_{PP}}{U_0^2}\,, \qquad \dot{v'} = \frac{\dot{v} L_{PP}}{U_0^2}\,, \qquad \dot{r'} = \frac{\dot{r} L_{PP}^2}{U_0^2}\,. \tag{4.6}$$

For the non-dimensional rudder forces in transversal (C_{Y_R}) and longitudinal direction (C_{X_R}), the rudder area A_R is used instead of L_{PP} and T:

$$C_{Y_R} = \frac{X_R}{0.5\rho U_0^2 A_R}\,, \qquad C_{X_R} = \frac{Y_R}{0.5\rho U_0^2 A_R}\,. \tag{4.7}$$

4.2. Nomoto Equation

The hydrodynamic forces are functions of velocity, acceleration, rudder angle and propeller rotation. There are several mathematical approaches to describe the hydrodynamic forces in dependence of this variables. One of the earliest approaches was proposed by Abkowitz

(1964), who represented the hydrodynamic forces using a third-order Taylor series expansion. Besides less precise empirical methods, e.g. Clarke et al. (1982), the corresponding force coefficients must be be directly measured via captive model tests or obtained through system identification of manoeuvring motions from free-running tests. These methods are complex and expensive and not useful for the design stage of a vessel or for fast determination and comparison of manoeuvring behaviours. For this cases linear approaches are considered.

Nomoto and Taguchi (1957) adopted a simplified mathematical approach to consider manoeuvring motion, particularly to more easily assess the turning and steering behaviour of a new vessel in the design stage. Based on the linearised equation of motion, he decoupled the longitudinal motion from the transverse and yaw motion of the ship by considering the velocity at the start of the manoeuvre, U_0, for the equations of Y and N. Hence, the deceleration of the ship caused by steering is neglected. Based on these decoupled linear equations for transverse and yaw motion eliminating the drift velocity, the second order Nomoto equation for yaw motion can be derived:

$$T_1 T_2 \ddot{r} + (T_1 + T_2)\dot{r} + r = K_N \; \delta + K_N \; T_3 \dot{\delta} \tag{4.8}$$

T_1 and T_2 denote course stability and time response for manoeuvring. While the former is related to response to midship rudder, the latter is related to adaptation of drift velocity and yaw rate after steering. K_N is an index for steady turning motion and T_3 defines the donation of steering speed to begin of a turning motion. Neglecting the cross-coupling terms $N_v v$ and $Y_r r$, the first order Nomoto equation is obtained (Nomoto and Taguchi, 1957; Lewis, 1989):

$$T_N \; \dot{r} + r = K_N \delta, \tag{4.9}$$

with

$$T_N = T_1 + T_2 - T_3 = \frac{(I_{zz} - N_{\dot{r}})}{N_r}\,, \qquad K_N = \frac{N_\delta}{N_r}\,. \tag{4.10}$$

For the case of a sudden rudder helm at straight-ahead cruise, the solution of Equation 4.9 is

$$r(t) = K_N \; \delta(1 - e^{-t/T_N})\,. \tag{4.11}$$

With sufficient time passed, the differences of the solutions between Equation 4.8 and Equation 4.9 vanish (Motora, 1960). K_N is a ratio of turning moment and hydrodynamic damping coefficient, representing an index for turning ability, and T_N is a ratio of mass moment of inertia and hydrodynamic damping coefficient, representing an index of steering response to change from one steady condition to another. Motora (1960) pointed out that T_N is very similar to T_1 (10 % to 20 % deviation) and therefore also represents the course stability of the ship. The Nomoto indices are usually stated in non-dimensional form:

$$T'_N = \frac{T_N \; U_0}{L_{PP}}\,, \qquad K'_N = \frac{K_N \; L_{PP}}{U_0}\,. \tag{4.12}$$

Based on the two Nomoto coefficients K_N and T_N, Norrbin proposed a 'course change quality number' P, also referred to as 'Norrbin parameter' (Nomoto and Norrbin, 1969):

$$P = \frac{K'_N}{2T'_N} \,. \tag{4.13}$$

Since P is a ratio of K'_N and T'_N, the yaw damping coefficient is shortened out and hence, the Norrbin parameter cannot evaluate those manoeuvring abilities which are strongly related to yaw damping effects, like the course stability. Thus, P is only a good parameter of evaluating the manoeuvrability for ships with good course stability. For ships with low course stability, Nomoto and Norrbin (1969) proposed an additional measure to consider, like the slope of yaw rate depending on ruder angle. Nomoto and Taguchi (1957) already pointed out that the coefficients K_N and T_N can be determined by the results of Zig-Zag manoeuvre. This is accomplished by integration of the rudder angle δ and course angle ψ of a Zig-Zag manoeuvre (Journée and Pinkster, 2002).

4.3. Manoeuvring Tests

This section provides brief descriptions of free-running standard manoeuvring tests as well as captive model tests. Further definitions and detailed information are given by the IMO (2002) and ITTC (2002, 2014, 2021).

4.3.1. Free-running Tests

A well-established method to determine the manoeuvrability of a vessel are the IMO standard manoeuvring tests. These standard manoeuvres are performed at sea trials for sea-going vessels before the ship is handed over to the owner by the shipyard. Beside the stopping manoeuvre, which is used to determine the stopping ability of the vessel, the two required manoeuvring tests are the turning circle and Zig-Zag manoeuvre. Furthermore, there are additional optional standard manoeuvres like the spiral manoeuvre or Dieudonné test, and the pull-out manoeuvre to assess the yaw stability of the vessel, see ITTC (2002).

The Zig-Zag manoeuvre is a standard test used to determine the manoeuvring characteristics of a ship, see Figure 4.2. After reaching a steady approach speed U_0, the manoeuvre is initiated when the rudder is commanded to move to stbd or port towards a prescribed angle. This rudder position is maintained until the ship reaches the desired course. At this point, the rudder is moved in the opposite direction. The ship now returns to its original course. As soon as the ship reaches the same deviation from the initial course in the opposite direction, counter rudder is applied again. This process is repeated several times. Relevant parameters of the Zig-Zag manoeuvre are:

- Inital turning time (t_a): Time from the start of the manoeuvre to the desired heading deviation.
- Yaw-checking time (t_s): Time interval from the application of counter rudder to the time of maximum heading angle.

- Overshoot angle (α): Difference between the heading angle at which counter rudder was applied and the maximum heading angle reached.

When the overshoot or maximum deviation angle is reached, the yaw rate of the ship is crossing the zero point and the trajectory is at its turning point. The maximum yaw rate is not necessarily at the point of counter rudder deflection but somewhat earlier as the increasing drift angle of the ship is decreasing the effective rudder inflow angle and therefore the magnitude of rudder transversal force, which mainly contributes to the increase in yaw rate.

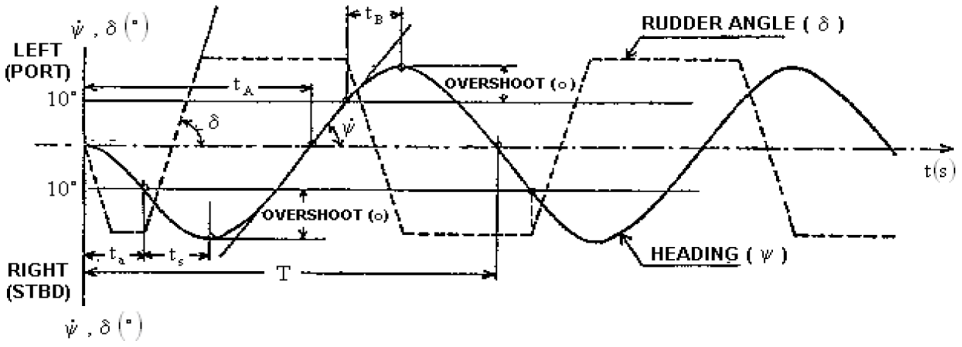


Figure 4.2.: Zig-Zag manoeuvre according to ITTC (Source: ITTC, 2002)

The turning circle manoeuvre is initiated under the same initial conditions. After travelling straight-ahead at a constant speed, the rudder is set to a certain angle to stbd/port and kept constant, see Figure 4.3. The turn is maintained until a constant yaw rate is achieved. Relevant turning circle parameters are:

- Advance: Longitudinal distance from manoeuvre initiation to 90° heading.
- Transfer: Transversal distance from manoeuvre initiation to 90° heading.
- Loss of speed: Difference between approach and steady turning speed.
- Tactical diameter: Transversal distance from manoeuvre initiation to 180° heading.
- Turning circle radius (TCR): Steady turning circle radius.
- Drift angle (β): Adjusted drift angle under steady turning circle conditions.

The turning circle can be divided into three different phases (Lewis, 1989): A first phase, where mainly accelerations occur, a second phase characterised by both accelerations and velocities, with all terms of the equations of motions being effective, and a third steady-state phase of the turning circle, where the accelerations $\dot{v}$ and $\dot{r}$ are equal to zero and the ship is turning with a constant radius.

Since the manoeuvrability of the ships can be easily derived from these tests, they are widely used for free-running model tests, as well. As the impact of scaling effects on manoeuvring behaviour is not yet fully understood, the model should be chosen as large

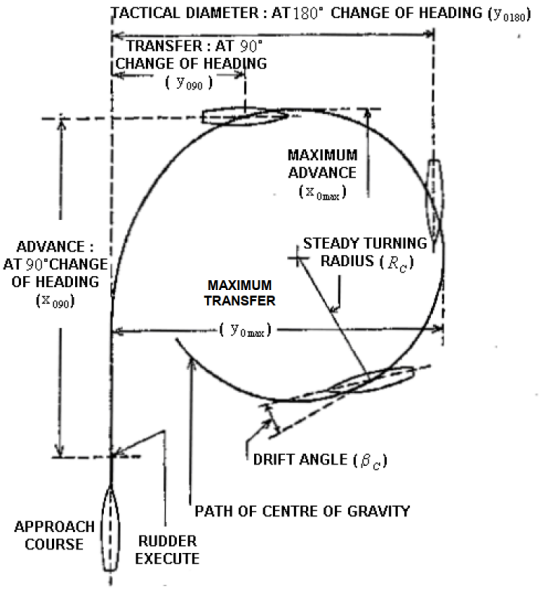


Figure 4.3.: Turning circle manoeuvre according to ITTC (Source: ITTC, 2002)

as possible, subject to the geometric constraints of the test basin. The model's loading condition should correspond to that of the full-scale vessel, particularly with respect to the aft and forward draught, as well as the GM, while the radii of gyration around the transverse and vertical axis k_{yy} and k_{zz} are set to values close to $0.25\,L_{PP}$ (ITTC, 2021).

The manoeuvring model tests are carried out in accordance with the Froude scaling law. Consequently, the drag resistance of the model ship is overestimated, which is the most relevant scaling effect affecting the model tests. In the absence of a friction correction force being applied to the free-running model, as is customary in towing tests, the model ship is not operating at the full scale propulsion point, requiring a comparatively higher propeller rotation rate n to achieve the desired velocity. Due to the higher wake at the propeller and higher thrust loading factor, the velocity at the rudder in the propeller stream is comparatively higher for model ships. Conversely, the velocity outside of the propeller stream is lower due to the higher wake of the model ship. For single screw ships, it is assumed that both contradictory effects roughly cancel each other out (Oltmann, 1978). Several authors have investigated the scaling effects on manoeuvring behaviour using captive (Motora and Couch, 1961; Bogdanov et al., 1987b) or free-running model tests (Shiba, 1960; Nomoto, 1966; Martinussen and Linnerud, 1987), which are described in more detail in chapter 2. Summarising the results for the latter, the free-running models are generally capable of capturing the main manoeuvring behaviour of a vessel, particularly for slender ships and higher rudder angles, but usually show slightly higher course stability than the full-scale vessel. Another effect that is usually neglected in free-running model tests, refers to the reduced n during full-scale manoeuvres, which result in high speed losses due to the engine's response. For model ships, n is typically kept constant throughout the manoeuvre, since reductions in propeller rotation rate of only 10 to 15 % are usually observed in diesel-powered engines (Lewis, 1989).

As already mentioned, the hydrodynamic derivatives described in section 4.2 can be determined by system identification of the manoeuvring results, but the most widely used

method is the captive model test.

4.3.2. Captive Model Tests

In contrast to the free-running model tests, the model in captive tests is fixed to a carriage and towed. The first, and still most easy to accomplish, captive manoeuvring tests used the towing carriage of the towing tank without additional subcarriages, which could superimpose further motions, performing stationary towing tests under straight-ahead condition or as oblique towing test with drift angle to obtain those coefficients related to surge, drift and rudder motion. Further pure stationary tests are the circular tests with rotating arms to obtain derivatives in dependence on yaw, rudder and drift motion. However, both methods are only capable of capturing coefficients depending on the velocity. Furthermore, the circular tests requires additional expensive rotating arm tanks. In order to detect all needed hydrodynamic derivatives, including those related to acceleration, and to utilise the available typically long and slender towing tanks, the Planar Motion Mechanism (PMM) or later Computerized Planar Motion Carriage (CPMC) was developed. The first CPMC was commissioned by the HSVA (Grim et al., 1976), which allowed to be flexibly controlled by using own computer program codes. Those carriages are equipped with independent motor controls for longitudinal, transverse and rotational movements. This allows pure motions of each variable independently, as well as a wide range of combined planar motions (ITTC, 2014), such as pure surge, sway, yaw, and combined sway/yaw and drift/yaw motions, with and without rudder motions or heeling angle.

Once the hydrodynamic derivatives are obtained, either by captive or free-running model tests, other manoeuvres can be simulated. External or environmental effects, such as towing and wind forces acting on the ship, can then be superimposed or included in the equation of motion as additional external forces. Shallow water by contrast, changes the manoeuvring behaviour entirely and requires separate model tests, performed in shallow water, in order to obtain another set of hydrodynamic coefficients. The basic principles of the changed manoeuvring behaviour in shallow water are described in the next section.

4.4. Influence of Shallow Water on Manoeuvrability

Despite the fact that the majority of seagoing vessels operate primarily in deep water, the requirements for manoeuvring behaviour are significantly higher in coastal areas and ports, where confined water is usually present. According to ITTC (2017), 'confined water' is referred to as the combination of 'restricted water' with an effective horizontal boundary, such as banks, and 'shallow water' with an effective vertical boundary, which is focused on here.

In deep water, the flow around the manoeuvring ship can be considered as three-dimensional. In shallow-water conditions, the flow under the keel is disturbed and the flow around the ship becomes increasingly two-dimensional as the UKC decreases, with more water flowing along the sides of the vessel. As a result the pressure distribution along the ship's hull is changed significantly, leading to a substantial increase in hydrodynamic

derivatives, as described in more detail in chapter 2 (e.g. Fujino, 1968; Toxopeus, 2013; Wang et al., 2023).

For a simplified illustration of the shallow-water effect the hull of a manoeuvring ship can be considered as a hydrofoil, similar to the rudder, as an ineffective hydrofoil, however, as the aspect ratio of the hull is approximately $2T/L$, with the waterline acting as a symmetry plane. For a stbd turning circle, the port side can generally be considered as the pressure side and the stbd side as the suction side, with the inflow velocity $-U$, see Figure 4.4. However, due to the superposition of the ship's yaw and drift motion, this can be different for the forward part of the ship, where the yaw motion is in the opposite direction to the drift motion. Due to the low aspect ratio, most of the transverse flow, acts as wingtip flow under the keel, equalising the pressure (similar to the creation of a wingtip vortex on an aeroplane).

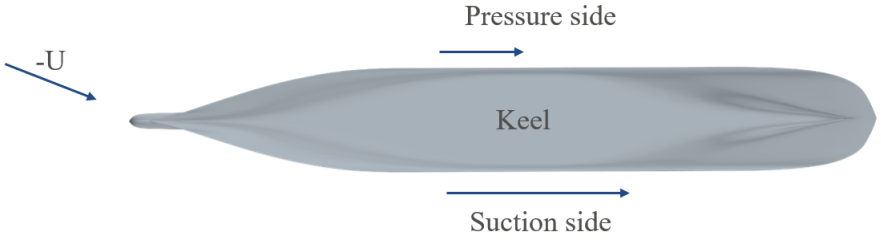


Figure 4.4.: Sketched principle of manoeuvring ship hull as hydrofoil for stbd turning

This changes as the water depth decreases. In extreme shallow-water conditions, the aspect ratio of the hull hydrofoil increases, theoretically to ∞ for prevented flow under the keel at $h/T = 1.00$, which transforms the hull into an effective hydrofoil. The wing tip flow under the keel is restricted what prevents the pressure equalization under the keel. As a result, the ship's sway motion v is drastically damped, resulting in a significant reduction in the drift angle of the manoeuvring ship. The ship's turning ability is thereby inhibited (e.g. Schmidt-Stiebitz, 1958a) and its course stability increased (e.g. Lee and Hong, 2017). Due to increased course-keeping and decreased turning ability, the overshoot angles of Zig-Zag manoeuvres usually decrease significantly in shallow water. As the drift angle of a ship is the main factor contributing to increased resistance during turning manoeuvres, there is a significant decrease in the speed loss of the ship compared to deep water, usually resulting in larger turning circles. Similar to the ship's hull, the aspect ratio of the rudder is increased as well, theoretically up to ∞, resulting in greater rudder effectiveness and forces in shallow water. However, the increased hydrodynamic forces of the hull usually dominate by far. Some exceptions are described in chapter 2 for wide twin-screw ships, which demonstrated reduced turning circles in shallow water (Yoshimura and Sakurai, 1989; Yasukawa and Kobayashi, 1995). Furthermore, the propeller inflow is strongly affected by the higher wake of the ship in shallow water, leading to a higher thrust loading factor. The resultant increase in thrust is often not sufficient to meet the increased resistance in shallow water. Consequently, the propeller typically operates at a higher revolution rate to attain the same speed as in deep water. Both effects lead to a higher rudder inflow in the propeller stream, resulting in increased rudder forces. Conversely, the counteracting effect of the higher wake outside the propeller stream reduces the rudder

inflow velocity, resulting in reduced rudder forces in this area. Usually, the former effects of increased rudder forces are dominating (e.g. Bogdanov et al., 1987a).

5. Experimental Investigations

The free-running manoeuvring tests with the model ships were carried out in the test facilities of the BAW in Hamburg. The shallow-water tank is 100 m long and 35 m wide. Water levels can be set up to a maximum of 0.6 m.

5.1. Model Ships

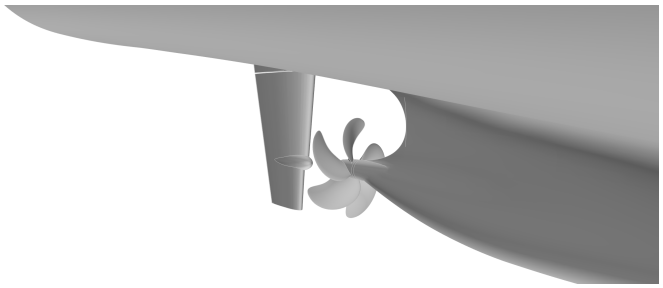


Figure 5.1.: Perspective view of the DTC aft ship with twisted rudder and propeller

The experimental investigations were conducted with two distinct ship types at a model scale of 1:60, a container ship and a bulk carrier. The Duisburg Test Case (DTC) is a benchmark ship representing a typical 14,000 TEU post-Panamax container ship (Moctar et al., 2012). The vessel is equipped with a twisted leading edge rudder with a Costa bulb, see Figure 5.1. The Japan Bulk Carrier (JBC) is a capesize bulk carrier that has also been designed as a benchmark ship for CFD validation (Hino et al., 2016). The main dimensions of both ships at full scale and model scale are listed in Table 5.1. Perspective views of the DTC and JBC are shown in Figure 5.2.

Table 5.1.: Main dimensions of the model ships

		DTC		JBC	
Main Particular	Symbols	Full Scale	Model Scale	Full Scale	Model Scale
Length btw. Perpendicular	L_{PP} [m]	355.00	5.92	280.00	4.67
Breadth at Waterline	B_{wl} [m]	51.00	0.85	45.00	0.75
Draught at midship	T_M [m]	14.50	0.242	16.50	0.275
Displacement Volume	V [m^3]	173467.00	0.803	178369.90	0.826
Block coefficient	c_B [-]	0.661	0.661	0.858	0.858
Wetted hull surface	S_w [m^2]	22032.00	6.12	19556.10	5.43
Long. centre of Gravity	x_{cg} [m]	174.06	2.90	147.13	2.45
Metacentric height	GM [m]	3.60	0.060	5.30	0.088
Moment of Inertia	K_{xx}/B_{wl} [-]	0.41	0.41	0.40	0.40
Moment of Inertia	K_{yy},K_{zz}/L_{PP} [-]	0.23	0.23	0.25	0.25

Two draughts were selected for the DTC: the design draught of 14.5 m and the partial draught of 12.5 m. The latter was tested not only on an even keel, but also trimmed by stern. For the JBC, two draughts were investigated as well: the design draught of 16.5 m and a partial draught of 13.8 m. The partial draught of the JBC is examined for even keel, trim by stern and trim by bow. The investigated loading conditions for the model ships are shown in Table 5.2 and Table 5.3.

Table 5.2.: Main dimensions of the DTC at the investigated floating conditions (full scale)

Main Particular	Symbol	Design	Partial even	Partial trimmed
Draught at APP	T_{APP} [m]	14.50	12.50	13.50
Draught at midship	T_M [m]	14.50	12.50	12.50
Draught at FPP	T_{FPP} [m]	14.50	12.50	11.50
Trim angle	ϑ [deg]	0.0	0.0	0.318
Displacement Volume	V [m^3]	173467	143640	143640
Long. centre of Gravity	x_{cg} [m]	174.06	176.10	171.84
Metacentric height	GM [m]	3.6	4.9	4.9

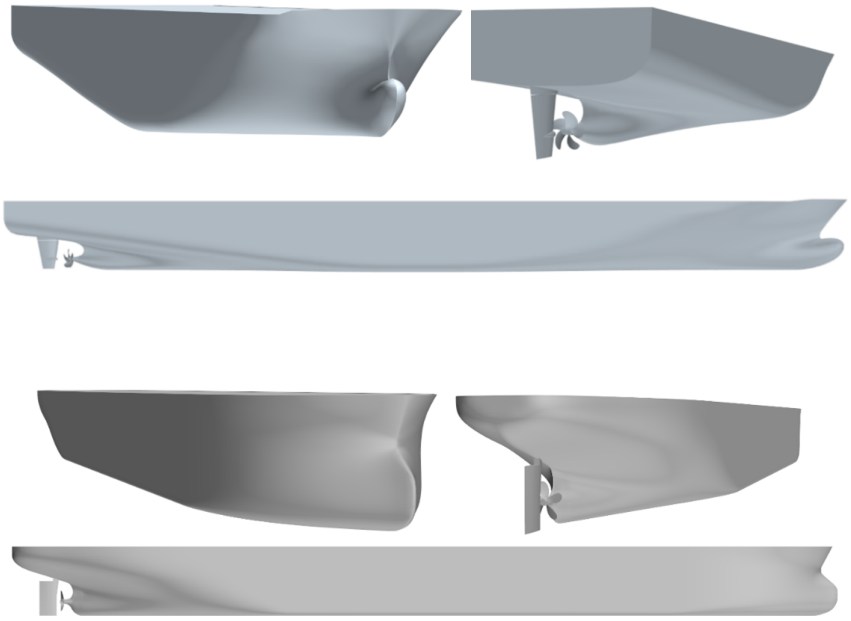


Figure 5.2.: Perspective views from the front, rear and side of the DTC (top) and JBC (bottom)

The selected h/T ratios are 2.00, 1.50, 1.20, 1.15 and 1.10. Additionally, a number of deep-water tests were performed outdoors for the DTC only. The test speeds were set to 6, 9, 12 and 15 knots. An additional speed of 19 knots was investigated for the DTC. This range reflects the actual operational conditions in the area of interest. On the river Elbe, a maximum speed of 12 kn applies for navigation in large sections of the waterway. In contrast, a typical speed for port manoeuvres is approximately 6 kn. Thus, 9 kn represents

Table 5.3.: Main dimensions of the JBC at the investigated floating conditions (full scale)

Main Particular	Symbol	Design	Partial even	Partial Aft	Partial Fwd
Draught at APP	T_{APP} [m]	16.50	13.80	14.60	13.00
Draught at midship	T_M [m]	16.50	13.80	13.80	13.80
Draught at FPP	T_{FPP} [m]	16.50	13.80	13.00	14.60
Trim angle	ϑ [deg]	0.0	0.0	0.327	-0.327
Displacement Volume	V [m^3]	173467	147096	147096	147096
Long. centre of Gravity	x_{cg} [m]	147.13	148.56	146.16	150.90
Metacentric height	GM [m]	5.3	6.1	6.2	6.0



Figure 5.3.: The DTC model ship during a manoeuvre in the BAW shallow-water basin

Table 5.4.: Manoeuvre matrix for the DTC at design conditions

Draught [m] float. cond.	14.50 even keel				
h/T	Deep water	2.00/1.50	1.20	1.15	1.10
TC 45° stbd	-	6, 9 kn	6, 9 kn	6, 9 kn	6, 9 kn
TC 45° port	-	6, 9 kn	6, 9 kn	6, 9 kn	6, 9 kn
TC 35° stbd	15, 19 kn	6, 9, 12, 15, 19 kn	6, 9, 12, 15 kn	6, 9, 12, 15 kn	6, 9 kn
TC 35° port	15, 19 kn	6, 9, 12, 15, 19 kn	6, 9, 12, 15 kn	6, 9, 12, 15 kn	6, 9 kn
Z 35-20 stbd	-	6, 9, 12, 15 kn	6, 9, 12 kn	6, 9, 12, 15 kn	6, 9, 12 kn
Z 35-20 port	-	6, 9, 12, 15 kn	6, 9, 12, 15 kn	6, 9, 12, 15 kn	6, 9, 12 kn
Z 20-10 stbd	15, 19 kn	6, 9, 12 kn	6, 9, 12 kn	6, 9, 12, 15 kn	6, 9, 12 kn
Z 20-10 port	15, 19 kn	6, 9, 12 kn	6, 9, 12 kn	6, 9, 12, 15 kn	6, 9, 12 kn
Z 20-20 stbd	6 kn	6 kn	-	-	-

an intermediate level, while 19 kn is the highest possible speed for the DTC for the chosen configuration, without skin friction correction force. However, the design speed is actually 25 kn. Figure 5.3 shows the DTC during a manoeuvre in the BAW shallow-water basin.

Table 5.5.: Manoeuvre matrix for the DTC at partial draught

Draught [m]	12.50				
float. cond.	even keel			2 m trimmed	
h/T	2.00	1.20	1.10	2.00	1.20
TC 45° stbd	6, 9 kn	6, 9 kn	6, 9 kn	6, 9 kn	6, 9 kn
TC 45° port	9 kn	9 kn	9 kn	9 kn	9 kn
TC 35° stbd	6, 9, 12, 15, 19 kn	6, 9, 12 kn	6, 9 kn	6, 9, 12, 15, 19 kn	6, 9, 12 kn
TC 35° port	9 kn	9 kn	9 kn	9 kn	9
Z 35-20 stbd	6, 9, 12, 15, 19 kn	6, 9, 12, 15 kn	6, 9, 12 kn	6, 9, 12, 15, 19 kn	6, 9, 12, 15 kn
Z 35-20 port	9 kn	9 kn	9 kn	9 kn	9 kn
Z 20-10 stbd	6, 9, 12, 15, 19 kn	6, 9, 12, 15 kn	6, 9 kn	6, 9, 12, 15, 19 kn	6, 9, 12, 15 kn
Z 20-10 port	9 kn	9 kn	9 kn	9 kn	9 kn

The models are free-running model ships equipped with a steering gear and an electric motor and are operated by remote control. For each manoeuvre, the model ship is accelerated to the specified speed at the target propeller rotation rate. At the start of the manoeuvre, the rudder must be in the neutral position and the ship's yaw rate must be close to zero. This prevents the measurement runs from being influenced by varying input conditions. Various manoeuvres were conducted at different rudder angles. The rudder angular speed of 22.5 degrees/s, which corresponds to 2.9 degrees/s in full scale, was set for all manoeuvres.

Table 5.6.: Manoeuvre matrix for the JBC at design conditions

Draught [m]	16.50				
float. cond.	even keel				
h/T	2.00	1.50	1.20	1.15	1.10
TC 45° stbd	6, 9 kn	6, 9 kn	6, 9 kn	6, 9 kn	6, 9 kn
TC 45° port	9 kn	9 kn	9 kn	9 kn	9 kn
TC 35° stbd	6, 9, 12, 15 kn	6, 9, 12, 15 kn	6, 9, 12, 15 kn	6, 9, 12 kn	6, 9 kn
TC 35° port	9 kn	9 kn	9 kn	9 kn	9 kn
Z 35-20 stbd	6, 9, 12, 15 kn	6, 9, 12, 15 kn	6, 9, 12, 15 kn	6, 9, 12 kn	6, 9 kn
Z 35-20 port	9 kn	9 kn	9 kn	9 kn	9 kn
Z 20-10 stbd	6, 9, 12, 15 kn	6, 9, 12, 15 kn	6, 9, 12, 15 kn	6, 9, 12 kn	6, 9 kn
Z 20-10 port	9 kn	9 kn	9 kn	9 kn	9 kn
Z 20-20 stbd	12, 15 kn	12, 15 kn	12, 15 kn	12 kn	-

The manoeuvres presented and discussed here are the 35° and 45° turning circle, and the 20-10, 35-20 and 20-20 Zig-Zag manoeuvres. Table 5.4 to Table 5.7 provides an overview of these manoeuvres. Tests at higher speeds were only possible at moderate shallow-water conditions. The JBC's port manoeuvres and the DTC's partial draught port manoeuvres were only carried out at a speed of 9 knots. For $h/T = 1.10$, the trimmed conditions were

Table 5.7.: Manoeuvre matrix for the JBC at partial draught

Draught [m] float. cond.	13.80 even keel			13.80 aft trimmed		13.80 fwd. trimmed	
h/T	2.00	1.20	1.10	2.00	1.20		
TC 45° stbd	6, 9 kn	6, 9 kn	6, 9 kn	6, 9 kn	6, 9 kn	6, 9 kn	6, 9 kn
TC 45° port	9 kn	9 kn	9 kn	9 kn	9 kn	9 kn	9 kn
TC 35° stbd	6, 9, 12, 15 kn	6, 9, 12 kn	6, 9 kn	6, 9, 12, 15 kn	6, 9 kn	6, 9, 12, 15 kn	6, 9, 12 kn
TC 35° port	9 kn	9 kn	9 kn	9 kn	9	9 kn	9 kn
Z 35-20 stbd	6, 9, 12, 15 kn	6, 9, 12 kn	6, 9 kn	6, 9, 12, 15 kn	6, 9 kn	6, 9, 12, 15 kn	6, 9, 12 kn
Z 35-20 port	9 kn	9 kn	9 kn	9 kn	9 kn	9 kn	9 kn
Z 20-10 stbd	6, 9, 12, 15 kn	6, 9, 12 kn	6, 9 kn	6, 9, 12, 15 kn	6, 9 kn	6, 9, 12, 15 kn	6, 9, 12 kn
Z 20-10 port	9 kn	9 kn	9 kn	9 kn	9 kn	9 kn	9 kn
Z 20-20 stbd	12, 15 kn	12 kn	-	12, 15 kn	-	12, 15 kn	12 kn
Z 10-10 stbd	12, 15 kn	12 kn	-	12, 15 kn	-	12, 15 kn	12 kn

not achievable.

5.2. Experimental Setup

The model ships are equipped with extensive measuring equipment for different measuring parameters. A fully equipped model ship is shown in Figure 5.4.

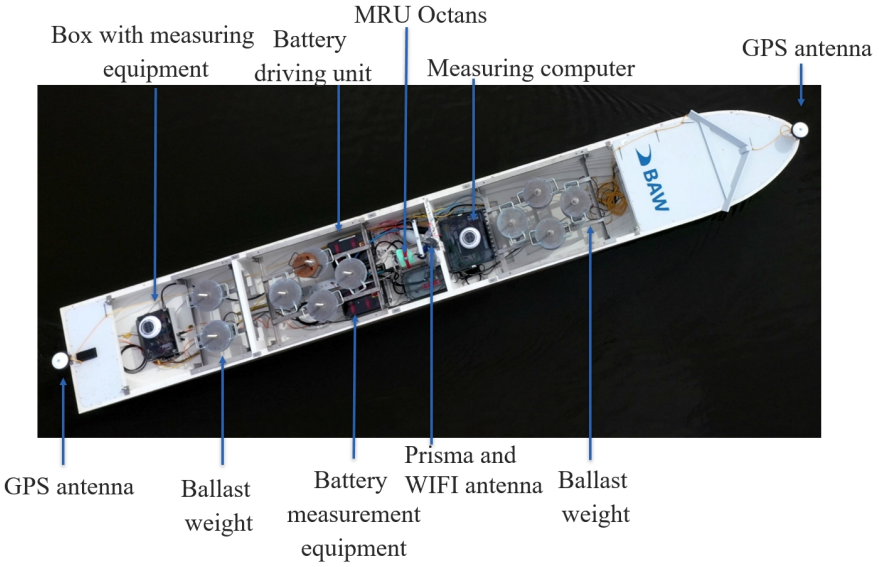


Figure 5.4.: Fully equipped model ship with measurement applications

A motions reference unit (MRU), a fibre optic gyro compass, was used to measure the rotational motion of the model ship, such as roll, pitch and yaw motion. The rudder forces and moments are captured with a 6-DoF sensor. The sensor is located in the sensor box above the rudder blade. A 3-DoF thrust measuring unit, mounted on the propeller shaft, measures the thrust forces. A rotating torque sensor on the shaft is used to measure the torque provided to the propeller. The rudder angle is set and recorded via an actuator and magnetic angle sensor. Translatory motions, such as surge, sway and heave, are measured externally via a 'total station' positioned next to the shallow-water

basin. This tachymeter automatically tracks the electronic prisma aboard the model ship. Figure 5.5 shows the transmitting prisma for the deep-water model tests outdoors during a manoeuvre. The diagram in Figure 5.6 illustrates the data acquisition on the model ship and provides details of the various measuring instruments, including their data rate and their respective accuracy.



Figure 5.5.: Total station measurement during a deep-water manoeuvre outdoors

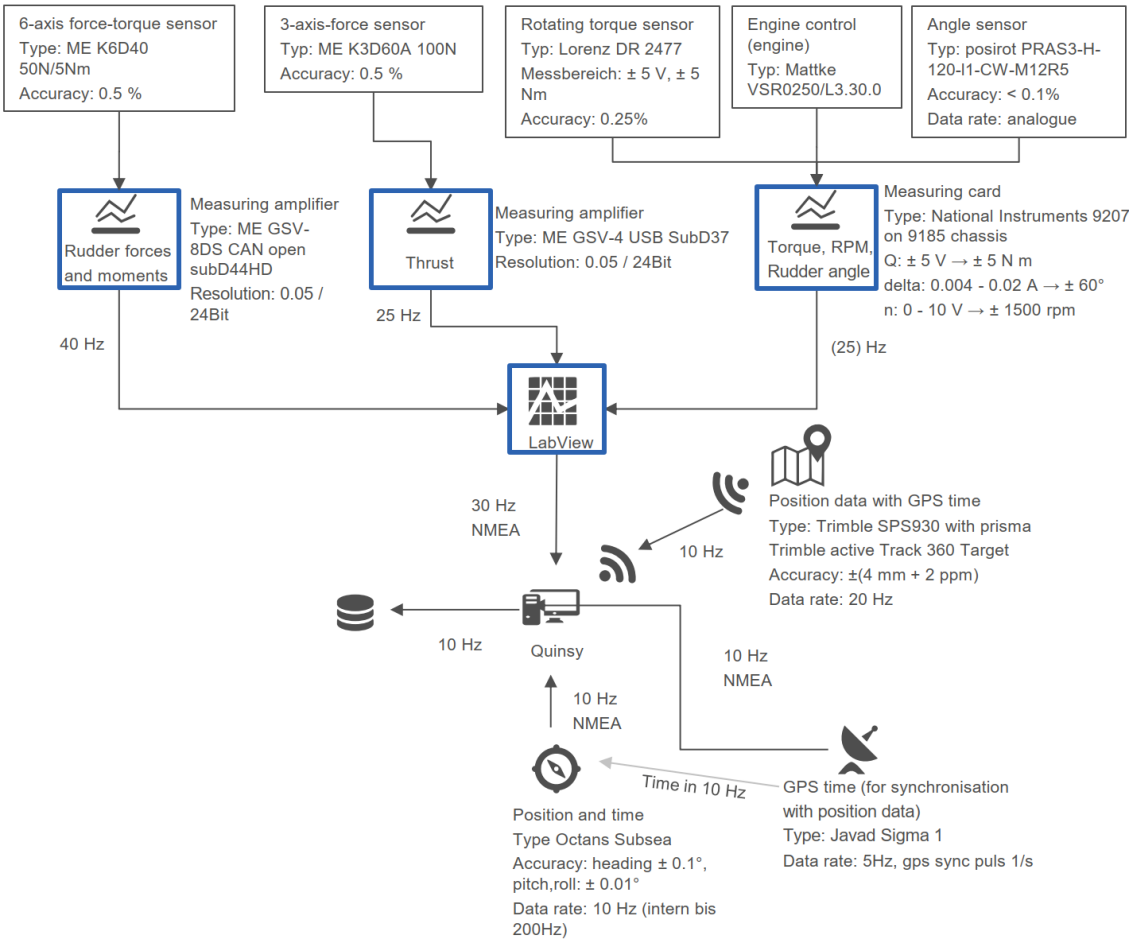


Figure 5.6.: Central data acquisition diagram

6. Numerical Investigations

In addition to the comprehensive conduction of model experiments, numerical simulations were performed for selected cases of both model ships. All simulations were performed in model scale as well, enabling direct comparisons of the results. In the following sections the numerical approach, computational domain, verification and validation of the numerical results are introduced.

6.1. Computational Domain

All Simulations are carried out using RANS-based CFD calculations with the commercially available Software Simcenter STAR-CCM+ of the version 2302. A rectangular numerical towing tank was created using the CAD models with the same dimensions for all setups, except for the vertical direction, which was adjusted according to the specific h/T ratio. Figure 6.1 illustrates the principle boundary conditions and the distance to the ship used for the simulations. A velocity inlet was set at the front and the side faces, while a pressure outlet was chosen at the back end of the calculation area. For deep-water conditions, the bottom was discretised as a velocity inlet, while for all other setups it was discretised as a wall to account for shallow-water effects. For the top boundary, which is set at the water line, a symmetry plane was used, and hence the ship considered as a double body model, neglecting the free surface. This simplification was adopted to reduce computational cost, as the free-running manoeuvres already represent complex and costly unsteady simulations involving a discretised rudder and propeller model, as well as the model's free motion. As the considered advance speeds of 6 and 9 kn are small, the wave resistance represents an insignificant proportion of the total force and can be neglected. The body motion was enabled by the dynamic fluid body interaction model (DFBI), where the ship is movable in 3 degrees of freedom, surge, sway and yaw. The background region moved horizontally in accordance with the surge, sway and yaw motions of the ship.

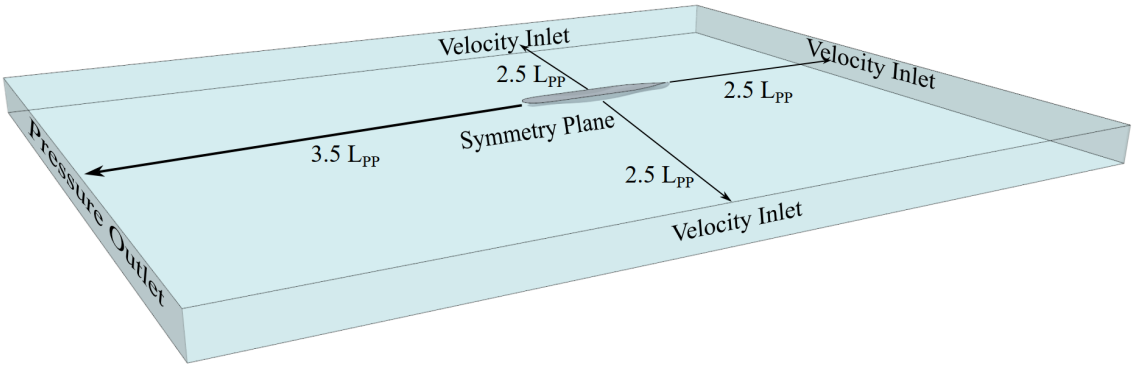


Figure 6.1.: Principle boundary conditions used for the numerical simulations

Table 6.1.: Boundary conditions

Location	Boundary	Distance to model APP at WL
Front	Velocity Inlet	2.5 L_{PP}
Back	Pressure Outlet	3.5 L_{PP}
Sides	Velocity Inlet	2.5 L_{PP}
Top	Symmetry Plane	0
Bottom	Wall	h

The propeller forces were modelled using a virtual disc. The propeller induced momentum at the mid of the actual propeller plane is achieved by considering an additional source term to the momentum equation (Siemens, 2023). In order to model the actual propeller effect, the k_T-k_Q curves of the model propellers based on open water model tests (Moctar et al., 2012; Hino et al., 2016) are used to calculate the forces based on the propeller inflow. The inflow of this body force propeller method was captured at the inflow velocity plane. This method uses the local velocity of each cell to calculate forces and advance coefficient J. Furthermore, the induced velocity correction method is applied, which is based on the approach described by Neitzel et al. (2015). This is necessary in order to account for the induced velocities of the propeller. For open water propeller tests, the thrust and torque are measured at a constant propeller rotation rate and varying inflow velocity (v_A). The inflow velocity v_A is without induced velocity. In the comparison with the propulsion test and open water diagram, this v_A is then also used indirectly, as the effective wake is determined via the thrust (or torque) identity. However, if the k_T is now determined in a running simulation of a ship surging straight ahead with running propeller (thrust initially unknown, only inflow and propeller rotation n known) using the inflow velocity v_A unadjusted for the propeller-induced velocities together with the open water diagram leads to incorrect values. The J becomes too high and the k_T or thrust too small. To calculate the corrected advance velocity accounting for the propeller-induced velocities an iterative approach is applied (Neitzel et al., 2015): The local advance coefficient for each control volume at the inflow plane J_{local} is

$$J_{local} = \frac{v_{a,local}}{nD_P \pm \frac{v_{T,local}}{\pi}}\,, \tag{6.1}$$

with $v_{A,local}$ being the advance velocity and $v_{T,local}$ the tangential velocity for a control volume at the inflow plane. The latter is necessary to account for oblique flow and set equal to the tangential velocity at the propeller plane. For the initial solution, the advance velocity is set equal to the inflow velocity at the propeller $v_{p,local}$ to obtain the initial solution for the thrust:

$$T_{local} = \frac{k_T}{J_{local}^2}\rho D_P^2 v_{A,local}^2\,. \tag{6.2}$$

Based on momentum theory a relation of the propeller inflow velocity and advance velocity can be derived:

$$v_{A,local} = \frac{2v_{p,local}}{1+\sqrt{1+\frac{8}{\pi}\frac{k_T}{J_{local}^2}}}\,. \tag{6.3}$$

As shown in Equation 6.1 the advance velocity is part of the advance coefficient, and hence an iterative procedure has to be applied for the solution of the advance velocity according to Equation 6.3 to obtain the correct propeller thrust.

To control the rudder deflection freely and independently of the ship, the grid area around the rudder was discretised using the overset technique. Table 6.2 summarizes the different regions of the domain and its grid type. As the background was moving according to the model ship motion, they were combined in one region using a trimmed cell mesh. A polyhedral mesh was used for the rudder, in order to capture its complex geometry more accurately. In total 11.9 and 8.7 million cells were used for the mesh of the DTC and JBC, respectively. Figure 6.2 and Figure 6.3 show some key perspectives of the grids that were used. The boundary layer along the ship hull was arranged with 36 prism layers to resolve the velocity profile properly. The resolution of the near-wall region was set up with a dimensionless wall distance $y^+ < 1$ for all simulations. The turbulence models used were the Standard k-ε low-Re model for the DTC and k-ω-SST model for the JBC (see section 3.2) as these were found to meet the validation model data best for each ship. A second-order upwind scheme was used for the convective term and a first-order backward Euler method to calculate implicitly the transient terms of the equations. The time step of the simulations was chosen in a way that the Courant number, representing the number of cells by which a field quantity moves per time step, was smaller than one for the major part of the domain. For the aft part of the ship, at the propeller and rudder region the Courant number was allowed to exceed the value of one, since the fine cells at the rudder would require an unreasonable small time step for the extensive simulation.

Table 6.2.: Grid sizes

Region	Grid Type	DTC Total cells in Mill.	JBC Total cells in Mill.
Tank and Ship	Trimmed	10.9	8.0
Rudder	Polyhedral	1.0	0.7
Total	-	11.9	8.7

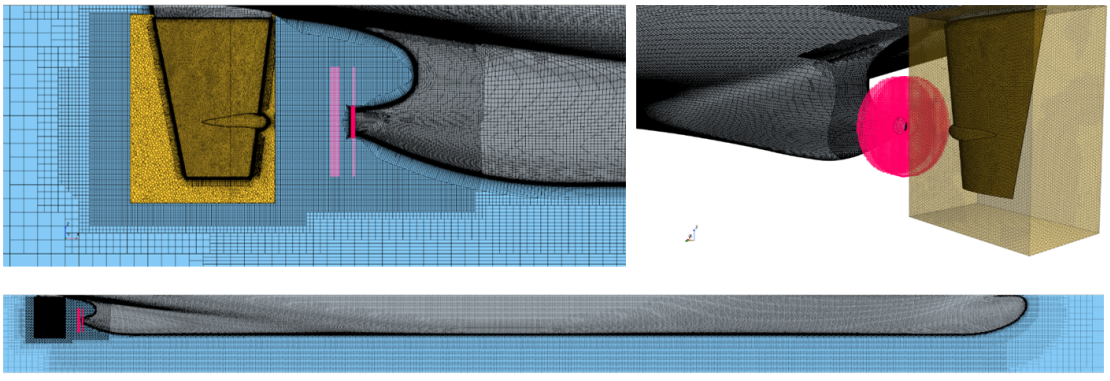


Figure 6.2.: Different perspectives of the computational mesh for the DTC

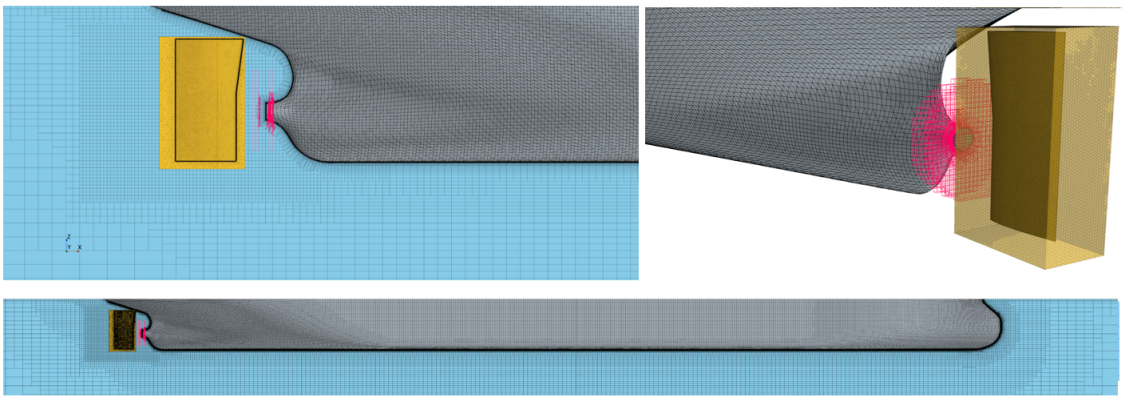


Figure 6.3.: Different perspectives of the computational mesh for the JBC

6.2. Uncertainty Analysis

Numerical methods applied for solving the Reynolds-Averaged-Navier-Stokes equations are based on model assumptions and discretise the solution domain into spatial grid cells (see also chapter 3). Both the modelling approach and the discretisation process may introduce errors and uncertainties. The estimation of the uncertainty of the numerical discretisation is referred to as verification, and of the modelling error as validation, which needs experimental data for comparison.

The verification can be divided into code verification and solution verification (ITTC, 2024). Code verification is considered to be the responsibility of the developer and as the used CFD solver Star-CCM+ is widely recognised by scientific and commercial user worldwide, no significant coding errors are expected. Solution verification, on the other hand, describes the uncertainty of the same computational model, which can provide different solutions due to different meshes or iteration numbers.

Validation refers to the estimation of the uncertainty in numerical models, which is based on the comparison of numerical results with experimental results. The validation of the numerical simulations is conducted for some straight-ahead propulsion tests as well as for the actual manoeuvres.

6.2.1. Verification

The uncertainty analysis of the used grids was made according to Stern et al. (Xing and Stern, 2010; ITTC, 2024). The grid convergence study was carried out using three different grids, the used medium sized grid, a coarse grid and a fine grid. The refinement ratio used was $r = \sqrt{2}$.

Table 6.3.: Grids used for the convergence study

Grid	DTC Number of Grid Points in Mill.	JBC Number of Grid Points in Mill.
Coarse	5.5	3.9
Medium	11.9	8.7
Fine	20.8	14.5

For the DTC the verification study was made according to available shallow-water resistance tests for the speed of 6 kn and three different water depths: deep-water, moderate shallow-water of $h/T = 2.00$ and shallow-water condition of $h/T = 1.20$. For the JBC the same h/T ratios were investigated for the speed of 9 kn. Furthermore, for both ships a grid convergence study was performed for a 35° turning circle manoeuvre at the speed of 9 kn and the h/T ratio of 1.50. Table 6.3 shows the used grids and the number of grid points for the turning circle manoeuvre. The same grids were used for the resistance tests, but with a symmetry plane along the ship and without the rudder being discretised. Due to variation of water depth, the grids of other h/T ratios result in slightly different grid cell numbers.

The convergence behaviour according to Stern et al. can be obtained by the ratio of the changed results between medium S_2 and fine grid S_1, $\varepsilon_{21} = S_2 - S_1$, and between the coarse and medium grid $\varepsilon_{32} = S_3 - S_2$:

$$R = \varepsilon_{21}/\varepsilon_{32}\,. \tag{6.4}$$

The solution has, depending on magnitude and sign of R, one of the four different behaviour:

- Monotonic convergence, for $0 < R < 1$
- Monotonic divergence, for $R > 1$
- Oscillatory convergence, for $-1 < R < 0$
- Oscillatory divergence, for $R < -1$

The correspondent order of accuracy p_{RE} and estimated error δ_{RE} can be obtained by

$$p_{RE} = \frac{ln(\varepsilon_{32}/\varepsilon_{21})}{ln(r)}\,, \tag{6.5}$$

$$\delta_{RE} = \frac{\varepsilon_{21}}{r^{p_{RE}} - 1}\,. \tag{6.6}$$

The distance metric to the asymptotic range P is defined for this method as the ratio of estimated order of accuracy p_{RE} to theoretical order of accuracy p_{th}:

$$P = \frac{p_{RE}}{p_{th}}\,. \tag{6.7}$$

Based on statistical analysis of analytical or numerical benchmarks by Xing and Stern (2010) the factor of safety FS is then calculated as a function of P by

$$FS(P) = \begin{cases} 2.45 - 0.85P, & 0 < P \leq 1 \\ 16.4P - 14.8, & P \geq 1 \end{cases}\,. \tag{6.8}$$

With this safety factor, the uncertainty U_{FS} can finally be estimated by

$$U_{FS} = FS\delta_{RE}\,. \tag{6.9}$$

Table 6.4.: Grid convergence study for the DTC based on resistance tests

	Coarse	Medium	Fine					
Water Depth	$C_{TM}(10^{-3})$ [-]			ε_{21}	ε_{32}	R	δ_{RE}	U_{FS}
Deep Water	4.5682	4.5555	4.5547	0.0009	0.0126	0.0689	0.0001	0.0031
$h/T = 2.00$	4.8829	4.8617	4.8617	0.0001	0.0211	0.0039	3.1867E-07	0.00004
$h/T = 1.20$	5.8492	5.8156	5.7991	0.0165	0.0336	0.4915	0.0159	0.032

Table 6.4 shows the results of the uncertainty analysis for the DTC. Since $0 < R < 1$ applies for all water depths, the solutions of the investigated grids converge monotonically. The estimated uncertainties correspond to approximately 0.07 %, 0.0008 % and 0.55 % of C_{TM} for deep water, h/T ratio of 2.00 and 1.20, respectively.

Table 6.5.: Grid convergence study for the JBC based on resistance tests

	Coarse	Medium	Fine					
Water Depth	$C_{TM}(10^{-3})$ [-]			ε_{21}	ε_{32}	R	δ_{RE}	U_{FS}
Deep Water	4.6362	4.6591	4.6743	-0.0152	-0.0229	0.6637	-0.0300	-0.0585
$h/T = 2.00$	4.9570	4.9725	4.9853	-0.0128	-0.0155	0.8274	-0.0613	-0.1360
$h/T = 1.20$	7.0061	7.0587	7.0972	-0.0385	-0.0526	0.7322	-0.1053	-0.2177

The uncertainty analysis based on the resistance test of the JBC is presented in Table 6.5. Again, the solutions of the grids converge monotonically, as $0 < R < 1$ applies for all investigated water depths. The estimated uncertainties correspond to -1.25 % for deep-water, -2.73 % for moderate-shallow and -3.06 % for shallow-water C_{TM} value.

Even though the direct calculations of the manoeuvres demand time-consuming and extensive simulations, for one manoeuvre at the shallow-water case of $h/T = 1.50$ grid studies are performed for both model ships. The results of the grid studies of this 35° turning circle manoeuvre are shown in Table 6.6 and Table 6.7.

Table 6.6.: Grid convergence study for the DTC based on a 35° turning circle manoeuvre at $h/T = 1.50$

Parameter	Coarse	Medium	Fine	ε_{21}	ε_{32}	R	δ_{RE}	U_{FS}	Convergence type
Advance [L_{PP}]	2.5410	2.5098	2.5450	-0.0352	0.0312	-1.1277	0.3107	0.8070	Oscillatory Diverging
Transfer [L_{PP}]	1.5663	1.5743	1.5726	0.0017	-0.0080	-0.2145	0.0005	0.0101	Oscillatory Converging
t_{90} [-]	4.0241	4.0283	4.0287	-0.0004	-0.0042	0.0970	0.0000	-0.0018	Monotonically Converging
Tactical Diameter [L_{PP}]	3.5466	3.5604	3.5549	0.0056	-0.0138	-0.4024	0.0038	0.0253	Oscillatory Converging
TCR [L_{PP}]	1.7115	1.6817	1.7010	-0.0193	0.0298	-0.6454	-0.0351	-0.0671	Oscillatory Converging
Steady Surge [-]	0.5879	0.5599	0.5769	-0.0170	0.0280	-0.6075	-0.0263	-0.0484	Oscillatory Converging
Steady Thrust [-]	0.0292	0.0295	0.0294	0.0002	-0.0003	-0.5516	0.0002	0.0004	Oscillatory Converging
Steady Drift [°]	8.2505	8.1641	8.1307	0.0334	0.0865	0.3857	0.0209	0.1621	Monotonically Converging
Steady Drift 90° [°]	8.3733	7.8150	8.3466	-0.5316	0.5584	-0.9521	-10.5600	-25.2360	Oscillatory Converging
Steady Sway [-]	-0.0852	-0.0803	-0.0824	0.0021	-0.0049	-0.4262	0.0016	0.0084	Oscillatory Converging
Steady Yaw Rate [-]	0.3471	0.3374	0.3427	-0.0052	0.0096	-0.5422	-0.0062	-0.0105	Oscillatory Converging
Yaw Rate 90°	0.3713	0.3676	0.3726	-0.0049	0.0037	-1.3450	0.0192	0.0539	Oscillatory Diverging
Steady Rudder Trans. Force [-]	-0.0084	-0.0085	-0.0085	0.0000	0.0001	-0.0959	0.0000	0.0000	Oscillatory Converging
Rudder Trans. Force 90° [-]	-0.0080	-0.0082	-0.0082	-0.0001	0.0002	-0.4110	-0.0001	-0.0003	Oscillatory Converging

The chosen verification parameters relate to turning circle conditions at 90° heading change and steady-state condition. These are beside the standard turning circle param-

Table 6.7.: Grid convergence study for the JBC based on a 35° turning circle manoeuvre at $h/T = 1.50$

Parameter	Coarse	Medium	Fine	ε_{21}	ε_{32}	R	δ_{RE}	U_{FS}	Convergence type
Advance [L_{PP}]	2.0073	2.3618	2.3242	0.0376	-0.3545	-0.1060	0.0045	0.1705	Oscillatory Converging
Transfer [L_{PP}]	1.2657	1.3988	1.3888	0.0099	-0.1330	-0.0746	0.0008	0.0373	Oscillatory Converging
t_{90} [-]	3.1819	3.6061	3.5690	0.0371	-0.4242	-0.0874	0.0036	0.1523	Oscillatory Converging
Tactical Diameter [L_{PP}]	2.7586	2.8877	2.8665	0.0212	-0.1291	-0.1643	0.0042	0.1165	Oscillatory Converging
TCR [L_{PP}]	1.2829	1.2863	1.2853	0.0010	-0.0034	-0.3005	0.0004	0.0060	Oscillatory Converging
Steady Surge [-]	0.5105	0.4805	0.4859	-0.0054	0.0300	-0.1799	-0.0012	-0.0305	Oscillatory Converging
Steady Thrust [-]	0.0293	0.0297	0.0296	0.0001	-0.0004	-0.3239	0.0001	0.0008	Oscillatory Converging
Steady Drift [°]	5.9979	6.3360	6.1838	0.1522	-0.3381	-0.4503	0.1247	0.5085	Oscillatory Converging
Drift 90° [°]	6.1221	5.9276	5.8908	0.0369	0.1945	0.1895	0.0086	0.2116	Monotonically Converging
Steady Rudder Trans. Force [-]	-0.0117	-0.0120	-0.0122	0.0002	0.0003	0.7379	0.0007	0.0014	Monotonically Converging
Rudder Trans. Force 90° [-]	-0.0135	-0.0157	-0.0154	-0.0003	0.0022	-0.1373	0.0000	-0.0015	Oscillatory Converging
Steady Yaw Rate [-]	0.3611	0.3978	0.3950	0.0027	-0.0367	-0.0750	0.0002	0.0104	Oscillatory Converging
Yaw Rate 90°	0.4770	0.4668	0.4650	0.0018	0.0102	0.1742	0.0004	0.0100	Monotonically Converging

eters, rudder and propeller forces, as well as the velocities. For the JBC, the R only assumes values between -1 and 1, and hence shows converging behaviour for all parameters. Nevertheless, only the drift angle and yaw rate at 90° heading change and the steady rudder transverse force show monotonically convergence, while the other variables are of oscillatory convergence type, with R close to zero, however.

For the DTC, it is similar, demonstrating only for t_{90} and steady drift angle monotonically convergence, while most of the other parameters show oscillatory convergence. For two parameters related to 90° heading change, the advance and yaw rate at 90°, it shows slight oscillatory divergent characteristics. However, the R is only approximately 12 % and 35 % below the limit of -1. As these two terms represent transient parameters, it confirms the challenges of applying the classic grid convergence study to transient problems, such as direct manoeuvring simulation, as already stated by Carrica et al. (2016).

6.2.2. Validation

The validation of the numerical results is based on the model experiments conducted in the BAW shallow-water basin. The 35° turning circle and Zig-Zag 35-20 manoeuvre at speeds of 9 kn are chosen for validation purpose for both ships. Furthermore, for the DTC some additional resistance and propulsion tests at speed of 6 kn are used to compare resistance and propeller thrust in deep, intermediate shallow and shallow water. For the JBC, the propeller thrust of the straight-ahead tests in the BAW model basin at speed of 9 kn are compared to simulation results.

The EFD and CFD results for the resistance and propulsion tests of the DTC are presented in Table 6.8. As expected, the results for higher water depth are closer to the model test results, but all differences are below 10 %. The resistance is slightly underestimated, with the deviation increasing as the water depth decreases. The highest deviation is the resistance in shallow-water conditions, with approximately 9 %. However, as the total resistance of the model ship at this low speed is only about 3 N, the absolute deviation is only small. The propeller thrust is slightly underestimated as well, which is consistent with the lower resistance for the CFD case.

As already mentioned, for the JBC, only the propeller thrust can be used as a validation parameter for non-manoeuvring cases. However, results for a greater variety of shallow-water conditions were available for comparison here. Table 6.9 summarises the results of

the straight-ahead tests for model experiments and CFD simulations. Except for the h/T ratio of 2.00, again the propeller thrust is slightly underestimated. However, for the JBC, the deviations are even smaller than for the DTC, with differences below 5 % for all water depths.

Table 6.8.: Results of the DTC resistance and propulsion tests for EFD and CFD

	Resistance			Propulsion		
	EFD	CFD		EFD	CFD	
h/T	$c_T(10^{-3})$	$c_T(10^{-3})$	Deviation c_T [%]	k_T	k_T	Deviation k_T [%]
4.00	4.6181	4.5556	-1.35	0.2727	0.2624	-3.77
2.00	5.1620	4.9109	-4.86	0.3010	0.2810	-6.64
1.20	6.4608	5.8742	-9.08	0.3407	0.3232	-5.13

Table 6.9.: Results of the JBC straight-ahead tests for EFD and CFD

	EFD	CFD	
h/T	k_T	k_T	Deviation k_T [%]
2.00	0.1935	0.1973	1.98
1.50	0.2109	0.2074	-1.63
1.20	0.2132	0.2128	-0.17
1.10	0.2271	0.2204	-2.96

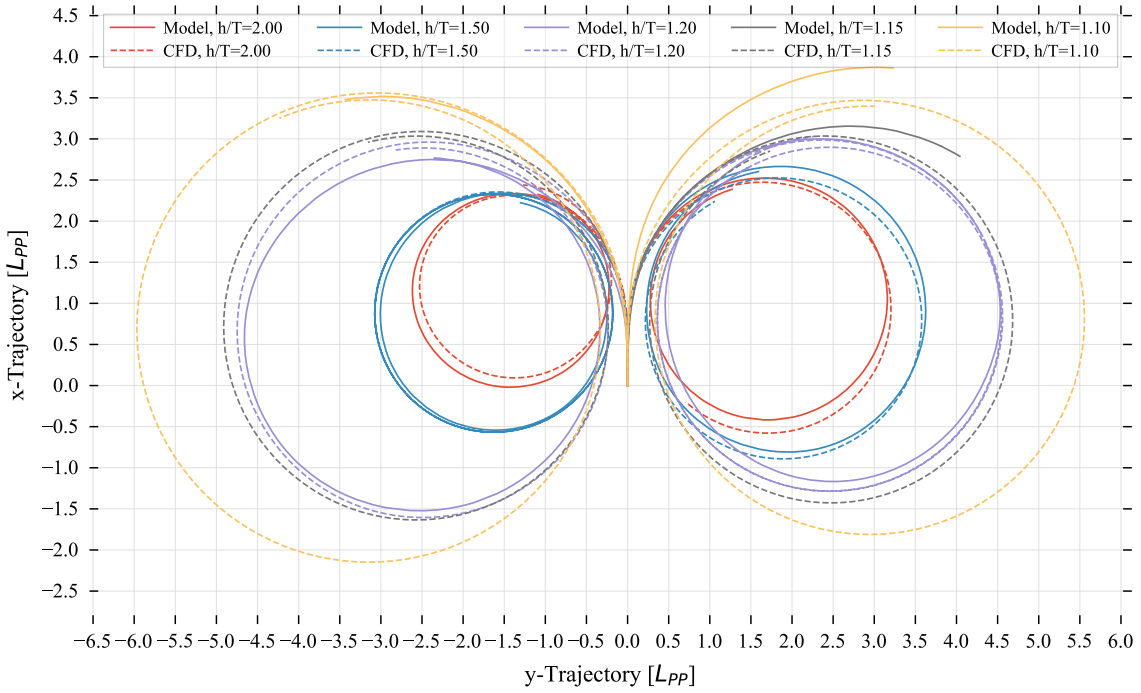
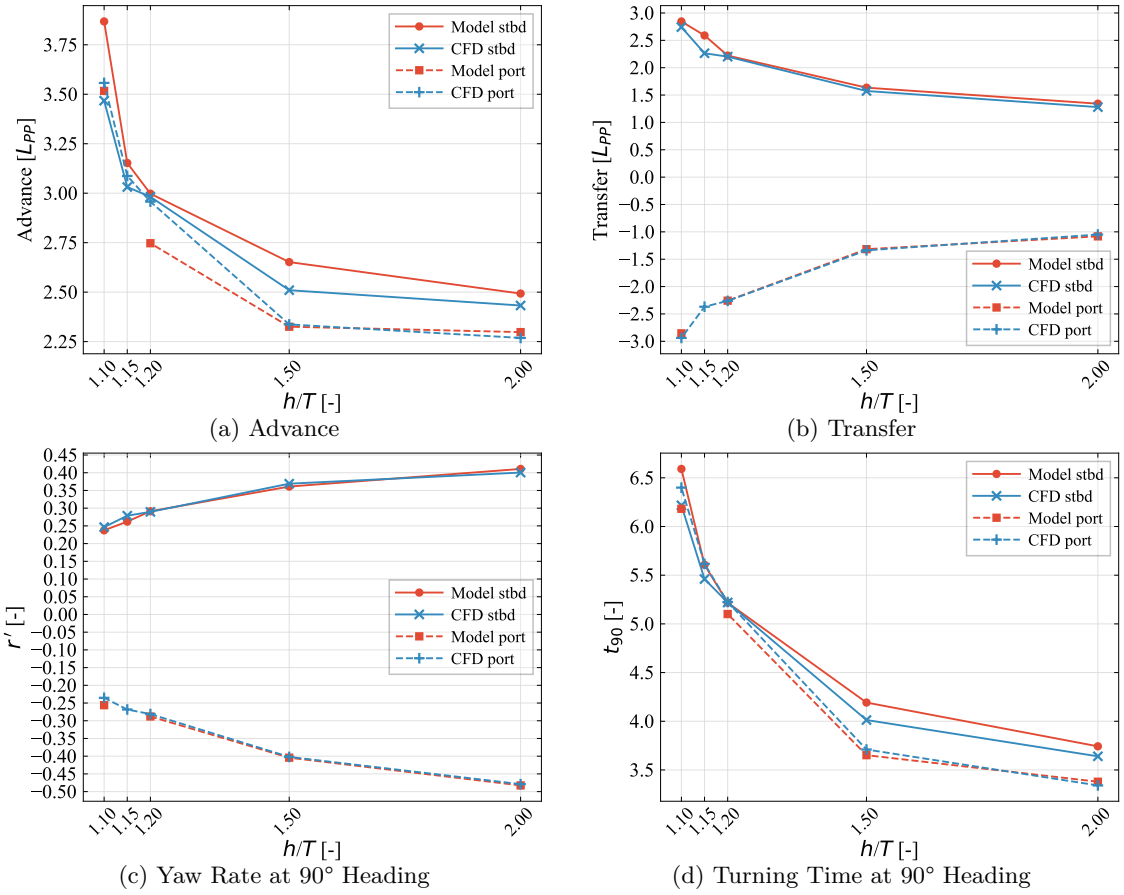


Figure 6.4.: Comparison of EFD and CFD trajectories for the 35° turning circle manoeuvre with an initial speed of 9 kn for the DTC



(a) Advance (b) Transfer

(c) Yaw Rate at 90° Heading (d) Turning Time at 90° Heading

Figure 6.5.: Validation plots for turning parameters related to 90° heading change with an initial speed of 9 kn for the DTC

The validation for the direct manoeuvring simulation was made by comparing the main manoeuvring parameters and significant dynamic parameters, like the yaw rate and rudder force. Figure 6.4 to Figure 6.6 show the results of the experimental tests (EFD) and the simulations (CFD) for the 35° turning circle manoeuvre to port and stbd. The CFD trajectories are generally in good agreement with the EFD data, see Figure 6.4. In contrast to the experiments, in CFD the turning circles could be completed even in extreme shallow-water conditions.

For these water depths, only those parameters were comparable related to 90° of heading change, which are presented in Figure 6.5. As can be seen, transfer, yaw rate and time for 90° heading change are in good agreement with model test data, for all shallow-water conditions. Only for the manoeuvre at h/T ratio of 1.15 to stbd side, the transfer shows higher deviations of approximately 14 %. The advance is slightly overestimated for port side for the h/T ratio of 1.20, and generally slightly underestimated for stbd side, particularly for extreme shallow water with deviations of 11.55 %. Generally, however, the curve progression and hence, the dependence on water depth of the parameters are well met.

This also applies for those parameters related to steady conditions, see Figure 6.6. The tactical diameter and steady yaw rate are met precisely, with deviations of less than 5 % for all comparable water depths, except for yaw rate at h/T ratios of 2.00 and 1.20 to port

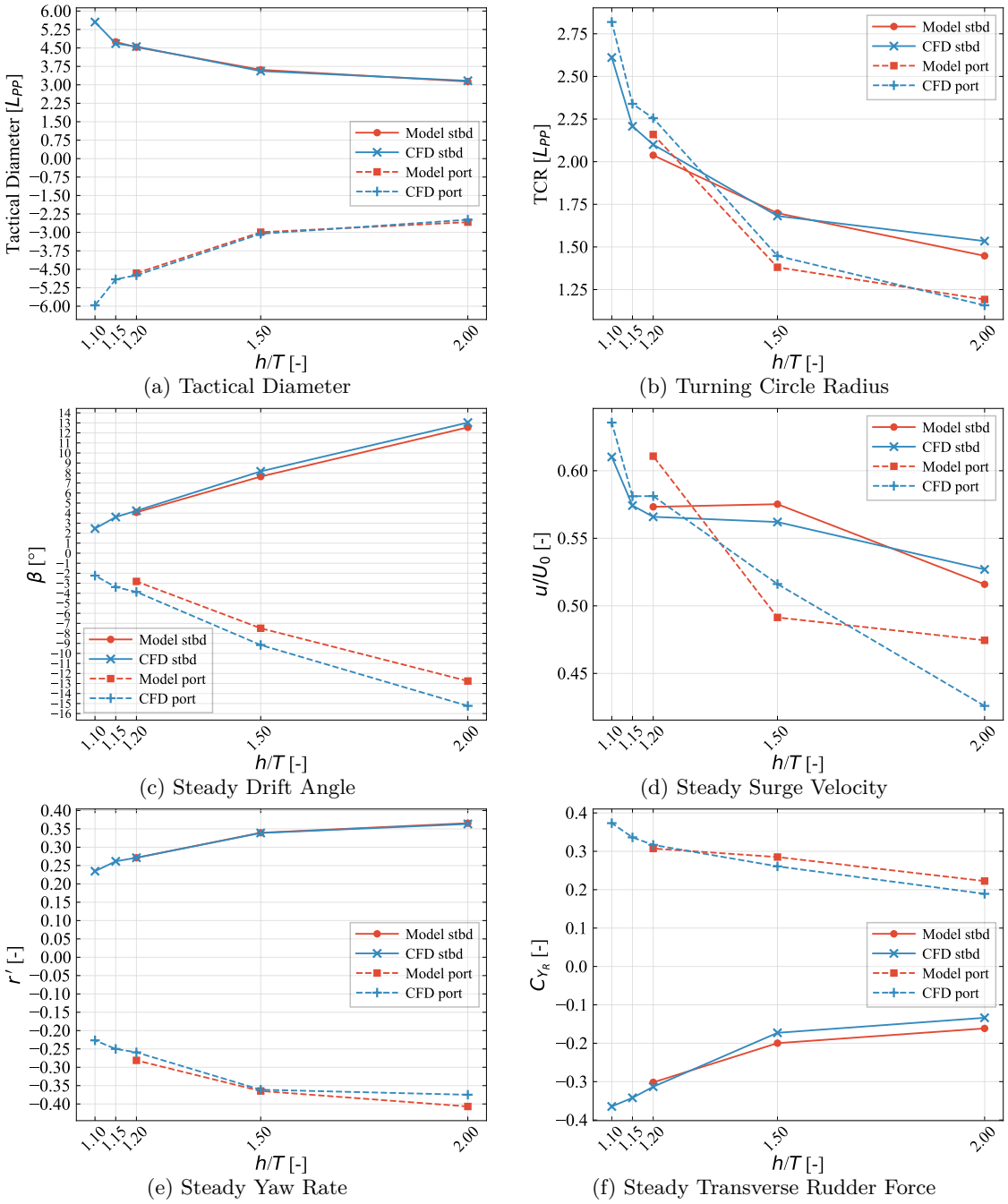
side. The rudder transverse force shows slightly higher deviations, especially for moderate shallow water of up to approximately 20 %. The steady surge velocity only shows some higher deviations for the manoeuvre at $h/T = 2.00$ to port side and the general curve progression is met, including the trend reversal in the transition to shallow-water conditions. This directional trend reversal, which is described in subsection 7.1.1, affecting the turning circle radius and tactical diameter in particular, is also well represented by CFD simulations. The steady drift angle to port side shows the highest deviations from the model test results, with partly over 20 % for $h/T = 1.20$. However, the absolute values approach each other as the water depth decreases, with deviations less than 1° in shallow-water conditions. For turning circle manoeuvre to stbd side, the steady drift angle is well met for all conditions.

The simulation of direct turning circle manoeuvres is quite complex and its evaluation includes many parameters. For this reason, the overall validation of the manoeuvring simulation was made by a validation table, containing all relevant parameters, see Table 6.10. The mean error was computed as the average of the absolute values of the errors for all parameters, without applying any weighting. For the h/T ratio of 1.15, valid model test data is only available for stbd direction. As can be seen the overall error of all turning circle manoeuvre parameters is close to, or even below, 5 %, and hence the turning circle manoeuvres of the DTC were able to be modelled generally in good agreement by the chosen CFD setup.

Table 6.10.: Differences between CFD and EFD results of the 35° turning circle manoeuvre in % for the DTC

Parameter	$h/T = 2.00$	$h/T = 1.50$	$h/T = 1.20$	$h/T = 1.15$	$h/T = 1.10$
Advance stbd	-2.48	-5.66	-0.53	-4.01	-11.55
Advance port	-1.30	0.50	7.11	-	1.14
Transfer stbd	-4.90	-3.87	-0.90	-14.38	-3.76
Transfer port	-3.13	1.58	0.18	-	2.85
t_{90} stbd	-2.82	-4.47	0.04	-2.67	-6.01
t_{90} port	-1.13	1.57	2.36	-	3.39
Yaw Rate 90°stbd	-2.55	2.20	-0.58	5.99	3.68
Yaw Rate 90°port	-0.75	-0.55	-2.41	-	-8.84
Tactical Diameter stbd	1.03	-1.46	0.56	-1.46	-
Tactical Diameter port	-4.03	2.10	1.81	-	-
TCR stbd	5.64	-0.99	2.99	-	-
TCR port	-2.96	4.60	4.24	-	-
Steady Drift stbd	3.64	6.37	3.75	-	-
Steady Drift port	16.28	18.26	27.12	-	-
Steady Surge stbd	2.09	-2.35	-1.31	-	-
Steady Surge port	-11.40	4.79	-5.08	-	-
Steady Yaw Rate stbd	-0.60	-0.21	0.05	-	-
Steady Yaw Rate port	-8.54	-0.94	-8.43	-	-
Steady Rudder Trans. Force stbd	-20.76	-15.58	3.66	-	-
Steady Rudder Trans. Force port	-17.59	-9.32	3.01	-	-
Mean Error	5.68	4.37	3.81	5.70	5.15

Besides the turning circle manoeuvre, for the DTC a Zig-Zag 35-20 manoeuvre to stbd



(a) Tactical Diameter
(b) Turning Circle Radius
(c) Steady Drift Angle
(d) Steady Surge Velocity
(e) Steady Yaw Rate
(f) Steady Transverse Rudder Force

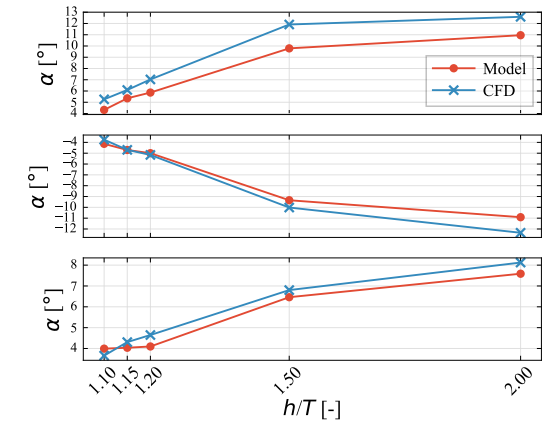
Figure 6.6.: Validation plots for steady-state turning parameters with an initial speed of 9 kn for the DTC

was simulated for all investigated shallow-water conditions. Figure 6.7 shows the curve progressions of the most important Zig-Zag parameters as a function of the h/T ratio, as well as the yaw rate and transverse rudder force as a function of time for model tests and CFD simulations. Generally, the deviations of the overshoot angles and yaw-checking times decrease for rising overshoot number. The overall curve progression is well met by the CFD results, except for extreme shallow-water conditions at third overshoot position. The overshoot angles with supporting rudder to both directions, port and stbd, are slightly overestimated by CFD. The initial turning time shows similar curve progression and generally slightly underestimated values, especially for h/T ratio of 1.10 with deviations of 11.44 %. The Nomoto coefficients, calculated with the first two overshoot angles, are in good agreement with the model test data, with maximum deviations of approximately 12 %. The trend reversal of T'_N within extreme shallow water however, is not reflected by CFD results. As no steady condition is comparable for Zig-Zag manoeuvres, the curve progression as a function of time is used for comparisons of the yaw rate and rudder transverse force. The highest deviation, again, for the yaw rate is observable for the first maxima, related to the first overshoot, particularly for extreme shallow-water conditions of $h/T = 1.10$, where the CFD simulations shows significantly larger slope than EFD curve progression, resulting in approximately 11 % higher yaw rate maxima. However, the further progression is well met by CFD results for all water depths. This is also the case for the rudder transverse force. Here, both extreme shallow-water conditions show the highest maximum deviations of approximately 10 %. Similar to the turning circle manoeuvre, a validation table summarize the most important parameters of the Zig-Zag manoeuvre, see Table 6.11. Overall, the deviations are slightly higher as for the turning circle manoeuvres, but all parameters show deviations less than 20 % and mostly below 10 %, resulting in mean errors for all water depths below 10 %.

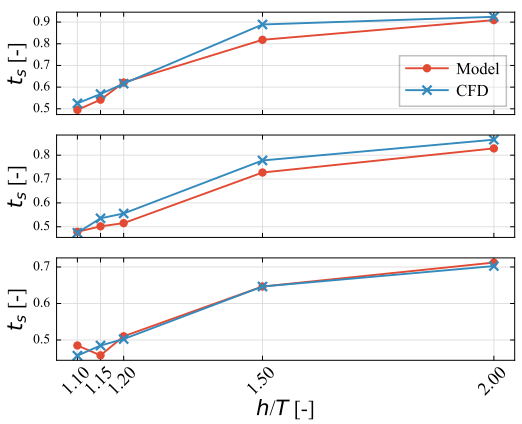
Table 6.11.: Differences between CFD and EFD results of the Zig-Zag 35-20 manoeuvre in % for the DTC

Parameter	$h/T = 2.00$	$h/T = 1.50$	$h/T = 1.20$	$h/T = 1.15$	$h/T = 1.10$
Overshoot 1	12.99	17.81	16.58	12.15	17.84
Overshoot 2	11.65	6.73	3.13	-0.27	-10.18
Overshoot 3	6.59	5.02	11.83	6.28	-9.16
Yaw-checking Time 1	1.64	7.95	-0.82	4.59	5.77
Yaw-checking Time 2	4.23	6.49	7.27	6.29	-0.85
Yaw-checking Time 3	-1.37	0.00	-1.51	5.56	-6.08
Initial turning time	5.08	0.21	-5.11	-3.92	-11.44
Mean Error	6.22	6.32	6.61	5.58	8.76

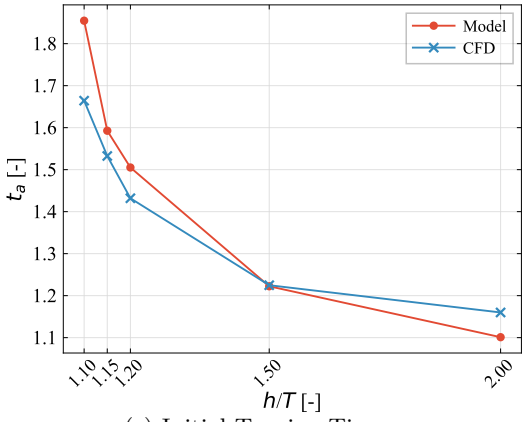
For the JBC, the validation of the turning circle was carried out for stbd direction only. The turning circle trajectories again, are in good agreement with model test data, see Figure 6.8. The curve progressions of parameters related to 90° of heading change as a function of h/T ratio are well met, with exceptions for the transfer at $h/T = 1.10$ and time and yaw at $h/T = 1.15$, while the total deviation is well below 10 % for all of these parameters.



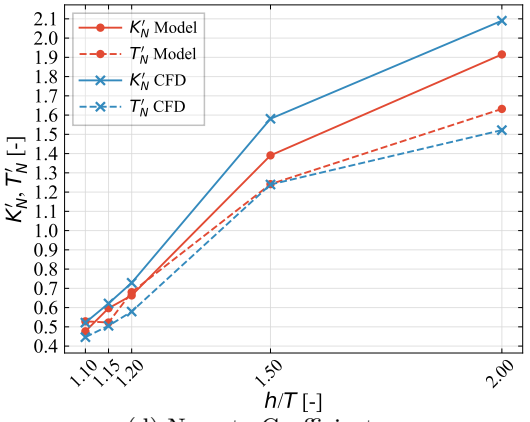
(a) First, Second and Third Overshoot Angle (from top to bottom)



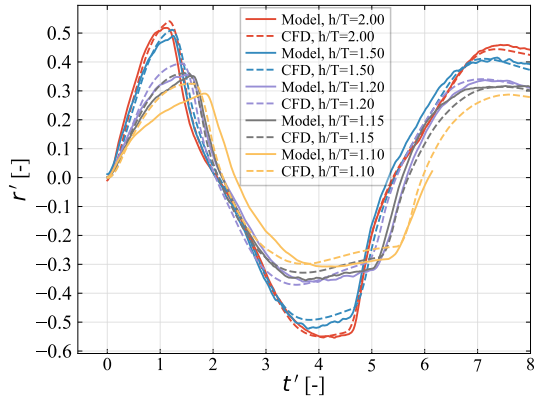
(b) First, Second and Third Yaw-checking Time (from top to bottom)



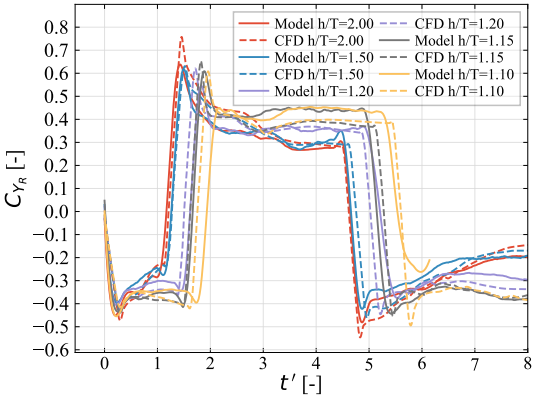
(c) Initial Turning Time



(d) Nomoto Coefficients



(e) Yaw Rate



(f) Transverse Rudder Force

Figure 6.7.: Validation plots for the Zig-Zag 35-20 stbd manoeuvre with an initial speed of 9 kn for the DTC

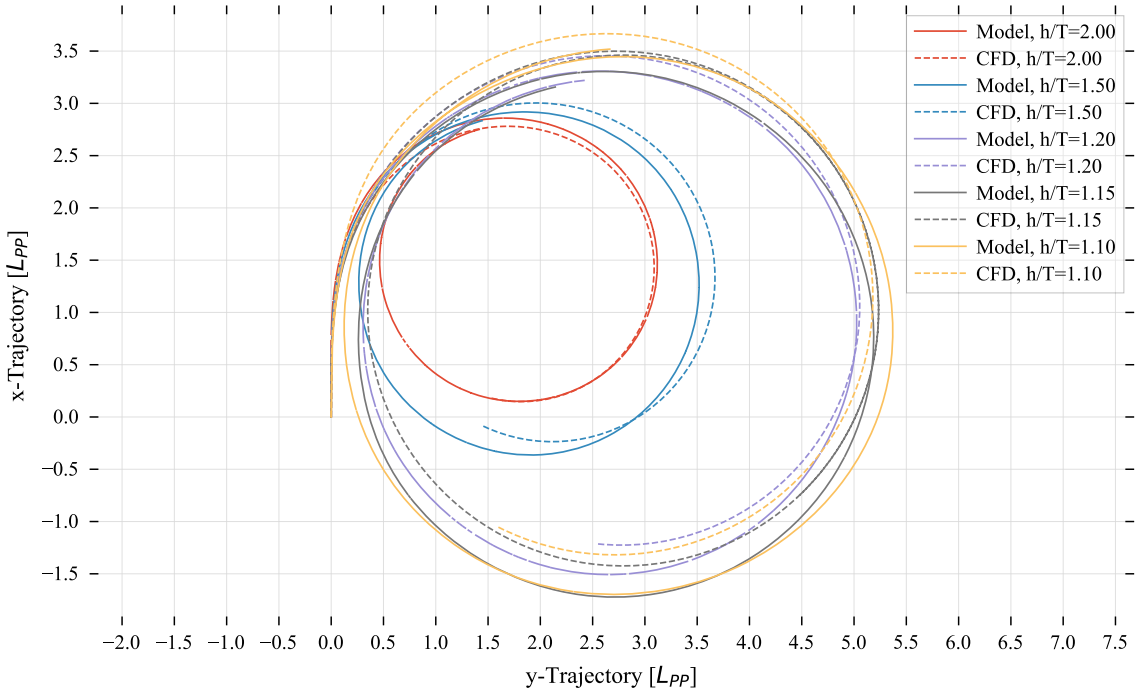
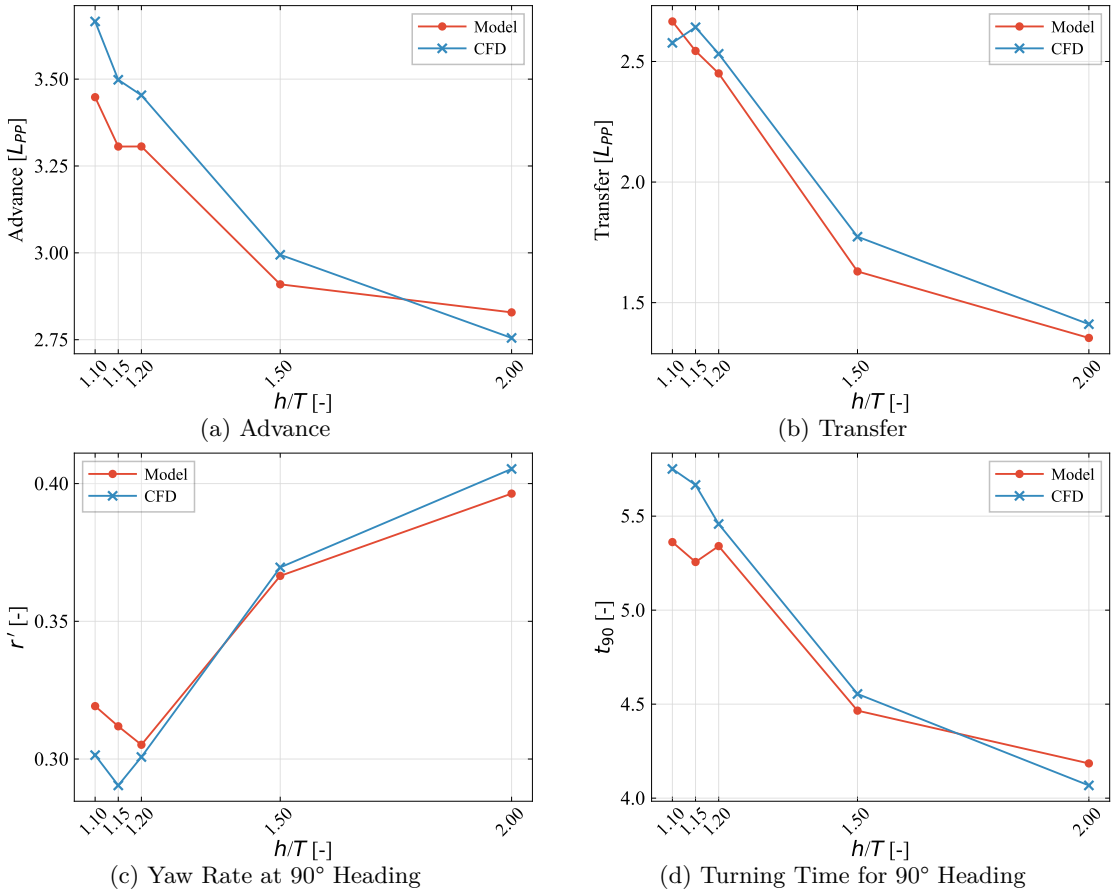


Figure 6.8.: Comparison of EFD and CFD trajectories for the 35° turning circle manoeuvre with an initial speed of 9 kn for the JBC

The dependency on water depth of those parameters related to steady-state conditions of the turning circle is in good agreement as well. The progression of each parameter, except for the tactical diameter within extreme shallow-water regime, is well met by CFD calculations, showing even the rise in the yaw rate in extreme shallow water after a steady decrease until the h/T of 1.20, albeit with a lower gradient. The deviations of tactical diameter, turning circle radius and yaw rate are mostly below 5 % and overall clearly below 10 %, see Table 6.12. The still relatively high mean error values of up to 11.74 % are caused by the high relative deviation of the drift angle, which is, however, constantly underestimated by max. 0.5°, except for $h/T = 2.00$, see Figure 6.10. Due to the significant decrease in drift angle with decreasing water depth, down to a value of approximately 1°, this rather constant deviation of 0.5° leads to a distinct deviation of over 54 %. Excluding this parameter from the calculation of the mean would result in mean values of only 2.73, 3.26, 2.85, 6.19 and 6.99 % for h/T ratios of 2.00, 1.50, 1.20. 1,15 and 1.10, respectively.

In addition to the turning circle manoeuvre, a Z 35-20 manoeuvre to stbd was simulated for all investigated shallow-water conditions with the JBC, see Figure 6.11. Similar to the DTC, the first overshoot position exhibits highest deviations of partly over 10 %, while yaw-checking times and overshoot angles for the second and third maxima differ by less than 10 % and mostly even by less than 5 %. The overall curve progressions with diminishing overshoot angles and yaw-checking times with decreasing water depth down to h/T ratio of 1.15 and the increase again for $h/T = 1.10$ are well met by CFD results. This is



(a) Advance (b) Transfer

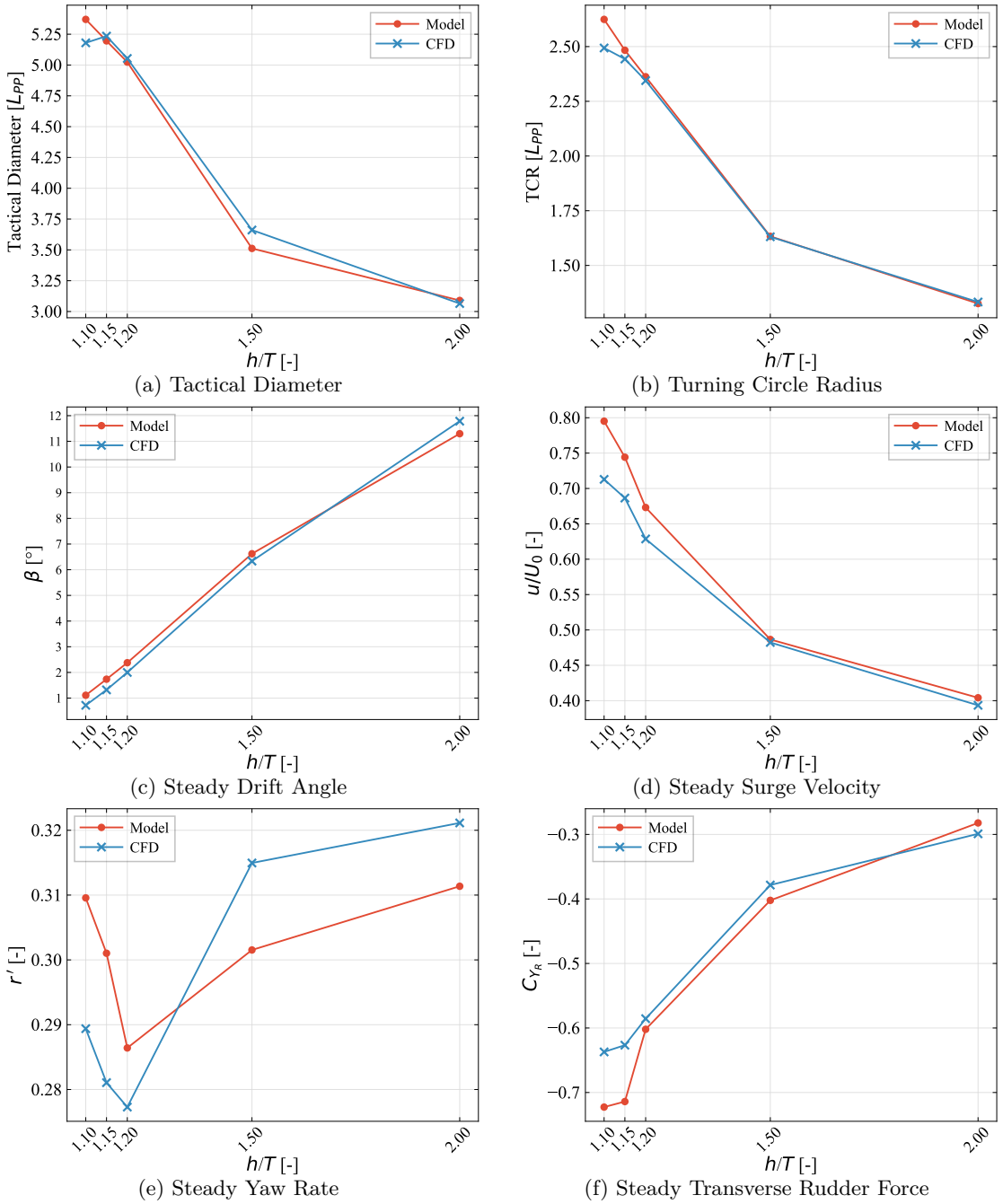
(c) Yaw Rate at 90° Heading (d) Turning Time for 90° Heading

Figure 6.9.: Validation plots for stbd turning parameters related to 90° heading change with an initial speed of 9 kn for the JBC

Table 6.12.: Differences between CFD and EFD results of the 35° turning circle manoeuvre in % for the JBC

Parameter	$h/T = 2.00$	$h/T = 1.50$	$h/T = 1.20$	$h/T = 1.15$	$h/T = 1.10$
Advance stbd	-2.67	2.84	4.27	5.49	5.95
Transfer stbd	4.04	8.12	3.21	3.72	-3.44
t_{90} stbd	-2.88	1.95	2.15	7.23	6.77
Yaw Rate 90° stbd	2.21	0.83	-1.47	-7.39	-5.90
Tactical Diameter stbd	-0.82	4.08	0.58	0.74	-3.67
TCR stbd	0.53	-0.12	-0.76	-1.65	-5.24
Steady Drift stbd	4.14	-4.50	-18.97	-31.46	-54.51
Steady Surge stbd	-2.72	-0.87	-7.08	-8.41	-11.54
Steady Yaw Rate stbd	3.04	4.26	-3.29	-7.10	-6.97
Steady Rudder Trans. Force stbd	5.64	-6.28	-2.82	-13.95	-13.42
Mean Error	2.87	3.39	4.46	8.71	11.74

also true for the Nomoto indices T'_N an K'_N, where the trend of the CFD curves agrees well with the model test results, showing, however, a slightly higher increase in T'_N and decrease in K'_N in the transition from the h/T of 1.15 to 1.10. The initial turning time for the h/T of 1.20 is slightly overestimated and for 1.15 underestimated, resulting in a trend reversal here for the CFD simulation. The values, however, only differ by less than 5 %. The curve progressions over time for yaw rate and transverse rudder forces agrees well with model



(a) Tactical Diameter
(b) Turning Circle Radius
(c) Steady Drift Angle
(d) Steady Surge Velocity
(e) Steady Yaw Rate
(f) Steady Transverse Rudder Force

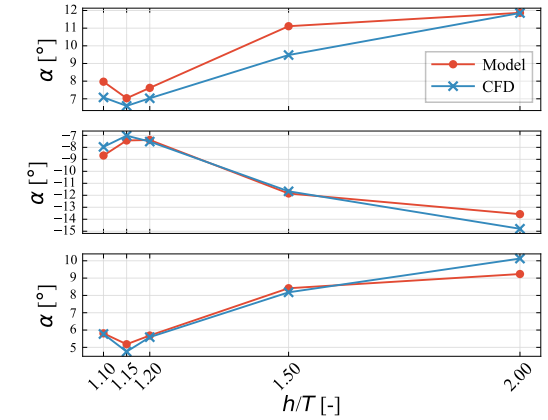
Figure 6.10.: Validation plots for steady-state stbd turning parameters with an initial speed of 9 kn for the JBC

test results. Both yaw rate and rudder forces, are slightly underestimated by CFD results. For the transverse force, valid model test data is only available for h/T ratios of 2.00, 1.50 and 1.10. Table 6.13 illustrates the errors in the CFD results, revealing an overall good agreement with model test data, with mean values less than 10 %, and mostly close to 5 %.

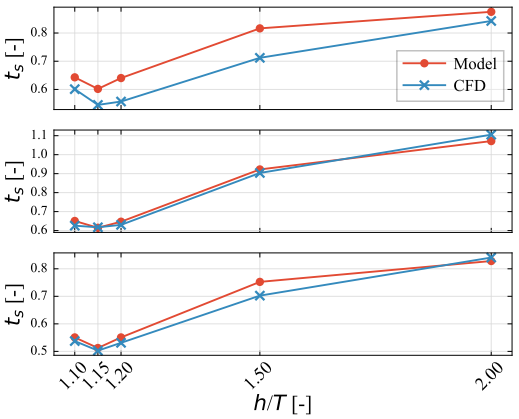
Table 6.13.: Differences between CFD and EFD results of the Zig-Zag 35-20 Manoeuvre in % for the JBC

Parameter	$h/T = 2.00$	$h/T = 1.50$	$h/T = 1.20$	$h/T = 1.15$	$h/T = 1.10$
Overshoot 1	-0.10	-17.22	-8.38	-6.57	-12.55
Overshoot 2	8.24	-1.55	1.81	-5.69	-9.06
Overshoot 3	8.82	-2.87	-1.58	-8.99	-0.64
Yaw-checking Time 1	-3.85	-14.66	-14.94	-10.41	-6.98
Yaw-checking Time 2	3.05	-2.06	-2.75	0.41	-3.97
Yaw-checking Time 3	1.50	-7.11	-3.61	-1.91	-2.47
Initial turning time	-0.63	-6.92	4.77	-3.57	3.27
Mean Error	3.74	7.48	5.41	5.36	5.56

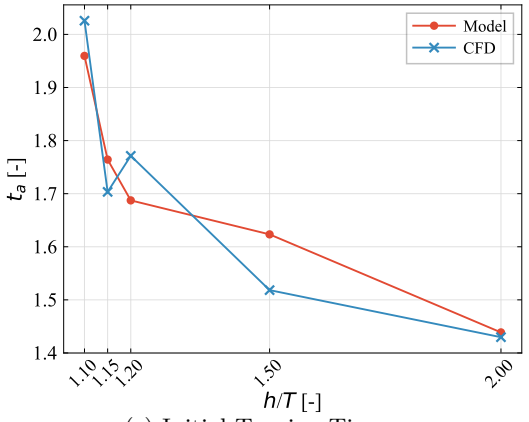
In summary, the chosen numerical setup has been shown to accurately reproduce the manoeuvring behaviour of the investigated ships in shallow water. Solution verification was performed for resistance tests and a full turning circle manoeuvre for both model ships. Except for two transient parameters of the DTC, all compared quantities demonstrated convergence. Validation of resistance, propulsion, and direct manoeuvres indicates overall good agreement with experimental data. For the turning circle, the numerical results capture the directional asymmetry of the DTC as well as the trend reversal in yaw rate of the JBC, though the latter is less pronounced than in the experiments. In the Zig-Zag manoeuvres, the deviation of parameters decreases with increasing overshoot number. Overall, mean errors are around 5 %, confirming the reliability of the simulations and supporting their application in detailed hydrodynamic analysis.



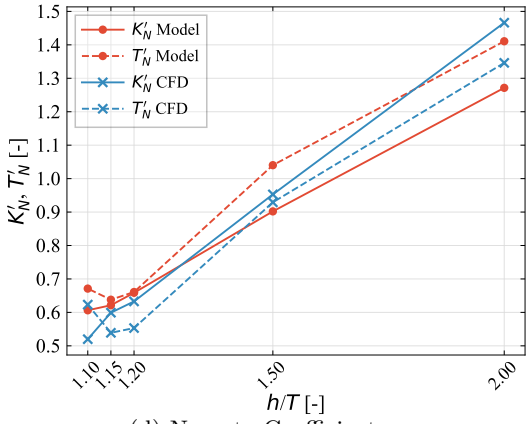
(a) First, Second and Third Overshoot Angle (from top to bottom)



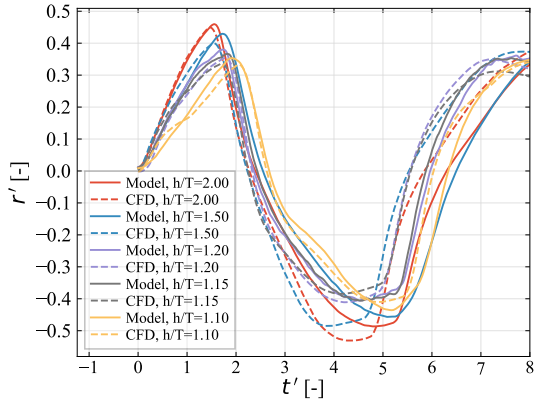
(b) First, Second and Third Yaw-checking Times (from top to bottom)



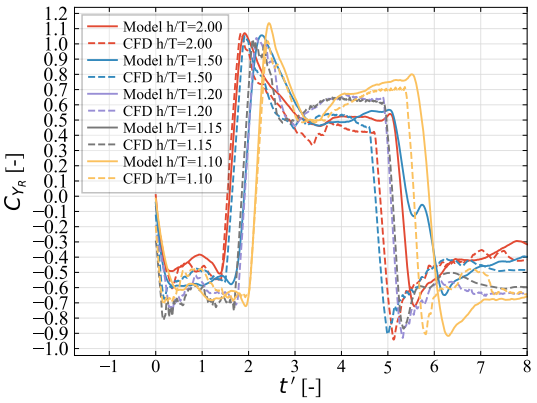
(c) Initial Turning Time



(d) Nomoto Coefficients



(e) Yaw Rate



(f) Transverse Rudder Force

Figure 6.11.: Validation plots for the Zig-Zag 35-20 stbd manoeuvre with an initial speed of 9 kn for the JBC

7. Results and Discussion

The results of the shallow-water manoeuvres are presented, interpreted and discussed below. In addition to the measured forces, trajectories and motions of the model ship, the typical parameters of the individual turning and Zig-Zag manoeuvres are evaluated in particular. To ensure a systematic presentation, each aspect is examined individually and considered for both model ships. Firstly, the influence of shallow water and depth Froude number on the manoeuvring behaviour in the design state is examined. In the subsequent stage of the investigation, the impact of the modified floating condition in shallow water is examined.

7.1. Influence of Depth Froude Number and h/T Ratio on Manoeuvring Behaviour at Design Condition

Most of the manoeuvres were performed in the design floating condition, as well as at partial draught for both model ships, see Table 5.4 to Table 5.7. The results for the design conditions will be analysed first. Owing to the breadth of the dataset, encompassing a wide range of water depths and velocities for this condition, and the resulting complexity of their interdependent effects on manoeuvring behaviour in shallow water, two complementary plotting approaches are adopted. One representation relates the measured parameters to the depth Froude number in order to highlight how the dependence on velocity changes with water depth. For each h/T ratio, a second-order polynomial regression curve is included to indicate the overall trend with respect to the depth Froude number; these plots are presented primarily in the following section. The second representation plots the parameters directly against the ratio h/T, which allows a clearer identification of direct water-depth effects, particularly in extreme shallow conditions; these figures are provided in the appendix. Both types of plots are referenced in the main text.

For the description of the influence of shallow water, a standardised written reference for the various stages of shallow water is used in terms of the ratio h/T according to ITTC (2014, 2021) and PIANC (1992). The ITTC definition of 'deep water' ($h/T > 4.00$) is used (ITTC, 2002, 2014), also referenced here as the h/T of 6.00, in the context of the described tests. Finer subdivisions of shallow water is made according to PIANC (1992):

- $h/T > 4.00$ is 'deep water',
- $h/T = 2.00$ and 1.50 are 'intermediate' or 'moderate shallow water',
- $h/T = 1.20$ is 'shallow water', and
- $h/T = 1.15$ and 1.10 are 'very' or 'extreme shallow water'.

7.1.1. Turning Circle Manoeuvres

Turning circle manoeuvres were performed at 35° and 45° rudder angles. The speed range for the 35° manoeuvre varies from 6 to 19 knots, depending on the model ship and under keel clearance available. With the DTC additional model tests were carried out in deep water at 15 and 19 knots. The turning circle test at 45° rudder angle was carried out for 6 and 9 knots to stbd and port side. It should be noted that, at the lowest water levels, not all manoeuvres could be accommodated into the BAW manoeuvring basin, see Figure 7.1. Apart from advance and transfer, all typical parameters of the turning circle according to ITTC are obtained during the steady phase. Therefore, the description and analysis of the steady phase of the turning circle, together with all standard parameters, will be presented first.

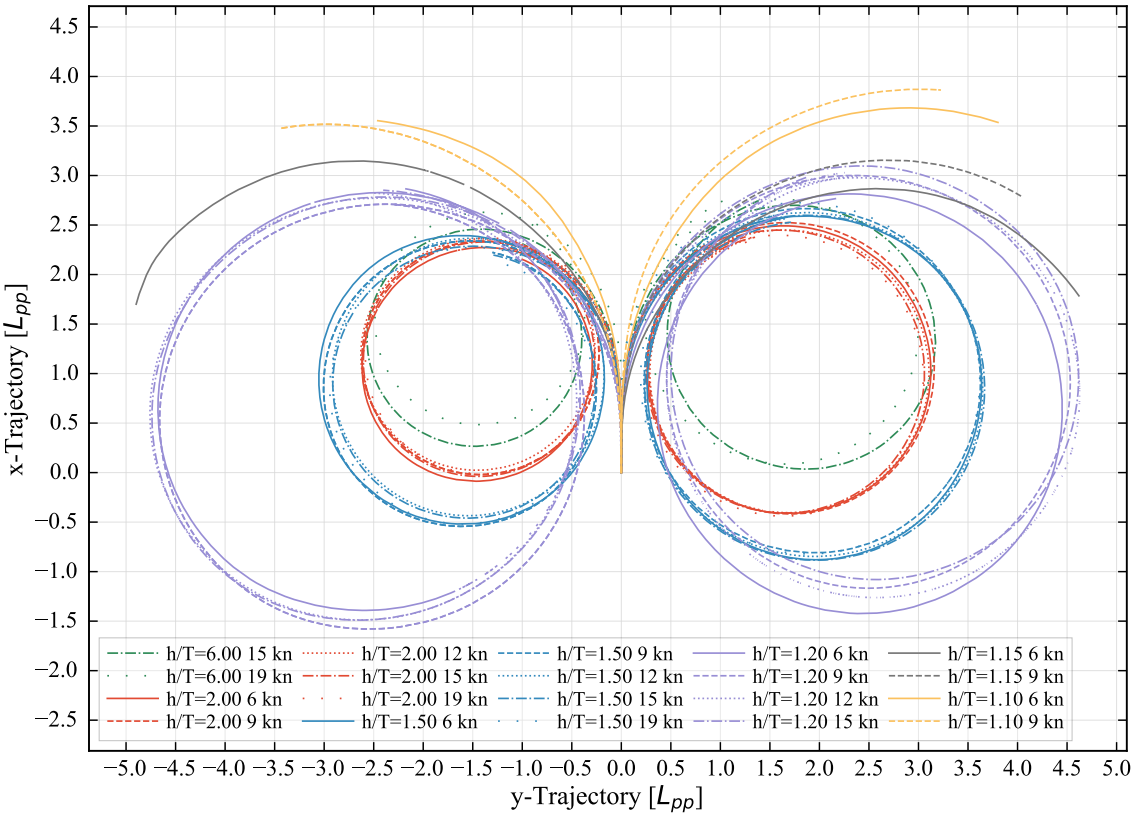


Figure 7.1.: Trajectories of the 35° turning circle manoeuvre for the DTC

Figure 7.1 and Figure 7.2 show the trajectories of the 35° turning circle manoeuvres at design draught for all investigated speeds to stbd and port. In general, it can be seen that the tactical diameter and turning circle radius increase significantly with decreasing h/T ratio. A more detailed picture of these parameters is shown in Figure 7.3 and Figure A.1. Both figures show a steadily increasing tendency of the tactical diameter as h/T decreases. For the DTC, even the gradient of the curves increases steadily with decreasing the under keel clearance. Overall, the turning ability of the ships, measured by the distance required

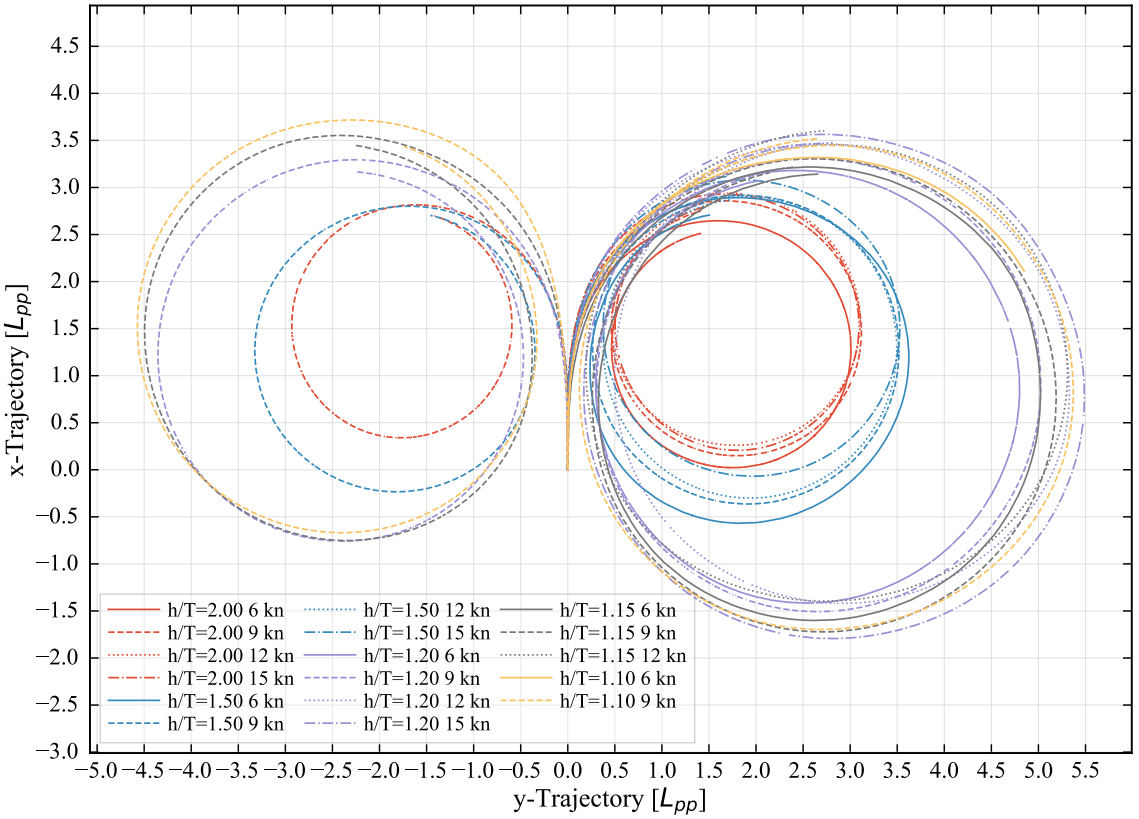


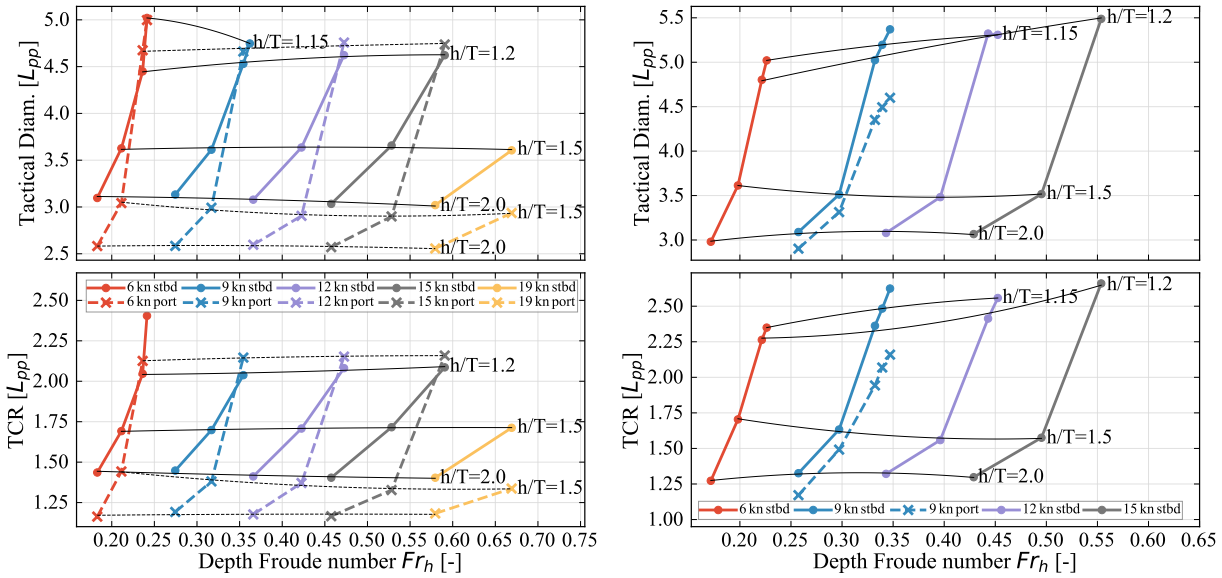
Figure 7.2.: Trajectories of the 35° turning circle manoeuvre for the JBC

for turning, is decreasing significantly with reducing water depth.

Generally, the increase in tactical diameter and turning circle radius shows only small differences across the different ship speeds. This is highlighted by the nearly horizontal regression curves over the depth Froude number for the DTC, see Figure 7.3. However, for the JBC, with beginning shallow-water conditions of $h/T = 1.20$, the speed influence is clearly visible. With increasing speed, both the tactical diameter and turning circle radius increase over the depth Froude number, so that the case of 15 kn for $h/T = 1.20$ assumes the greatest value for both parameters, even compared to lower velocities at the most extreme case of $h/T = 1.10$. Hence, the widely known low impact of speed on turning circle parameters does not necessarily apply to shallow water conditions, as shown here for the JBC.

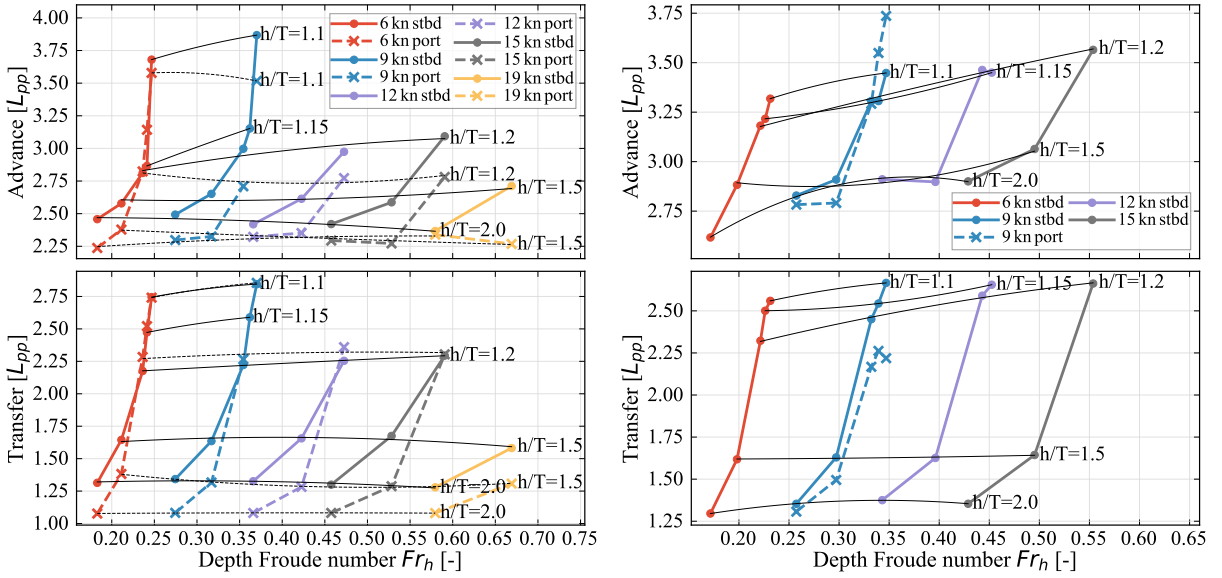
For the JBC, the advance and transfer exhibit comparable dependence on speed and both increase with decreasing h/T ratio, see Figure 7.4 and Figure A.2. The advance however, shows this trend already at moderate shallow water conditions. The transfer of both ships increases similarly, approximately doubling from moderate to extreme shallow-water conditions. The DTC, again, shows only minor speed dependencies under moderate shallow water. At shallow and extreme shallow water, however, a pronounced increase in advance is observed at depth Froude numbers from 0.25 to 0.38, for stbd side. Comparing the advance along constant speed curves, the DTC exhibits a significantly stronger increase, particularly at shallow- and extreme shallow-water conditions, see Figure A.2.

Following predominantly small changes in advance from shallow to extreme shallow water, a pronounced increase in advance is observed for both ships in the transition from h/T ratios of 1.15 to 1.10. For the DTC, this transition represents the largest increase across all investigated h/T ratios, highlighting the influence of the extreme shallow-water condition of $h/T = 1.10$ on the initial turning ability.



(a) DTC (b) JBC

Figure 7.3.: Tactical diameter and TCR of the 35° turning circle manoeuvre

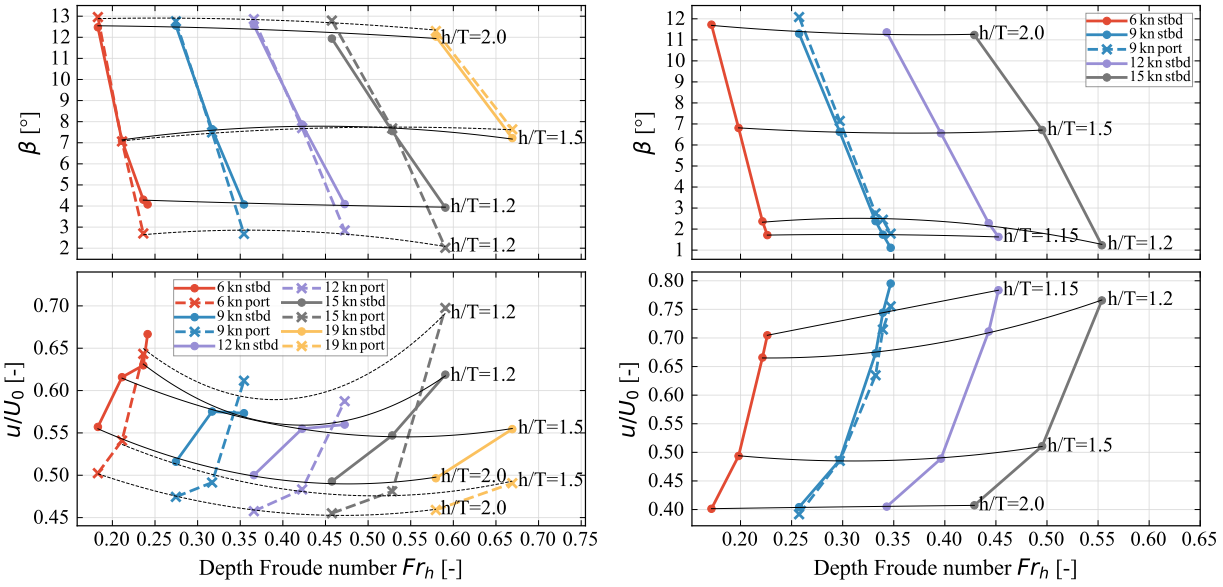


(a) DTC (b) JBC

Figure 7.4.: Advance and transfer of the 35° turning circle manoeuvre

The observed increase in turning-circle parameters is primarily attributable to the significant increase in hydrodynamic damping as the under-keel clearance decreases, which

in turn reduces the drift angle. This reduced drift angle substantially affects the ship's resistance and, consequently, its velocity during the manoeuvre. Figure 7.5 and Figure A.3 shows the steady drift angle and the steady surge velocity in relation to straight-ahead speed at the beginning of the manoeuvre. For the DTC, the steady advance speed and drift angle demonstrates a similar progression as a function of h/T for all velocities, except for shallow water ($h/T = 1.20$), where a steep increase in advance speed can be found. During the port and stbd turning manoeuvre, the steady advance speed at 15 knots increases significantly over the depth Froude number compared to the lower ship speeds. Comparing the surge speed over the depth Froude number, a clearly decreasing trend is observed along the regression lines for constant h/T ratios, followed by an increase at higher depth Froude numbers, see Figure 7.5. The depth Froude number at which the increase occurs is strongly dependent on the h/T ratio, occurring at lower values for smaller h/T. Furthermore, the magnitude of the increase also grows with decreasing h/T, resulting in a greater curvature of the polynomial regression curves. Since the drift angle exhibits consistent trends and only a limited dependence on the depth Froude number, this phenomenon cannot be attributed to it. Rather, it can be associated with the progression of the regression curves for the rudder forces at constant h/T ratios, see Figure 7.6a, which closely follow the same trend over the depth Froude number as the steady-state velocity. This indicates that the altered rudder–propeller interaction at the stern is strongly dependent on velocity and h/T. As a result, the rudder force exhibits a highly non-linear response, which directly correlates with the observed velocity loss during the turning manoeuvre.

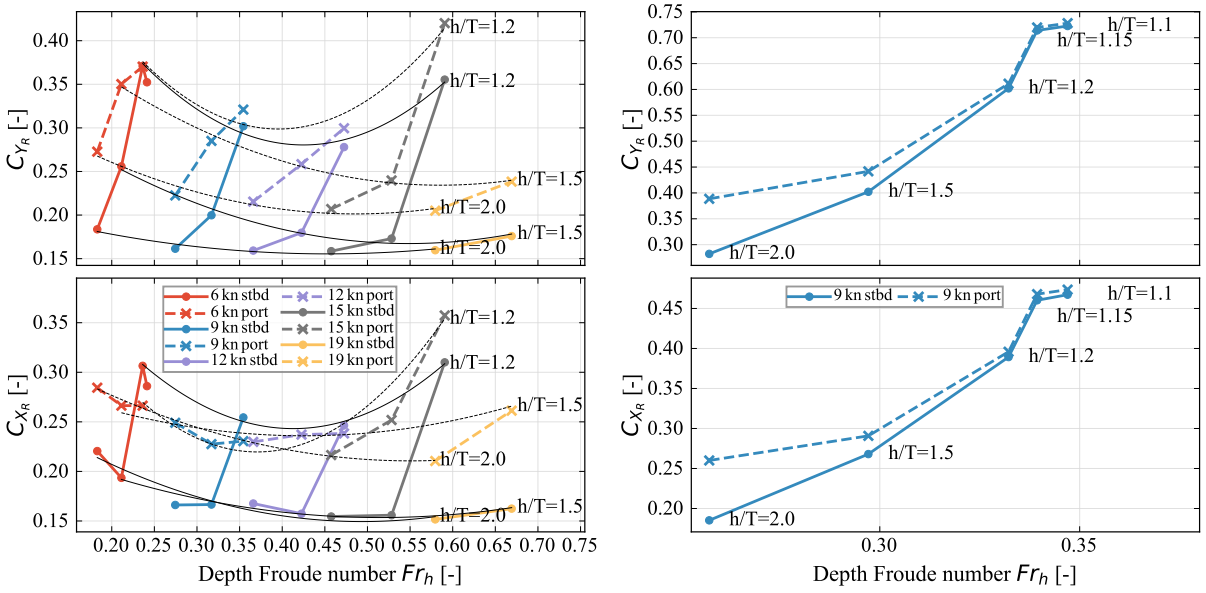


(a) DTC (b) JBC

Figure 7.5.: Steady drift angle and surge velocity of the 35° turning circle manoeuvre

These effects are reflected quantitatively in the rudder forces: at 15 kn, the longitudinal and transverse forces increase by more than 100 % for the stbd manoeuvre and by approximately 40 % and 70 %, respectively, for the port side, within an h/T range of 1.50–1.20. At lower advance speeds, the stbd forces rise less sharply, while the port-side forces remain nearly constant, further illustrating the velocity- and h/T-dependent non-linear behaviour

of the rudder forces, see Figure A.4a.

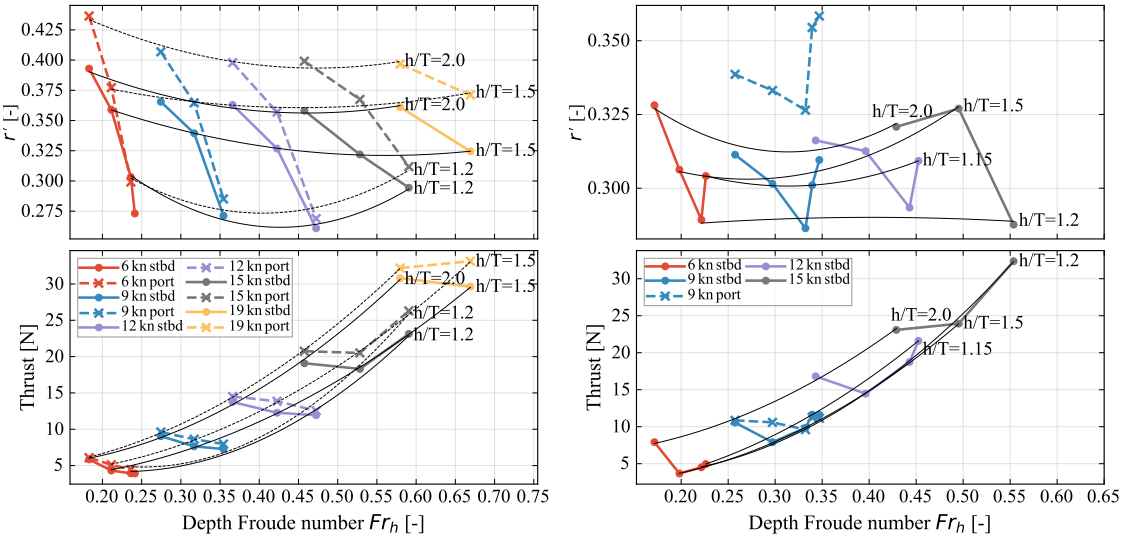


(a) DTC (b) JBC

Figure 7.6.: Steady rudder transverse and longitudinal force of the 35° turning circle manoeuvre

Figure 7.7 and Figure A.5 show the propeller thrust during the steady phase of the turning circle manoeuvre. Generally, the steady propeller thrust is initially decreasing within moderate h/T ratios for both ships. For the further progression, again, the higher velocities show a different behaviour than the lower velocities. For the DTC the 15 kn and for the JBC the 12 and 15 kn cases, show a significant increase in steady thrust in the transition from moderate shallow to shallow water, whereas at lower velocities, there are only slight changes. Two opposing effects and one additional effect generally influence the propeller thrust of a manoeuvring ship in shallow water. On the one hand, the thrust loading factor, and thus the thrust, increases with increasing wake fraction for decreasing h/T ratio. On the other hand, the thrust loading factor, and thus the thrust, decreases with higher advance speed as the water depth decreases. In addition, the thrust changes with decreasing h/T, due to the propeller experiencing a decrease in oblique flow. At lower velocities, the thrust appears to correspond more closely to the lesser loaded propeller due to the higher speeds associated with a decreasing h/T. The higher wake fraction at ship speeds of 15 knots or 12 and 15 knots, respectively, is responsible for a higher propeller loading at h/T of 1.20, and thereby for a completely different propeller inflow, as the thrust rises significantly from an h/T of 1.50 to 1.20.

Based on the observed trends of drift angle, a pronounced non-linearity in the speed dependence is evident, when transitioning from moderate shallow to shallow water, particularly for the JBC. This results in significantly higher relative speeds in steady-state condition of the turning circle at 15 knots for both ships. This effect is likewise evident in the propeller thrust and rudder forces. The trends in velocity along the regression curves become increasingly non-linear with decreasing UKC and, in the case of the DTC, are closely correlated with the changes in rudder forces, reflecting the h/T- and speed-



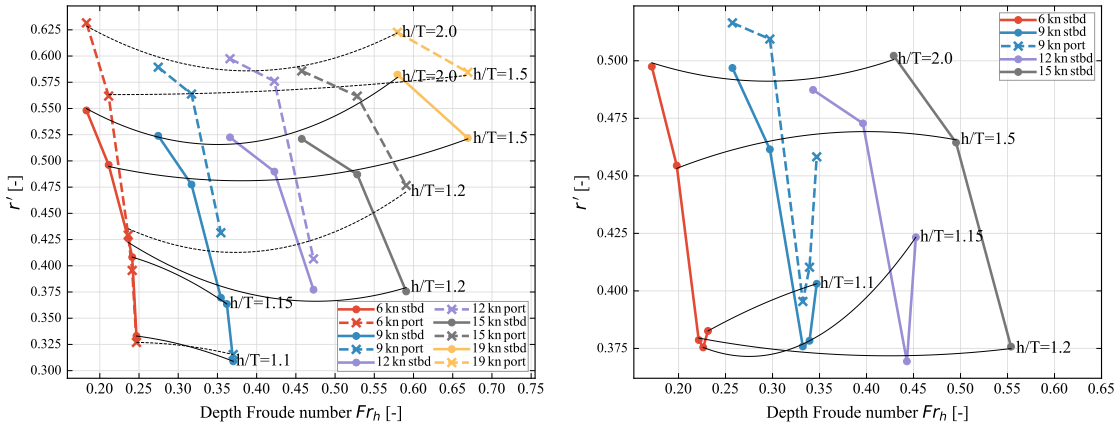
(a) DTC (b) JBC

Figure 7.7.: Steady yaw rate and propeller thrust of the 35° turning circle manoeuvre

dependent variation in rudder–propeller interaction. Consequently, the non-linear response of the propeller directly governs the corresponding velocity loss during manoeuvring, highlighting the critical role of the stern flow conditions and rudder configuration in shallow water.

The steady yaw rate is generally decreasing in the transition from moderate shallow-water to shallow-water conditions, particularly for the DTC, and again, increasing for extreme shallow-water conditions for the JBC, see Figure 7.7 and Figure A.5. This increase is significant, as the yaw rate shows similar or even exceeding values compared to the h/T ratio of 2.00. The DTC's speed dependency on yaw rate, illustrated by the regression lines, exhibits a similar pattern to that of the surge velocity: the yaw rate decreases at lower depth Froude numbers before increasing at higher values, with the point and magnitude of the increase both growing as h/T decreases, resulting in more pronounced curvature of the regression curves. This behaviour is, again, strongly correlated with the rudder forces, as the transverse component exhibits a similar trend along the depth Froude number, see Figure 7.6a.

For the DTC no steady values are available at extreme shallow-water conditions, as no complete turning circles were achieved for this conditions. To compare the results obtained for each ship in extreme shallow-water conditions, the transient phase of the turning circle can be investigated. One possibility is to check the maximum yaw rate, which is clearly achieved before reaching 90° of heading change within phase two of the turning circle, see Figure 7.8 and Figure A.6. It can be seen that the maximum yaw rate reveals similar behaviour in moderate shallow- and shallow-water conditions, but entirely different behaviour in extreme shallow-water conditions. While the DTC exhibits steadily decreasing maximum yaw rates for constant speed, with even steeper gradients in extreme shallow water, the JBC shows a significant increase in the maximum yaw rate in extreme shallow-water conditions, up to 16 %, with the gradient becoming more pronounced at higher depth Froude numbers. An explanation of this particular manoeuvring behaviour



(a) DTC (b) JBC

Figure 7.8.: Maxiumum yaw rate at the 35° turning circle manoeuvre

of the JBC, is given in subsection 7.1.2, analysing the transient phase of the turning motion together with the Zig-Zag manoeuvre, where yaw accelerations are still present, with the use of CFD results.

Overall, the trend reversal of yaw rate for the JBC in extreme shallow water is remarkable. The DTC's dependency of yaw rate on depth Froude number mirrors that of the steady surge velocity during turning and is closely associated with the rudder forces, reflecting the altered rudder–propeller interaction at the stern.

A remarkable aspect concerning the standard manoeuvring parameters of the turning circle, relates to the asymmetric turning behaviour in dependence on the water depth for the DTC, leading to a trend reversal of the tactical diameter and turning circle radius in the transition from moderate shallow- to shallow-water conditions, see Figure 7.3a and Figure A.1b. Comparing the turning circle to stbd and port side for the DTC, it is noticeable that at moderate shallow water, the port turning circles still have smaller diameters, but from $h/T = 1.50$ downwards, a trend reversal takes place. Particularly in the transition from h/T of 1.50 to 1.20, the port parameters increase significantly stronger. This means that the DTC model ship's manoeuvrability is affected differently by shallow-water conditions depending on whether it is turning to stbd or port. Main influence factors are the rotational direction of the propeller and its interaction with the rudder. The trend reversal is mainly due to the lower forward speed during the manoeuvre to stbd compared to port in this case, as the yaw rate for stbd turning generally keeps lower values than that for port side, see Figure 7.5a and Figure 7.7a. The propeller-hull and propeller-rudder interaction is significantly altered in shallow water. One contributing factor is the restriction of vertical inflow towards the propeller, which modifies the propeller-induced asymmetric pressure distribution on the hull. Moreover, the increased and altered wake fraction in shallow water changes the inflow distribution along the vertical direction of the propeller, thereby affecting both the asymmetric force component of the propeller and the asymmetric propeller-inflow to the rudder. Presumably due to the altered propeller-rudder inflow comparable resultant transverse rudder forces are observed for stbd and port turns at $h/T = 1.20$, but with a significantly higher rudder longitudinal force, see Figure 7.6a.

At the same time, for 35° turning circle, there is a higher drift angle for stbd compared to port, see Figure 7.5a. As a result, the model ship is decelerated more strongly in the stbd than in the port turning circle, and manoeuvres with similar yaw rates result in a smaller turning circle. The asymmetries in both drift angle and surge velocity grow with increasing depth Froude number. Furthermore, for $h/T \leq 1.50$, higher thrust is observed during port-side manoeuvres, which may additionally explain the increased steady-ahead speed, see Figure 7.7a. The trend reversal can be seen even more clearly and already for an h/T ratio of 1.50 for the 45° turning circle manoeuvre, see Figure 7.9.

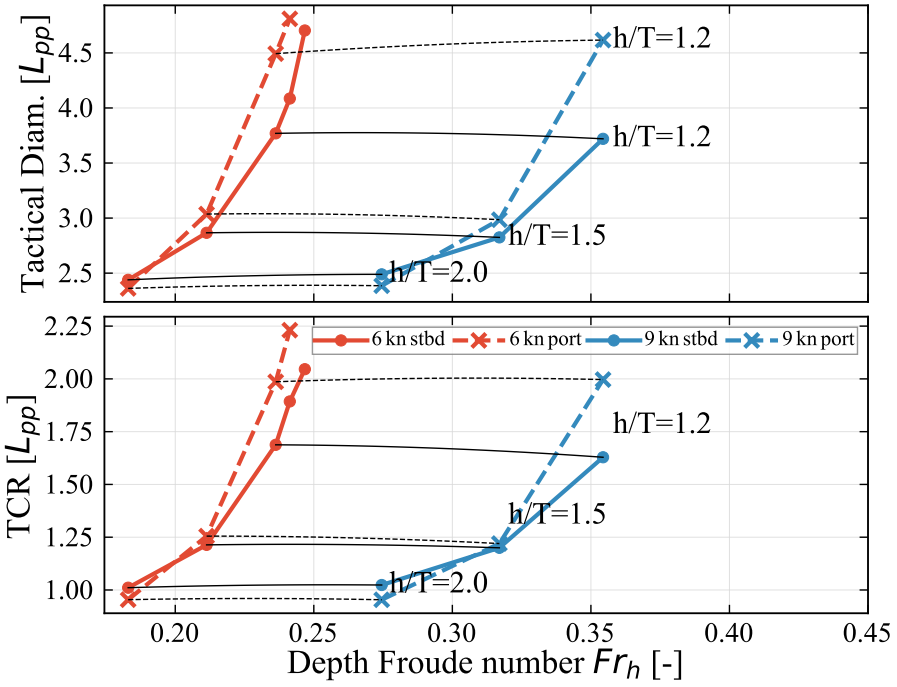


Figure 7.9.: Tactical diameter and turning circle radius of the 45° turning circle manoeuvre

The JBC is not subjected to that kind of strong changed asymmetric turning behaviour with dependence on the water depth, as most of the parameters are considerably smaller for the port side than for the stbd side, which is reflected in lower drift angles, higher velocity losses (Figure 7.5b and Figure A.3b), and higher yaw rates (Figure 7.7 and Figure A.5) for port side direction. However, it also shows a trend reversal for the initial turning behaviour, most obvious for the advance coefficient, showing higher values for port side in extreme shallow-water condition, see Figure 7.4b and Figure A.2b.

In summary, shallow water has a significant impact on the asymmetric turning behaviour of the ships investigated. The propeller-rudder interaction changes such that a trend reversal occurs with decreasing water depth, resulting in port turning-circle parameters exceeding the corresponding stbd values. In case of the DTC this rather affects the steady-state parameters, and in the case of the JBC the transient advance parameter.

Having considered primarily the steady phase, phase 3, of the turning circle, the transient phases 1 and 2, are described below, particularly those aspects which differ from those of

the steady phase of the turning circle. To provide a general overview, CFD results for the unsteady progression of the turning circle manoeuvre, the transient phases and the transition to a steady condition are described in dependence on the h/T ratio, using the different forces acting on the DTC and JBC as a function of the heading. Figure 7.10 and Figure 7.11 show the transversal forces acting on the model ship hulls during a 35° stbd turning circle manoeuvre, divided into hydrodynamic, rudder, centrifugal and inertia (acceleration) forces, obtained by CFD Simulations.

At the start of the manoeuvre (phase 1), essentially only accelerations are present, generated by the rapidly increasing rudder force. During this relatively short phase, neither yaw nor sway velocity has yet developed. Therefore, centrifugal forces are negligible and drift acceleration is mainly determined and generated by the rudder forces. Due to the barely existing lateral speed, the hydrodynamic forces are also insignificant. As the water depth decreases, the accelerations are increasingly damped by the hydrodynamic lateral forces already at slightest heading deflections. With decreasing UKC, these forces have ever greater gradients at the beginning, so that even at a heading of 0.5° the deep-water acceleration is three times the acceleration at h/T ratio of 1.10, for both ships. This considerably higher inertia force is balanced by higher centrifugal, lower hydrodynamic, and similar rudder forces at the beginning, compared to shallower water conditions.

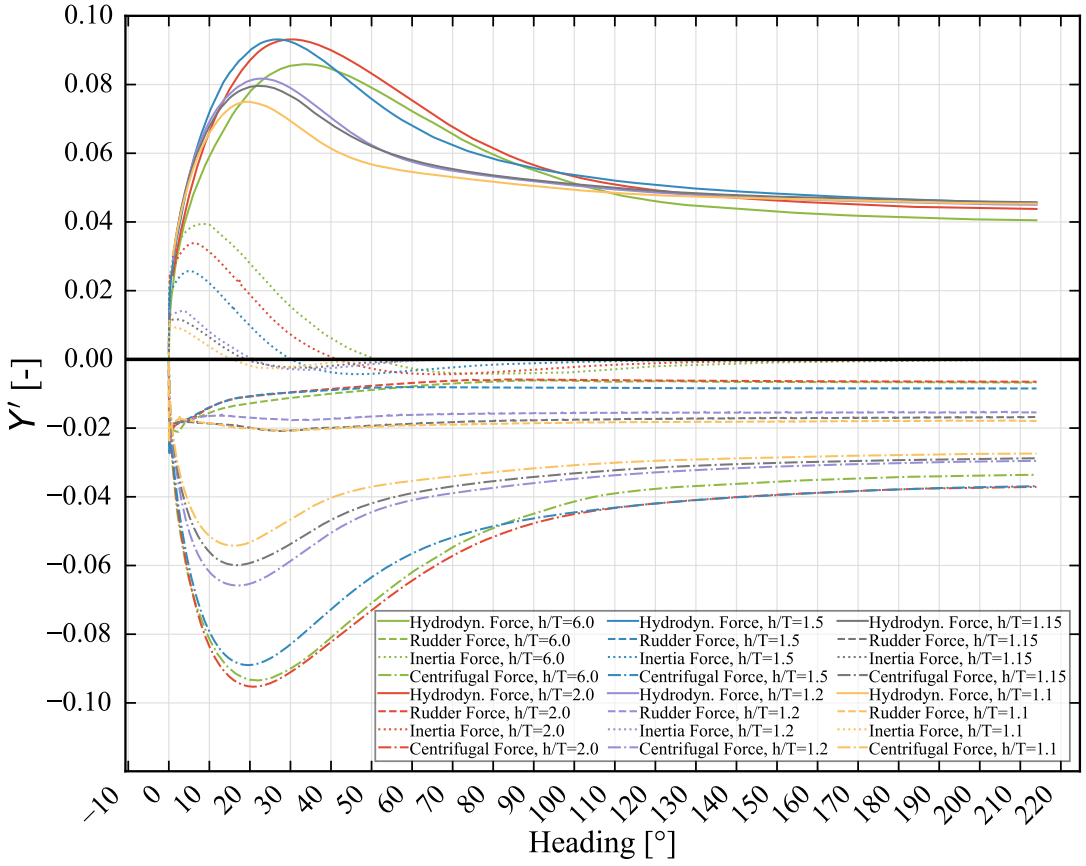


Figure 7.10.: Force components acting on the DTC during a 35° stbd turning circle manoeuvre with an initial speed of 9 kn at design condition, nondimensionalised according to Equation 4.4

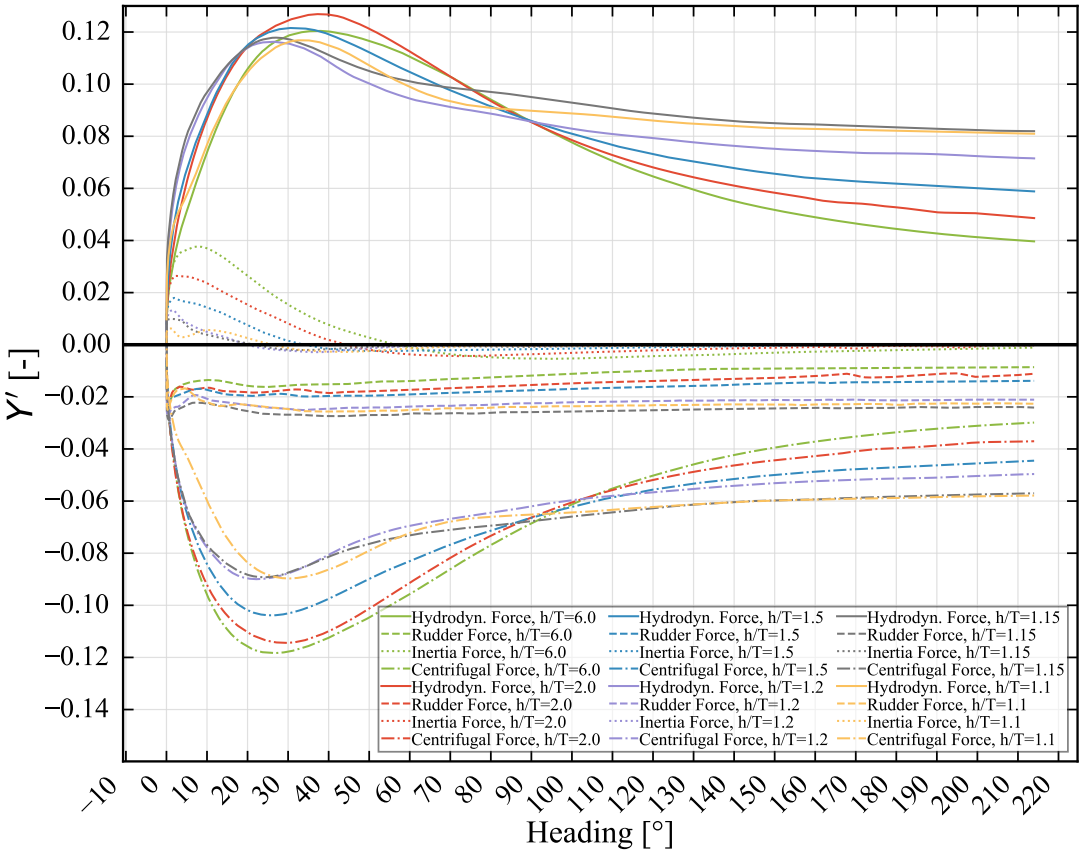


Figure 7.11.: Force components acting on the JBC during a 35° stbd turning circle manoeuvre with an initial speed of 9 kn at design condition, nondimensionalised according to Equation 4.4

Due to higher damping forces in shallow and extreme shallow water in phase 2, the inertia forces already intersect the abscissa at heading values between 15° and 30° and change its effective direction towards small values, converging to zero at heading values of 70°–80°. In moderate shallow and deep water, inertia forces intersect the x-axis only at 35° to 55° and converge to zero. After initially higher hydrodynamic transverse forces in shallow and extreme shallow water, these are below the deep-water values. However, the most extreme case of $h/T = 1.10$ shows a significant lower gradient similar to deep water due to considerably lower transverse velocity and intersects the deep-water curve before its maximum at approximately 25°. Hydrodynamic force at an h/T ratio of 1.50 remains above the deep-water values up to an angle of approximately 40°. The curves for an h/T ratio of 2.00 remain above the hydrodynamic transverse forces in deep water for the entire manoeuvre. In an angle range of approximately 75°–110°, the deep-water curve intersects the other shallow-water curves and assumes a minimum. Thus, for phase 2, the hydrodynamic forces in moderate shallow water, particularly for the h/T ratio of 2.00, assumes the highest values, while the shallow- and extreme shallow-water curves assume values below the deep-water curve. Following an initial increase in rudder forces that was similar across all shallow-water conditions, the rudder forces in shallow-water and extreme shallow-water conditions, are significantly higher than the values in deep and moderate shallow water. For the JBC again, the rudder force at h/T ratio of 1.15 reveals slightly

higher values compared to 1.10. The centrifugal forces increase significantly stronger in deep and moderate shallow water due to higher yaw rates and have similar maxima. Conversely, at the h/T ratio of 1.10, the maxima of centrifugal force are approximately 40 % (DTC) and 30 % (JBC) lower compared to deep-water values and converges faster to its steady value than in moderate shallow water and deep water. The curve for the h/T ratio of 1.10 of the JBC shows a significantly delayed progression, compared to 1.15 and 1.20. For the DTC, the centrifugal force in shallow and extreme shallow water remain below, and in moderate shallow water above deep-water values. For the JBC, moderate shallow water behave similar. However, the centrifugal forces in shallow- and extreme shallow-water conditions intersect the curves for moderate shallow- and deep-water conditions at around 90° of heading change and assume significantly higher values than in deep water and moderate shallow water, which corresponds to the increased yaw rates of the JBC in extreme shallow water (Figure 7.7). Overall, for the majority of phase 2, the hydrodynamic transverse forces were significantly reduced in both shallow and extreme shallow water and were counterbalanced by lower and shorter-acting effective inertia forces together with reduced centrifugal forces. Conversely, the hydrodynamic forces in moderate shallow water are significantly increased compared to deep-water conditions.

In steady conditions (phase 3), the hydrodynamic forces show a significantly different dependence on the h/T ratio for the two investigated model ships. For the DTC, in the steady region of the hydrodynamic transverse forces only the three areas of deep water, h/T=2.00 (8 % above the deep-water value) and the remaining shallow-water states (approximately 12 % above the deep-water value) can be identified in ascending order. By contrast, the hydrodynamic damping force of the JBC in steady-state conditions vary significantly in dependence on the h/T ratio. Under extreme shallow-water conditions, the values are approximately twice those observed in deep water. While the rudder forces are similar to the DTC values, the centrifugal forces are significantly higher, opposing the higher hydrodynamic forces. Under extreme shallow-water conditions, the centrifugal forces are approximately double those observed for the DTC. This corresponds to the increased yaw rate, which increases the JBC's centrifugal force in extreme shallow water, while the DTC showed decreased yaw rates for the same water depths.

In the third phase of the turning circle, both ships experience increased hydrodynamic forces in shallow and extreme shallow water, after exhibiting the lowest values in phase 2. Under steady conditions in phase 3, the deep-water hydrodynamic force curve attains a minimum across all investigated water depths. The bulk carrier shows a considerably higher hydrodynamic transverse force than the container ship in shallow and extreme shallow water; this increase is balanced by proportionally higher centrifugal forces.

A shallow-water effect during the transient phase 2 of the turning circle can be observed in the transition from deep water to intermediate shallow water, particularly with respect to the advance coefficient. Since the deep-water trials were only performed at 15 and 19 knots, only these velocities are compared to each other. Figure 7.1 shows the trajectories for deep-water turning circle trials at 15 and 19 knots. As illustrated in Figure 7.1 and Figure 7.12, the transfer coefficient and turning circle radius increase only slightly from deep water to intermediate shallow water and rapidly at h/T of 1.50 and lower. Conversely, the advance coefficient (Figure 7.12) initially shows a clear decrease of up to 7 % in the

transition from deep water to 2.00. For stbd turning circles, the advance coefficients then increase in the transition to 1.50 by approximately 7–10 %. In the port case, however, the advance continues to decrease slightly. Here, it first increases significantly at 15 knots in the transition to 1.20 by approximately 22 % and thus, above the deep-water values. The curve progressions of speed and drift angle at 90° heading change do not clarify this phenomenon, as the speed for moderate shallow water, as expected, does not drop so sharply and the drift angle in this region, similar to the further progression, decreases moderately, see Figure 7.12. Remarkable are the considerably larger transverse and longitudinal rudder forces at 90° heading change for the port case at both speeds 15 and 19 knots and the reversed order of magnitude between transverse and longitudinal forces. There is only little change in the rudder transverse and longitudinal force in the transition to moderate shallow water. It is only rising slightly at the h/T of 1.50 and rising significantly at the h/T of 1.20. The curve progression of the yaw rate for the 19 knots manoeuvre (Figure 7.12) however, reveals a significant higher maxima at an h/T of 2.00 compared to deep water, being approximately 10–15 % higher for port and stbd direction, respectively. Further progression sees the yaw rate of $h/T = 2.00$ remain at a higher level, settling at a level similar to, but slightly higher than, that in deep water for a steady condition. The curve for the h/T of 1.50 for port side has a similar progression to that in deep water, with a slightly higher maximum, levelling out on a similar value than in deep water for steady-state condition. Conversely, the stbd side shows already a strongly delayed progression with a similar maxima than deep water being slightly lower for steady conditions than in deep water.

The higher maximum yaw rates observed in the initial stage of the turning circle, particularly for $h/T = 2.00$, lead to an improved initial turning behaviour and are likely caused by changes in the hydrodynamic pressure distribution along the hull; however, this hypothesis can only be verified through CFD simulations.

As the turning motion is strongly dependent on the hydrodynamic yaw moment, the change of the distribution of the yaw moment over the heading angle is described first. Figure 7.13 shows the results of CFD simulations regarding hydrodynamic yaw moment for the 35° stbd turning circle manoeuvre in dependence on the heading angle for four different sections of the ship: the aft section before the aft shoulder of the ship, the aft midship section until midship frame, the forward midship section until forward shoulder and the fore section at the bow of the ship. The proportions of the total hydrodynamic yaw moment are changing drastically as a function of the heading in dependence on water depth. In the following, the three cases, deep water, and h/T ratio of 2.00 and 1.10 shall be considered in particular. It should be noted that a negative yaw moment (in stbd case) counteracts the turning motion, and vice versa.

The yaw moment at the aft section of the ship is growing fast and strong in deep and moderate shallow water, with maxima at around 35° heading change and contributes the largest proportion to the damping of the ship's yaw motion. By contrast, in extreme shallow water, the absolute yaw moment at the stern is increasing only slightly and, with amounts of only approximately one third of the fore ship yaw moment in steady case,

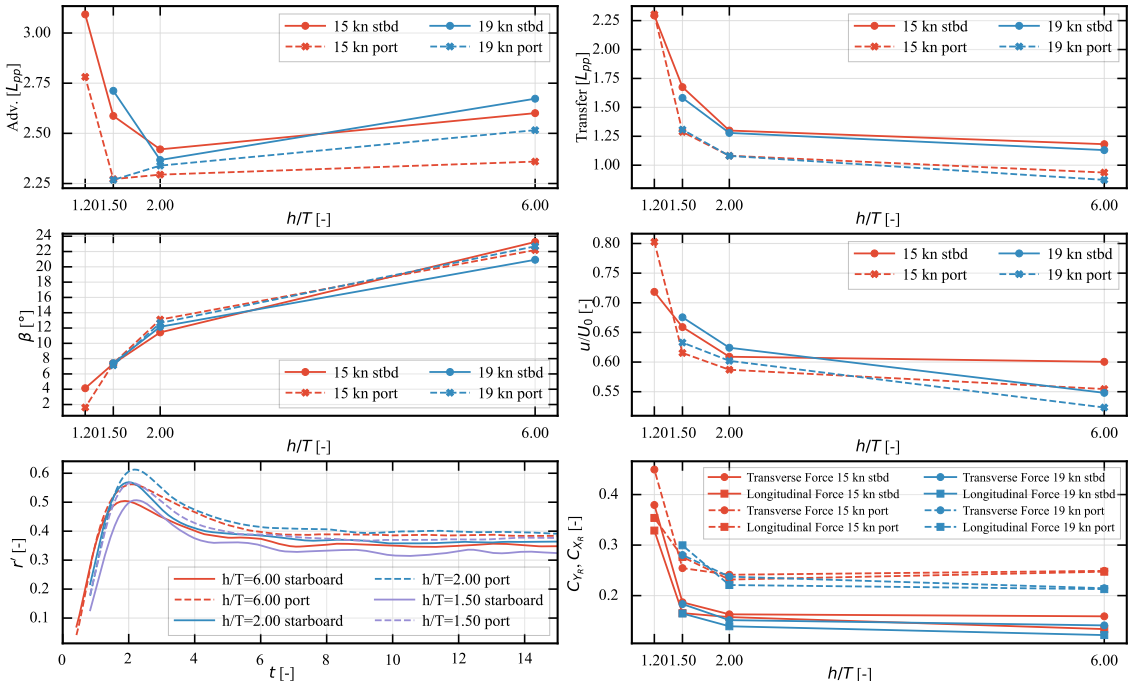


Figure 7.12.: Turning circle parameters and steady-turning values of drift angle β, speed loss u/U_0, and non-dimensional rudder transverse (C_{Y_R}) and longitudinal (C_{X_R}) force coefficients at 90° heading change, and the time history of the non-dimensional yaw rate r' with an initial speed of 19 kn for the 35° turning circle manoeuvre in deep and shallow water. For comparison, the values for port manoeuvres of β, r' and C_{Y_R} are multiplied by -1.

makes only a small contribution to the damping of the turning motion. In the initial stage of e.g. 15° heading, the yaw moment of the aft section is only approximately 12 % of the fore section yaw moment. Conversely, in deep-water conditions, the proportion of damping of the turning motion of the fore section is higher than that of the aft section only up to a heading angle of 5° (10° for $h/T = 2.00$ and 15° for $h/T = 1.50$) and assumes positive values from a heading of approximately 15°, and starts to contribute to the turning motion of the ship. For the h/T ratio of 2.00, the yaw moment at the fore ship section counteracts the turning motion of the ship until a heading of approximately 30° and remains close to zero for steady-state condition. In the aft midship section, the hydrodynamic force damps the ship's turning motion during the initial stage and then diminishes to near zero. In shallow and extreme shallow water on the other hand, its magnitude increases initially and remains at moderate negative values. The hydrodynamic force acting on the forward midship section contributes to the turning motion of the ship in all water depths. It initially increases most in shallow- and extreme shallow-water conditions, but is greatest in moderate shallow water at a heading range of approximately 15° to 70°. By contrast, in the case of deep water, this yaw moment only increases slightly and remains at significantly lower values than in other water depths. In steady-state conditions, the moment is of comparable magnitude to that of the fore ship, with both contributing similarly to the amplification of the turning motion.

Generally, the yaw moment counteracting the turning motion of the ship is strongly shifting from the aft ship section to the fore ship section, with decreasing water depth.

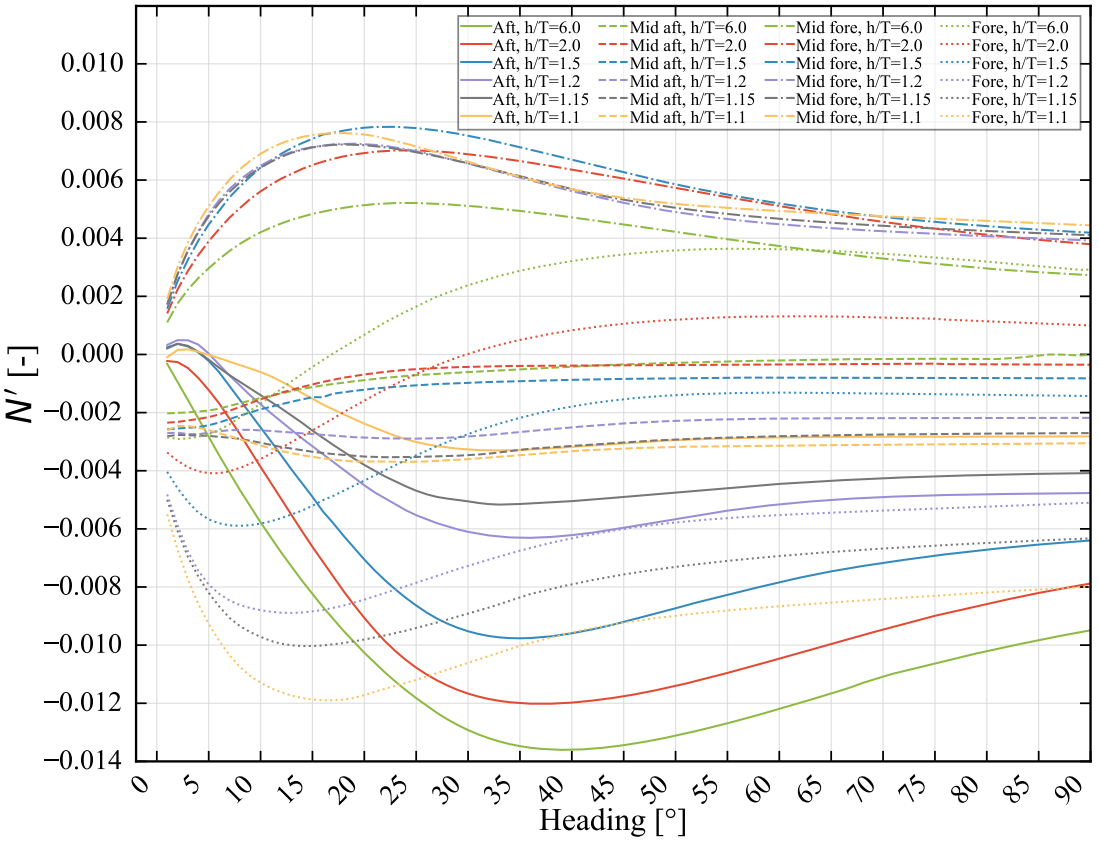
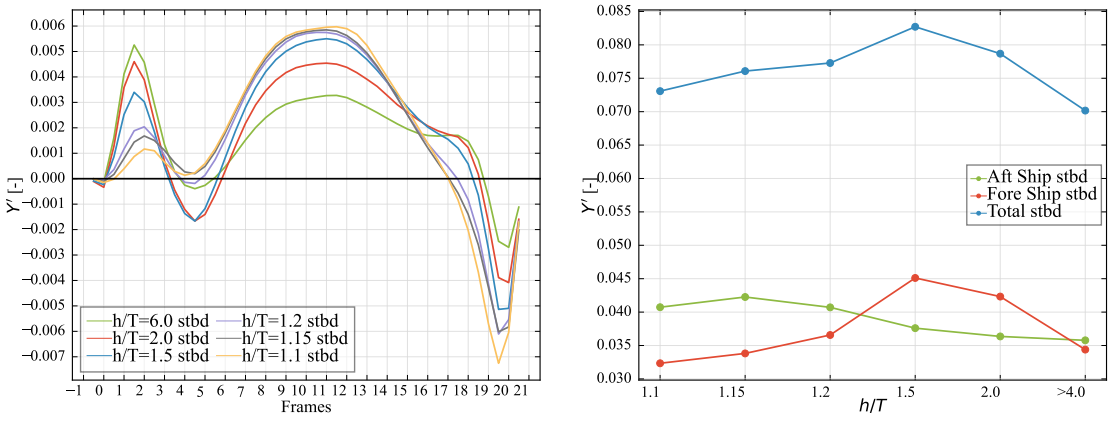


Figure 7.13.: Calculated hydrodynamic yaw moment as a function of heading angle for different ship sections of the DTC for a 35° stbd turning circle manoeuvre with an initial speed of 9 kn, nondimensionalised according to Equation 4.4

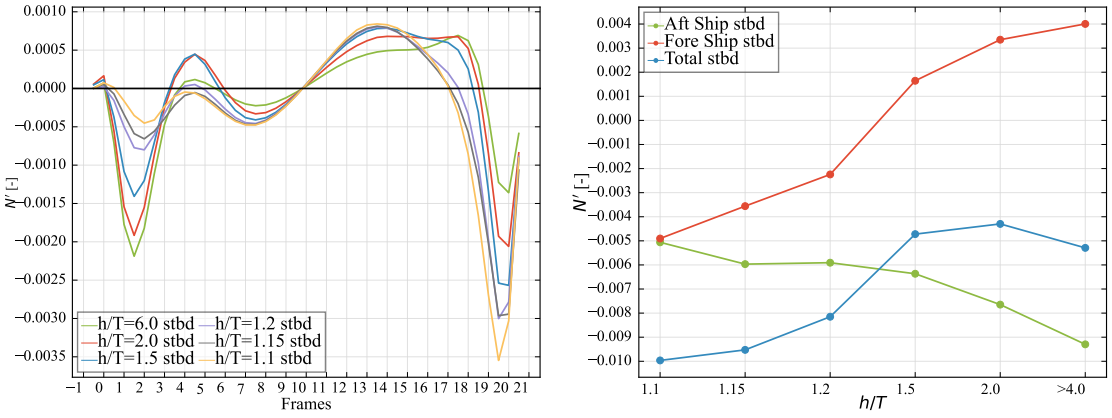
In moderate shallow water, the proportion of the fore section counteracting the turning motion increases and changes only slightly for the mid aft section. In contrast, the contribution of the mid-fore section to the amplification of the turning motion increases compared to deep-water conditions.

Since the transient phase is relevant only for investigating changes in advance coefficients as a function of the water depth, the case of a 15° heading change is used as illustration for further investigations. Figure 7.14a shows the hydrodynamic lateral forces for this case along the longitudinal direction of the ship, referenced by frame positions. As can clearly be seen here, the stern-heavy lateral force distribution in deep water clearly shifts to a bow-heavy distribution in extreme shallow water. However, the increase at the bow clearly exceeds the decrease at the stern, which leads to a significantly greater hydrodynamic moment counteracting the rotation in very shallow water. However, for the transition from deep-water to moderate shallow-water conditions, the yaw moment supporting the turn initially increases in the forward midship area. This is due to the significantly increased hydrodynamic transverse forces in this region in front of the centre of gravity (at frame 9.8), even in moderate shallow water. At the same time, the negative transverse force



(a) Forces as a function of ship's frames (b) Summed Forces for aft and fore ship

Figure 7.14.: Hydrodynamic lateral forces for a 35° stbd turning circle manoeuvre with an initial speed of 9 kn at 15° heading change, nondimensionalised according to Equation 4.4



(a) Yaw Moments as a function of ship's frames (b) Summed Yaw Moments for aft and fore ship

Figure 7.15.: Hydrodynamic yaw moment for a 35° stbd turning circle manoeuvre with an initial speed of 9 kn at 15° heading change, nondimensionalised according to Equation 4.4

damping the turning motion at the bow increases by a similar amount to that by which the positive force damping the turning motion at the stern decreases in moderate shallow water and shows a similar zero crossing as in deep water close to frame 18.5.

Comparing the total transverse forces and the transverse forces in the fore and in the aft ship as a function of the h/T ratio (Figure 7.14b), the initial increase in fore-ship forces in the transition to moderate shallow water is notable. This generally leads to an increased assisting hydrodynamic moment in moderate shallow water, resulting in improved turning ability.

However, considering the yaw moment in the same way in Figure 7.15b, it becomes clear that the balance of forces in the bow and stern is decisive as the forward yaw moment is decreasing steadily with decreasing water depth. Generally, the damping yaw moment of the ship is shifting from the aft part to the forward part of the ship with decreasing h/T ratios. While in deep and moderate shallow water the forward part of the ship actually contributes to the turning motion of the ship, in shallow and extreme shallow water it adds to the damping moment. For the h/T ratio of 1.10, hydrodynamic yaw moments of aft

and forward parts are almost of equal size. The aft part of the hydrodynamic yaw moment has a damping effect on the turning motion for all h/T ratios. However, particularly from deep water down to an h/T ratio of 1.20, the aft yaw moment increases significantly (less negative) by about 35 %, stays constant for h/T ratios 1.20 and 1.15, and drops about another 16 %, showing a similar value than the forward part at h/T of 1.10.

It is evident that, despite the occurrence of an increase in lateral damping during the initial transition from deep to moderate shallow water, the total yaw moment of the fore ship experiences a decrease, see Figure 7.15b. However, due to the described increased positive distribution of the lateral force in the forward midship section, the yaw moment of the fore ship, which actually supports the turning motion of the ship, decreases only slightly in moderate shallow-water and significantly in the transition to shallow-water conditions. Concurrently, the opposing yaw moment of the aft ship increases significantly (less negative) in the transition to moderate shallow water. Combined, the absolute value of the total damping yaw moment of the ship decreases in moderate shallow water, which leads to a higher initial turning ability of the ship compared to deep-water conditions.

Considering the hydrodynamic yaw moment as a function of the ship's length in Figure 7.15a, the significantly increased assisting yaw moments in the ranges of the sections 3–5.5 and 10–18.5 can be identified as the main factor influencing the variation of hydrodynamic yaw moments when transitioning from deep to moderate shallow water. In moderate shallow water, the changed peaks of yaw moments at the stern and the bow are roughly cancelling each other out. In shallow and extreme shallow water, however, the increased peak at the bow is dominating the decrease at the stern by far, as the zero crossing in the fore midship section is shifting significantly backwards to frame 17.

This significantly increased countermoment at the bow in extreme shallow water is also clearly visible in the pressure distribution, see Figure 7.16. The stagnation point of the flow is shifting to the stbd side of the bow in extreme shallow water, showing a significantly increased area of positive pressure towards the forward shoulder of the ship, which means that the supporting yaw moment occurs only considerably further aft and weaker in this water depth. Conversely, in moderate shallow water, the pressure distribution at stern and bow looks similar to that in deep water, while the negative pressure in the midship section of the ship is already increased significantly. Due to the already significantly restricted region for the flow below the keel for moderate shallow water and the simultaneously still existing effective drift angle, a strong negative pressure region forms around the ship on the suction side, such that the hull acts as a short-winged hydrofoil. This negative pressure further increases under extreme shallow-water conditions; however, the negative pressure on the theoretical pressure side increases as well. As a result, the total net force acting on the midship section changes only slightly for water depths below moderate shallow-water conditions (see also Figure 7.14a).

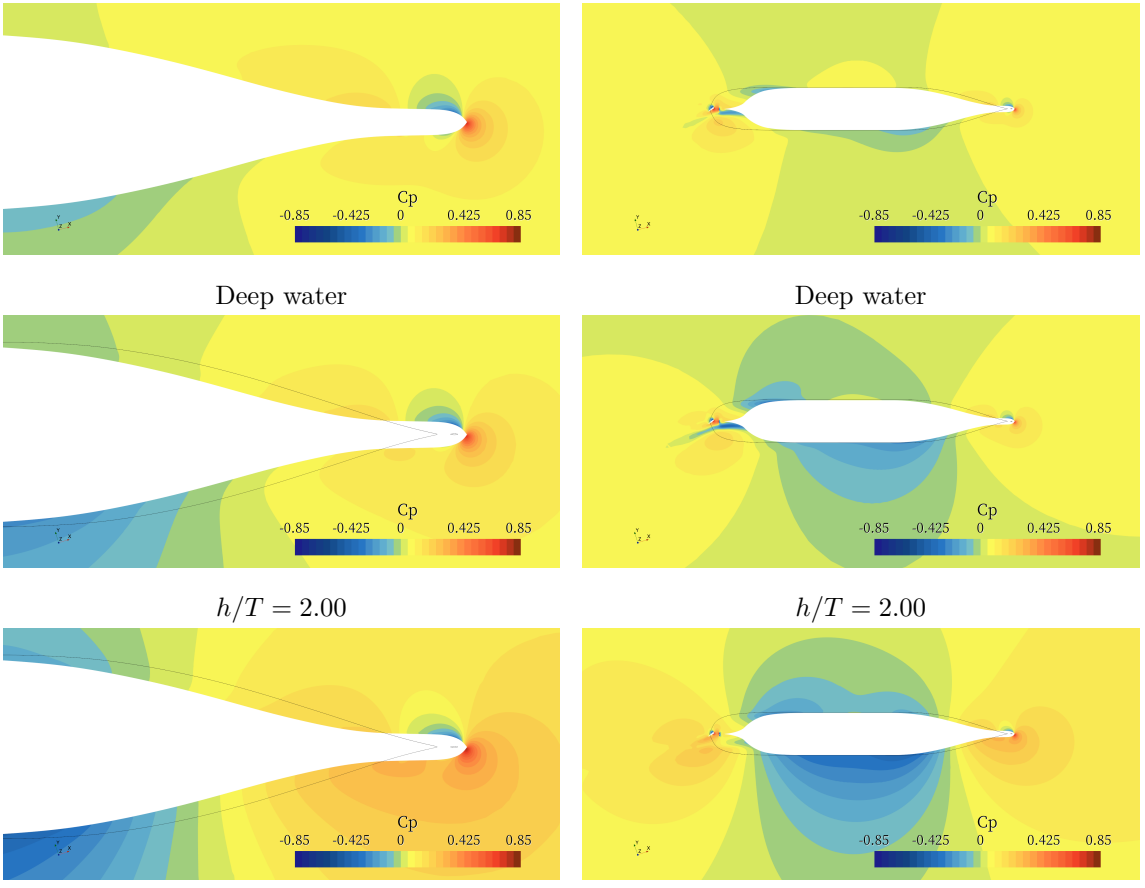
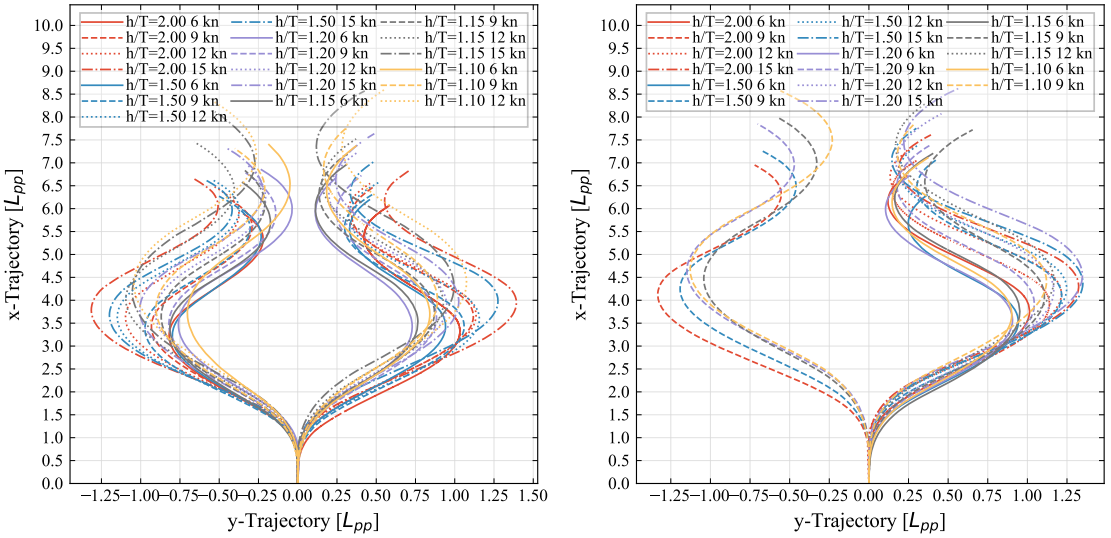


Figure 7.16.: Pressure distribution at 5.5 m below waterline (full scale) for the bow area (left) and the entire hull (right), shown in terms of the pressure coefficient C_P with the initial straight-ahead speed (9 kn) as reference speed, for a 15° heading angle at 35° stbd turning circle manoeuvre for the DTC

7.1.2. Zig-Zag Manoeuvres

Zig-Zag manoeuvres were performed for a heading change of 20° with 35° rudder deflection (Z 35-20) and 10° heading change with 20° rudder deflection (Z 20-10), initiated in both port and stbd directions. The manoeuvres were carried out for a speed range of 6 to 15 knots. For design condition, all h/T ratios of 2.00, 1.50, 1.20, 1.15 and 1.10 were investigated. Depending on the water level, not all speeds were executable at all h/T ratios. For the Z 20-20 manoeuvre, deep-water tests at velocities of 6 knots were also conducted with the DTC. The analysis made is mainly focusing on the first two overshoot angles. This is due to the fact that the range of the first overshoot angles is most likely to be relevant to safety in real operation.



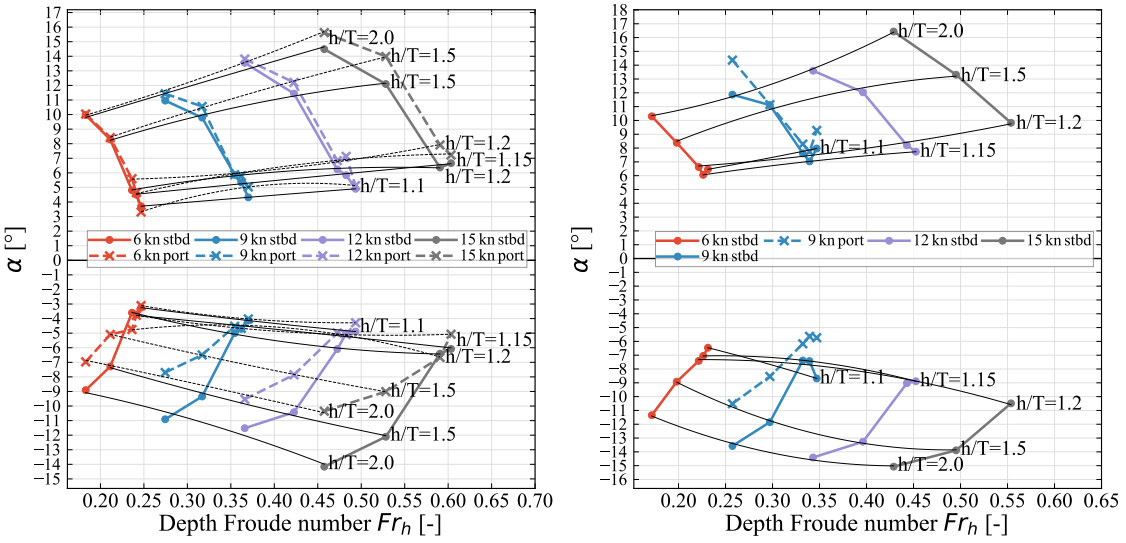
(a) DTC (b) JBC

Figure 7.17.: Trajectories of the Z 35-20 manoeuvre for different initial speeds at design condition

Figure 7.17 shows the measured tracks of the first 3 overshoot angles for all investigated h/T ratio and velocity combination for the Z 35-20 manoeuvre. For the trajectory, it can be clearly seen that both, h/T ratio as well as advance speed, have a significant impact. Nevertheless, these two parameters influence the trajectory in a distinct manner. Whereas the speed particularly affects the value of the maximum transverse motion y_{max}, which still occurs at similar longitudinal positions, the h/T ratio rather affects the shape of the trajectory and shifts the longitudinal positions x_{max}, where the y_{max} takes place. In extreme shallow-water conditions, higher velocities lead to a considerable shift of x_{max} to higher x-values, compared to other h/T ratios. The higher the h/T ratio, the sharper the shape of the trajectory. The lower the h/T ratio, the higher the x-positions of maxima and minima of y-values. y_{max} decreases as the h/T ratio is reduced to 1.15–1.20, then increases again for smaller values, as observed in most cases. These observations are particularly evident for the DTC.

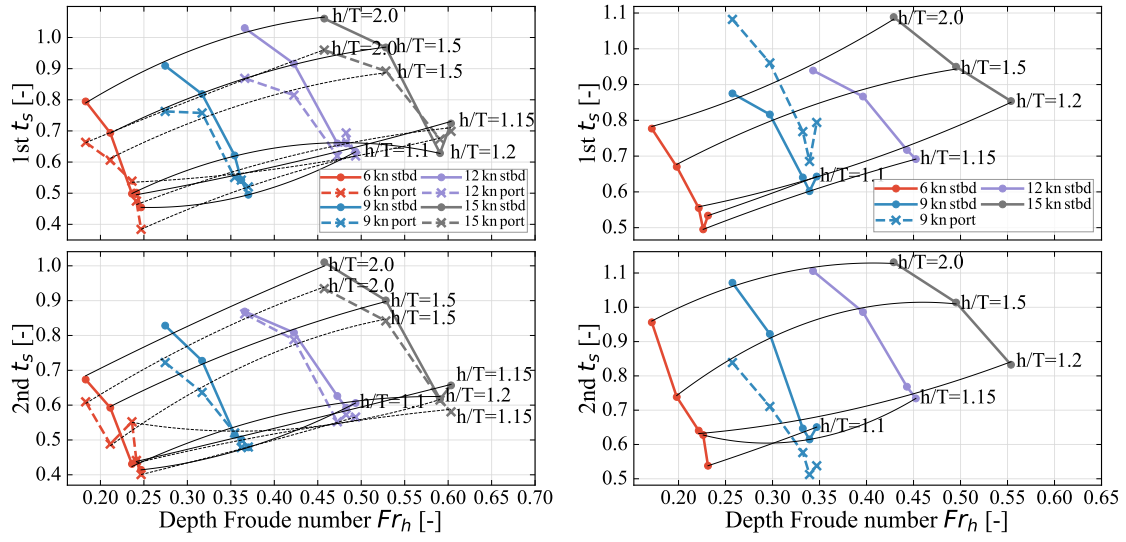
Overall, the trajectory-based analysis reveals that the speed predominantly affects y_{max}, causing it to increase, while the h/T ratio primarily affects x_{max}, which increases with decreasing h/T. Generally, y_{max} is decreasing with decreasing water depth. By contrast,

under extreme shallow-water conditions, especially at $h/T = 1.10$, the influence of speed extends to both parameters, leading to a trend reversal of increasing y_{max} values, particularly for higher velocities.



(a) DTC (b) JBC

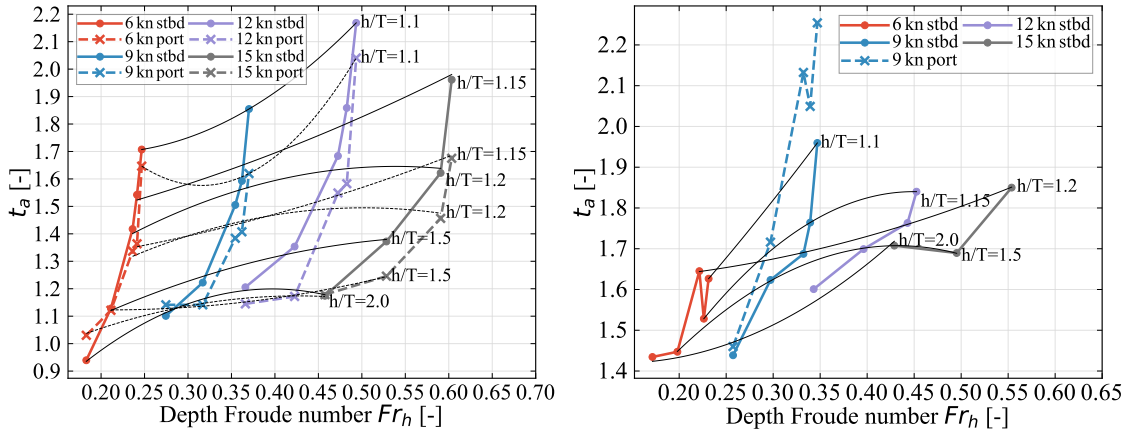
Figure 7.18.: First (positive) and second (negative) overshoot angles of the Z 35-20 manoeuvre at design condition



(a) DTC (b) JBC

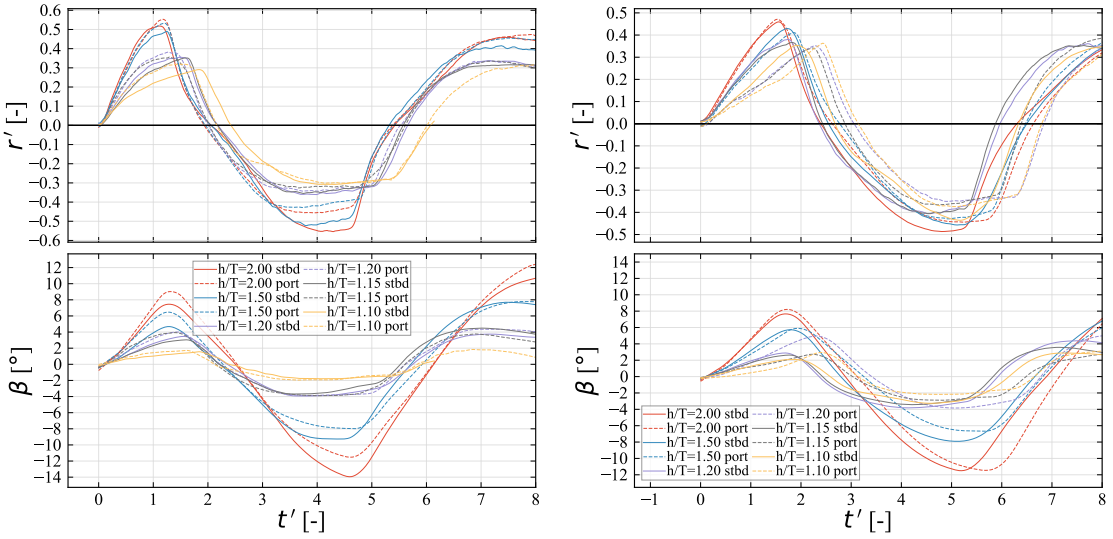
Figure 7.19.: Yaw-checking times for the 35-20 Zig-Zag manoeuvre at design condition

Considering all standard Zig-Zag parameters as a function of the under keel clearance (Figure 7.18 to Figure 7.20 and Figure B.1 to Figure B.3), it becomes apparent that the overshoot angles and yaw-checking times become smaller with decreasing water depth, but



(a) DTC (b) JBC

Figure 7.20.: Initial turning time for the 35-20 Zig-Zag manoeuvre at design condition



(a) DTC (b) JBC

Figure 7.21.: Yaw rate and drift angle of the 35-20 Zig-Zag manoeuvre with an initial speed of 9 kn at design condition. For comparison, the values for manoeuvres with an initial port rudder are multiplied by −1.

the initial turning times increase. This demonstrates that the ships become increasingly course stable and have an increased yaw-checking ability, but a decreased initial turning ability as water depth decreases. Course stability is the ability of a ship to maintain a given course with minimum effort and is strongly connected to the yaw-checking time (Nomoto, 1963). Yaw-checking ability refers to the ability of a ship to counteract a turning motion or to respond to counter-rudder while turning and is reflected by the overshoot angles. The initial turning or course-changing ability on the other hand, refers to the turning response of the ship to reach a desired change of course and can be quantified by the dimensionless initial turning time.

This observation can be illustrated using the ship's turning rate. Figure 7.21 shows the yaw rate of the first and second overshoot angle of the Zig-Zag 35-20 manoeuvre at a speed of 9 kn at design draught. It may be noted that the port values are multiplied by -1 for easier comparison of both directions. At zero, the manoeuvre begins to stbd/port, the

yaw rate builds up to a certain point, where the first opposite rudder is applied and the yaw rate drops to the other side. It can be observed that the turning rate builds up more slowly as the water becomes shallower. At $h/T = 1.10$, the yaw-rate gradient decreases by 50–70 % compared to $h/T = 2.00$. This is reflected in the increased initial turning time, see Figure 7.20 and Figure B.3. At the same time, the shallower the water, the less total turning rate is built up. For the DTC, the yaw rate at $h/T = 1.10$ is less than the half of that at $h/T = 2.00$ for both sides. For the JBC it is approximately 25 % lower. Therefore, the turning rate can also be reduced again more quickly by a course-stable vessel, as can be seen from the smaller overshoot angles and yaw-checking times, see Figure 7.18, Figure B.1, Figure 7.19 and Figure B.2, which includes all examined velocities and h/T ratios.

Port manoeuvre at first overshoot and stbd manoeuvre at the second overshoot exhibit the higher maximum yaw rates (Figure 7.21), revealing the stronger rudder effect of port deflection for the DTC. During the first yaw-checking phase, asymmetry intensifies as water depth decreases and the depth Froude number rises, further accentuating the asymmetric course-changing ability, see Figure 7.20a. For the JBC, by contrast, a trend reversal is evident with decreasing water depth: the yaw-rate gradient associated with the initial port rudder deflection decreases markedly more than that for the stbd side. This leads to higher yaw-rate gradients and thus improved course-changing ability for stbd manoeuvres, see Figure 7.20b and Figure 7.21b.

In general, the h/T ratios of 1.20 and 1.15 adopt similar progressions and maxima of the yaw rate, whereas the h/T ratio of 1.10 shows markedly lower values and a strongly delayed curve progression. This trend is observed for both investigated model ships. The shallow-water effect on asymmetric initial turning behaviour is pronounced, leading to an increase or even reversal of the initial asymmetry at decreasing water depths for the DTC and JBC, respectively.

The overshoot angles (Figure B.1) reveal another conspicuous feature. Three different sections can be identified in the graphs: The moderate shallow-water regime (h/T of 2.00 and 1.50) with relatively small changes of maximum 20 % for both ships, and the depth to draught ratio from $h/T = 1.20$ to 1.15, where the curve is also flat and the overshoot angles differ only slightly (maximum of approximately 20 % for the DTC and 10 % for the JBC) and the extreme shallow-water condition of 1.10 with maximum change of approximately 30 % for the DTC and 20 % for the JBC, compared to the h/T of 1.15. For the JBC however, the overshoot angles are even increasing again in most cases for this water depth, emphasising again the changed influence on the manoeuvring behaviour for the h/T ratio of 1.10. In terms of the shallow water effect, these three conditions – moderate shallow water (h/T from 2.00 to 1.50), the h/T ratio range from 1.20 to 1.15 and the extreme shallow water of $h/T = 1.10$ – are therefore particularly distinct and show decreases up to 50 % (for the transition from moderate shallow water to shallow water).

When the two model ships are compared, similar overshoot angles are evident in moderate shallow water, but the DTC shows a significantly stronger reduction when transitioning to shallow and extreme shallow water, attaining overshoot angles which are roughly half of those of the JBC at $h/T = 1.10$. Generally, the three identified shallow-water regimes become more clearly recognisable with increasing speed, indicating a distinctly non-linear

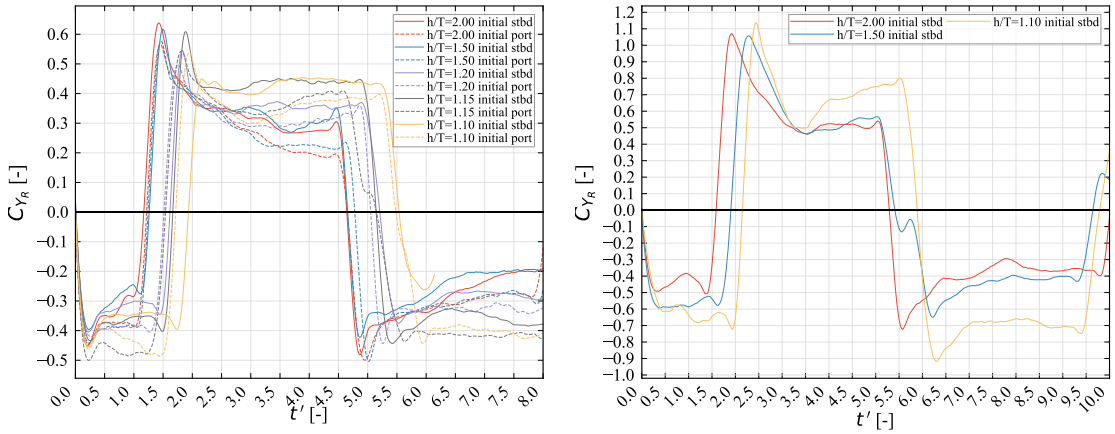
velocity effect in shallow water. For the DTC, it is also dependent on the rudder direction, showing a stronger decrease from moderate shallow water to shallow water (h/T from 1.50 to 1.20) for counter rudder to stbd. In shallow and extreme shallow-water, the difference between directions diminishes or even reverses The dependency on speed, illustrated by the regression lines in Figure 7.18, reveals an increasing trend at higher depth Froude numbers, with the slope generally decreasing for lower h/T ratios, but increasing again at $h/T = 1.10$.

The yaw-checking time for the first overshoot angle (Figure 7.19 and Figure B.2) shows a similar progression, with a strong decrease from moderate shallow water to shallow water for both model ships. Even though the initial stbd manoeuvres show smaller first overshoot angles in moderate shallow water, the yaw-checking time is higher in this region for the DTC. This changes again in the region of shallow and extreme shallow water from h/T ratios of 1.20 to 1.10, showing a trend reversal or similar values of yaw-checking time. The higher yaw-checking times coincide with the later zero crossings of the yaw rate after reaching the maximum, see Figure 7.21a. One reason for this apparent contradiction is the difference in drift angle between port and stbd manoeuvre. As shown in Figure 7.21a the drift angle for port side is approximately 25 % ($h/T = 2.00$) and 35 % ($h/T = 1.50$) higher than stbd side for first overshoot in moderate shallow water. This difference is getting smaller for h/T ratios of 1.20 (20 %) and 1.15 (5 %) and again slightly higher in extreme shallow water of 1.10 (25 %). Comparing the first overshoot angles of port and stbd direction, the size ratios show a similar progression. This indicates that the overshoot angles are strongly influenced by the drift angles. A further indication for this statement is provided by the comparison of the trajectories, which shows that the stbd transverse offset for the first maxima is always (up to 20 %) higher than port side even though the initial slopes of the curves are similar. For the JBC, the yaw-checking time for port side is always higher than for stbd side, showing a better yaw-checking capability for port counter rudder. In contrast to the overshoot angles, yaw-checking times exhibit negligible changes in sensitivity to depth Froude number with decreasing h/T.

Overall, the overshoot angles and yaw-checking times demonstrate a similar dependence on water depth, revealing three different regions to consider in particular (moderate shallow water, h/T of 1.20 and 1.15, and $h/T = 1.10$), especially for the DTC, which become increasingly distinguishable at higher speeds. Unlike the overshoot angles, the yaw-checking times exhibit little change in speed sensitivity with decreasing h/T. The trend reversal of both parameters at $h/T = 1.10$ for the JBC is remarkable. The directional dependence of both parameters for the DTC is decreasing with reduced water depth. The overshoot angles are noticeably affected by the drift angles.

Despite higher drift angles, the rudder transverse force for port deflection stays higher than stbd deflection for all h/T ratios, shown in Figure 7.22a. For better comparison of both directions, the port rudder transverse forces are multiplied by -1. The maxima of both directions are similar, but the rudder transverse force decreases faster for stbd deflection. For the first rudder angle, the maxima and further progression is higher for lower h/T ratios, with the highest values at h/T of 1.15 for the DTC.

For the JBC, again, only for a few manoeuvres to stbd valid rudder data were avail-



(a) DTC (b) JBC

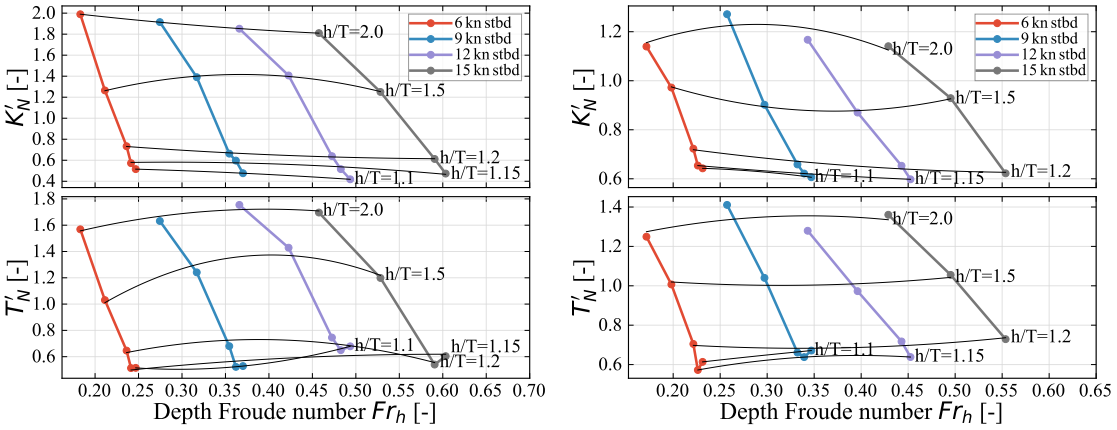
Figure 7.22.: Rudder transverse force for the 35-20 Zig-Zag manoeuvre with an initial speed of 9 kn at design condition. For comparison, the values for manoeuvres with an initial port rudder are multiplied by −1.

able, see Figure 7.22b. However, for the first maxima it shows the same progression in dependence on the water depth as the DTC. For the DTC, at the first counter rudder, the maximum is highest for higher h/T ratios, probably due to the significantly higher drift angles prior to the counter rudder in moderate shallow water, leading to higher effective rudder angles. For the JBC on the other hand, the maximum in extreme shallow water is highest again, as probably the higher propeller loading and therefore higher rudder inflow in the propeller stream is dominating in this case. In addition, the further progression, again, is higher in extreme shallow-water conditions for both ships. One reason for this is the higher drift angle to the opposite side, resulting in lower rudder inflow angle in moderate shallow water. The rudder transverse force coefficients show a time delay with decreasing h/T ratios, showing, despite lower overshoot angles and transverse offsets, the increasing execution time for the Zig-Zag manoeuvre.

The non-dimensionalised initial turning time (Figure 7.20 and Figure B.3) increases significantly with decreasing h/T ratio, especially when transitioning from 1.15 to 1.10 for both ships. The speed dependency illustrated by the regression lines for decreasing water depth does not exhibit a clear monotonic trend, owing to scatter between individual curves, which partly arise from the uneven distribution of test velocities across the h/T ratios. This ambiguity is more evident for the JBC, whereas the DTC nonetheless suggests an overall tendency toward increasing slope with decreasing UKC.

The increase in initial turning time for the transition from h/T ratio of 1.15 to 1.10 is significant for both ships, especially for the JBC as the increase follows up an only small change in the transition from 1.20 to 1.15, displaying the highest gradient in the curve progression for $h/T = 1.10$. Generally, the influence of velocity becomes increasingly pronounced as water depth decreases.

Other parameters for assessing manoeuvrability are the Nomoto indices, which are based on a first order differential equation, focusing on the yaw motion only. They can be determined from results of Zig-Zag manoeuvres, see section 4.2. The non-dimensionalised



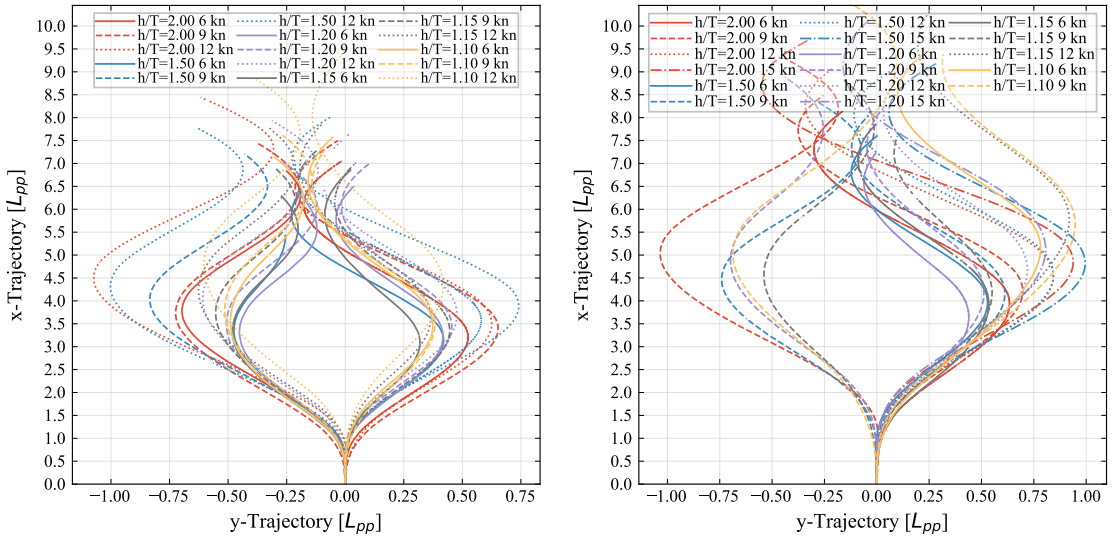
(a) DTC (b) JBC

Figure 7.23.: Nomoto coefficients K'_N and T'_N for the 35-20 Zig-Zag manoeuvre at design condition

Nomoto coefficients, calculated for the range of first two overshoot angles, are shown in Figure 7.23 and Figure B.4. Higher K'_N-values correspond to higher yaw rates, hence for better turning behaviour. Lower T'_N-values in contrast, correspond to faster responsiveness to the rudder, hence a higher course stability. Nomoto (1963) pointed out that these indices enables a more differentiated quantification of manoeuvring behaviour as the overshoot angle, which is nearly proportional to $K_N T_N$ at fixed rudder angle. Hence, for a measured overshoot angle, it can not be distinguished whether it is achieved by large K'_N and small T'_N or vice versa. One of the reasons for this is, that lower turning ability necessarily leads to lower rotational rate at target angle which in turn can be reduced more easily with counter rudder. As the h/T ratio decreases, both Nomoto parameters are steadily falling, which implies a decreasing turning behaviour and an increasing course stability for both model ships in shallow water. Overall, higher velocities show poorer manoeuvrability (higher T'_N-values and lower K'_N-values), particularly in extreme shallow-water conditions, while the lowest velocity of 6 kn reveals the highest manoeuvring ability.

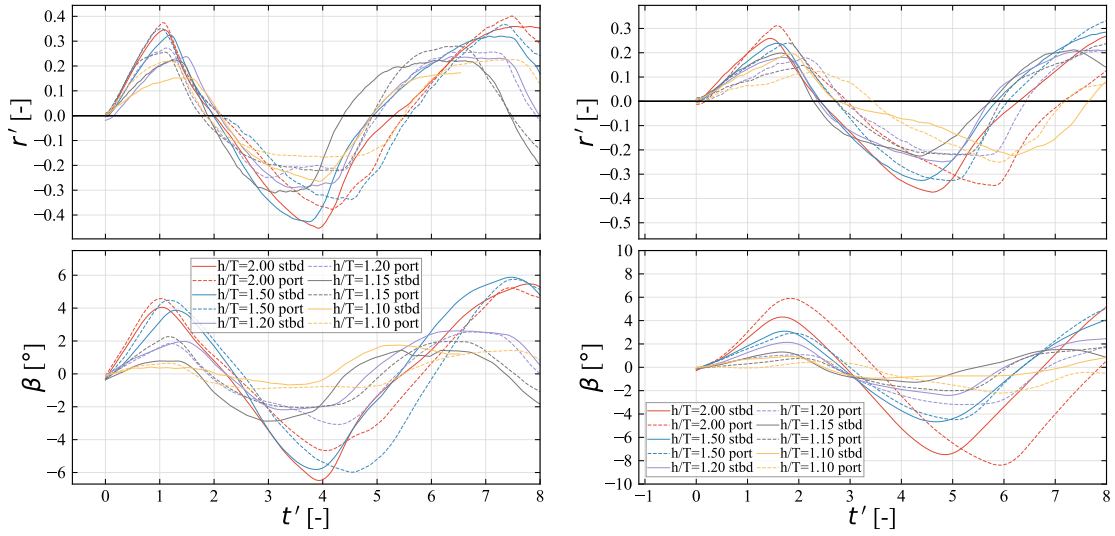
In the transition from h/T ratio of 1.15 to 1.10, the K'_N still decreases significantly for the DTC and slightly for the JBC, meaning still decreasing turning ability, whereas the T'_N is remaining on the same level or is mostly even increasing again, meaning no improvement or even deterioration of course-keeping ability in this range of extreme shallow water, see Figure B.4. Only for 15 kn for the DTC this increase is already observable for the transition to $h/T = 1.15$. Hence, for the Zig-Zag 35-20 of the DTC the steep decrease of overshoot angles within extreme shallow-water regime is not associated with a higher yaw-checking ability but can be explained by a decrease in K'_N and a rather constant progression of T'_N. This observation reinforces the presence of a pronounced transition between h/T of 1.15 to 1.10, revealing a trend reversal from improving to deteriorating course-keeping ability, accompanied by a continued degradation of turning ability.

Another Zig-Zag manoeuvre was performed for 10° heading change with 20° rudder deflection angle. Overall, the trajectory of the Zig-Zag 20-10 manoeuvre (Figure 7.24)



(a) DTC (b) JBC

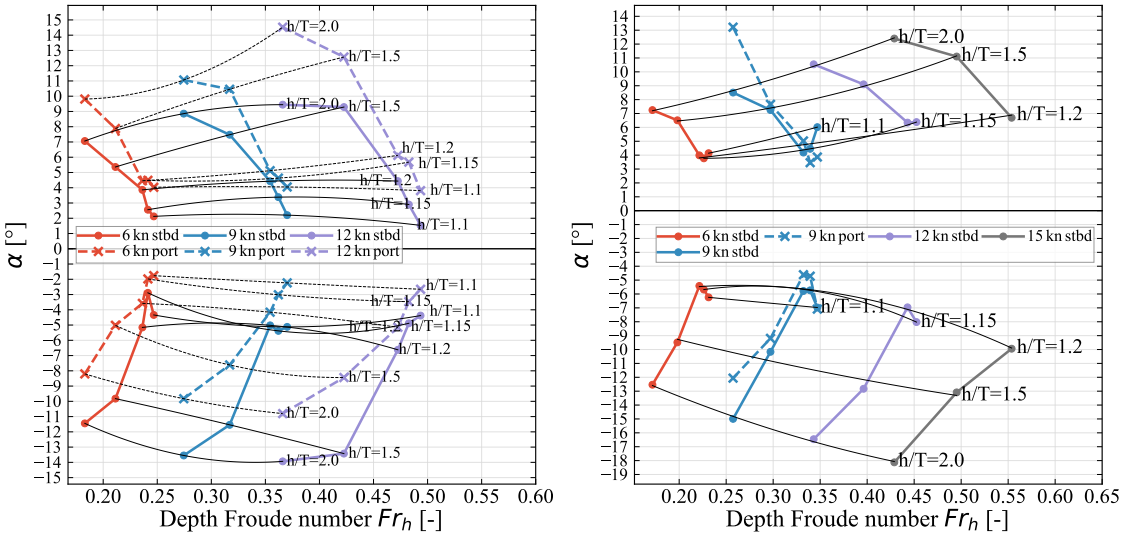
Figure 7.24.: Trajectories of the Z 20-10 manoeuvre for different initial speeds at design conditions



(a) DTC (b) JBC

Figure 7.25.: Yaw rate and drift angle of the 20-10 Zig-Zag manoeuvre with an initial speed of 9 kn at design condition. For comparison, the values for manoeuvres with an initial port rudder are multiplied by −1.

show smaller transverse offsets y_{max} than the 35-20 manoeuvre. However, the 20° rudder angle shows a significant different yaw-checking capability of port and stbd deflection, which is noticeable in a strong asymmetry of the path, especially for the DTC. Immediately after the start of the manoeuvre, the DTC is turning faster to port side, recognizable by the slope of the trajectory and the curve progression of the yaw rate, see Figure 7.25. The first counter rudder to stbd then results in a significantly larger y-offset motion to port than port counter rudder on the stbd side, shifting the trajectory on the port side in both the y- and x-direction. For the Z 35-20 manoeuvre in contrast, the initial slope of the trajectory for both sides are similar, resulting in a generally higher y_{max} to stbd side. The asymmetry for Z 20-10 trajectory is generally stronger for higher h/T ratios and



(a) DTC (b) JBC

Figure 7.26.: First (positive) and second (negative) overshoot angles of the Z 20-10 manoeuvre at design condition

speeds. For the JBC, the asymmetry of both sides can only be investigated for 9 knots, as this speed was conducted for the port side only. The asymmetric trajectory is dependent on the water depth here. While for an h/T ratio of 2.00 the trajectory of the stbd side shows approximately 20 % higher x_{max} and approximately 50 % higher y_{max} for the first maximum, it shifts to the port side for an h/T ratio of 1.10, showing approximately 10 % higher x_{max} and approximately 30 % higher y_{max} at the port side compared to stbd for the first maximum. As the JBC has a symmetric rudder this asymmetric behaviour has to be only influenced by changed propeller-rudder interaction during the manoeuvre with decreasing water depth.

As with the Z 35-20 manoeuvre, y_{max} is generally increasing with higher h/T ratios and speeds. For the DTC, the 15 knots manoeuvre was executed at an h/T ratio of 1.15 only, showing a similar track as the 12 knots manoeuvre at h/T ratio of 1.10 with high x_{max} and y_{max} values. For the JBC, this similar track is also the case comparing h/T of 1.15 at 12 knots with h/T of 1.10 at 9 knots, as well as h/T of 1.20 at 15 knots with h/T of 1.10 at 6 knots, highlighting again the significant decrease in manoeuvrability at h/T ratio of 1.10.

Considering the y_{max} in the transition from moderate shallow to shallow water, it shows for all cases an initial decrease. In dependence on the direction and speed it then decreases further in the transition to h/T ratio of 1.15, or already increase again. For the transition to h/T ratio of 1.10 it increases in all cases, revealing a trend reversal of required lateral space to perform the manoeuvre in extreme shallow-water regime.

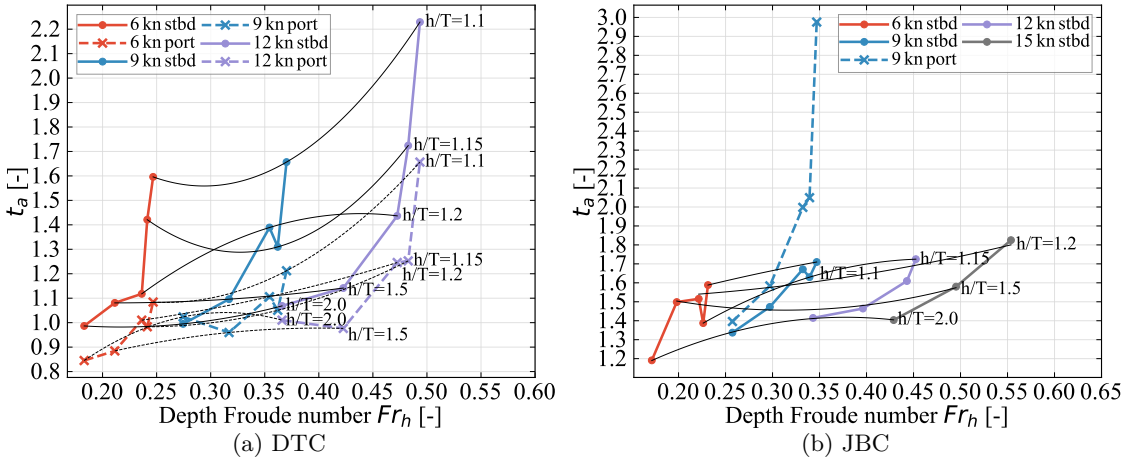
Overall, the trajectory analysis confirmed the observed trend of increasing y_{max} for the Z 35-20 manoeuvre with increasing water depth and speed, with pronounced effect of speed in extreme shallow water. Nevertheless, the Z 20-10 manoeuvre demonstrates a higher asymmetry, which is reduced for decreasing water depth and even leads to a trend reversal for the JBC, revealing a stronger shallow-water effect on asymmetric manoeuvring behaviour for 20° rudder angle compared to 35°. The h/T ratio of 1.10 is pronounced,

by showing particularly high x_{max} values even for low velocities and a trend reversal of required lateral space.

Figure B.6 present the overshoot angles of the Zig-Zag 20-10 manoeuvre as a function of the h/T ratios for all examined velocities. Similar to the Zig-Zag 35-20 manoeuvre, moderate shallow water (h/T of 2.00 to 1.50) represents a distinctive region compared to shallow and extreme shallow water (h/T ratio of 1.20 to 1.10), showing significantly higher overshoot angles and a relatively constant progression between h/T of 2.00 and 1.50, especially for higher velocities for the DTC. In contrast to Zig-Zag 35-20 manoeuvre, the first overshoot angles of the DTC show, for most of the cases, a rather constant decrease in the range of $h/T = 1.20$ downwards. The second overshoot angles in the transition from 1.15 to 1.10 are rather stagnant. The Overshoot angles for the JBC in contrast, show, similar to the Zig-Zag 35-20 manoeuvre, a trend reversal in the transition from 1.15 to 1.10, leading to increasing overshoot angles in this region.

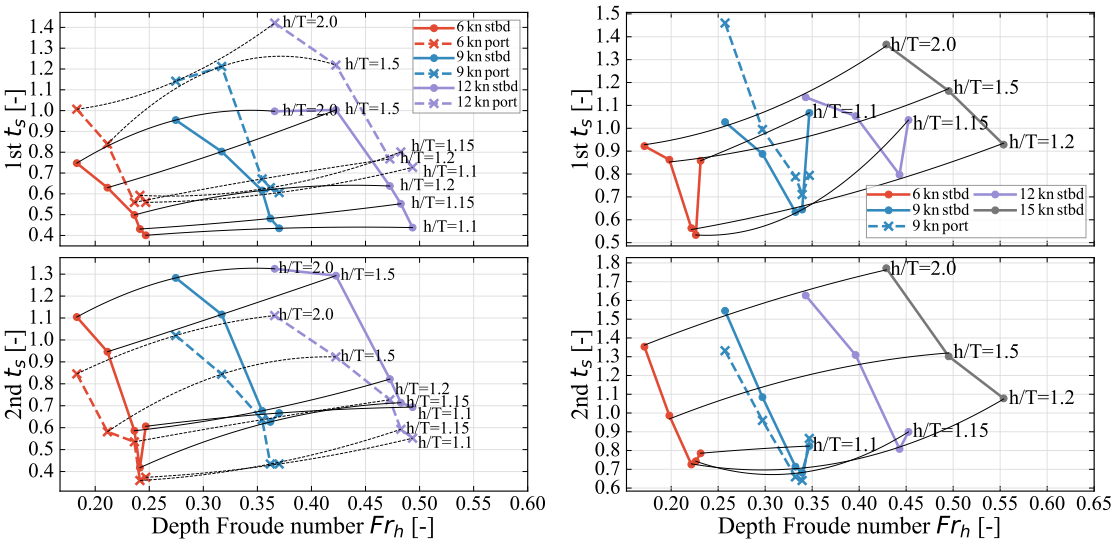
Generally, higher velocities again lead to larger overshoot angles, with this effect diminishing as water depth decreases, as illustrated by the reducing slopes of the regression lines in Figure 7.26. For the DTC however, compared to the Z 35-20 manoeuvre, the curve progressions appear to be governed more by the initial direction, indicating a stronger directional dependence of the rudder deflection on the manoeuvre. For constant velocities, yaw-checking capacity of 20° port rudder is significantly stronger than stbd rudder with diminishing effect for decreasing water depth. Conversely, in extreme shallow water, the JBC shows a trend reversal, leading to higher overshoot angles for counter rudder to port, which is also reflected in the higher y_{max} of the trajectory for this case.

The curve progression of the initial turning time of the Z 20-10 manoeuvre (Figure 7.27 and Figure B.5) looks similar to that of the Z 35-20 manoeuvre. Generally, higher velocities leads to higher non-dimensionalised initial turning times, with increasing tendency in extreme shallow water conditions, especially for the DTC. Both model ships show only little change or even decrease in the transition from h/T of 1.20 to 1.15 but the highest gradient when transitioning to $h/T = 1.10$. The disparity between port and stbd increases with decreasing water depth, reinforcing the asymmetric course-changing ability.



(a) DTC (b) JBC

Figure 7.27.: Initial turning time for the 20-10 Zig-Zag manoeuvre at design condition



(a) DTC (b) JBC

Figure 7.28.: Yaw-checking times for the 20-10 Zig-Zag manoeuvre at design condition

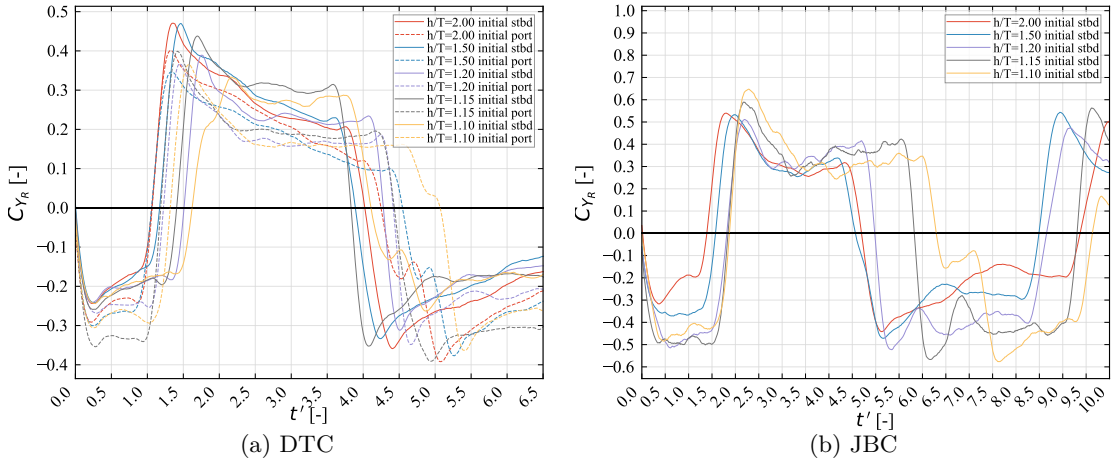
The yaw-checking time for the first overshoot angle (Figure 7.28 and Figure B.7) in contrast, is generally decreasing as water depth reduces due to lower built-up yaw rate in shallower water, which can therefore also be diminished more quickly, see Figure 7.25. In contrast to the Z 35-20 manoeuvre, the manoeuvres of the DTC with counter rudder to stbd show for constant speeds over all h/T ratios significantly higher yaw-checking times than port counter rudder, which matches quiet well with the higher first overshoot angles for initial port direction. Furthermore, the overshoot angles are considerably less affected by the drift angle (see Figure 7.25), which attains significantly smaller values compared to Z 35-20 manoeuvre. For the JBC, there are also higher yaw-checking times for counter rudder to stbd, at least until extreme shallow-water conditions, showing a trend reversal here, which agrees also well with the progression of the overshoot angles.

In general, the Z 20-10 manoeuvre demonstrates the same distinct regions for overshoot and yaw-checking times as Z 35-20 but less pronounced in extreme shallow water regime, particularly for the DTC. The JBC shows the same trend reversal of increasing overshoot angles and yaw-checking time in the transition to $h/T = 1.10$. The parameters show higher dependence on direction. Port counter rudder reveals greater yaw-checking capacity across all h/T ratios. Only for the JBC, there is a trend reversal in extreme shallow water, matching the trend reversal for the trajectory here. This transition to $h/T = 1.10$ is again emphasised by the steepest increase in initial turning time and the largest directional disparity.

The curve progressions of yaw rate (Figure 7.25) for the first overshoot angle confirms the strong influence of the direction with decreasing h/T ratio. For the DTC at h/T of 2.00, the stbd direction shows a similar slope and maximum of the curve as port direction. This difference increases significantly with decreasing h/T ratios, which reveals a strong direction-dependency on the shallow-water influence on the initial course-changing ability with 20° rudder angle. For the JBC, this relation of directional dependence on water depth is more pronounced, showing even a trend reversal from higher maxima (approximately

20 %) of initial port direction at h/T of 2.00, equalizing at h/T of 1.50 and shifting to an even considerably lower maximum of approximately 35 % at h/T of 1.10.

The curve progression of the rudder transverse force of the Z 20-10 manoeuvre (Figure 7.29) is similar to the Z 35-20 manoeuvre, with about 30–70 % lower transverse forces. Again, the h/T ratio of 1.15 shows the highest rudder transverse forces for the first overshoot for both ships. Rudder deflection to port causes constantly higher values than rudder deflection to stbd for the DTC.



(a) DTC (b) JBC

Figure 7.29.: Rudder transverse force for the 20-10 Zig-Zag manoeuvre with an initial speed of 9 kn at design condition. For comparison, the values for manoeuvres with an initial port rudder are multiplied by −1.

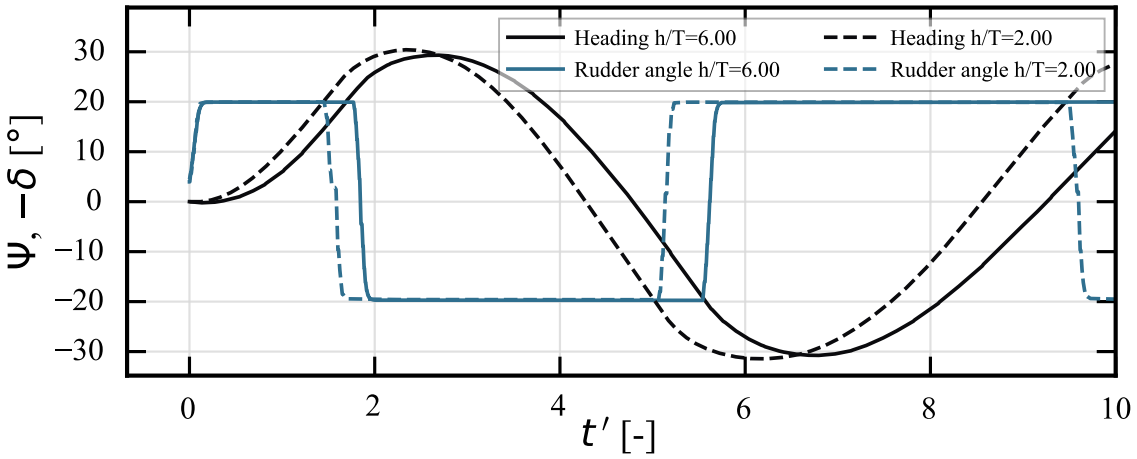


Figure 7.30.: Heading and rudder angle for the 20-20 Zig-Zag manoeuvre with an initial speed of 6 kn in deep and moderate shallow water for the DTC at design condition

As already mentioned, for the DTC, there were also Zig-Zag manoeuvres performed in deep-water conditions in order to analyse the influence of moderate shallow water separately. Figure 7.30 shows the curve progressions of heading and rudder angle for the first two overshoot angles. As shown above, the overshoot angles and yaw-checking times constantly decreases and initial turning time increases continuously for declining shallow-water conditions. However, when it comes to the transition from deep to moderate shallow

water, it is initially the other way around. The first overshoot angle increases by 12 %, the yaw-checking time by 20 %, and the initial turning time decreases by 18 %.

Thus, in the transition from deep water to moderate shallow water, the DTC demonstrates increased initial turning ability and less yaw-checking ability, which presumably results in higher yaw instability. The reason for the changed initial turning behaviour was already described and explained in subsection 7.1.1, based on the results of CFD simulations. The further progression of the Zig-Zag manoeuvre for the DTC shall now be investigated in a similar manner.

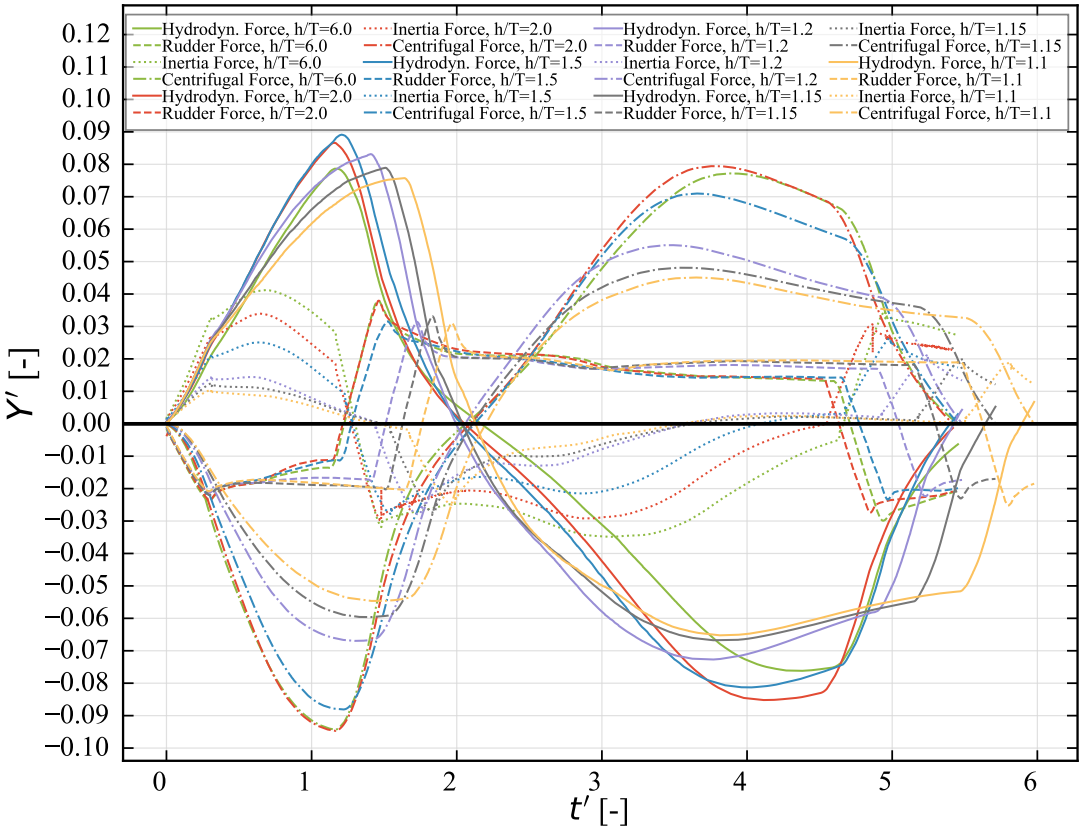


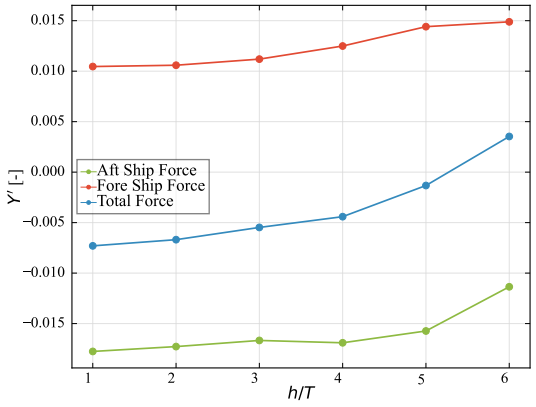
Figure 7.31.: Force components acting on the DTC during a 35-20 Zig-Zag manoeuvre with an initial speed of 9 kn at design condition, nondimensionalised according to Equation 4.4

The dependence of the manoeuvring behaviour on water depth is further investigated through an analysis of the hydrodynamic forces and moments acting on the DTC during the 35–20 Zig-Zag manoeuvre, based on CFD simulation results. The transverse force components as a function of time for the first two overshoot angles are shown in Figure 7.31. Following the initial rudder setting at $t' = 0$, the total hydrodynamic forces exhibit similar initial slopes across all investigated h/T ratios, resulting however in substantially reduced accelerations and centrifugal forces for decreasing water depths due to higher damping. At lower water depths, the surge velocity is less reduced as a result of smaller drift angles. Consequently, the decrease in yaw rate dominates the centrifu-

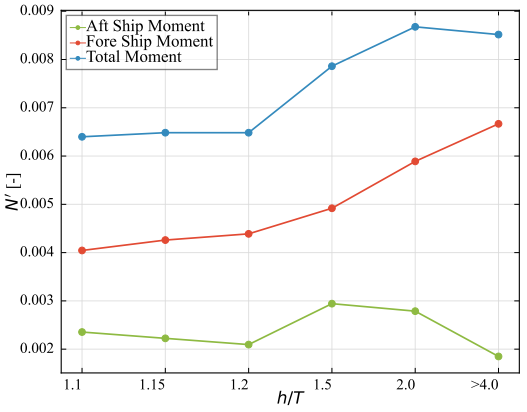
gal force ($m \cdot u \cdot r$) (see Equation 4.2) for most shallow-water cases. Only the moderate shallow-water condition ($h/T = 2.00$) shows marginally higher centrifugal forces for the majority of the manoeuvre when compared to deep water. Both moderate shallow-water conditions show significantly higher hydrodynamic transverse forces than in deep water, reaching their maxima at similar times. Shallow-water and extreme shallow-water conditions show significantly delayed maxima. The maximum hydrodynamic forces at h/T ratios of 1.20 and 1.15 are still slightly higher than in deep-water conditions, while in extreme shallow water of $h/T = 1.10$ it is even lower. This is mainly due to the strongly decreased transverse force at the fore ship (see Figure 7.32c) as a result of the increased negative transverse force at the bow section, see the transverse force distribution along the ship length at position of first counter rudder in Figure 7.33c. While in deep and moderate shallow water the acceleration is still significant at first counter rudder, which can also be seen in the high slope of hydrodynamic forces, it is close to zero for h/T ratios of 1.20 and 1.15 and even negative for 1.10, resulting in stagnating hydrodynamic forces before counter rudder. For the second overshoot angles, this conditions is reached even sooner and can be observed for all shallow-water conditions.

Considering the total forces at fore, aft and whole ship at the onset of the first counter rudder (Figure 7.33c), the force distribution is as expected similar to those of the 35° turning circle at 15° heading change (see Figure 7.14b). The total hydrodynamic transverse force and yaw moment initially increase in moderate shallow water, but significantly and steadily decrease in shallow- and extreme shallow-water conditions, showing the minimum transverse force and yaw moment at h/T of 1.10, mainly due to the negative peak at the bow of the model ship, see Figure 7.32c and Figure 7.33c. The increase in pressure at the bow for decreasing water depth is primarily caused by the enlarged positive pressure area at the stbd side and the shifting of the stagnation point to stbd due to the increased yaw to drift ratio at the fore ship, see top of Figure 7.34.

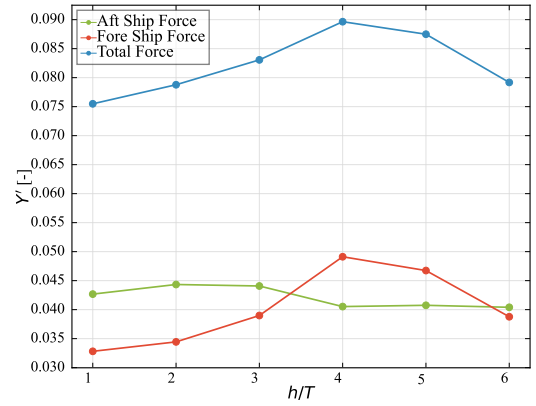
At the instant of the first overshoot however, the total yaw moment is decreasing significantly in the transition from moderate shallow to shallow water, but stagnates for a further decrease in water depth as the yaw moment at the aft ship increases to a similar amount as it decreases at the fore ship, see Figure 7.32b. While the total transverse forces at this stage of the Zig-Zag manoeuvre are greatly reduced and only about 5 % of those at first counter rudder setting (Figure 7.32a), the absolute hydrodynamic yaw moment still assumes values of 60–70 % of those at the onset of first counter rudder (Figure 7.32b). This is due to the significantly changed pressure distribution along the hull, which can be seen in the third row of Figure 7.34. For the midship section, the pressure distribution increasingly looks point-symmetrical with respect to the main frame with decreasing water depth. Compared to the transverse force distribution at the time of the first counter rudder, the absolute values of the extrema as a function of h/T are twisted, see Figure 7.33a. In deeper water, there is now a strong peak at the bow with a twisted sign and only a minimal peak at the stern. In the bow area, the forces acting against (counter-)turning are now significantly stronger in deeper water as the drift motion is considerably more pronounced, shifting the stagnation point at the bow to the port side, see third row of



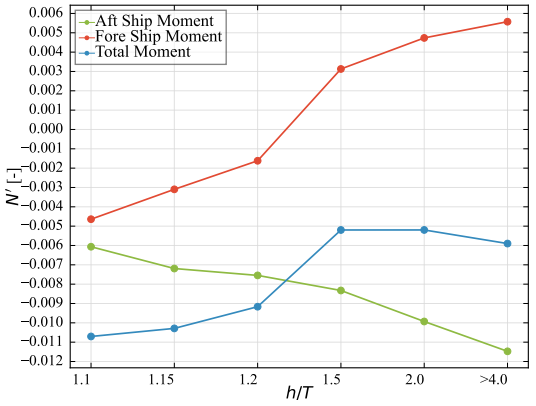
(a) Summed hydrodynamic forces at first overshoot



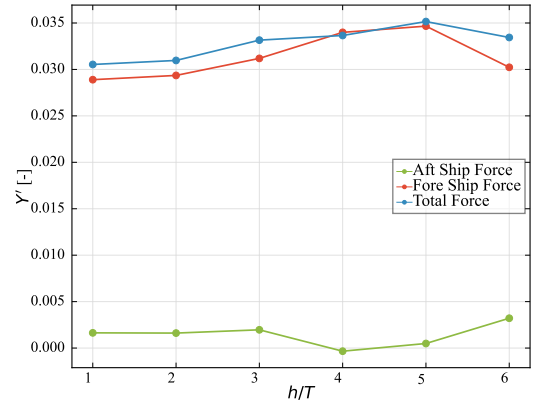
(b) Summed hydrodynamic moments at first overshoot



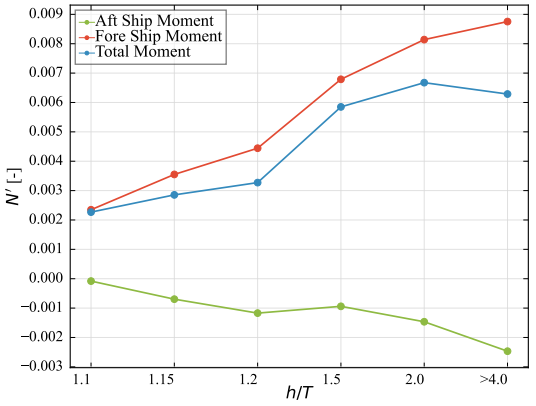
(c) Summed hydrodynamic forces at first counter rudder



(d) Summed hydrodynamic moments at first counter rudder

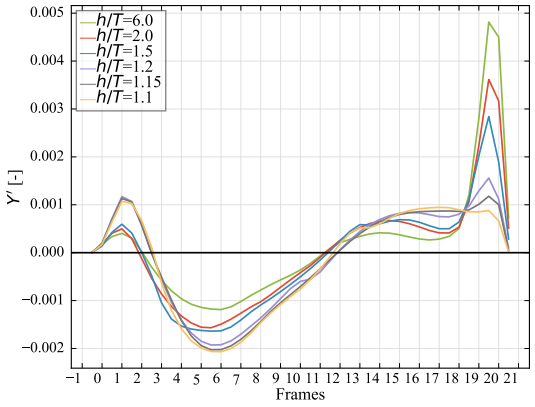


(e) Summed average hydrodynamic forces between first counter rudder and first overshoot

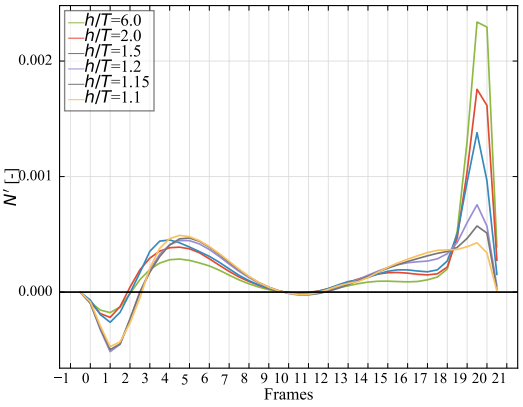


(f) Summed average hydrodynamic moments between first counter rudder and first overshoot

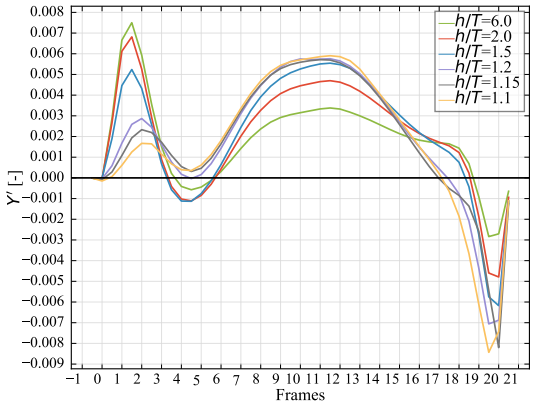
Figure 7.32.: Summed hydrodynamic forces and moments on the fore ship, aft ship, and entire hull of the DTC for the Z 35-20 manoeuvre with an initial speed of 9 kn



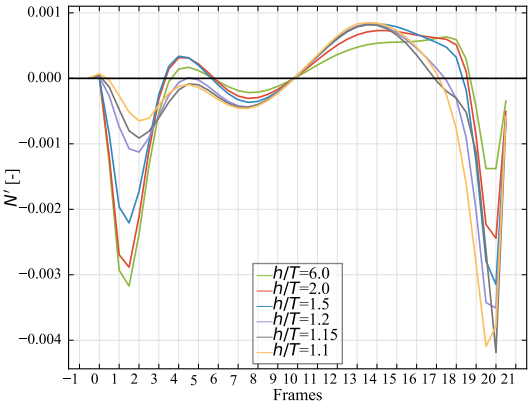
(a) Hydrodynamic forces at first overshoot



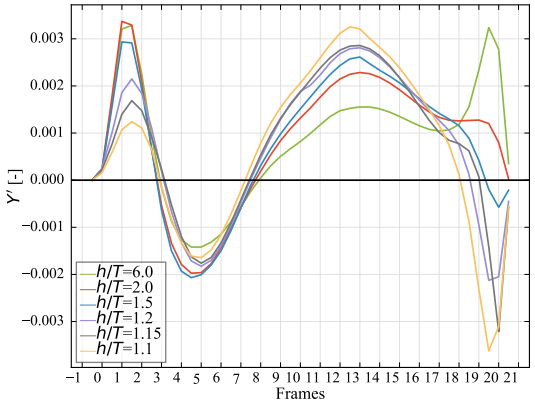
(b) Hydrodynamic moments at first overshoot



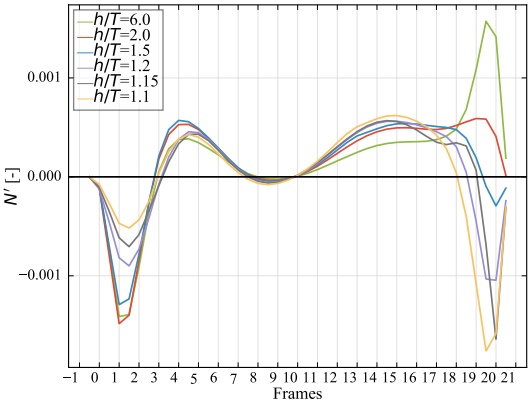
(c) Hydrodynamic forces at first counter rudder



(d) Hydrodynamic moments at first counter rudder



(e) Average hydrodynamic forces between first counter rudder and first overshoot



(f) Average hydrodynamic moments between first counter rudder and first overshoot

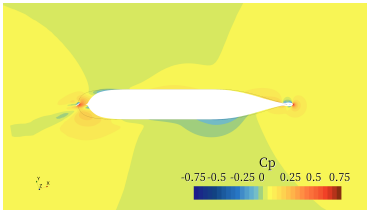
Figure 7.33.: Hydrodynamic forces and moments acting on the DTC as a function of ship's frames for the Z 35-20 manoeuvre with an initial speed of 9 kn

Figure 7.34. While in deep and moderate shallow water, the hydrodynamic damping yaw moment is mainly due to the strong peak at the bow, this peak considerably decreases as the water depth reduces, becoming a plateau at h/T ratio of 1.10 (Figure 7.33b), as the hydrodynamic transverse force shows a slightly decreasing progression for the fore ship (Figure 7.33a) due to the central stagnation point in extreme shallow water, see third row of Figure 7.34. While the peak magnitudes in the stern region are negligible, the aft midship area behind the main frame experiences the greatest damping forces under shallow-water and extreme shallow-water conditions. This is also reflected in the yaw moment. The total yaw moment acting against the yaw-checking behaviour (positive values) is significantly reduced in shallow water and extreme shallow water (Figure 7.32b and Figure 7.33b). Here, the areas that cause counter-moments are particularly closer to the midship area, where it is significantly reduced in deep-water conditions. Conversely, in moderate shallow water, these areas are also already significantly increased, particularly in the rear midship area, while the bow peak remains pronounced.

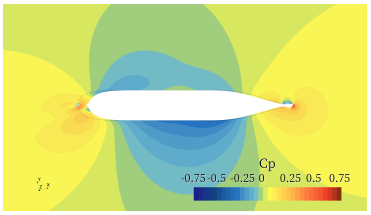
Finally, this ensures that the damping moment in the stern area in moderate shallow water initially increases significantly, and more than it decreases in the fore ship area (see Figure 7.32b), so that the total moment in the transition from deep water to moderate shallow water increases overall. Consequently, the DTC exhibits greater overshoot angles (approximately 10 %), increased yaw-checking times (approximately 5 %), and increased T'_N (approximately 20 %) and K'_N (approximately 18 %) at an h/T ratio of 2.00 compared to deep-water conditions, similar to the described Zig-Zag 20-20 model experiment.

This initial increase can also be seen for the average total yaw moment for the same transition, see Figure 7.32f. The time averaged values represent the mean hydrodynamic forces and moments acting on the ship during the yaw-checking phase of the Zig-Zag manoeuvre, from the onset of the first counter rudder until the overshoot angle is reached. Hence, the transverse force and yaw-moment distributions along the ship frames, shown in Figure 7.33e and Figure 7.33f, do not correspond to instantaneous values but rather illustrate the average hydrodynamic effects during this phase. The actual pressure distributions of the mid of the yaw-checking phase for three different water depths are shown in row 2 of Figure 7.34. The average hydrodynamic transverse forces for the yaw-checking phase (Figure 7.32e) show only little dependence on the water depth, only changing by a maximum of approximately 12 % for the total force. The transverse force at the aft body is small due to the increased negative pressure at the mid aft section of the ship, seen in row 2 of Figure 7.34. Conversely, the distribution of the transverse forces is significantly different in dependence on the water depth, which can already be seen by the significantly reduced average yaw moment (Figure 7.32f), counteracting the turning motion in this phase, with a maximum decrease of approximately 75 %. The mean yaw moment at the aft ship decreases as the water depth is reduced, eventually approaching zero for $h/T = 1.10$.

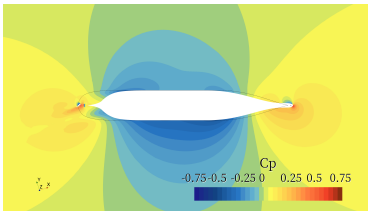
Figure 7.33e provides a more detailed picture of the average transverse force distribution during the yaw-checking phase. The force distribution is generally similar to that at the onset of the first counter rudder, particularly the forward midship section and the aft peak, but with lower absolute values. However, distinct regions of the distribution differ



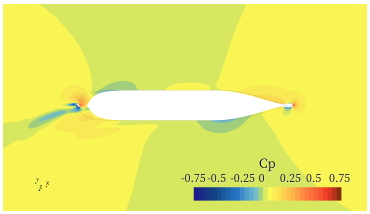
Deep water, start of yaw-checking phase (first counter rudder)



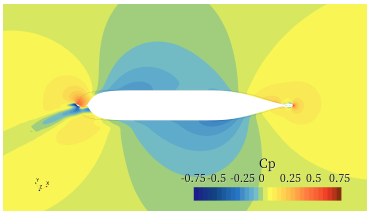
$h/T = 1.50$, Start of yaw-checking phase (first counter rudder)



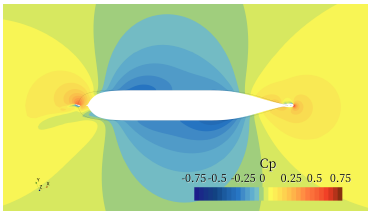
$h/T = 1.10$, start of yaw-checking phase (first counter rudder)



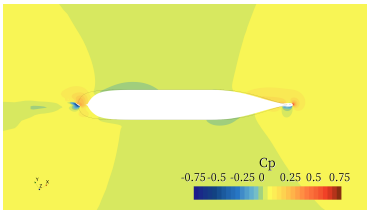
Deep water, mid of yaw-checking phase



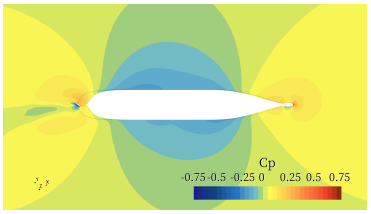
$h/T = 1.50$, mid of yaw-checking phase



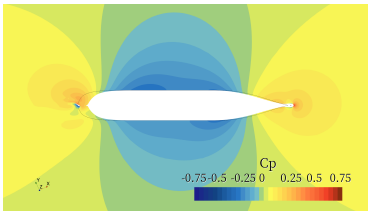
$h/T = 1.10$, mid of yaw-checking phase



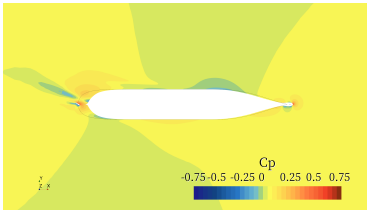
Deep water, end of yaw-checking phase (overshoot position)



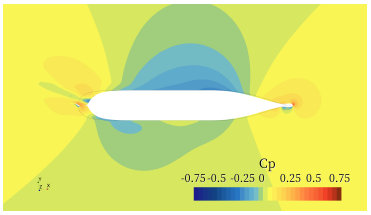
$h/T = 1.50$, end of yaw-checking phase (overshoot position)



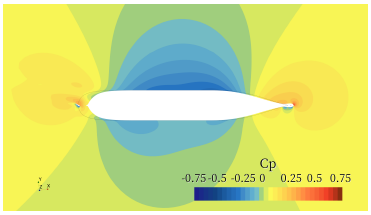
$h/T = 1.10$, end of yaw-checking phase (overshoot position)



Deep water, maximum yaw rate to port



$h/T = 1.50$, maximum yaw rate to port



$h/T = 1.10$, maximum yaw rate to port

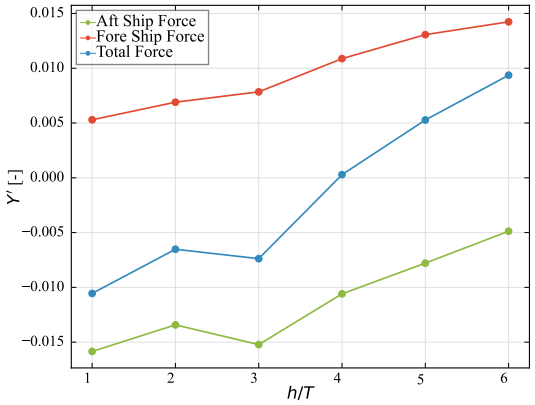
Figure 7.34.: Top view of hydrodynamic pressure distribution at 2.5 m below water line (full scale), shown in terms of the pressure coefficient C_P with the initial straight-ahead speed (9 kn) as reference speed, for deep water (left), $h/T = 1.50$ (mid) and $h/T = 1.10$ (right) for the positions of first counter rudder, mid of first yaw-checking phase, first overshoot and maximum yaw rate to the opposite direction (from top to bottom) for the DTC

considerably. This is, on the one hand, the significantly increased negative transverse force at the aft shoulder for all h/T ratios, which opposes the counter-turning motion, and on the other hand, the diminishing peak at the bow for $h/T = 2.00$ and twisted peak for deep-water condition, which, on average, generates a positive yaw moment opposing the counter-turning motion.

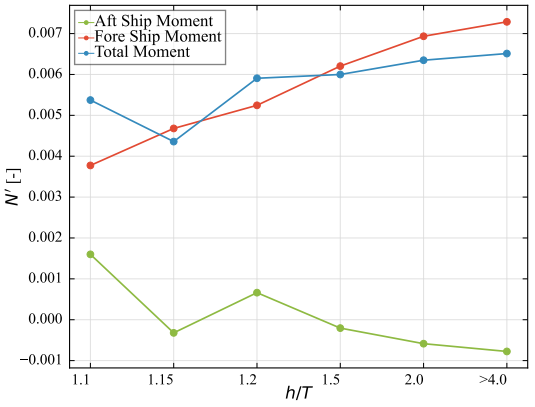
In shallow and extreme shallow water, the negative pressure peak at the fore ship, which supports the counter-turning motion, dominates this phase on average. This effect ultimately causes the significantly reduced average damping yaw moment observed in Figure 7.32f. In addition to the lower built-up yaw rate at smaller h/T ratios, this reduction is another reason for the reduced overshoot angles of the DTC in shallow water.

Following the same approach as for the DTC, the 35-20 Zig-Zag stbd manoeuvre of the JBC is examined. For the JBC, the decreased yaw-checking and course-keeping ability in the transition from h/T of 1.15 to 1.10 is notable, resulting in increased overshoot angles, yaw-checking times and T'_N values, and is examined in more detail using CFD simulation results. Furthermore, the increased yaw rate in extreme shallow-water condition, observed for the turning circle (Figure 7.8b) is investigated. As shown in subsection 6.2.2, both trend reversals within extreme shallow-water conditions are captured by CFD calculations.

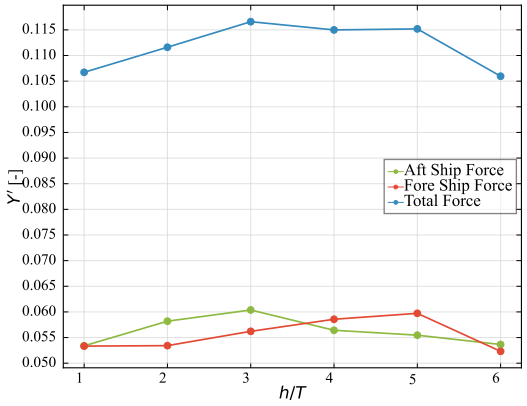
The reason for the increased built-up yaw rate, has to be found in the transient phase of the turning circle, when accelerations are still present. To illustrate the description of the hydrodynamic force progression in the transient phase of the turning circle, the situation immediately prior to the first counter-rudder movement is used to explain this manoeuvring behaviour. Firstly, considering the summed hydrodynamic moments at the fore and aft, as well as the whole ship (Figure 7.35d), the curve progression at the time right before the first counter-rudder is applied, shows a consistently decreasing trend for the fore ship and vice versa for the aft ship. Overall, this results in a decreasing total yaw moment (i.e. higher negative) down to $h/T = 1.20$, which means an increased counteracting moment against the turning motion of the ship. As the aft ship moment increases at a similar rate as the fore ship moment decreases during the transition to extreme shallow water, the total counteracting moment rather stagnates here, even though the rudder forces are still increasing, see Figure 7.11. For the transition from h/T of 1.15 to 1.10, the hydrodynamic yaw moment at the aft ship even increase significantly stronger, resulting in an increased total yaw moment (i.e. less negative), which means less damping yaw moment. Considering the hydrodynamic force distribution at this position in the turning motion (Figure 7.36c), similar to the DTC, a strong shift of hydrodynamic forces from the aft to the fore ship is observable. However, there are some distinct differences compared to the DTC. First of all, the change of hydrodynamic forces below h/T ratios of 1.50 is higher in the midship and fore section of the JBC. Due to the significant decrease (i.e. higher negative) of the transversal force at the bow, the fore ship moment decreases significantly in the transition from moderate shallow to shallow water, resulting in the overall increased damping moment, see Figure 7.35d. This decrease at the bow becomes only slightly more pronounced with further reduction in water depth. At the same time, the drastic and steady decrease in transversal force at the aft ship with decreasing water depth is not as



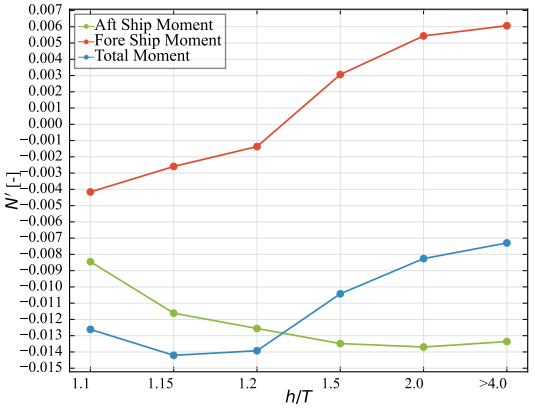
(a) Summed hydrodynamic forces at first overshoot



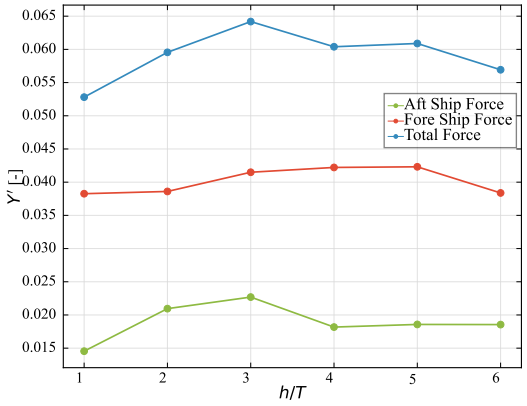
(b) Summed hydrodynamic moments at first overshoot



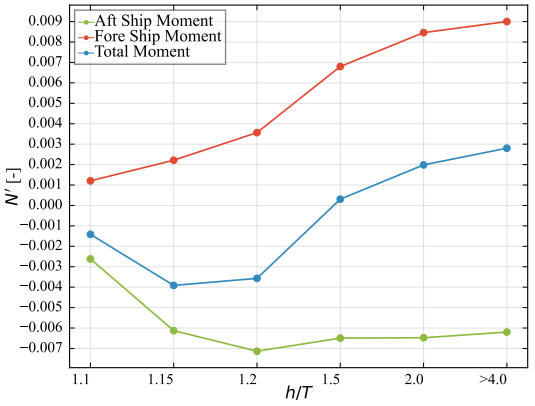
(c) Summed hydrodynamic forces at first counter rudder



(d) Summed hydrodynamic moments at first counter rudder

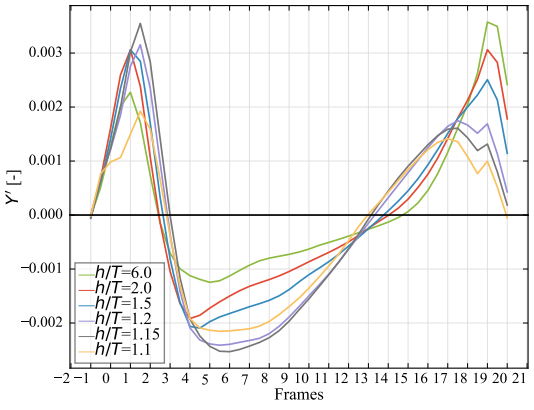


(e) Summed average hydrodynamic forces between first counter rudder and first overshoot

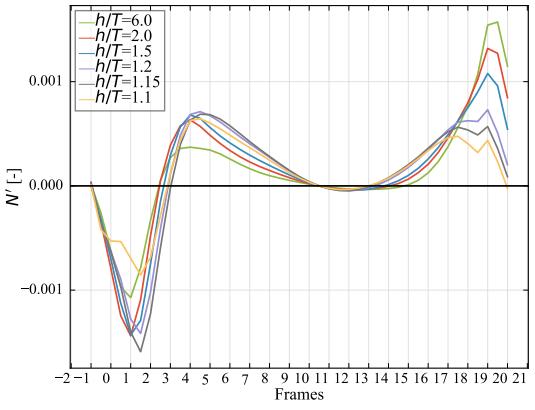


(f) Summed average hydrodynamic moments between first counter rudder and first overshoot

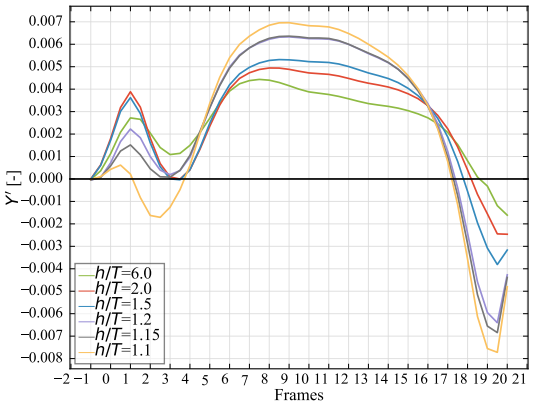
Figure 7.35.: Summed hydrodynamic forces and moments on the fore ship, aft ship, and entire hull of the JBC for the Z 35-20 manoeuvre with an initial speed of 9 kn



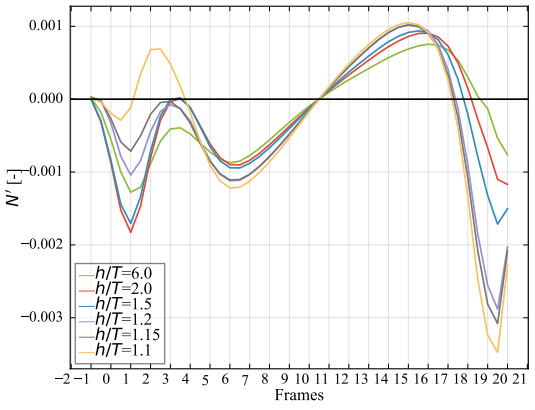
(a) Hydrodynamic forces at first overshoot



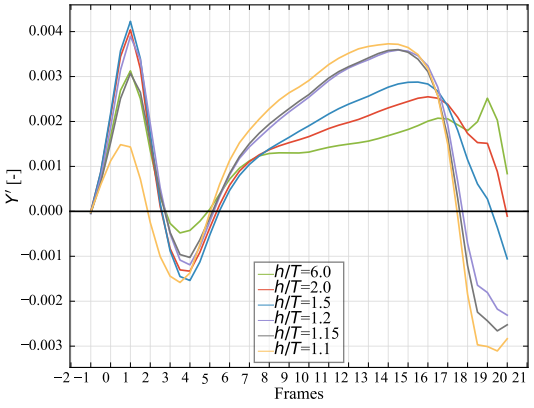
(b) Hydrodynamic moments at first overshoot



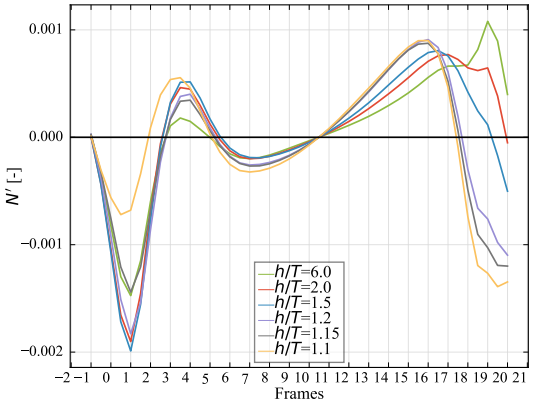
(c) Hydrodynamic forces at first counter rudder



(d) Hydrodynamic moments at first counter rudder



(e) Average hydrodynamic forces between first counter rudder and first overshoot



(f) Average hydrodynamic moments between first counter rudder and first overshoot

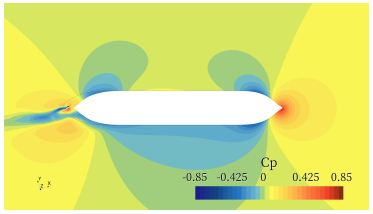
Figure 7.36.: Hydrodynamic forces and moments acting on the JBC as a function of ship's frames for the Z 35-20 manoeuvre with an initial speed of 9 kn

pronounced as for the DTC, showing even an initial increase for the transition from deep to moderate shallow water for the JBC. However, for lower water depth, this force at the aft section decreases considerably, attaining even negative values at $h/T = 1.10$.

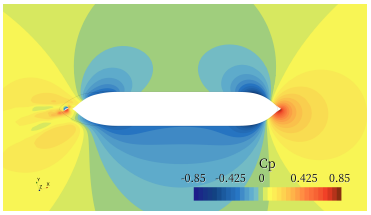
Due to this decrease in transversal force at the aft ship, the yaw moment in extreme shallow water is significantly increased at the aft (Figure 7.36d). Simultaneously, the transverse force at the bow decreases only slightly, leading to the overall increase (i.e. less negative) in the total hydrodynamic yaw moment (Figure 7.35d). As a result, the damping to the ship's turning motion is reduced, which explains the observed higher built-up yaw rate at $h/T = 1.10$ during the turning circle.

For the yaw-checking phase of the first overshoot angle, this increased (less negative) yaw moment remains on average (Figure 7.35f). In this phase, however, a negative yaw moment assists the counter-turning motion of the ship, resulting on average in higher yaw-checking capability for h/T ratios of 1.20 and 1.15. While the transversal forces at the fore ship show a rather constant progression in shallow and extreme shallow water (Figure 7.35e), the forces at the aft ship decrease significantly in the transition to the h/T of 1.10. A corresponding decrease at the aft ship is also evident at the position where the overshoot angle is reached (Figure 7.35a). Figure 7.36a reveals the change of maxima at the aft ship around frame 2, again, as the reason for this decrease. In deep water down to an h/T of 1.15, this peak increases steadily, but exhibits a significant decrease when transitioning to an h/T of 1.10. On average, during this yaw-checking phase (Figure 7.36e), the maximum value of $h/T = 1.15$ at the aft is only similar to that in deep-water conditions. However, there is still a considerable decrease in the transition to h/T of 1.10. Conversely, at the fore ship, the transversal force, on average, assumes higher negative values for lower water depths, resulting in higher yaw-checking capability at the fore ship in shallower water, see Figure 7.36f and Figure 7.35f. Comparing the position of rudder execution and overshoot, the forces at the fore ship shows, similar to the DTC, a trend reversal of absolute extrema in dependence on water depth. This is due to lower drift angle in shallower water, shifting the stagnation point at the bow from port to midship with decreasing water depth at overshoot position, see third row of Figure 7.37. This consistently improving yaw-checking capability at the fore ship with decreasing water depths, however, is in case of $h/T = 1.10$ clearly dominated by the decreased yaw-checking capability at the aft ship, ultimately leading to the observed increased overshoot and yaw-checking times for this extreme shallow water regime.

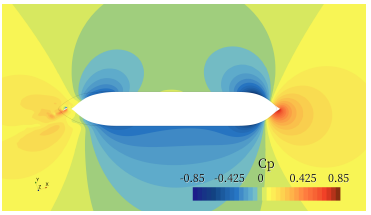
Examining the overall pressure distribution at various positions of the yaw-checking phase (Figure 7.37) reveals a considerable increase in negative pressure distribution when transitioning from moderate shallow water to shallow water, while the actual negative pressure peaks remain at similar positions. For the transition from shallow to extreme shallow water, the difference in pressure distribution is relatively small. Differences are particularly observable for the bow section, as already described above, and the aft section. While the port side shows only little differences for pure turning motion and yaw-checking phase (row 1 to 3 of Figure 7.37), the stbd side reveals a significantly larger area of negative pressure at the aft in shallow-water condition, leading on average to considerably higher



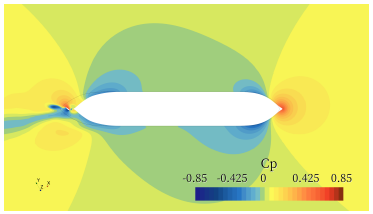
h/T = 2.00, start of yaw-checking phase (first counter rudder)



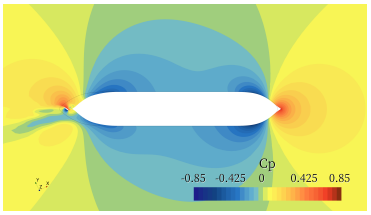
h/T = 1.20, start of yaw-checking phase (first counter rudder)



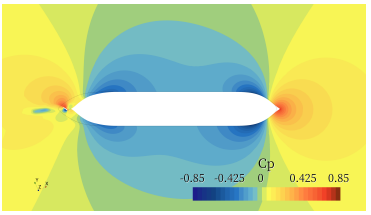
h/T = 1.10, start of yaw-checking phase (first counter rudder)



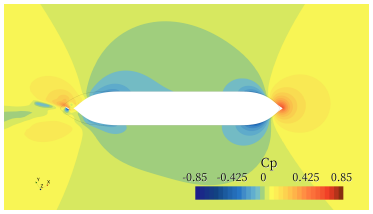
h/T = 2.00, mid of yaw-checking phase



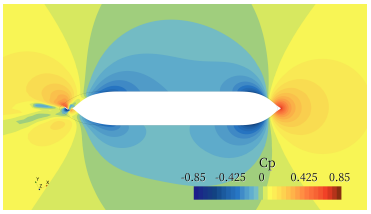
h/T = 1.20, mid of yaw-checking phase



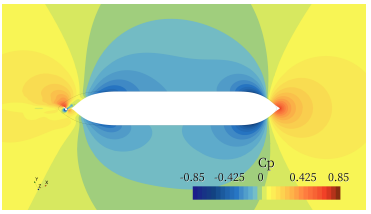
h/T = 1.10, mid of yaw-checking phase



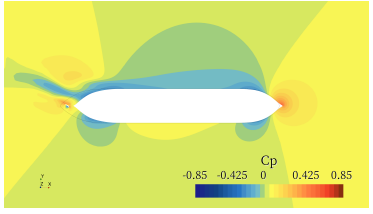
h/T = 2.00, end of yaw-checking phase (overshoot position)



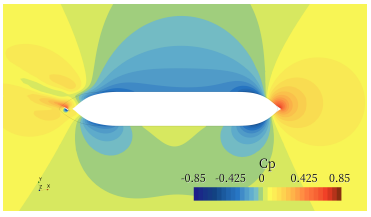
h/T = 1.20, end of yaw-checking phase (overshoot position)



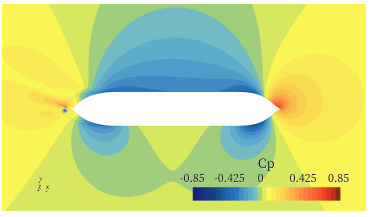
h/T = 1.10, end of yaw-checking phase (overshoot position)



$h/T = 2.00$, maximum yaw rate to port



$h/T = 1.20$, maximum yaw rate to port



$h/T = 1.10$, maximum yaw rate to port

Figure 7.37.: Top view of hydrodynamic pressure distribution at 6.0 m below water line (full scale), shown in terms of the pressure coefficient C_P with the initial straight-ahead speed (9 kn) as reference speed, for $h/T = 2.00$ (left), $h/T = 1.20$ (mid) and $h/T = 1.10$ (right) for the positions of first counter rudder, mid of first yaw-checking phase, first overshoot and maximum yaw rate to the opposite direction (from top to bottom) for the JBC

positive forces in shallow water compared to $h/T = 1.10$.

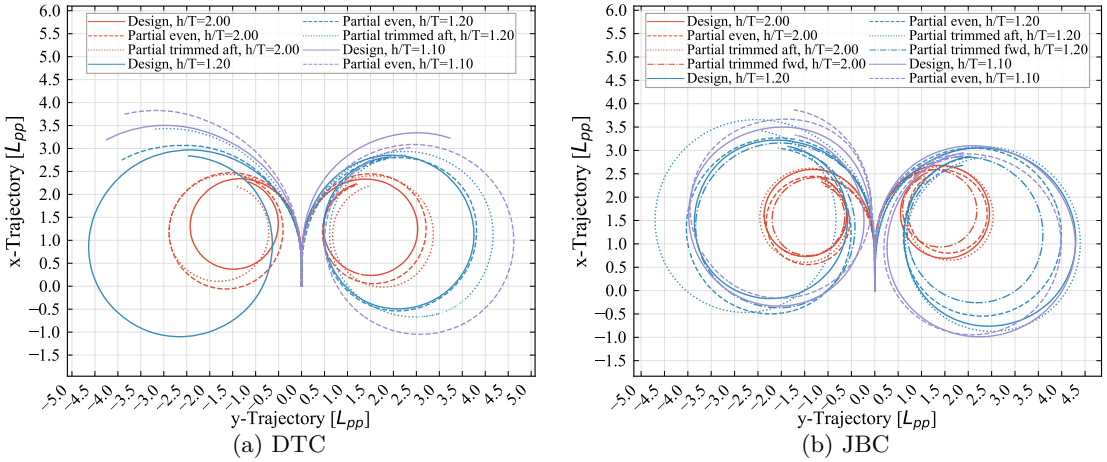
This change in pressure distribution in the stern region is the main reason for the significant change of transverse force at the aft ship, resulting in the higher built-up yaw rate for the turning motion and the overall decreased yaw-checking capability of the JBC in this extreme shallow-water condition.

7.2. Influence of Floating Condition on Manoeuvring Behaviour in Shallow Water

The following chapter investigates the impact of altered floating conditions on shallow-water manoeuvring behaviour. In addition to the design conditions, the DTC was also examined with a partial draught of 12.50 m on an even keel and trimmed 2 m by stern. For the JBC, the partial draught of 13.80 m on even keel as well as 2.60 m trimmed by bow and stern was considered, see also Table 5.2 and Table 5.3 in section 5.1. For these off-design conditions, the manoeuvres were not carried out to the same extent as in the design state. The h/T ratios of 2.00, 1.20 and 1.10 were considered only. Likewise the JBC in design conditions, the port manoeuvres for the DTC were now also carried out at 9 knots only, while the stbd manoeuvres were examined at the same range of velocities as in design conditions. It is worth noting that the h/T ratio always refers to mean draught. Therefore, due to the increased draught at the stern, it was not possible to examine the trimmed conditions at h/T of 1.10.

7.2.1. Turning Circle Manoeuvres

The 45° turning circle manoeuvre was carried out at 6 and 9 knots in stbd direction and only for 9 knots in port direction. Therefore the analysis of this manoeuvre is focusing on the speed of 9 knots. Figure 7.38a shows the trajectories of the different floating conditions for h/T ratios of 2.00, 1.20 and 1.10 for the DTC.

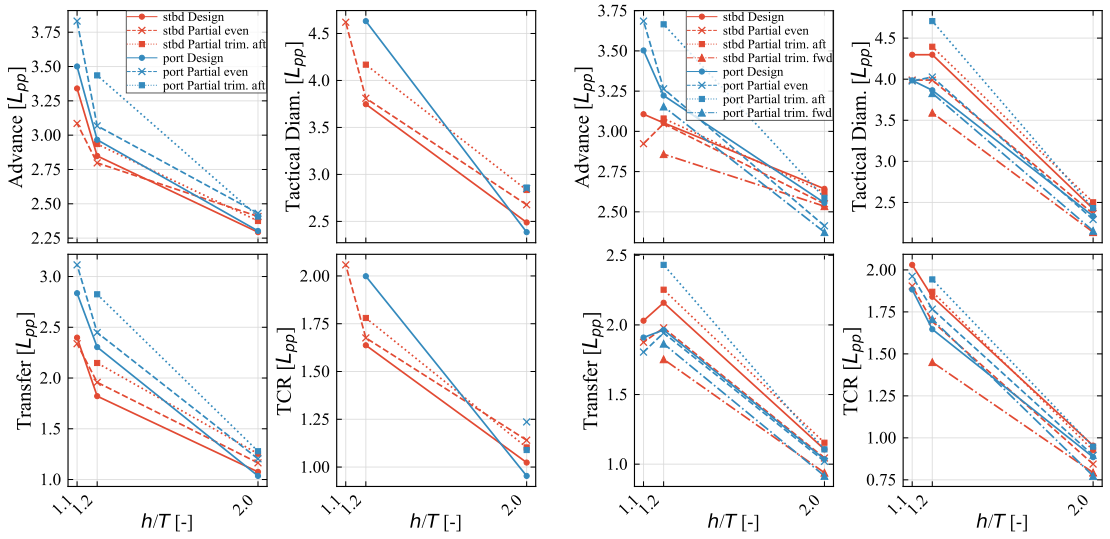


(a) DTC (b) JBC

Figure 7.38.: Trajectories of the 45° turning circle manoeuvre with an initial speed of 9 kn for different floating conditions

In general, it is noticeable that the port turning circles for the partial draught are

larger than the stbd turning circles for both floating conditions in all tested h/T ratios, and already for an h/T of 1.20 no longer fit into the manoeuvring basin. For the design condition, this was only the case at smaller h/T ratios. The described trend reversal between stbd and port for design condition with decreasing water depth, is not present for partial draught, as port side manoeuvre parameters are already slightly higher than those to stbd in moderate shallow-water conditions.



(a) DTC (b) JBC

Figure 7.39.: Advance, transfer, tactical diameter and TCR of the 45° turning circle manoeuvre with an initial speed of 9 kn for different floating conditions

For the port turning circle, only parameters with a 90° heading change can be analysed for smaller h/T ratios, see also Figure 7.39a. While the advance at $h/T = 2.00$ shows hardly any influence of the changed trim and is even slightly smaller than that on even keel at partial draught, the effect becomes clearly noticeable at $h/T = 1.20$. At h/T of 1.10, only the effect of the draught modification can be assessed. For partial draught, the advance increases, and this effect becomes more pronounced as h/T decreases.

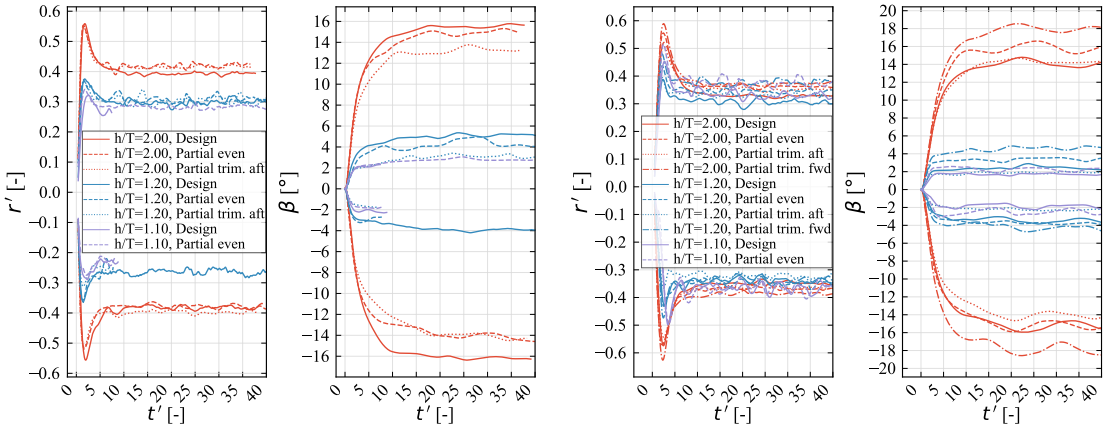
The influence of trim shows a similar, albeit significantly smaller, effect for the stbd direction. The turning circle radius at partial draught is approaching the value of the design condition with decreasing h/T ratio and gets even smaller at h/T of 1.10, so that it even fits completely within the basin at this extreme shallow-water condition. In the stbd direction, the influence of the draught difference on the turning circle manoeuvre with decreasing h/T thus has the opposite effect as in the port direction. Conversely, the transfer is similarly influenced by the altered floating conditions in both directions. Both parameters increase the most for the trim change.

The change of floating condition for the JBC has different influence on both sides of turning direction as the water depth reduce, see Figure 7.38b and Figure 7.39b. For stbd direction the partial draught on even keel overall shows smaller values for the geometric standard parameters compared to design condition for all water depths, demonstrating a similar curve progression. For port direction, the parameters are similar to or slightly higher than those in the design condition, showing a trend reversal for the advance co-

efficient in the transition from moderate shallow to shallow water. In extreme shallow water with partial draught, an even higher advance value is assumed, amplifying the trend reversal for the advance between the stbd and port sides.

The trimmed condition by stern shows overall higher values of turning circle parameters than those at the even keel condition, and generally slightly higher values for stbd and significantly higher values for port compared to design condition. The opposite is true for trimmed condition to bow, showing generally lower standard parameters for port and significantly lower values for stbd direction compared to even keel conditions. The difference between the two trimmed conditions increases significantly in the transition from moderate shallow to shallow water.

The difference in drift angle for these two floating conditions of the JBC changes in a similar manner from approximately 30 % in moderate shallow-water to 115 % in shallow-water conditions, see Figure 7.40b. Overall, trim by stern results in smaller drift angles, whereas trim by bow leads to larger drift angles, corresponding to the highest and lowest turning-circle parameters, respectively. In extreme shallow water, the trend reversal, seen for standard parameters, can also be observed for the drift angle, where the design condition for port assumes the minimum for all cases.



(a) DTC (b) JBC

Figure 7.40.: Yaw rate and drift angle of the 45° turning circle manoeuvre with an initial speed of 9 kn for different floating conditions

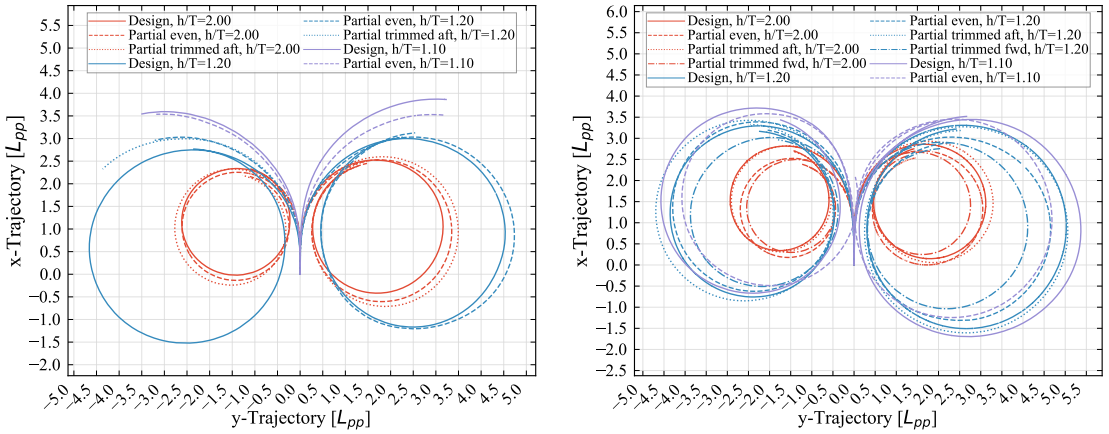
The drift angle of the DTC for stbd direction (Figure 7.40) is only slightly smaller at partial draught on an even keel, compared to design state at an h/T of 2.00 as well as for an h/T of 1.20. When trimmed by stern, the DTC shows the smallest drift angles as well, which for $h/T = 2.00$ are approximately 20 % and 1.20 approximately 50 % below the design values. At the same time, it is evident that the effect of the h/T is significantly greater than the effect of the draught difference.

The situation is different for the trim, at least in shallow water. At $h/T = 1.20$, the DTC at trimmed condition has approximately the same drift angle as at 1.10 on an even keel at partial draught, although the turning circle radius is approximately 15 % smaller. This is similar for the drift angle of the JBC, but in this case both conditions show not only similar drift angles, but also similar parameters for steady conditions. It is evident

that the impact of drift angle, strongly influenced by the trim, has a significant impact on the parameters of the turning circle, as lower drift angles results generally in bigger turning circles and vice versa. Moreover, the effect of trim on the drift angle increases with decreasing water depth.

Nevertheless, the drift angle has only little influence on the steady yaw rate of the model ships, see Figure 7.40. Both model ships show the highest maximum of yaw rate in moderate shallow water. For the JBC, the forward-trimmed condition yields the highest yaw rates, both at the peak and under steady-state conditions. However, there is generally little difference across all the investigated floating conditions of maximum 20 % within the same h/T ratio.

For the DTC, the yaw rate is generally more influenced by the limited water depth, particularly in the transition from moderate shallow to shallow water. The curve progression of the yaw rate with design draught, initially shows the greatest maximum, with the exception of the case $h/T = 1.10$ in the stbd direction. However, in steady-state conditions, the partial draught has a rotation rate that is similar or mostly slightly higher, see Figure 7.40. Nevertheless, the yaw rate curves are similar overall across all floating conditions.

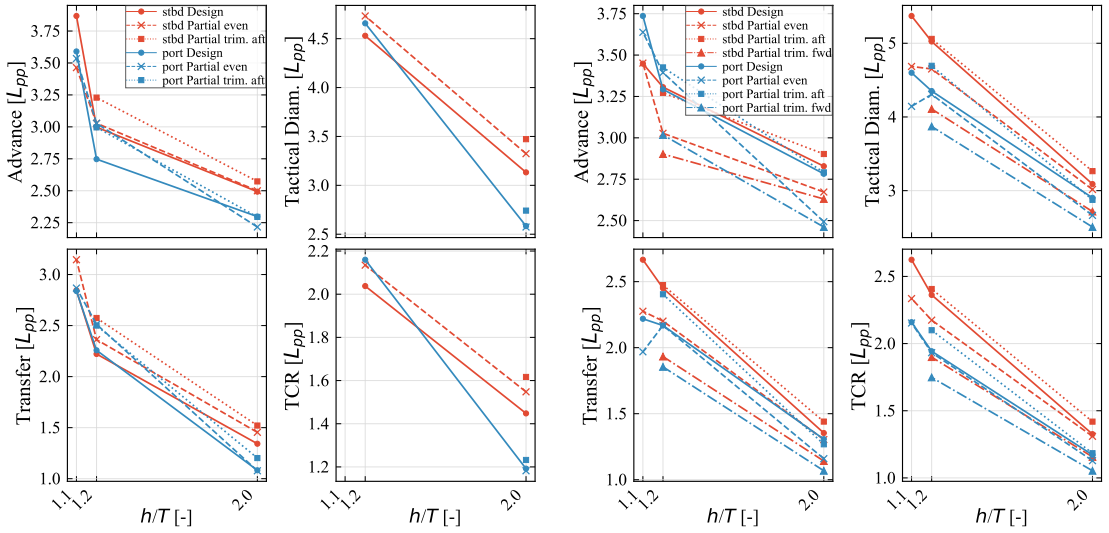


(a) DTC (b) JBC

Figure 7.41.: Trajectories of the 35° turning circle manoeuvre for different floating conditions

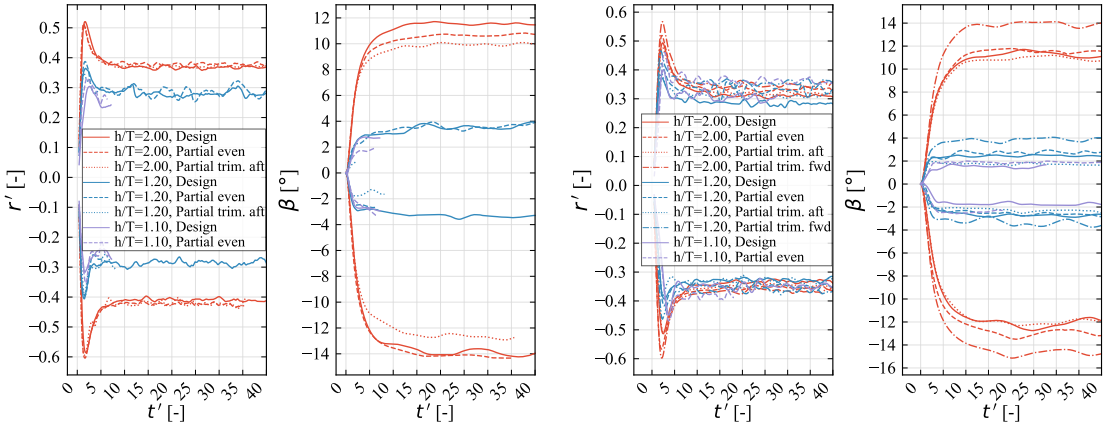
Generally, the 35° turning circle shows similar influence of floating conditions as the 45° turning circle, albeit to a lesser extent, see Figure 7.41 and Figure 7.42. For the JBC, especially the trim by stern condition shows less difference compared to even keel condition and less amplification with decreasing water depth, showing only slightly higher or even less tactical diameter for aft trimmed condition in shallow water compared to even keel in extreme shallow water. The relationship between drift angle and yaw rate is comparable to that of the 45° turning circle, see Figure 7.43, showing again the minimum drift angle in extreme shallow water for design conditions.

For the DTC, the change of floating conditions also have lesser influence on the turning circle parameters than for 45° turning circle manoeuvre. However, there is still different influence of the directions on the turning circle parameters in dependence on the water



(a) DTC (b) JBC

Figure 7.42.: Advance, transfer, tactical diameter and TCR of the 35° turning circle manoeuvre with an initial speed of 9 kn for different floating conditions



(a) DTC (b) JBC

Figure 7.43.: Yaw Rate and drift angle curve progression of the 35° turning circle manoeuvre with an initial speed of 9 kn for different floating conditions

depth. Under even-keel conditions at partial draught, the advance coefficient exhibits a stronger increase on the port side than on the stbd side as the water depth decreases, resulting in a trend reversal in extreme shallow water. Independent of floating condition, at $h/T = 2.00$ all turning circle parameters (see Figure 7.41a) of the stbd turning circles are clearly higher compared to port. This changes already for an h/T of 1.20, showing higher transfer and turning circle radius for design and partial draught on even keel for port side. For trimmed condition however, the stbd turning circle parameters remain higher than those for port, indicating the influence of the floating condition on this shallow-water effect.

In summary, the draught modification increase the asymmetric turning behaviour with decreasing water depth. The effect of improving turning ability for stbd side and deteriorated turning ability to port side increase with decreasing water depth, most obvious for the advance coefficient. For the DTC, the asymmetry in the advance increases for the

45° turning circle, whereas for the 35° turning circle a trend reversal occurs, such that the advance for the port turn exceeds that for the stbd turn at $h/T = 1.10$, which is not the case under design conditions. For the JBC, an increasing asymmetry of the advance coefficient is likewise observed with decreasing water depth. The impact of trim, in which trim by stern leads to deteriorated turning ability and trim by bow has the opposite effect, increases with decreasing water depth. The asymmetry between the two different trim conditions, investigated only for the JBC, is amplified as the water depth is reduced. The effect of trim on the drift angle increases with decreasing water depth.

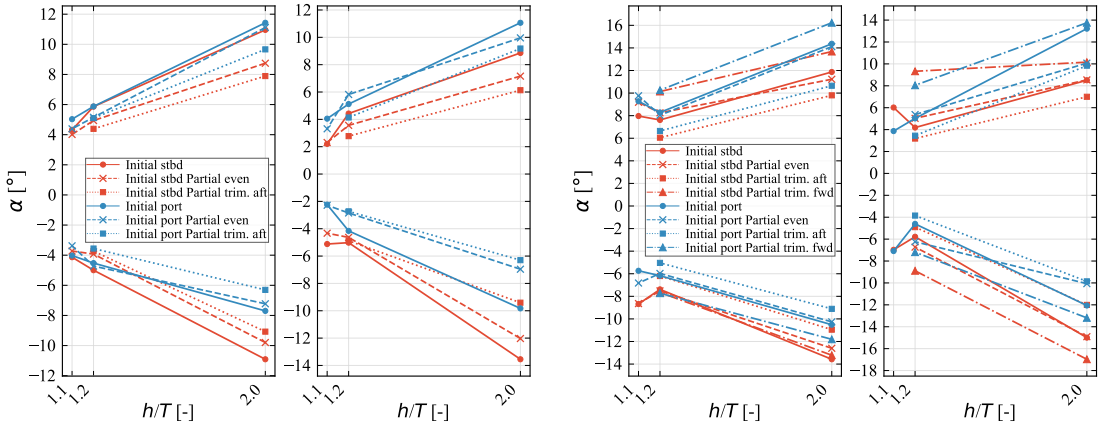
7.2.2. Zig-Zag manoeuvres

The analysis of the altered floating conditions for the Zig-Zag manoeuvres focuses on the speed of 9 knots only. The DTC exhibits similar dependency on water depth on dynamic manoeuvring behaviour when operating at partial draught on even keel or aft trimmed condition, albeit to a slightly different extent. The curve progressions of the overshoot angle for Z 35-20 and Z 20-10 (see Figure 7.44) resemble each other. The overshoot angle generally decreases for the partial draught and even more for the aft trimmed condition. The predominantly parallel curve progression reveals a relative constant influence of the modified floating condition in moderate shallow and shallow water. The first Z 35-20 overshoot angle initially to port, for example, demonstrates a difference between design and trimmed condition of about 18 % for h/T of 2.00 and 16 % at an h/T of 1.20. With the exception of the first overshoot angle for initial port manoeuvre, the influence of the altered floating condition then becomes even smaller at an h/T of 1.10, with differences smaller than 10 %.

The overshoot angles of the JBC show generally low influence of the pure draught modification, showing a similar curve progression with decreasing overshoot angles in the transition to shallow water and an increase in the transition to extreme shallow water. Overall, forward trimmed condition exhibits the highest and aft trimmed condition the lowest overshoot angles. For the Z 35-20 manoeuvre, the curve progressions are mostly parallel to each other for all floating conditions, showing only little influence in dependence on the water depth. For the Z 20-10 manoeuvre, the partial draught on even keel exhibits a trend reversal relative to the design condition, as the overshoot angles for the design condition decrease more sharply in the transition from moderate shallow to shallow water.

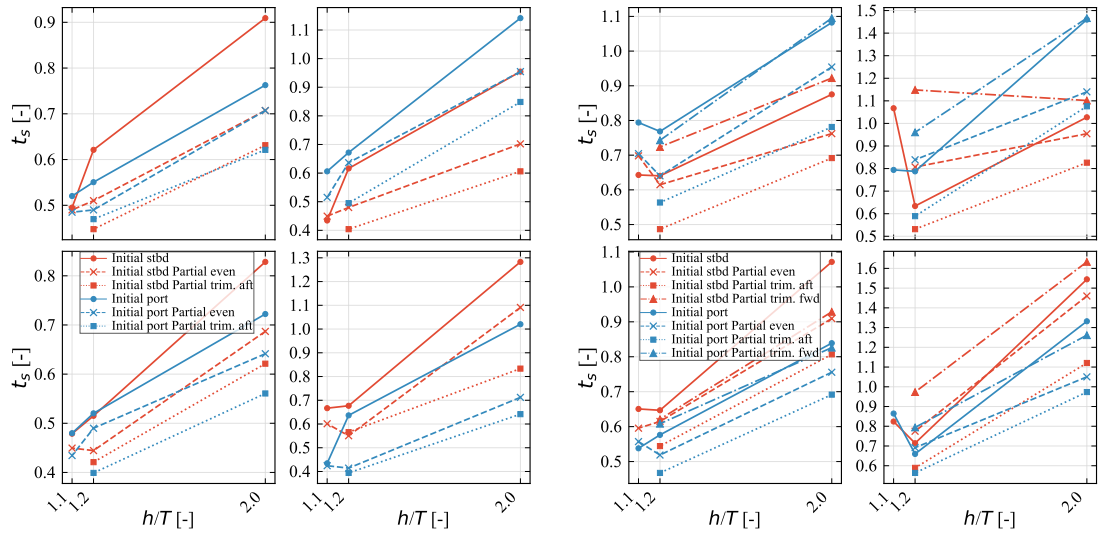
The first and second yaw-checking time (Figure 7.45) shows the same principal curve progression as the overshoot angle for both model ships. For the DTC, again, the yaw-checking time is similarly influenced by the changed floating condition between h/T of 2.00 and 1.20 and less influenced for 1.10 with the same exception as for the overshoot angles.

In moderate shallow and shallow water, the initial turning time for reduced draughts generally shows values that are similar to or slightly lower than those for design conditions, see Figure 7.46. The trim by stern has only a minor effect. The trimmed condition to bow, exhibits generally the lowest initial turning time, with increasing effect with decreasing



(a) DTC (b) JBC

Figure 7.44.: First (pos.) and second (neg.) overshoot angles of the Z 35-20 (left) and 20-10 (right) manoeuvre with an initial speed of 9 kn for different floating conditions



(a) DTC (b) JBC

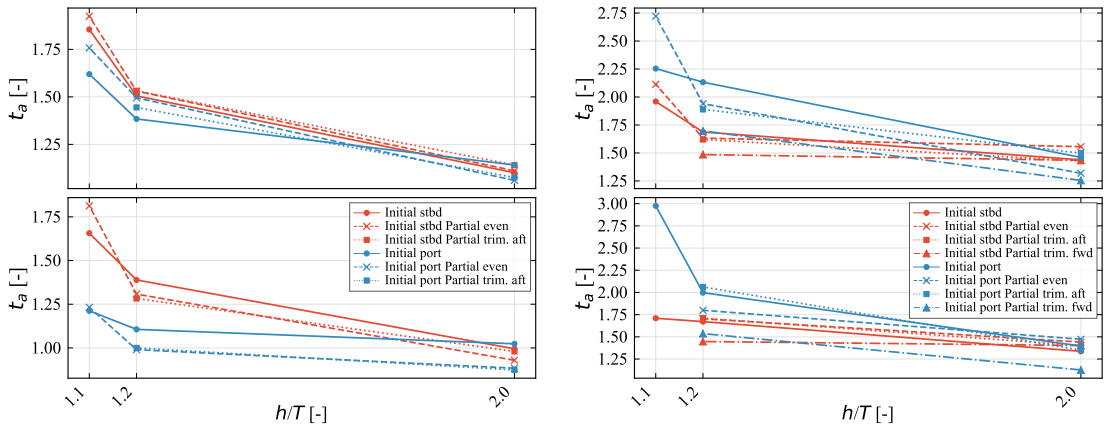
Figure 7.45.: First (top) and second (bottom) yaw-checking time of the Z 35-20 (left) and 20-10 (right) manoeuvre with an initial speed of 9 kn for different floating conditions

water depth.

In extreme shallow water of $h/T = 1.10$, this relation changes for both manoeuvres and both ships. The initial turning time for partial draught is increasing significantly compared to design condition, leading to significantly higher turning times for partial draught of maximum 25 % difference for the DTC, and 41 % for the JBC compared to design condition.

The curve progression of DTC's yaw rate for the Z 20-10 manoeuvre (Figure 7.47) illustrates the trend reversal of worse turning ability in extreme shallow water for partial draught. At the h/T of 2.00 and 1.20 the partial draught shows a faster increase of the yaw rate and, with the exception for the case of initial stbd direction at h/T of 1.20, larger maxima. This changes for both directions at the h/T of 1.10, showing lower slope and maxima of the curve. The results indicate that variations in draught have a decreasing influence on overshoot angle and yaw-checking time as water depth reduces, particularly

for the DTC. Furthermore, a significant increase in initial turning time is observed in extreme shallow water conditions. These results imply that the relative h/T ratio is not the dominant parameter. Rather, it appears that absolute under-keel clearance has a greater impact on the vessel's manoeuvring performance.



(a) DTC (b) JBC

Figure 7.46.: First initial turning time of the Z 35-20 (top) and 20-10 (bottom) manoeuvre with an initial speed of 9 kn for different floating conditions

The curves of K'_N and T'_N (Figure 7.48) provide an even more differentiated insight into the changed manoeuvrability in shallow water for the considered draughts. The Nomoto coefficients are considerably lower for partial draught than for the design condition in moderate shallow water. This is particularly true of the T'_N, which is related to course-keeping ability. This difference already decreases in the transition to shallow water. For the transition to extreme shallow water, the T'_N of partial draught already increase again or stagnate, while this has only been observed for the design draught at the transition from h/T of 1.15 to 1.10. As a result, the partial draught has similar or even higher T'_N values for $h/T = 1.10$. At the same time, K'_N exhibits a slightly larger decrease for partial draught in the transition to extreme shallow water, attaining still lower values compared to design draught. For the Z 20-10 manoeuvre of the JBC, unfortunately, there are no data available for the Nomoto coefficients in extreme shallow water.

The curve progression of the Norrbin Parameter P, as presented in section 4.2, summarises this finding, see Figure 7.49. In the transition from moderate shallow to shallow water, P demonstrates an only slightly decrease for the DTC and even an increase for the JBC, particularly for the Z 35-20 manoeuvre for aft trimmed condition, which generally shows the highest P value across all conditions of both ships. Except for the Z 20-10 manoeuvre of the JBC, the differences of P between design and partial draught stay rather constant in moderate shallow and shallow water. In the transition from shallow to extreme shallow water, however, P shows a remarkably stronger decrease for partial draught, attaining similar or even smaller values than for design draught.

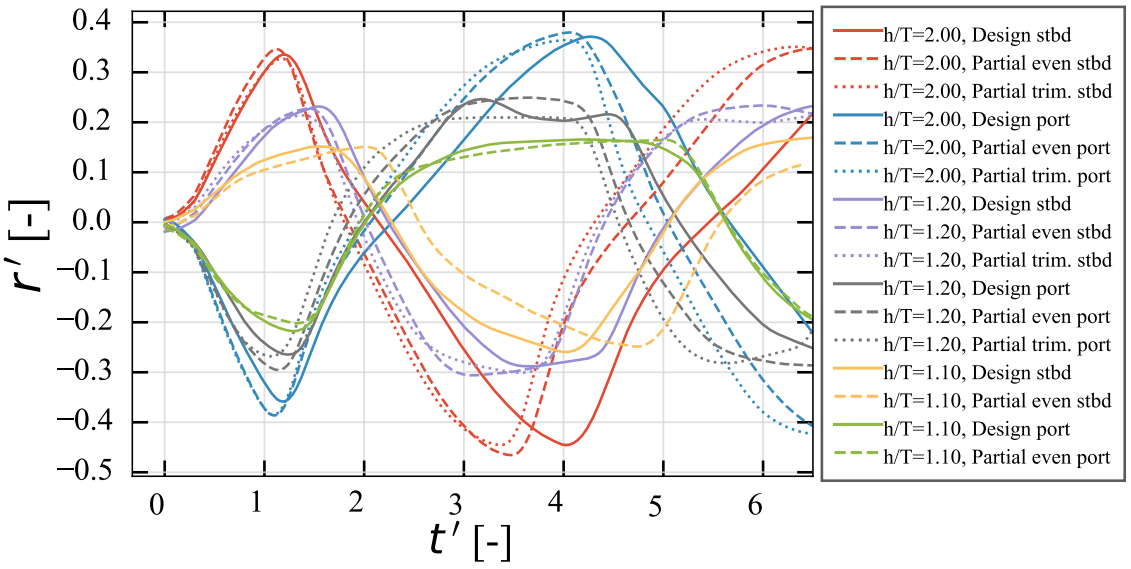
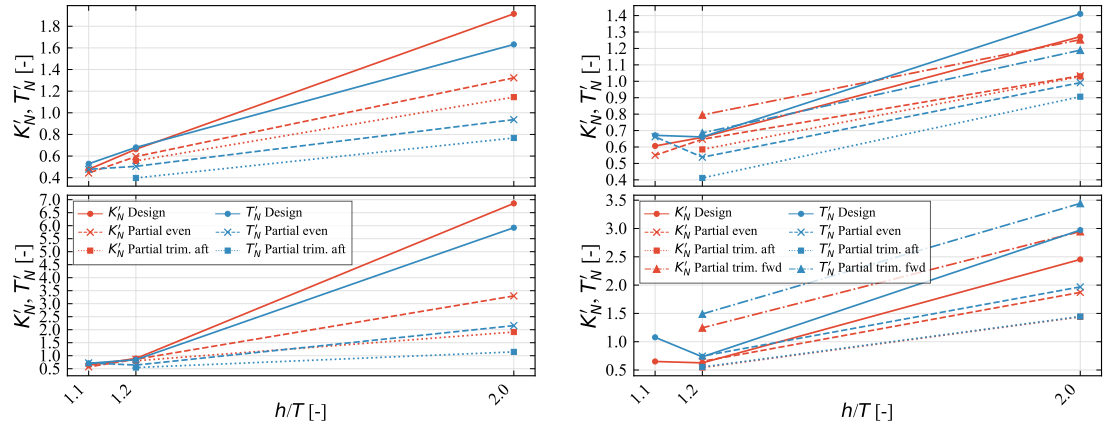


Figure 7.47.: Yaw rate of the Z 20-10 manoeuvre with an initial speed of 9 kn for different floating conditions for the DTC

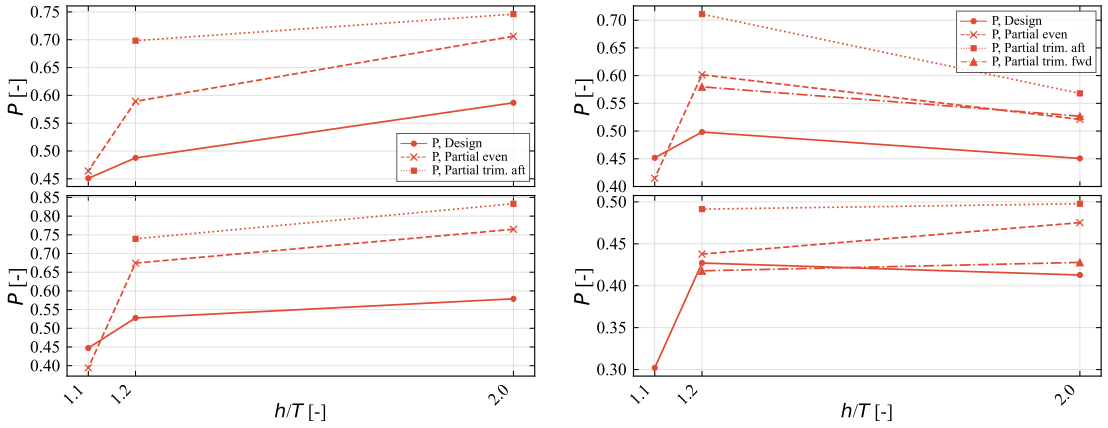


(a) DTC (b) JBC

Figure 7.48.: Nomoto coefficients K'_N and T'_N for the Z 35-20 (top) and 20-10 (bottom) manoeuvre with an initial speed of 9 kn for different floating conditions

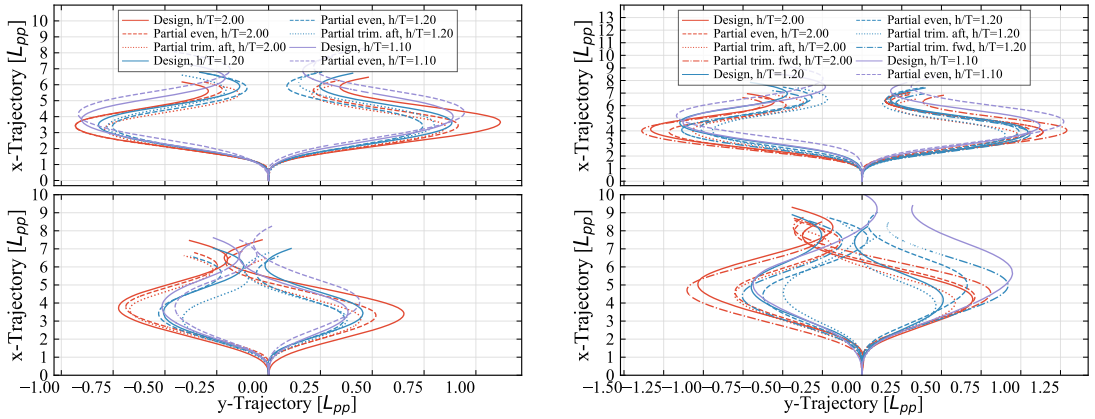
Another indication of this fact are the curve progressions of the trajectory for both Z manoeuvres, see Figure 7.50. In general, it can be observed that the transverse motion of the DTC and JBC at partial draught is reduced or similar to design draught condition in moderate shallow and shallow water. The transverse motion of the aft trimmed condition is similar to that of the partial draught or even stronger reduced, while the forward trimmed condition shows the highest y_{max} values, even compared to design condition. For the h/T of 1.10, however, the transverse motion increases significantly stronger for the partial draught for both model ships, compared to design condition (with the exception of Z 20-10 to port for the DTC).

Overall, the results of the Zig-Zag manoeuvres for different floating conditions indicate



(a) DTC (b) JBC

Figure 7.49.: Norrbin Parameter P for the Z 35-20 (top) and 20-10 (bottom) manoeuvre with an initial speed of 9 kn for different floating conditions



(a) DTC (b) JBC

Figure 7.50.: Trajectories of the Z 35-20 (top) and 20-10 (bottom) manoeuvre with an initial speed of 9 kn for different floating conditions

that in extreme shallow water the h/T ratio alone is no longer sufficient to characterise the manoeuvring behaviour. Whereas for moderate shallow and shallow water the initial turning time under even-keel conditions at partial draught are significantly lower compared to design condition, they increase considerably stronger in extreme shallow water exceeding the values for design conditions. This trend reversal is also obvious for x_{max} and y_{max} of the trajectory. A particularly strong measure of the effect of extreme shallow water under partial-draught conditions is the Norrbin parameter, with partial-draught values being consistently higher than those of the design conditions under moderate shallow- and shallow-water conditions, but exhibiting a considerably stronger decrease when transitioning to extreme shallow water.

8. Summary, Conclusion and Outlook

8.1. Summary

Shallow water significantly affects the manoeuvring performance of vessels, making its understanding crucial for navigational safety. Increasing ship sizes further amplify the operational challenges in confined and shallow-water environments.

Consequently, substantial research has been conducted on this topic over the past decades. Free-running and captive model tests, revealed increased hydrodynamic damping on the ship hull, resulting in increased course stability and decreased turning ability. Recent studies have demonstrated that RANS-based CFD can accurately reproduce such model test results. However, most investigations focus on stationary conditions and primarily capture qualitative changes in hydrodynamic coefficients. The fundamental mechanisms governing the redistribution of hydrodynamic hull forces with decreasing water depth is largely unresolved. Existing free-running studies have mostly addressed moderate shallow-water conditions, leaving the influence of extreme shallow water ($h/T < 1.20$) insufficiently understood. Similarly, the role of the depth Froude number has been largely neglected, as most previous studies were conducted at a single speed, limiting understanding of speed-dependent shallow-water effects.

Accordingly, this study systematically investigated ship manoeuvring over a broad range of speeds and water depths, including extreme shallow-water conditions, with additional variations in draught, trim, and turning direction. Global manoeuvring performance was linked to water-depth-dependent changes in local flow through detailed analysis of hull pressure distributions obtained from CFD simulations. Despite advances in numerical methods, model tests remain the state of the art. Therefore, a combined model test-CFD approach was adopted: model tests were used both for validation and for the detection and analysis of characteristic shallow-water effects, while CFD provided detailed insight into the associated forces and flow mechanisms governing manoeuvring behaviour.

The free-running model tests of the container ship (DTC) and bulk carrier (JBC) at model scale of 1/60 were conducted in the BAW shallow-water basin. Turning circle and Zig-Zag manoeuvres were performed across five shallow water conditions and up to five ship speeds, considering design and partial draughts under even-keel and trimmed conditions. The tests captured trajectories, rudder angles, ship orientation, rudder forces, and propeller thrust using comprehensive measurement equipment.

Additional numerical simulations were performed for all examined h/T ratios at model scale for a speed corresponding to 9 kn at full scale. Verification studies included resistance tests in moderate shallow and shallow water and a full free-running turning circle manoeuvre at $h/T = 1.50$. Most parameters exhibited convergent behaviour, with only

two transient parameters showing noticeable deviations for the DTC.

Comparison with model test data demonstrated good agreement across all parameters, with mean errors predominantly around 5 %. The most important depth-dependent changes in manoeuvrability were captured, even for extreme shallow water conditions.

The model test results presented revealed different shallow-water effects on the manoeuvring behaviour of the investigated model ships. A key finding is the trend reversal in the directional asymmetry between stbd and port turning as a function of the h/T ratio. For the DTC, this affected the steady turning characteristics, and for the JBC the transient phase of the turning motion. The disparity between stbd and port in the initial turning ability is increased significantly with decreasing water depth for both ships. This effect is attributed primarily to modified inflow to the rudder and the clockwise-rotating propeller.

It has been shown that RANS-based CFD simulations can reproduce the model tests with satisfactory accuracy and capture the most important shallow-water effects. They have provided highly valuable information for analysing the varying contribution of individual force components during a manoeuvre and the change in hydrodynamic force and moment distribution along the ship, such as the strong shift of transversal forces from the aft ship in deep water to the fore ship in shallow water during turning motion. Furthermore, it could be demonstrated, how hydrodynamic transversal forces change in dependence on water depth, and relates to the other force components, such as rudder, inertia and centrifugal force. Thereby, significantly reduced hydrodynamic transverse forces over most of phase 2 of the turning circle in shallow and extreme shallow water were revealed. These are balanced by significantly smaller and more rapidly decaying inertia forces and lower centrifugal forces. Hydrodynamic forces exceeded deep-water levels only as steady-state conditions were approached, slightly for the DTC and markedly for the JBC.

The initially improved turning and reduced course-keeping of the DTC during the transition to moderate shallow water were reproduced and explained by CFD-derived hull-pressure distributions. Increased forward-midship transverse force together with a pronounced reduction at the stern decreases the hydrodynamic yaw-damping moment, enhancing turning. Simultaneously, a strengthened stern yaw moment and still-pronounced bow contribution delay yaw checking, leading to larger overshoot angles and yaw-checking times.

Another key result concerns the pronounced influence of the extreme shallow-water condition $h/T = 1.10$ compared with 1.15 and 1.20. Parameters associated with turning ability – such as advance, initial turning time, yaw-rate gradient and K'_N – continue to increase towards $h/T = 1.10$. In contrast, course-keeping and yaw-checking indicators – such as yaw-checking time and T'_N – stagnate or increase again when transitioning from h/T of 1.15 to 1.10, as also reflected by the rising overshoot angles and yaw-checking times in the JBC Zig-Zag manoeuvres. A further trend reversal is observed in the increased yaw rate of the JBC during turning. The calculated pressure distributions identify a strengthened negative pressure field at the aft stbd region in extreme shallow water as the primary cause. The resulting increase (less negative) yaw moment at the stern exceeds the reduced yaw moment contribution at the bow, leading to reduced hydrodynamic yaw damping and higher built-up yaw rates during turning. During yaw-checking, however, the

increased total yaw moment more strongly opposes the counter-turning motion, thereby degrading yaw-checking ability and course stability of the JBC at $h/T = 1.10$.

In moderate shallow and shallow water, partial draught generally exhibits improved yaw-checking and course-keeping ability and similar initial turning performance compared with design draught. However, when approaching extreme shallow-water conditions, this trend weakens or reverses: yaw-checking times converge towards those of the design draught, while the initial turning ability of the partial-draught condition deteriorates more strongly and can exceed the corresponding design-draught values at $h/T = 1.10$. This increased sensitivity of partial draught to extreme shallow water is also reflected in the vessel trajectories, where partial draught shows reduced transverse motion at moderate depths but larger longitudinal and transverse excursions in extreme shallow water. Consistent trends are observed in the Norrbin parameter: while partial draught indicates superior course-keeping behaviour in moderate shallow and shallow water, its advantage diminishes in extreme shallow water, with the parameters approaching or even dropping below those of the design draught.

The influence of stern trim does not change markedly between moderate shallow and shallow-water conditions. Overall, trim by stern improves course-keeping and yaw-checking ability – reflected in reduced yaw-checking times, overshoot angles and lower T'_N – but limits its turning ability, as indicated by increased transfer and tactical diameter. The associated drift angles are substantially reduced compared with even-keel condition, with the relative difference increasing as water depth decreases. Trim by bow exhibits a depth dependence similar to even keel but with opposite manoeuvring tendencies. In this condition, course-keeping and yaw-checking ability deteriorate – expressed by increased yaw-checking times, overshoot angles and T'_N – while turning ability improves, reflected by reduced turning-circle parameters and higher Nomoto coefficient K'_N. These trends are closely linked to the markedly increased drift angles under bow-trimmed conditions.

By examining various speeds across different shallow-water conditions, the influence of the depth Froude number on manoeuvrability was systematically assessed. While the DTC exhibits a largely similar depth trend at all speeds during turning, the JBC shows a markedly stronger increase in turning-circle parameters at higher speeds when transitioning to shallow water. Steady-turning velocity and yaw-rate responses plotted against depth Froude number display increasing non-linearity with decreasing UKC. These trends are attributed to speed-dependent changes in propeller–rudder interaction, emphasizing the role of stern flow conditions and rudder configuration in shallow water.

For the Zig-Zag manoeuvres, the advance speed has a significant impact on its parameters. Higher speeds generally produce larger overshoot angles, longer yaw-checking and initial turning times, and higher transverse positions. The sensitivity of overshoot angles to the depth Froude number decreases with decreasing h/T, while the sensitivity of yaw-checking time remains nearly constant. In contrast, the speed dependence of initial turning time increases as the water depth decreases, with the strongest amplification occurring in shallow and extreme shallow water. This also modifies the Zig-Zag trajectory, as the longitudinal positions of extrema shift progressively with increasing speed at lower depths. Overall, the Nomoto indices indicate that lower advance speeds yield better manoeuvrability across all examined shallow-water conditions.

8.2. Conclusion

The experimental and numerical results show that the established view of shallow-water manoeuvring behaviour captures only part of the actual depth dependency, see section 1.2. As under-keel clearance decreases into the extreme shallow-water range, the manoeuvring characteristics diverge in their response and can no longer be described by a single monotonic trend.

- Turning ability: The expected deterioration with decreasing water depth is confirmed, but the present investigation shows that this decline intensifies markedly in extreme shallow water, particularly for the hull forms with low block coefficient. The underlying mechanism is the progressive redistribution of damping forces from the aft toward the fore ship, which shifts the yaw-moment balance unfavourably for turning manoeuvres. For lower h/T ratios, the turning ability becomes strongly speed-dependent, particularly for the hull forms with high block coefficient. This challenges the common assumption that turning ability is largely insensitive to speed, demonstrating that such independence does not hold under shallow-water conditions. The steady yaw rate does not necessarily decrease continuously, as is conventionally assumed, but exhibits a trend reversal in extreme shallow water for the hull forms with high block coefficient. Consequently, turning characteristics obtained at moderate clearances cannot be extrapolated toward extreme shallow water conditions. Furthermore, the pronounced directional asymmetry of turning performance with decreasing water depth, driven by depth-induced alterations of stern flow and the associated propeller-rudder inflow, necessitates explicit consideration in manoeuvring prediction.

- Initial turning/course-changing ability: The initial turning ability exhibits an even stronger sensitivity to both water depth and speed. While earlier shallow-water studies often reported only modest depth effects, the present results demonstrate a rapid degradation of the initial turning response with increasing velocity, particularly in extreme shallow water. This has direct operational implications, as it reduces the effectiveness of evasive manoeuvres at higher approach speeds in confined waterways. In addition, a pronounced increase in directional asymmetry of the course-changing ability is observed with decreasing water depth, with a directional trend reversal occurring for the hull forms with high block coefficient. This asymmetric shallow-water behaviour represents a significant hydrodynamic effect that must be accounted for in ship operation under shallow-water conditions.

- Yaw-checking and course-keeping ability: Increased damping in shallow water is generally considered to improve yaw-checking and course-keeping performance. By contrast, the results reveal a stagnation and eventual deterioration of yaw-checking ability and course stability in extreme shallow water, most clearly at $h/T = 1.10$ for the bulk carrier. The pronounced design-partial draught trend reversal observed at $h/T = 1.10$ in yaw-checking and course-keeping characteristics further indicates that absolute under-keel clearance, rather than the depth-to-draught ratio alone, governs response in this regime. Accordingly, this ratio constitutes a distinct shallow-water condition characterised by particularly strong shifts in the hydrodynamic force

balance between bow and stern governing yaw-checking behaviour across shallow-water conditions. While the speed sensitivity of yaw-checking ability decreases with decreasing under-keel clearance, the speed dependence of course stability remains essentially unaffected.

It follows that shallow-water manoeuvring performance cannot be described by a single global depth trend, nor assessed uniformly across manoeuvring characteristics. Instead, each characteristic exhibits a distinct sensitivity to speed and shallow-water regime, requiring a differentiated evaluation. Analysis of pressure and force distributions along the hull shows that the governing mechanism is not adequately represented by increased global damping alone, but by a depth-dependent redistribution of local hydrodynamic loads. By linking these local flow modifications to the observed global manoeuvring response, the study explains the altered manoeuvring behaviour and the identified regime-dependent trend reversals. Extreme shallow water of $h/T = 1.10$ should be regarded as a separate hydrodynamic regime, rather than as a continuation of shallow-water trends, and manoeuvring prediction, simulation and operational limits must account explicitly for depth-Froude-number effects and stern-flow modification.

8.3. Outlook

This study has revealed some new effects of shallow water on manoeuvring behaviour, while also confirming phenomena already documented in the literature. The useful applicability of RANSE-based CFD simulations has been demonstrated, giving detailed insight of the changed hydrodynamics in shallow water. However, this investigation related exclusively to model ships, which may be subject to scaling effects due to the model-related too low Reynolds number, such as flow separation, changing the pressure distribution at the hull. Furthermore, only two different ship types were investigated and even though the key findings could be verified for both model ships, the DTC and JBC already showed some outlined differences on shallow-water effects. To prove the found shallow-water effect on full scale ships and further ship types, should be part of future research.

In order to further utilise this shallow-water investigation, it would be particularly useful to incorporate the results into ship handling simulators, which are important for improving the navigational safety of professionals as well as for the dimensioning of waterways. Allowing the shallow-water effects to be represented accurately in simulators requires the development of a system identification method to determine the manoeuvring coefficients in shallow water on the basis of as few manoeuvres as possible, potentially with the use of modern AI tools. This would increase the benefit and applicability of the experience gained in the simulator and the reliability of the results of nautical investigations. The large amount of data generated, evaluated and analysed in this study would be particularly suitable for developing practical methods in this respect.

Bibliography

Abdel-Maksoud, M. Manövrierfähigkeit von Schiffen. Lecture Notes Hamburg University of Technology.

Abkowitz, M. A. *Lectures on Ship Hydrodynamics – Steering and Manoeuvrability.* Hydro- og Aerodynamisk Laboratorium, 1964.

Azcueta, R. Steady and unsteady RANSE simulations for Littoral Combat Ships. In National Research Council, editor, *Twenty-Fifth Symposium on Naval Hydrodynamics*, Washington, D.C., 2005. The National Academies Press. ISBN 978-0-309-29811-7.

Baker, G. S. Steering of ships in shallow water and canals. *Transactions of the Institution of Naval Architects*, 66, 1924.

Barnaby, N. On the Steering of Ships. *Transactions of the Institution of Naval Architects*, 4, 1863.

Bindel, S. Experiments on ship maneuverability in canals as carried out in the Paris model basin. In David Taylor Model Basin, editor, *First Symposium on Ship Maneuverability*, David Taylor Model Basin Report. David Taylor Model Basin, Washington, DC, 1960.

Bogdanov, P., Lefterova, M., and Milanov, E. Some Pecularities of the changes in hull - propeller- rudder interaction characteristics in deep and shallow water. In ITTC, editor, *Proceedings of the 18th International Towing Tank Conference (Vol. 2) - Session on Manoeuvrability*, pages 211–214, 1987a.

Bogdanov, P., Vassilev, P., Lefterova, M., and Milanov, E. "Esso Osaka" tanker manoeuvrability investigations in deep and shallow water, using PMM. *International Shipbuilding Progress*, 34(390):30–39, 1987b. ISSN 0020868X. doi:10.3233/ISP-1987-3439002.

Carrica, P. M., Ismail, F., Hyman, M., Bhushan, S., and Stern, F. Turn and zigzag maneuvers of a surface combatant using a URANS approach with dynamic overset grids. *Journal of Marine Science and Technology*, 18(2):166–181, 2013. ISSN 0948-4280. doi:10.1007/s00773-012-0196-8.

Carrica, P. M., Mofidi, A., Eloot, K., and Delefortrie, G. Direct simulation and experimental study of zigzag maneuver of KCS in shallow water. *Ocean Engineering*, 112: 117–133, 2016. ISSN 00298018. doi:10.1016/j.oceaneng.2015.12.008.

Chen, X. N., Gronarz, A., List, S., and Stuntz, N. Flow around ships sailing in shallow water, experimental and numerical Results. In National Research Council, editor, *Twenty-Third Symposium on Naval Hydrodynamics.* National Academy Press, Washington, District of Columbia, 2001. ISBN 978-0-309-25467-0.

Clarke, D., Gedling, P., and Hine, G. The application of manoeuvring criteria in hull design using linear theory. *Transaction of the Royal Institution of Naval Architects*, 124, 1982.

Crane, C. L. *Maneuvering trials of the 278,000 DWT ESSO OSAKA in shallow and deep waters: Marine Research Program. Report Number EII. 4TM. 79.* Exxon International Company Tanker Department - Research and Development, Florham Park, N.J., 1979.

Cura, A. Computation of the turbulent flow around a ship model in steady turn and in steady oblique motion. In National Research Council, editor, *Twenty-Second Symposium on Naval Hydrodynamics*. National Academy Press, Washington, DC, 1999. ISBN 978-0-309-18453-3.

Cura, A. Virtual PMM tests for manoeuvring prediction. In Istituto Nazionale per Studi ed Esperienze di Architettura Navale, editor, *26th Symposium on Naval Hydrodynamics*, pages 17–22, 2006.

Dand, I. Low-speed manoeuvring criteria: some considerations. In International Marine Simulator Forum, editor, *International Conference on Marine Simulation and Ship Manoeuvrability 2003 (MARSIM'03)*, volume 1. Curran Associates, Inc., 2003. ISBN 978-1-62276-667-3.

de Verdieére, G. and Audren, V. Influence des Formes de Navires et de Gouvernails sur la Navigation en Canala. Comparaison du Modéle et du Réel. *Bulletin de l'Association Technique Maritime et Aéronautique*, 50, 1951.

Eloot, K. and Vantorre, M. Development of a tabular manoeuvring model for hull forces applied to full and slender ships in shallow water. In International Marine Simulator Forum, editor, *International Conference on Marine Simulation and Ship Manoeuvrability 2003 (MARSIM'03)*, volume 3. Curran Associates, Inc., 2003. ISBN 978-1-62276-667-3.

Eloot, K., Delefortrie, G., Vantorre, M., and Quadvlieg, F. Validation of Ship Manoeuvring in Shallow Water Through Free-Running Tests. In The American Society of Mechanical Engineers, editor, *Proceedings of the ASME 34th International Conference on Ocean, Offshore and Arctic Engineering - 2015*, New York, NY, 2015. ASME. ISBN 978-0-7918-5655-0. doi:10.1115/OMAE2015-41912.

Eloot, K., Vantorre, M., Delefortrie, G., and Lataire, E. Running Sinkage and Trim of the DTC Container Carrier in Harmonic Sway and Yaw Motion: Open Model Test Data for Validation Purposes. In Uliczka, K., Böttner, C.-U., Kastens, M., Eloot, K., Delefortrie, G., Vantorre, M., Candries, M., and Lataire, E., editors, *4th MASHCON - International Conference on Ship Manoeuvring in Shallow and Confined Water with Special Focus on Ship Bottom Interaction*, page 251, Karlsruhe, 2016. Bundesanstalt für Wasserbau. doi:10.18451/978-3-939230-38-0_29.

EMSA. Safety Analysis of EMCIP Data: Analysis of Navigation Accidents. V1.0, 2022, URL: `https://www.emsa.europa.eu/newsroom/latest-news/item/4830-safety-analysis-of-emcip-data-analysis-of-navigation-accidents.html` (accessed 01.10.2025).

Farmer, J., Martinelli, L., Cowles, G., and Jameson, A. Fully non-linear CFD techniques for ship performance analysis and design. In American Institute of Aeronautics and Astronautics, editor, *12th Computational Fluid Dynamics Conference*, Reston, Virigina, 1995. American Institute of Aeronautics and Astronautics. doi:10.2514/6.1995-1690.

Ferziger, J. H. and Perić, M. *Numerische Strömungsmechanik*. Springer, Berlin and Heidelberg, 2008. ISBN 978-3-540-67586-0. doi:10.1007/978-3-540-68228-8.

Ferziger, J. H., Perić, M., and Street, R. L. *Computational methods for fluid dynamics*. Springer, Cham, fourth edition edition, 2020. ISBN 978-3-319-99693-6. doi:10.1007/978-3-319-99693-6.

Fröhlich, J. *Large Eddy Simulation turbulenter Strömungen*. SpringerLink Bücher. B.G. Teubner Verlag / GWV Fachverlage GmbH, Wiesbaden, 2006. ISBN 978-3-8351-9051-1. doi:10.1007/978-3-8351-9051-1.

Fujino, M. Experimental studies on ship manoeuvrability in restricted waters. *International Shipbuilding Progress*, 15(168):279–301, 1968. ISSN 0020868X. doi:10.3233/ISP-1968-1516801.

Grim, O., Oltmann, P., Sharma, S. D., and Wolff, K. CPMC - A Novel Facility for Planar Motion Testing of Ship Models. *Hamburg University of Technology (TUHH). Schriftenreihe Schiffbau*, 345, 1976. doi:10.15480/882.750.

Gronarz, A. Application of hydrodynamic coefficients to manoeuvring simulation on variable water depth. In *Hydronav '99 - Manoeuvring '99*, pages 328–337. Technical University of Gdansk,, 1999. ISBN 8390956640.

Hachiya, Y., Sano, M., Okuda, R., Furukawa, Y., and Yasukawa, H. False Bottom Effect on the Hydrodynamics Forces Acting on a Ship Hull During an Oblique Towing Test and Countermeasures. In Candries, M., Lataire, E., Yuan, Z., Eloot, K., and Delefortrie, G., editors, *6th MASHCON*, pages 58–71. Knowledge Centre Manoeuvring in Shallow and Confined Water, 2022.

He, S., Kellett, P., Yuan, Z., Incecik, A., Turan, O., and Boulougouris, E. Manoeuvring prediction based on CFD generated derivatives. *Journal of Hydrodynamics*, 28(2):284–292, 2016. ISSN 1001-6058. doi:10.1016/S1001-6058(16)60630-3.

Hino, T., Hirata, N., Ohashi, K., Toda, Y., Zhu, T., Makino, K., Takai, M., Nishigaki, M., Kimura, K., Anda, M., et al. Hull form design and flow measurements of a bulk carrier with an energy-saving device for CFD validations. In Nielsen, U. D. and Jensen, J. J., editors, *2016 PRADS 13th triennial: Proceedings of the 13th International Symposium on Practical Design of Ships and Other Floating Structures*, pages 4–9. DTU Mechanical Engineering Technical University of Denmark, Lyngby, 2016. ISBN 9788774754732.

Hinostroza, M. A., Xu, H. T., and Guedes Soares, C. Manoeuvring test for a self-running ship model in various water depth conditions. In Georgiev, P. and Soares, C. G., editors, *Sustainable Development and Innovations in Marine Technologies*, pages 187–196. CRC Press, Place of publication not identified, 2019. ISBN 9780367810085. doi:10.1201/9780367810085-24.

Hirano, M., Takashina, J., Moriya, S., and Nakamura, Y. An Experimental Study on Maneuvering Hydrodynamic Forces in Shallow Water. *Transactions of the West-Japan Society of Naval Architects*, 69:101–110, 1985. doi:10.14856/wjsna.69.0_101.

IMO, editor. *Standards for ship manoeuvrability: Resolution MSC.137(76)*, London, 2002.

Ishiguro, T., Tanaka, S., and Yoshimura, Y. A study on the accuracy of the recent prediction technique of ship's manoeuvrability at early design stage. In Chislett, M. S., editor, *Marine Simulation and Ship Manoeuvrability: Proceedings of the international conference MARSIM '96*, pages 547–561, Leiden, The Netherlands, 1996. CRC Press/A. A. Balkema. ISBN 978-90-5410-831-3.

ITTC, editor. *Proceedings of the 9th International Towing Tank Conference - Manoeuvrability*, 1960.

ITTC, editor. *Proceedings of the 11th International Towing Tank Conference - Report of Manoeuvrability Comittee*, 1966.

ITTC, editor. *Recommended Procedures and Guidelines: Full Scale Manoeuvring Trials*, 2002.

ITTC, editor. *Proceedings of the 24th International Towing Tank Conference (Vol. 1): The Manoeuvrability Comittee - Final Report and Recommendations to the 25th ITTC*, 2005.

ITTC, editor. *Proceedings of the 25th International Towing Tank Conference (Vol. 1): The Manoeuvrability Comittee - Final Report and Recommendations to the 25th ITTC*, 2008.

ITTC, editor. *Recommended Procedures and Guidelines: Captive Model Test Procedure*, 2014.

ITTC, editor. *Proceedings of the 28th International Towing Tank Conference (Vol. 1): The Manoeuvrability Comittee - Final Report and Recommendations to the 28th ITTC*, 2017.

ITTC, editor. *Recommended Procedures and Guidelines: Free Running Model Tests*, 2021.

ITTC, editor. *Recommended Procedures and Guidelines: Uncertainty Analysis in CFD Verification and Validation Methodology and Procedures*, 2024.

Jones, W. and Launder, B. The prediction of laminarization with a two-equation model of turbulence. *International Journal of Heat and Mass Transfer*, 15(2):301–314, 1972. ISSN 00179310. doi:10.1016/0017-9310(72)90076-2.

Journée, J. and Pinkster, J. *Introduction in Ship Hydromechanics.* Delft University of Technology, 2002.

Kaneko, T. and Kijima, K. On Estimation for Hydrodynamic Forces Acting on a Ship Hull in Shallow Water. *Transactions of the West-Japan Society of Naval Architects*, 102, 2001.

Kempf, G. Manövriernorm für Schiffe: 248. Mitteilung der Hamburgischen Schiffbau-Versuchsanstalt. *HANSA*, 81(27/28):372–377, 1944.

Kijima, K. Ship Maneuverability in Shallow Water. In National Research Council, editor, *Twenty-Fifth Symposium on Naval Hydrodynamics*, Washington, D.C., 2005. The National Academies Press. ISBN 978-0-309-29811-7.

Kijima, K., Furukawa, Y., Eshima, M., and Yamamoto, K. Influence of Roll Motion on Ship Manoeuvrability. *Transactions of the West-Japan Society of Naval Architects*, 93: 35–46, 1997. doi:10.14856/wjsna.93.0_35.

Kim, D., Tezdogan, T., and Incecik, A. Hydrodynamic analysis of ship manoeuvrability in shallow water using high-fidelity URANS computations. *Applied Ocean Research*, 123: 103176, 2022. ISSN 01411187. doi:10.1016/j.apor.2022.103176.

Kim, G. and Lim, S. Development of an Interpretable Maritime Accident Prediction System Using Machine Learning Techniques. *IEEE Access*, 10:41313–41329, 2022. ISSN 2169-3536. doi:10.1109/ACCESS.2022.3168302.

Koseki, N., Yamanouchi, Y., Matsuoka, S., and Yamazaki, Y. Some Model Experiments on Shallow Water Effects upon Turning Ability. *Journal of Zosen Kiokai*, 1965(117): 139–145, 1965. ISSN 1884-2062. doi:10.2534/jjasnaoe1952.1965.139.

Launder, B. E. and Sharma, B. I. Application of the energy-dissipation model of turbulence to the calculation of flow near a spinning disc. *Letters in Heat and Mass Transfer*, 1(2): 131–137, 1974. ISSN 00944548. doi:10.1016/0094-4548(74)90150-7.

Lee, S. and Hong, C. Study on the course stability of very large vessels in shallow water using CFD. *Ocean Engineering*, 145:395–405, 2017. ISSN 00298018. doi:10.1016/j.oceaneng.2017.09.064.

Leigh, E. On the Steering of Ships. In Institution of Naval Architects, Reed, E. J., Woolley, A. S., and Holmes, G., editors, *Transactions of the Institution of Naval Architects*. Institution of Naval Architects, 1871.

Lewis, E. V., editor. *Principles of naval architecture. Volume III, Motions in waves and controllability*. The Society of Naval Architects and Marine Engineers, Jersey City, NJ, 2nd revision edition, 1989. ISBN 0-939773-02-3.

Li, Y., Landsburg, A. C., Barr, R. A., and Calisal, S. M. Improving Ship Maneuverability Standards as a Means for Increasing Ship Controllability and Safety. In *Oceans 2005*, pages 1–10, Piscataway, NJ, 2006. IEEE Operations Center. ISBN 0-933957-34-3. doi:10.1109/OCEANS.2005.1640048.

Lien, F. S., Chen, W. L., and Leschziner, M. A. Low-Reynolds-Number Eddy-Viscosity Modelling Based on Non-Linear Stress-Strain/Vorticity Relations. In Rodi, W. and Bergeles, G., editors, *Engineering turbulence modelling and experiments 3*, Elsevier series in thermal and fluid sciences, pages 91–100. Elsevier Science, 1996. ISBN 978-0-444-82463-9. doi:10.1016/B978-0-444-82463-9.50015-0.

Liu, Y., Zou, Z. J., and Zou, L. RANS-based Numerical Simulation of Captive Model Tests in Shallow Water for the DTC Container Carrier. In Uliczka, K., Böttner, C.-U., Kastens, M., Eloot, K., Delefortrie, G., Vantorre, M., Candries, M., and Lataire, E., editors, *4th MASHCON - International Conference on Ship Manoeuvring in Shallow and Confined Water with Special Focus on Ship Bottom Interaction*, Karlsruhe, 2016. Bundesanstalt für Wasserbau. doi:10.18451/978-3-939230-38-0_10.

Liu, Y., Zou, Z., Zou, L., and Fan, S. CFD-based numerical simulation of pure sway tests in shallow water towing tank. *Ocean Engineering*, 189:106311, 2019. ISSN 00298018. doi:10.1016/j.oceaneng.2019.106311.

Lu, H. S., Chu, W. W., Fei, N. Z., and Wang, W. F. Some results from free-sailing model tests on water depth effect on manoeuvring performance. In ITTC, editor, *Proceedings of the 18th International Towing Tank Conference (Vol. 2) - Session on Manoeuvrability*, pages 215–217, 1987.

Maljković, M., Pavić, I., Meštrović, T., and Perkovič, M. Ship Maneuvering in Shallow and Narrow Waters: Predictive Methods and Model Development Review. *Journal of Marine Science and Engineering*, 12(8):1450, 2024. ISSN 2077-1312. doi:10.3390/jmse12081450.

Martinussen, K. and Linnerud, I. Techniques for predicting manoeuvring characteristics of ships at the design stage. In The Royal Institution of Naval Architects, editor, *International Conference on Ship Manoeuvrability–Prediction and Achievement*, 1987.

Mehr, J. and Javanmardi, M. Influence of water depth on roll motion of large commercial vessels in shallow water regions. 2023, URL: `https://figshare.utas.edu.au/articles/conference_contribution/Influence_of_water_depth_on_roll_motion_of_large_commercial_vessels_in_shallow_water_regions/25209656` (accessed 07.10.2025).

Menter, F., Kuntz, M., and Langtry, R. B. Ten years of industrial experience with the SST turbulence model. In Hanjalić, K., Nagano, Y., and Tummers, M. J., editors, *Turbulence, heat and mass transfer 4*. Begell House, New York, NY, 2003. ISBN 1567001963.

Menter, F. R. Two-equation eddy-viscosity turbulence models for engineering applications. *AIAA Journal*, 32(8):1598–1605, 1994. ISSN 0001-1452. doi:10.2514/3.12149.

Milanov, E. M. and Chotukova, V. Y. Roll Motion of Containership in Shallow Water. In Eloot, K. and Vantorre, M., editors, *International Conference on Ship Manoeuvring in Shallow and Confined Water: Bank Effects*, pages 99–104, London, 2009. The Royal Institution of Naval Architects. ISBN 9781905040469. doi:10.3940/rina.bank.2009.10.

Moctar, O. e., Shigunov, V., and Zorn, T. Duisburg Test Case: Post-Panamax Container Ship for Benchmarking. *Ship Technology Research*, 59(3):50–64, 2012. ISSN 0937-7255. doi:10.1179/str.2012.59.3.004.

Motora, S. Proposed Manoeuvrability Indices as a Measure of the Steering Qualities of Ships. In ITTC, editor, *Proceedings of the 9th International Towing Tank Conference - Manoeuvrability*, 1960.

Motora, S. and Couch, R. B. *Manoeuvrability of full bodied ships in restricted waters.* Society of Naval Architects and Marine Engineers, 1961.

Nakao, I., Iseki, T., and Ohtsu, K. The Effect of Heading Angle on Ship Maneuvering in Confined Water. *The Journal of Japan Institute of Navigation*, 93(0):171–178, 1995. ISSN 0388-7405. doi:10.9749/jin.93.171.

Neitzel, J. C., Pergande, M., Berger, S., and Abdel-Maksoud, M. Influence of the numerical propulsion modelling on the velocity distribution behind the propulsion device and maneuvering forces. In *Fourth International Symposium on Marine Propulsors smp'15*, 2015. ISBN 978-0-9964594-4-0.

Nomoto, K. A simplified analysis on ship motion under manoeuvre and proposed steering quality indices. In ITTC, editor, *Proceedings of the 10th International Towing Tank Conference (Vol. 2) - Manoeuvrability Comittee Formal Contributions*, 1963.

Nomoto, K. Analysis of the ITTC Manoeuvrability Tests for the Mariner Type Ship in terms of Steering Quality Indices K and T. In ITTC, editor, *Proceedings of the 11th International Towing Tank Conference - Report of Manoeuvrability Comittee*, 1966.

Nomoto, K. and Norrbin, N. A review of methods of defining and measuring the manoeuvrability of ships. In ITTC, editor, *Proceedings of 12th International Towing Tank Conference - Report of Manoeuvrability Comittee*, 1969.

Nomoto, K. and Taguchi, K. On Steering Qualities of Ships (2). *Journal of Zosen Kiokai*, 1957(101):57–66, 1957. ISSN 1884-2062. doi:10.2534/jjasnaoe1952.1957.101_57.

Ohmori, T. A study on hydrodynamic characteristics of a maneuvering ship in shallow water by a finite-volume method. In *MAN'98: International Symposium and Workshop on Forces Acting on a Manoeuvring Vessel*, 1998.

Ohmori, T. Viscours Flow Simulation of KVLCC2 in Shallow Water. In *SIMMAN 2020: Workshop on Verification and Validation of Ship Manoeuvring Simulation Methods: Workshop Proceedings*, 2024.

Oltmann, P. Bestimmung der Manövriereigenschaften aus den Bahnkurven freimanövrierender Schiffsmodelle. *Hamburg University of Technology (TUHH). Schriftenreihe Schiffbau*, 364, 1978. doi:10.15480/882.679.

Oltmann, P. and Sharma, S. D. Simulation of combined engine and rudder maneuvers using an improved model of hull-propeller-rudder interactions. *Hamburg University of Technology (TUHH). Schriftenreihe Schiffbau*, 444, 1984. doi:10.15480/882.929.

PIANC. *Capability of ship manoeuvring simulation models for approach channels and fairways in harbours: Report of Working Group no. 20 of Permanent Technical Committee II.* Supplement to Bulletin 77. Permanent International Association of Navigation Congresses, Bruxelles, 1992. ISBN 2872230408.

Quadvlieg, F. and van Coevorden, P. Manoeuvring criteria: more than IMO A751 requirements alone! In International Marine Simulator Forum, editor, *International Conference*

on Marine Simulation and Ship Manoeuvrability 2003 (MARSIM'03), volume 2. Curran Associates, Inc., 2003. ISBN 978-1-62276-667-3.

Quadvlieg, F., Stern, F., Simonsen, C. D., and Otzen, J. F., editors. *SIMMAN 2014: Workshop on Verification and Validation of Ship Manoeuvering Simulation Methods: Workshop Proceedings*, 2014.

RoyChoudhury, S., Dash, A. K., Nagarajan, V., and Sha, O. P. CFD simulations of steady drift and yaw motions in deep and shallow water. *Ocean Engineering*, 142:161–184, 2017. ISSN 00298018. doi:10.1016/j.oceaneng.2017.06.058.

Sadler, C. The resistance of some merchant ship types in shallow water. In Society of Naval Architects and Marine Engineers, editors, *Transactions - The Society of Naval Architects and Marine Engineers*, volume 19. New York, Society of Naval Architects and Marine Engineers, 1911.

Sakamoto, N., Ohashi, K., Kobayashi, H., and Hino, T. Overset RaNS simulations and validations for the effect of false bottom to the KCS under static drift and static rudder in shallow water. *Journal of Marine Science and Technology*, 28(1):248–269, 2023. ISSN 0948-4280.

Sato, T., Izumi, K., and Miyata, H. Numerical Simulation of Maneuvering Motion. In National Research Council, editor, *Twenty-Second Symposium on Naval Hydrodynamics*. National Academy Press, Washington, DC, 1999. ISBN 978-0-309-18453-3.

Saunders, H. E. *Hydrodynamics in Ship Design Vol. 3: Author's Notes for Volume Three on Maneuvering and Wavegoing. Edited by R. Taggart.* Society of Naval Architects and Marine Engineers, New York, N. Y., 1965.

Schlichting, H. and Gersten, K. *Grenzschicht-Theorie: Mit 22 Tabellen*. Springer, Heidelberg, 10. überarbeitete auflage edition, 2006. ISBN 9783540329855. doi:10.1007/3-540-32985-4.

Schlichting, O. Schiffswiderstand auf beschränkter Wassertiefe - Widerstand von Seeschiffen auf flachem Wasser. In Schiffbautechnische Gesellschaft, editor, *Jahrbuch der Schiffbautechnischen Gesellschaft*, volume 35. Deutsche Verlagswerke Strauß, Vetter & Co, 1934.

Schmidt-Stiebitz, H. Einfluß der Hauptspantform auf den Drehkreis von Flachwasserschiffen. *Schiffstechnik: Forschungshefte für Schiffbau u. Schiffsmaschinenbau*, Band 5(28): 140–148, 1958a. ISSN 0036-6064.

Schmidt-Stiebitz, H. *Forschungsberichte des Wirtschafts- und Verkehrsministeriums Nordrhein-Westfalen Nr. 476: Einfluß der Hinterschiffsform auf das Manövrieren von Schiffen auf flachem Wasser*. Westdeutscher Verlag, Köln und Opladen, 1958b. ISBN 978-3-663-03585-5.

Schmidt-Stiebitz, H. Untersuchungen über den Einfluß der Hauptspantform auf das Drehkreisverhalten von Flachwasserschiffen: Teil II: Schrägschleppfahrten. *Schiffstechnik: Forschungshefte für Schiffbau u. Schiffsmaschinenbau*, Band 6(32):117–129, 1959. ISSN 0036-6064.

Schwarze, R. *CFD-Modellierung: Grundlagen und Anwendungen bei Strömungsprozessen*. Springer Berlin Heidelberg, Berlin, Heidelberg, 2012. ISBN 978-3-642-24378-3. doi:10.1007/978-3-642-24378-3.

Shiba, H. Model experiments about the maneuverability and turning of ships. In David Taylor Model Basin, editor, *First Symposium on Ship Maneuverability*, David Taylor Model Basin Report. David Taylor Model Basin, Washington, DC, 1960.

Siemens. *Simcenter STAR-CCM+ 2302 User Guide*. Unpublished manual. 2023.

Simonsen, C. D. and Stern, F. RANS Maneuvering Simulation of Esso Osaka With Rudder and a Body-Force Propeller. *Journal of Ship Research*, 49(02):98–120, 2005. ISSN 0022-4502. doi:10.5957/jsr.2005.49.2.98.

Sturtzel, W. and Schmidt-Stiebitz, H. *Bei Flachwasserfahrten durch die Strömungsverteilung am Boden und an den Seiten stattfindende Beeinflussung des Reibungswiderstandes von Schiffen*, volume 366 of *Forschungsberichte des Wirtschafts- und Verkehrsministeriums Nordrhein-Westfalen*. VS Verlag für Sozialwissenschaften, Wiesbaden, 1957. ISBN 978-3-663-03254-0. doi:10.1007/978-3-663-04443-7.

Tahara, Y., Longo, J., and Stern, F. Comparison of CFD and EFD for the Series 60 CB = 0.6 in steady drift motion. *Journal of Marine Science and Technology*, 7(1):17–30, 2002. ISSN 0948-4280. doi:10.1007/s007730200010.

Taylor, D. W. Relative resistances of some models with block coefficient constant and other coefficients varied. *Transactions - The Society of Naval Architects and Marine Engineers*, 21:1–7, 1913. ISSN 0081-1661.

Toxopeus, S. L. Viscous-Flow Calculations for KVLCC2 in Deep and Shallow Water. In Eça, L., Oñate, E., García-Espinosa, J., Kvamsdal, T., and Bergan, P., editors, *MARINE 2011, IV International Conference on Computational Methods in Marine Engineering*, volume 29 of *Computational Methods in Applied Sciences*, pages 151–169. Springer, Dordrecht, 2013. ISBN 978-94-007-6142-1. doi:10.1007/978-94-007-6143-8_9.

van Hoydonck, W., Delefortrie, G., and Eloot, K. Prediction of hydrodynamic forces on KVLCC2 in shallow water using rans simulations. In *SIMMAN 2020: Workshop on Verification and Validation of Ship Manoeuvring Simulation Methods: Workshop Proceedings*, pages 56–61, 2024.

Vantorre, M. and Eloot, K. Hydrodynamic phenomena affecting manoeuvres at low speed in shallow navigation areas. In Smitz, H. and Thues, G., editors, *International Harbour Congress, 11th, Proceedings*, pages 535–546. Royal Flemish Society of Engineers. Section on Harbour Techniques, 1996. ISBN 9052040303.

Wang, H. M., Chen, X. Y., Yu, H. M., Chen, L., Wang, T., Xu, J. R., and Wang, X. F. Numerical simulation of the viscous flow around ships turning in shallow water. *International Journal of Maritime Engineering*, 164(A3), 2023. ISSN 1479-8751. doi:10.5750/ijme.v164iA3.1242.

Wilcox, D. C. Reassessment of the scale-determining equation for advanced turbulence models. *AIAA Journal*, 26(11):1299–1310, 1988. ISSN 0001-1452.

Wilcox, D. C. *Turbulence modeling for CFD*. DCW Industries, La Cañada, California, 3. ed edition, 2006. ISBN 978-1-928729-08-2.

Xing, T. and Stern, F. Factors of Safety for Richardson Extrapolation. *Journal of Fluids Engineering*, 132(6), 2010. ISSN 0098-2202. doi:10.1115/1.4001771.

Xu, L. and Wang, Y. Y. The Fine Optimization of Ship Hull Lines in Resistance Performance By Using CFD Approach. In *Practical design of ships and other floating structures*, pages 59–65. Elsevier, Amsterdam and New York, 2001. ISBN 9780080439501. doi:10.1016/B978-008043950-1/50008-9.

Yamanouchi, Y. Series model experiments on the effect of ship form and proportions on manoeuvrability in Japan. In ITTC, editor, *Proceedings of the 11th International Towing Tank Conference - Report of Manoeuvrability Comittee*, 1966.

Yasukawa, H. Maneuvering Response of a Slender Ship with Sinusoidal Steering in Shallow Waters. *Transactions of the West-Japan Society of Naval Architects*, 94:89–99, 1997. doi:10.14856/wjsna.94.0_89.

Yasukawa, H. and Kobayashi, E. Shallow water model experiments on ship turning performance. In *Mini Symposium on Ship Manoeuvrability*, volume 26, pages 71–83, 1995.

Yasukawa, H. and Yoshimura, Y. Introduction of MMG standard method for ship maneuvering predictions. *Journal of Marine Science and Technology*, 20(1):37–52, 2015. ISSN 0948-4280. doi:10.1007/s00773-014-0293-y.

Yeo, D. J., Yun, K., and Kim, Y. Experimental Study on the Manoeuvrability of KVLCC2 in Shallow Water. In Uliczka, K., Böttner, C.-U., Kastens, M., Eloot, K., Delefortrie, G., Vantorre, M., Candries, M., and Lataire, E., editors, *4th MASHCON - International Conference on Ship Manoeuvring in Shallow and Confined Water with Special Focus on Ship Bottom Interaction*, pages 287–294, Karlsruhe, 2016. Bundesanstalt für Wasserbau. doi:10.18451/978-3-939230-38-0_32.

Yoshimura, Y. Mathematical Model for the Manoeuvring Ship Motion in Shallow Water. *Journal of the Kansai Society of Naval Architects*, 200:41–51, 1986. ISSN 2433-104X. doi:10.14856/kansaiks.200.0_41.

Yoshimura, Y. Mathematical Model for the Manoeuvring Ship Motion in Shallow Water (2nd Report): Mathematical Model at Slow Forward Speed. *Journal of the Kansai Society of Naval Architects*, 210:77–84, 1988. ISSN 2433-104X. doi:10.14856/kansaiks.210.0_77.

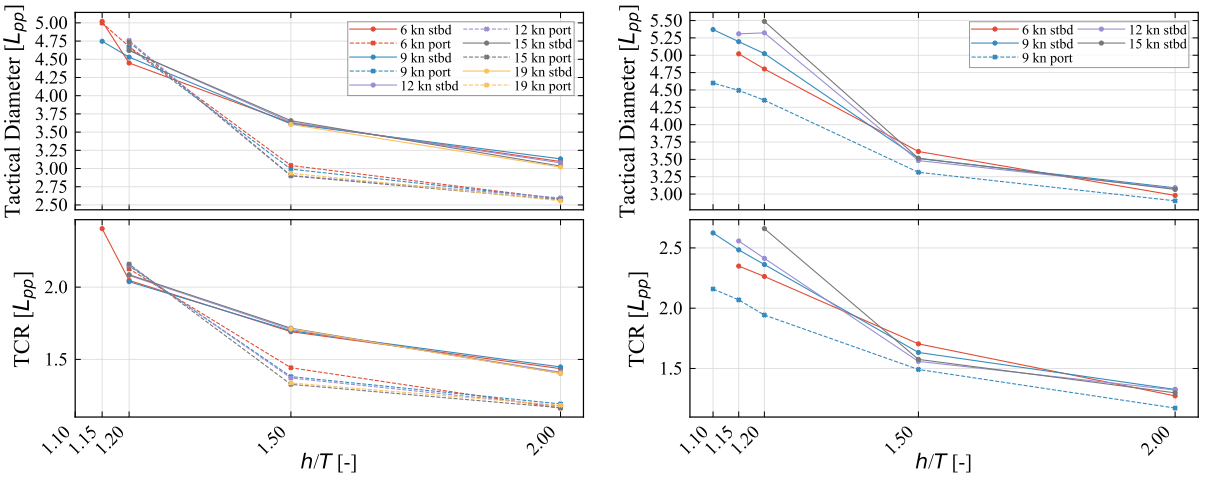
Yoshimura, Y. and Sakurai, H. Mathematical Model for the Manoeuvring Ship Motion in Shallow Water (3rd Report): Manoeuvrability of a Twin-propeller Twin-rudder ship. *Journal of the Japan Society of Naval Architects and Ocean Engineers*, 211:115–126, 1989. ISSN 1881-1760. doi:10.14856/kansaiks.211.0_115.

Yun, K., Yeo, D. J., and Park, B. A Study on the Manoeuvrability of KVLCC2 in Shallow Water by Free Running Model Test. *Journal of the Society of Naval Architects of Korea*, 52(6):494–500, 2015. ISSN 1225-1143. doi:10.3744/SNAK.2015.52.6.494.

Zwart, P. J., Godin, P. G., Penrose, J., and Rhee, S. H. Simulation of unsteady free-surface flow around a ship hull using a fully coupled multi-phase flow method. *Journal of Marine Science and Technology*, 13(4):346–355, 2008. ISSN 0948-4280. doi:10.1007/s00773-008-0012-7.

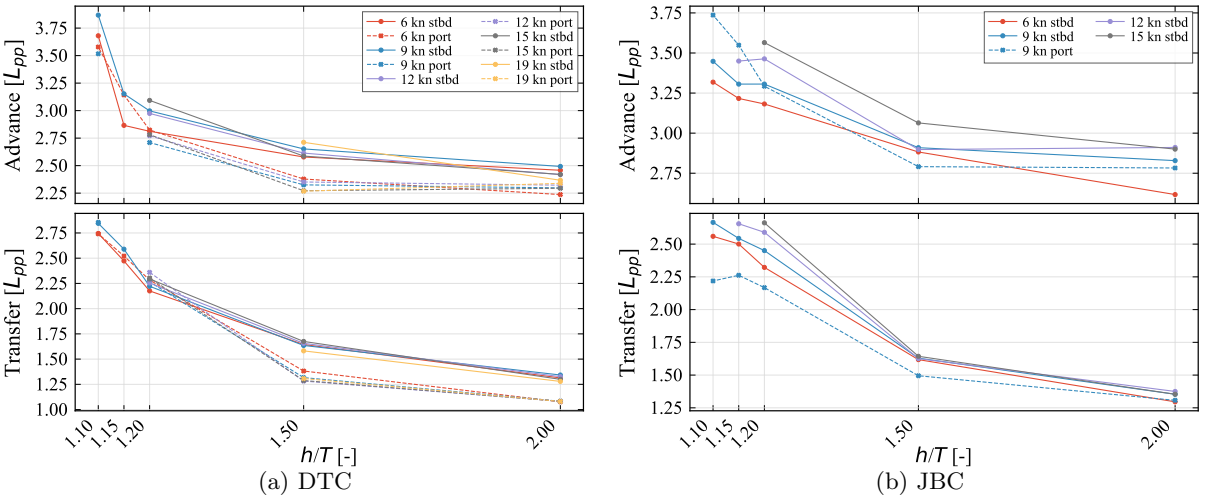
Appendices

A. Turning Circle Parameters as a Function of the h/T Ratio



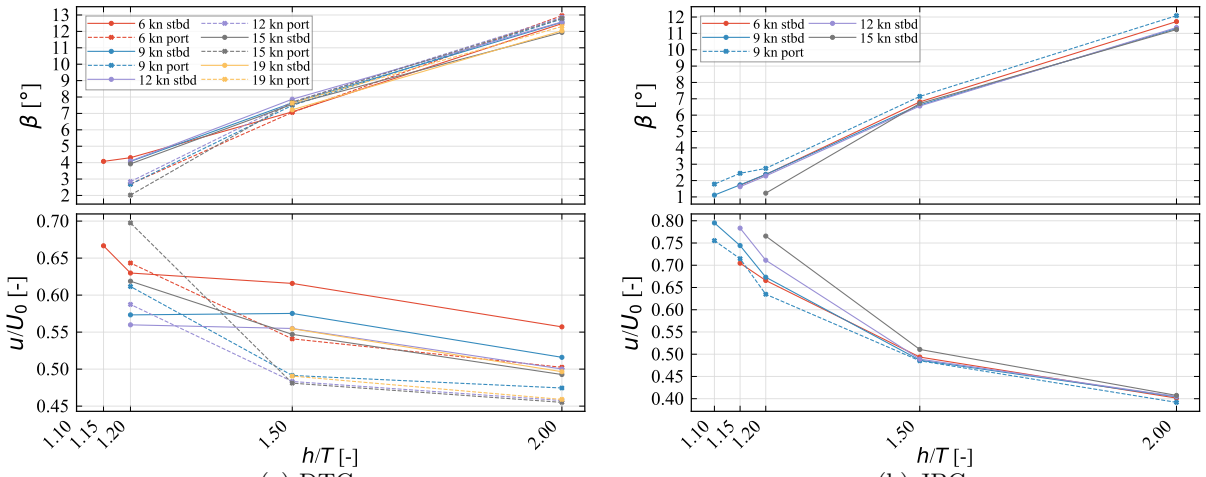
(a) DTC (b) DTC

Figure A.1.: Tactical diameter and TCR of the 35° turning circle manoeuvre at design condition



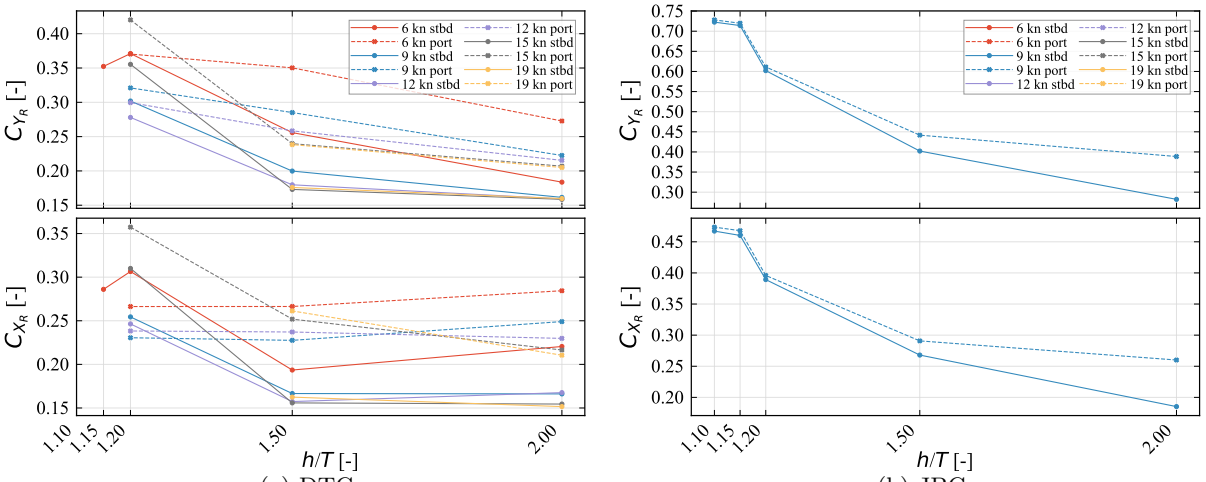
(a) DTC (b) JBC

Figure A.2.: Advance and transfer of the 35° turning circle manoeuvre at design condition



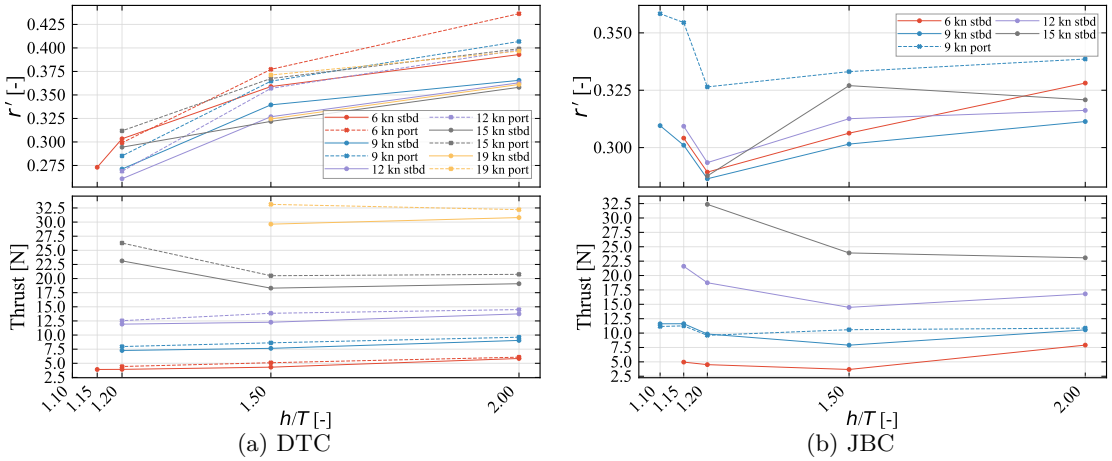
(a) DTC (b) JBC

Figure A.3.: Steady drift angle and surge velocity of the 35° turning circle manoeuvre at design condition



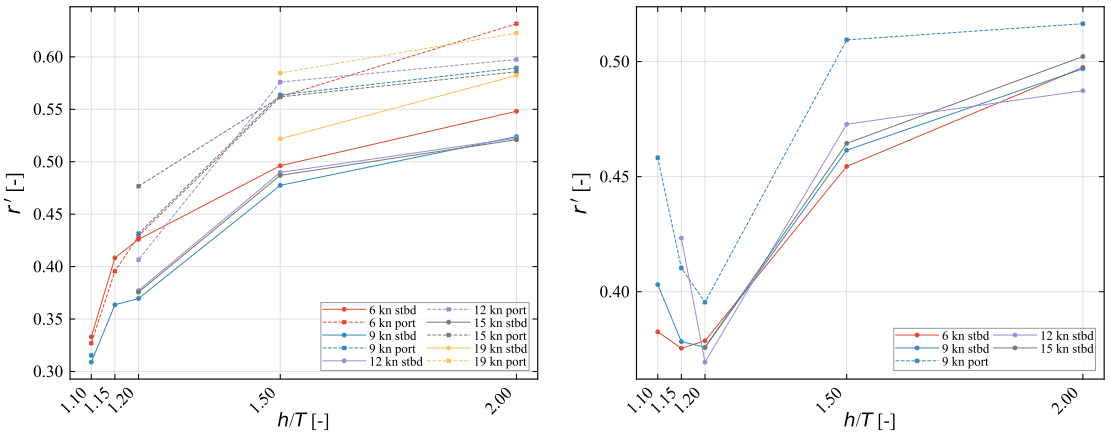
(a) DTC (b) JBC

Figure A.4.: Steady rudder transverse and longitudinal force of the 35° turning circle manoeuvre at design condition



(a) DTC (b) JBC

Figure A.5.: Steady yaw rate and propeller thrust of the 35° turning circle manoeuvre at design condition



(a) DTC (b) JBC

Figure A.6.: Maxiumum yaw rate for the 35° turning circle manoeuvre at design condition

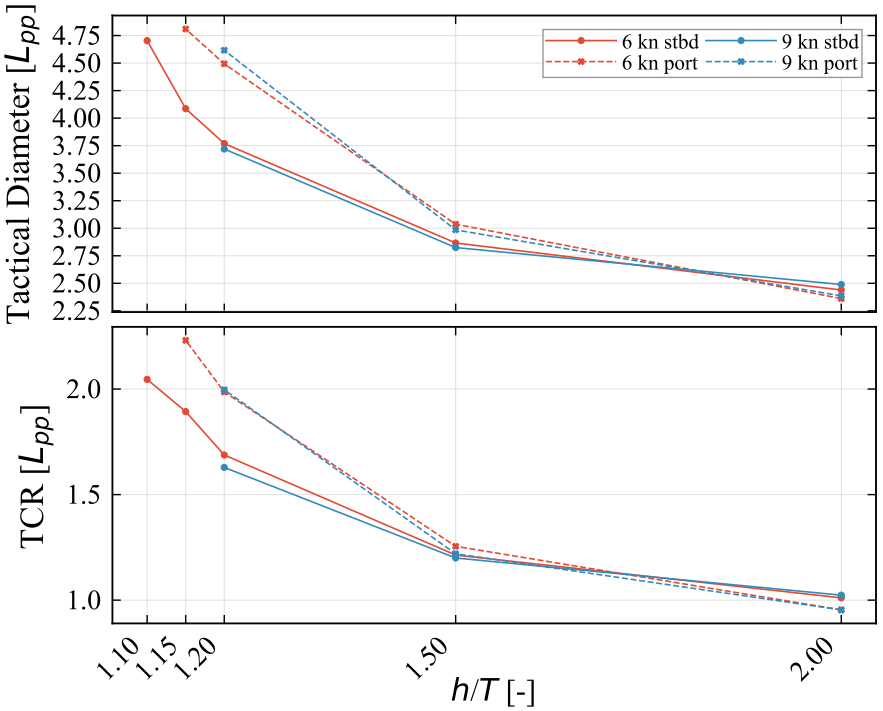
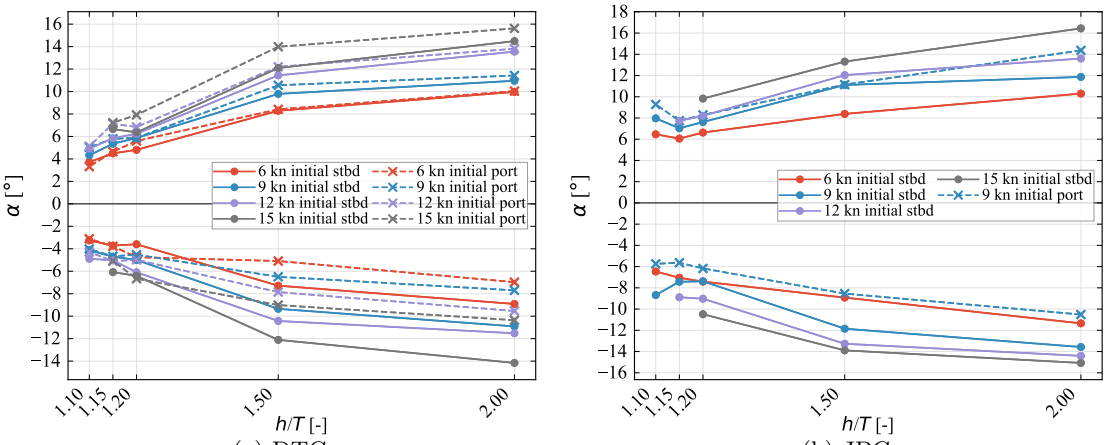


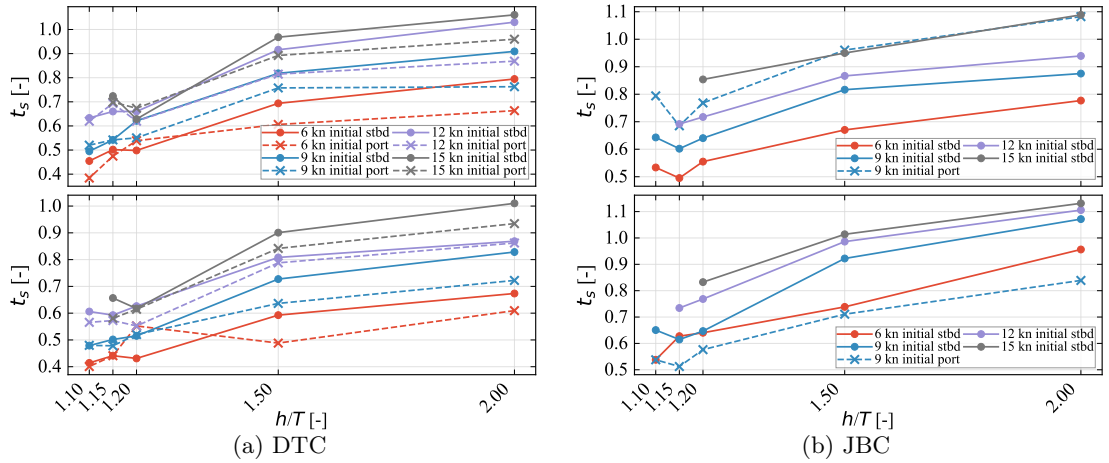
Figure A.7.: Tactical diameter and turning circle radius of the 45° turning circle manoeuvre at design condition

B. Zig-Zag Parameters as a Function of the h/T Ratio



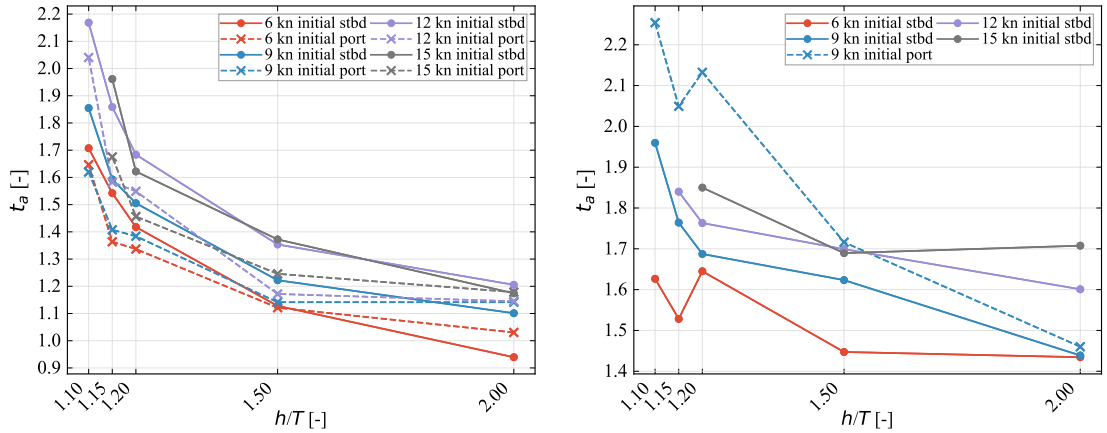
(a) DTC (b) JBC

Figure B.1.: First (positive) and second (negative) overshoot angles of the Z 35-20 manoeuvre at design condition



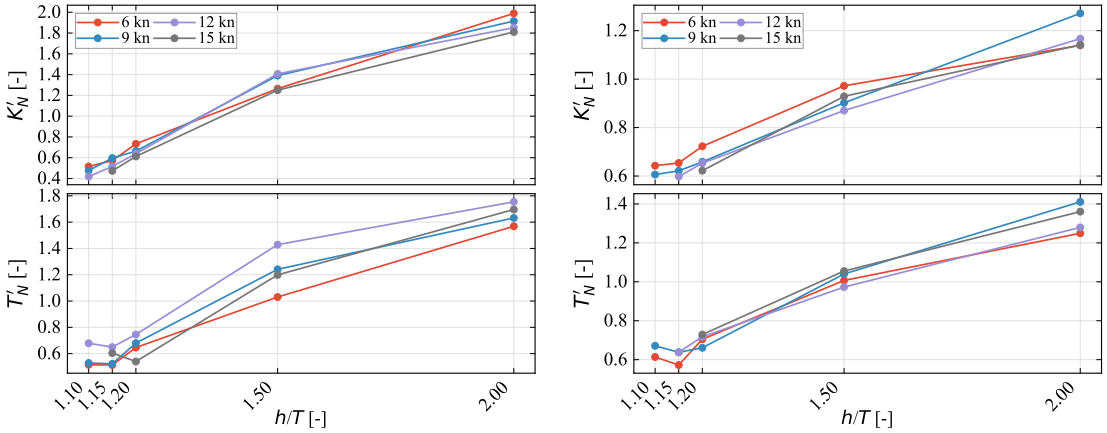
(a) DTC (b) JBC

Figure B.2.: First (top) and second (bottom) yaw-checking time for the 35-20 Zig-Zag manoeuvre at design condition



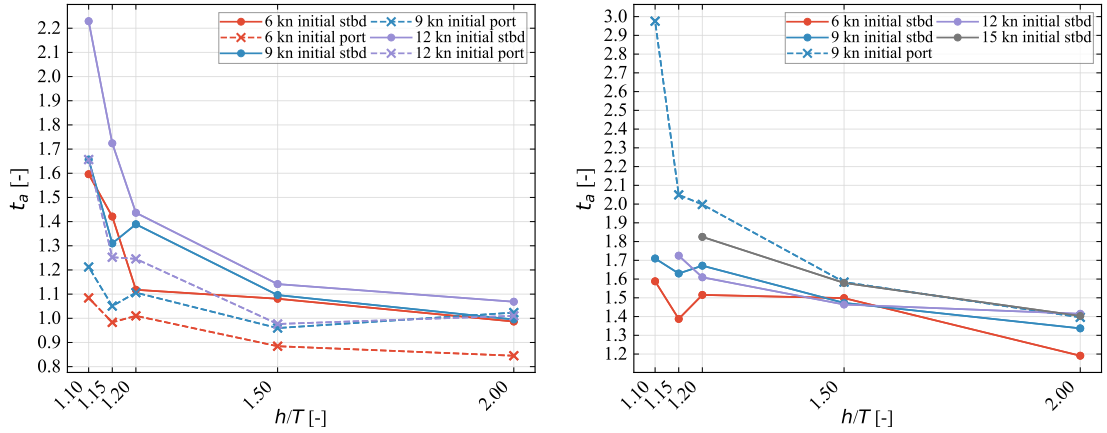
(a) DTC (b) JBC

Figure B.3.: Initial turning time for the 35-20 Zig-Zag manoeuvre at design condition



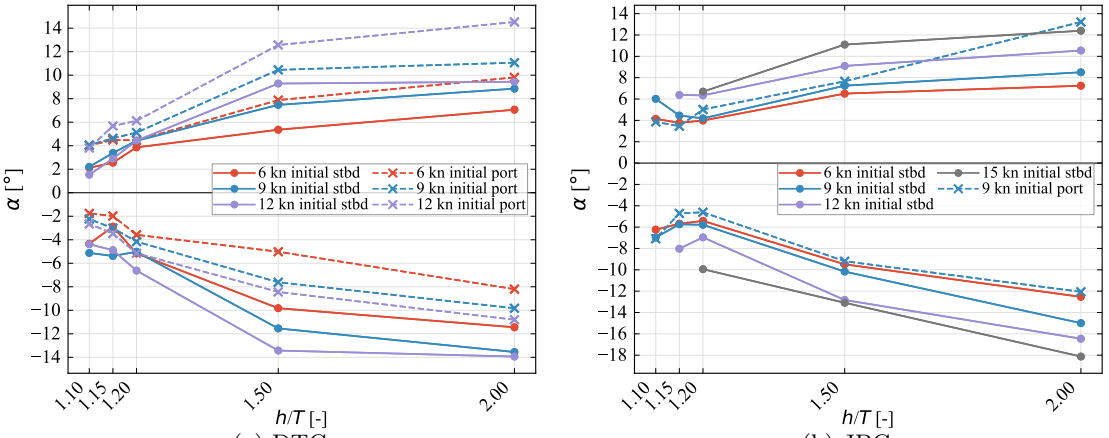
(a) DTC (b) JBC

Figure B.4.: Nomoto coefficients K'_N and T'_N for the 35-20 Zig-Zag manoeuvre at design condition



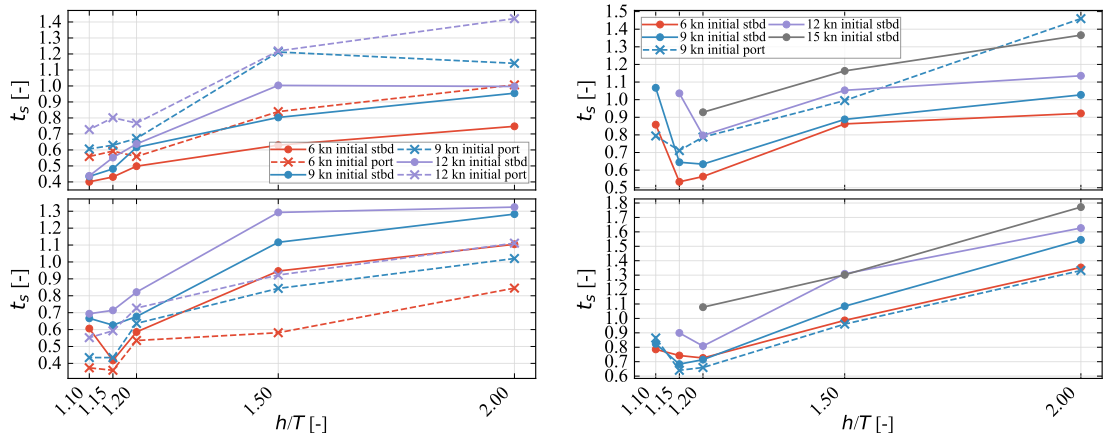
(a) DTC (b) JBC

Figure B.5.: Initial turning time for the 20-10 Zig-Zag manoeuvre at design condition



(a) DTC (b) JBC

Figure B.6.: First (positive) and second (negative) overshoot angles of the Z 20-10 manoeuvre at design condition



(a) DTC (b) JBC

Figure B.7.: First (top) and second (bottom) yaw-checking time for the 20-10 Zig-Zag manoeuvre at design condition